Study of the production of (anti-)hypertriton at the LHC with the ALICE experiment

Stefano Trogolo

Ph.D. Thesis

Università degli studi di Torino
Scuola di Dottorato in Scienze della Natura e della Tecnologie Innovative
Dipartimento di Fisica

Supervisor: Prof.ssa Elena Botta

Co-supervisor: Prof.ssa Stefania Bufalino

Abstract

In the ultra-relativistic heavy ion collisions at the CERN Large Hadron Collider (LHC), a state of matter, called Quark Gluon Plasma (QGP), is created. A typical signature of a heavy ion collision related to the production of the QGP is the large number of particles produced ($\mathrm{d}N_{\mathrm{ch}}/\mathrm{d}\eta$ up to 2000 in Pb–Pb collisions at $\sqrt{s_{\mathrm{NN}}}$= 5.02 TeV). This high multiplicity environment is a big experimental challenge, since the experiments have to cope with a high density of signals in their sensitive volume. A Large Ion Collider Experiment (ALICE) has been designed to deal with such environment in order to study in details the characteristics of the QGP. Among the several particles produced in a heavy ion collision, light (anti-)hypernuclei are of special interest since the production mechanism of such loosely bound states is not clear at present in high energy collisions. In particular, this thesis is focused on the study of the production and the measurement of the lifetime of the lightest known Λ-hypernucleus, the hypertriton ($^{3}_{\Lambda}\mathrm{H}$) which is a bound state of a proton, a neutron and a Λ. The production rate at the LHC for this light hypernucleus is of the order of one every ten thousands Pb–Pb collisions with the highest charged particle density.

The first goal of this work is the measurement of the $^{3}_{\Lambda}\mathrm{H}$ and $^{3}_{\Lambda}\overline{\mathrm{H}}$ production in Pb–Pb collisions at $\sqrt{s_{\mathrm{NN}}}$= 5.02 TeV with the ALICE experiment. In particular the hypertriton transverse momentum spectra have been studied together with their evolution with the particle multiplicity of the collision to have a comparison with the prediction of the models that are tipically used to describe the particle production in heavy ion collision, namely statistical-thermal and coalescence models.

The second part of this thesis is related to an open question of the hypernuclear physics and in particular to the lifetime of the hypertriton. Indeed, since the beginning of the research in this field, the theory pre-

dicted the hypertriton lifetime to be close to the one of the free Λ. Many experiments using different techniques tried to face this challenge and recently new interest on this topic has been raised by the results obtained in heavy ion collision experiments, which showed a trend well below the expectation. Thus the measurement of the ${}^{3}_{\Lambda}\mathrm{H}$ lifetime by analysing the data sample of Pb–Pb collisions at $\sqrt{s_{\mathrm{NN}}}$= 5.02 TeV collected by the ALICE experiment has been determined. In particular, it will be presented the lifetime determination via 2 body decay channel (${}^{3}_{\Lambda}\mathrm{H} \rightarrow {}^{3}\mathrm{He} + \pi^{-}$) using two different methods and the first estimate of the lifetime obtained via 3 body decay channel (${}^{3}_{\Lambda}\mathrm{H} \rightarrow \mathrm{d} + \mathrm{p} + \pi^{-}$).

Sommario

Nelle collisioni ultrarelativistiche tra ioni pesanti al Large Hadron Collider (LHC) del CERN viene creato uno stato della materia chiamato Plasma di Quark e Gluoni (QGP). Una delle caratteristiche peculiari delle collisioni fra ioni pesanti legata alla creazione del QGP è l'abbondante produzione di particelle ($\mathrm{d}N_{\mathrm{ch}}/\mathrm{d}\eta$ fino a 2000 in collisioni Pb–Pb all'energia $\sqrt{s_{\mathrm{NN}}}$= 5.02 TeV). L'identificazione e la ricostruzione di un così elevato numero di particelle prodotte rappresenta una sfida per gli esperimenti, che devono essere in grado di acquisire una grande densita di segnali nei loro rivelatori di particelle. A Large Ion Collider Experiment (ALICE) è stato progettato per far fronte alle condizioni estreme delle collisioni fra ioni pesanti e per studiare nel dettaglio le caratteristiche del QGP. Tra le molte particelle prodotte in una collisione, gli (anti-)ipernuclei leggeri sono di particolare interesse poichè il meccanismo di produzione ad alta energia di questi stati debolmente legati non è ancora chiaro. In particolare, questa tesi riguarda lo studio della produzione e la misura della vita media del più leggero Λ-ipernucleo conosciuto, l'ipertrizio ($^{3}_{\Lambda}\mathrm{H}$), uno stato legato di protone, neutrone e Λ. Il tasso di produzione per questo ipernucleo è di uno ogni mille collisioni Pb–Pb centrali, ossia quelle con la maggior densità di particelle cariche prodotte.

Il primo obiettivo di questo lavoro è la misura della produzione di $^{3}_{\Lambda}\mathrm{H}$ e $^{\overline{3}}_{\overline{\Lambda}}\overline{\mathrm{H}}$ nelle collisioni Pb–Pb a $\sqrt{s_{\mathrm{NN}}}$= 5.02 TeV usando l'esperimento ALICE. In particolare sono stati studiati gli spettri di produzione di $^{3}_{\Lambda}\mathrm{H}$ e l'evoluzione con la molteplicità di particelle cariche prodotte nella collisione. Questi risultati sono stati confrontati con le predizioni dei modelli tipicamente utilizzati per descrivere la produzione di particelle in collisioni di ioni pesanti, ossia i modelli termodinamici e quelli di coalescenza.

La seconda parte di questa tesi è dedicata a una delle domande ancora senza risposta della fisica ipernucleare: la vita media dell'ipertrizio. Infatti, fin dall'inizio della ricerca in questo campo di fisica, le predizioni teoriche sostenevano che la vita media fosse simile a quella dell'iperone Λ. Molti esperimenti, usando diverse tecniche sperimentali, hanno provato ad affrontare questa sfida e, recentemente, un nuovo interesse su questo argomento è stato prodotto dai nuovi risultati ottenuti dagli esperimenti con collisioni di ioni pesanti, i quali mostrano un andamento al di sotto delle attese. Quindi, in questa tesi, è stata determinata la vita media dell'ipertrizio analizzando i dati delle collisioni Pb–Pb a $\sqrt{s_{\mathrm{NN}}}$= 5.02 TeV raccolti dall'esperimento ALICE. Nello specifico, verranno presentate la vita media ottenuta studiando il canale di decadimento a 2 corpi ($^{3}_{\Lambda}\mathrm{H} \rightarrow {}^{3}\mathrm{He} + \pi^{-}$) con due diversi metodi e la prima stima del valore di vita media mediante l'analisi del canale di decadimento a 3 corpi ($^{3}_{\Lambda}\mathrm{H} \rightarrow \mathrm{d} + \mathrm{p} + \pi^{-}$).

Contents

Chapter 1.

High energy nuclear physics

"The world is broken, halos fail to glisten"
— Muse, "*Neutron star collision*" 2010

The Standard Model (*SM*) is currently the most detailed description of the building blocks of our universe. The model describes our universe in terms of matter (*fermions*) and forces (*bosons*). The fermion group contains six quarks, six leptons and their anti-particles. The bosons are the mediators of the fundamental forces: *electromagnetic*, *weak force* and *strong force*. The strong force is responsible for binding the quarks inside the hadrons, that are the constituents of the ordinary matter and this phenomenon is called *confinment*. Nevertheless, according to the current Big-Bang cosmology, the energy density and temperature in the early universe were so high that the fundamental components could not bind to form hadrons.

The properties of the hot and dense matter in the early stages of the universe as well as the transition from the deconfined phase to the ordinary matter, are the main subject of the high energy nuclear physics.

1.1. Quantum Chromo-Dynamics

In the 1960s a large number of new hadronic states were discovered but there was not a theory able to explain these experimental observations.

In 1963, Gell-Mann [1] and Zweig [2] proposed a model that explained the spectrum of strongly interaction particles in terms of elementary constituents called *quarks*. In its first formulation the quark model was a static model, that was able to describe the hadron

zoology in terms of fractional charge. It was also able to predict the existence of the Ω baryon starting from the three flavour (u, d, s) families classification, SU(3), of the hadrons.

Nevertheless, despite the phenomenological success, the original quark model had two serious problems. First, particle with fractional charge could not be found. Second, the observed spectrum of baryons required the wavefunction of the three quarks to be totally symmetric, while quarks should obey Fermi-Dirac statistics. A new quantum number, the *colour*, was proposed [3] to solve this contradiction and consequentely to explain the existence of the Δ^{++} baryon. Many experimental results confirmed the quark model with the colour degree of freedom and, from the comparison with the theory, found that the number of colours is 3.

Nowadays, the theory describing the strong interaction [4], also known as Quantum Chromodynamics (QCD), is formulated in terms of the Quark Model with colour interaction mediated by massless coloured gauge bosons, the gluons.

The dynamic of the quarks and gluons is controlled by the locally gauge invariant QCD Lagrangian:

$$\mathcal{L}_{QCD} = \mathcal{L}_{gluons} + \mathcal{L}_{quarks} = -\frac{1}{4} F^a_{\mu\nu} F^{\mu\nu}_a + \sum_f \overline{\psi}^i_f \left(i\gamma^\mu (D_\mu)_{i,j} - m_f \delta_{i,j} \right) \psi^j_f \tag{1.1}$$

where $F^a_{\mu\nu}$ is the gluon tensor, a the gluon color index, ψ^i_f is the Dirac spinor of the quark field, f is the flavour index, i,j the quark color index, γ^μ are the Dirac matrices, m_f is the quark mass and $\delta_{i,j}$ is the Dirac delta function.

The gluon tensor $F^a_{\mu\nu}$ has an additional term, due to the non-abelian nature of the symmetry group of $\mathcal{L}_{QCD}$, with respect to the photon tensor in QED:

$$F^{\mu\nu}_a = \partial^\mu G^\nu_a - \partial^\nu G^\mu_a - g_S \sum_{b,c=1}^{8} f_{abc} G^{\mu b} G^{\nu c} \tag{1.2}$$

where G^ν_a are the gluon fields.

The last term in Eq.1.2 produces two self interaction vertices for the gluons, that have the effect of increasing the field at large distance, the so-called *anti-screening* effect of the colour interaction.

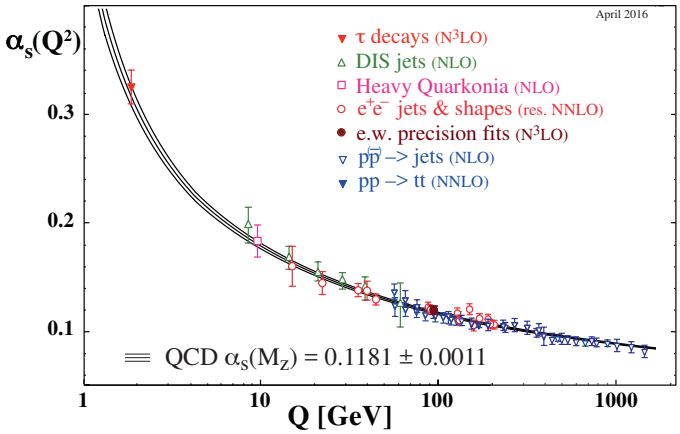

Figure 1.1.: Summary of the experimental values measured for the α_S coupling (from [5]) as a function of the process transfer momentum.

A fundamental consequence is that the QCD coupling constant α_S evolves with the transferred momentum Q (*running coupling constant*) :

$$\alpha_S(Q^2) = \frac{\alpha_0}{1 + \alpha_0 \frac{33-2n_f}{12\pi} ln \frac{Q^2}{\mu^2}} \tag{1.3}$$

where n_f is the number of flavours, μ is a quantity with the dimension of a mass and α_0 is the coupling constant at the renormalization scale of the theory. It is possible to distinguish two different regimes, depending on the transferred momentum. For small values of Q the coupling constant is large and quarks remain bound in the hadrons, the so-called *confinement* regime. At high transferred momenta α_S goes to zero and the QCD becomes a perturbative theory, this is called *asymptotic freedom* regime. Several experimental results, over the years, confirmed the predicted trend for the QCD coupling constant as shown in Figure 1.1.

The behaviour of the QCD coupling constant has an important consequence from the theoretical point of view. Indeed, the standard perturbative approach (pQCD) can be used only when Q^2 is much larger than the renormalization scale energy ($\alpha_S \ll 1$), while, at low transferred momenta, a different approach is required.

In the regime of small Q^2 it is still possible to evaluate the Green's functions of the QCD Lagrangian but these calculations are performed on a lattice, where the four dimensional space-time is discretized. This method is called *lattice QCD* (lQCD) and was proposed for

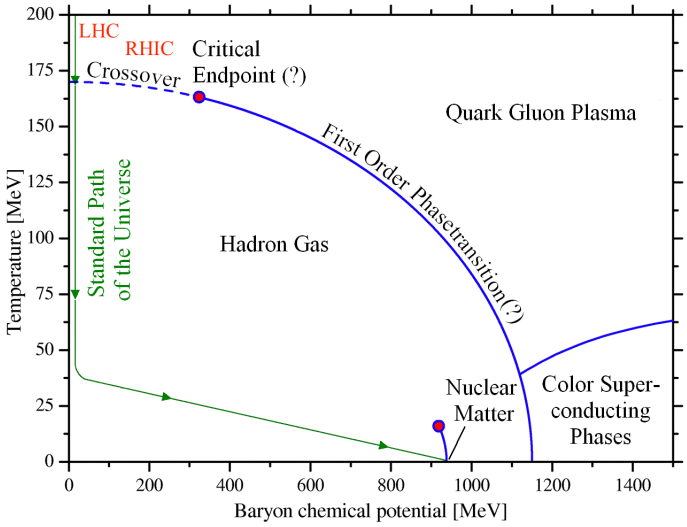

Figure 1.2.: Schematic nuclear phase diagram taken from [7]. The dotted line is the region probed by collider experiments at the Relativistic Heavy Ion Collider (RHIC) and at the LHC. The green arrow represents the evolution path of the universe as calculated in [8].

the first time in 1974 [6]. The main challenge of the lattice QCD is to reduce the lattice pitch a in order to approach the continuum ($a \to 0$).

1.2. QCD phase diagram

In everyday life we realize that matter comes in various forms and we distinguish between the solid, liquid and gas phase. Transitions between phases can be achieved by variations of external conditions or control parameters. Similarly in QCD, a fascinating consequence of the running of α_S is the existence of a phase transition between the hadronic matter, where quarks and gluons are confined, and a plasma, where partons are essentially free. This phase probably existed in the early universe during the first 10 μs after the Big Bang.

It is useful to describe this phase transition using variables typical of thermodynamics like temperature (T) and chemical potential (μ). In statistical mechanics, the chemical potential[1] is the energy that can be absorbed or released due to a change of the particle number of a given species. In case of a system with more components the chemical potential is defined for each component. Figure 1.2 shows the phase diagram of the QCD matter predicted by the theory and the values of temperature T and baryon chemical potential μ_B which are accessible experimentally in high energy heavy ion collisions.

[1] $\mu = \partial E/\partial N$ with E the *internal energy* and N the *number of particles*.

The origin of the phase diagram (T = μ_B = 0 GeV) is the QCD vacuum and, moving along the μ_B axis, the baryon chemical potential is the energy required to create a baryonic state. Ordinary QCD matter (protons, neutrons and nuclei) sits approximately at μ_B = 1 GeV. Along the μ_B axis there is a phase transition to a state, the Color Superconducting Phase, that has been hypothesised to be present in the core of the neutron stars [9].

Similarly it is possible to move along the T axis and for T $\gg \Lambda_{QCD}$, where Λ_{QCD} is the renormalization scale of QCD (typically $\approx$ 200 MeV), and $\mu \approx 0$ the system undergoes a crossover transition to a deconfined state called *Quark Gluon Plasma* (QGP). As the temperature increases, the average momentum exchange between the constituents increases as well and the interaction becomes less and less strong. Quarks and gluons are no longer confined in colour singlets and they constitute a plasma of free coloured partons. The phase transition between the hadronic matter and the plasma is expected to be a first order transition at high net baryon density while a smooth transition, called *crossover*, is forseen at small μ_B and high T. The point where the first order phase transition becomes a crossover is called *critical point*.

A first approximation of the pressure p and the energy density ϵ of the QGP can be obtained using the equations of state (EoS) of an ideal gas of massless particles confined in a bag of volume V [10]:

$$p = \frac{n_{DOF}\pi^2}{90}T^4 \qquad \epsilon = 3p$$

where n_{DOF} is the number of different particles states populating the system. This simple model predicts a rapid increase of pressure on the edge of the first order transition from a pion gas, with 3 DOF, to the QGP, containing (16 + $\frac{21}{2}$ n_f) DOF. The prediction is qualitatively in agreement with more detailed predictions from the Hadron Resonance Gas (HRG) model [11] and from the lattice QCD calculations.

Figure 1.3 shows the evolution of p as a function of the temperature of the medium. The red symbols represent the results of the lattice QCD calculations and the blue dotted line is the prediction obtained with the EoS from the HRG model. These predictions foresee an exponential increase of the pressure in the temperature interval 140 - 160 MeV, where the phase transition is expected.

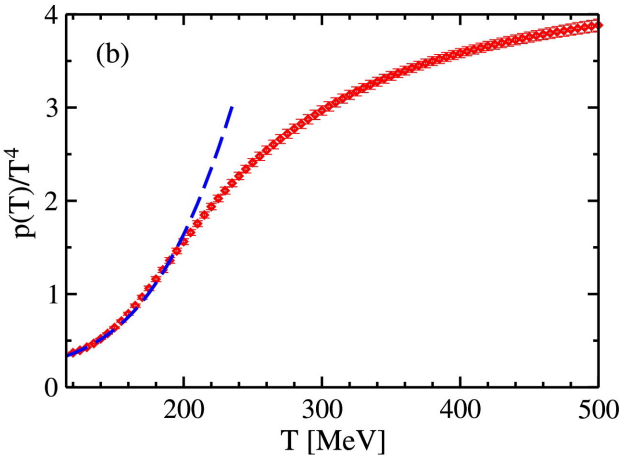

Figure 1.3.: Pressure as functions of the temperature T from [12]. The red symbols depict the lattice QCD calculations, while the dashed curves show the results of the employed HRG model.

1.3. Heavy ion collisions

The only known way to cross the phase boundary between ordinary hadronic matter and QGP in the laboratory is by colliding ultrarelativistic heavy ions. In the fall of 1986, the first heavy ion experiments started simultaneously at the *Super Proton Syncrotron* (SPS) at CERN and at the *Alternate Gradient Syncrotron* (AGS) at Brookhaven with O ions at fixed target energies of 200 GeV/A and 14.6 GeV/A respectively[2]. Nowadays there are two main hadron colliders which can be used for heavy ion collisions experiments: the *Relativistic Heavy Ion Collider* (RHIC) at the Brookhaven National Laboratory (BNL) and the *Large Hadron Collider* (LHC) at CERN. In the next years a new accelerator, the *Schwerionensynchrotron* (SIS) at the *Gesellschaft für Schwerionenforschung* (GSI) will operate with experiments dedicated to the study of the QGP at fixed target.

1.3.1. The little bang geometry

The collision between atomic nuclei, which are composite systems with finite dimensions, can be modelled starting from the nuclear constituents. It is natural to imagine the heavy ion collision as the superposition of the interactions between the constituent nucleons of the colliding nuclei. The key parameters in such description are the number of nucleons participating in the interactions between nuclei N_{part} and the number of binary collisions between nucleons N_{coll}. Due to the finite dimension of the nuclei, these two parameters

[2]The center-of-mass energy $\sqrt{s_{\mathrm{NN}}}$ depends on the target. Typical center-of-mass energy ranges were 6-13 GeV/c at SPS and 2-8 GeV/c at AGS [13]

are correlated with the impact parameter of the collisions $\overrightarrow{b}$ which is defined as the vector connecting the centres of the two colliding nuclei[3] projected on the transverse plane to the nuclei momenta. Figure 1.4 shows a sketch of the collision (*side view*) and how the impact parameter is defined (*beam-line view*).

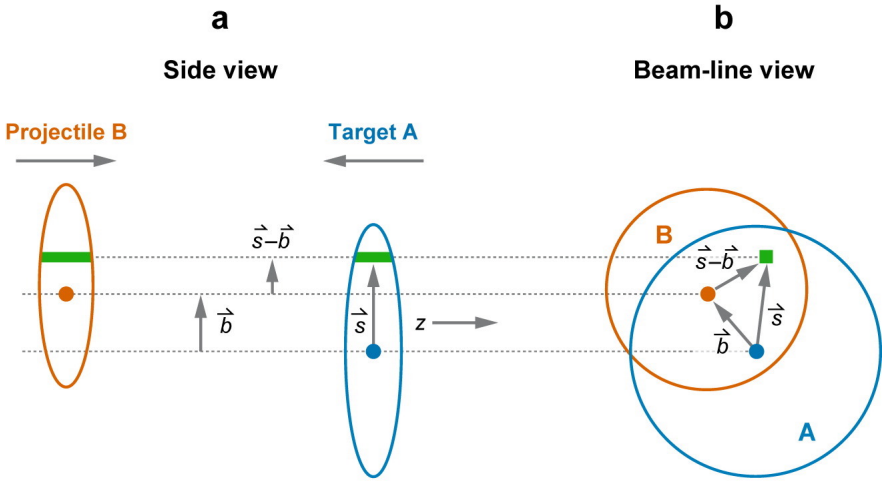

Figure 1.4.: Sketch of the longitudinal and transverse view of an heavy ion collision taken from [14]. In the side view, the colliding nuclei are squeezed to represent the Lorentz boost contraction due to their momentum.

The typical atomic nucleus radius is of the order of some femtometres and this represents the maximum impact parameter, thus a direct experimental measurement of $\overrightarrow{b}$ is precluded. Similarly the direct measurements of N_{part} and N_{coll} are not possible. However, it is possible to correlate these microscopic variables with measurable quantities, like the total number of particles produced in the collisions. This can be obtained using a phenomenological model of heavy ion collision, called the Glauber Model [14].

This model assumes nucleons to be point like and independent inside the colliding nuclei, it considers only hadronic interactions (i.e. no difference dealing with neutrons and protons) and each interaction does not deflect the trajectories of colliding nucleons. Moreover the model assumes a continuous nuclear density function $\rho(r)$ and that the interaction cross section does not depend on the number of collisions they undergo. These assumptions are known as *optical limit* and allow us to derive an analytical expression for N_{coll}.

The approach illustrated in [14] starts defining the nuclear overlap function for two colliding nuclei (A and B) as the probability of finding a nucleon in both the colliding nuclei inside the overlap region in the transverse plane. Using the notation introduced in

[3] One of the two colliding nuclei is arbitrarily taken as the target and the impact parameter vector points towards the projectile centre

Figure 1.4 it is written as:

$$T_{AB}(\vec{b}) = \int T_A(\vec{s})T_B(\vec{s} - \vec{b})\mathrm{d}^2 s \tag{1.4}$$

where $T_A(\vec{s})$ and $T_B(\vec{s} - \vec{b})$ are called the *thickness functions* for the nuclei A and B. They represent the probability of finding a nucleon in the unit transverse area located at $\vec{s}$:

$$T(\vec{s}) = \int \rho(\vec{s}, z)\mathrm{d}z \tag{1.5}$$

where $\rho(\vec{s}, z)$ is the probability per unit volume.

Then, the probability of observing an interaction between two nucleons located in the overlap region is defined as the product of the nuclear overlap function and the total inelastic cross section between two nucleons σ_{inel}. As already introduced, each nucleon does not deflect its trajectory after the interaction with another nucleons. As a consequence each nucleon can participate in more than one binary collision and the probability of having n binary collisions between the nuclei A and B, having A and B nucleons respectively, can be computed using the binomial statistics:

$$P(n, \vec{b}) = \frac{(AB)!}{n!(AB-n)!}[T_{AB}(\vec{b})\sigma_{inel}]^n[1 - T_{AB}(\vec{b})\sigma_{inel}]^{AB-n} \tag{1.6}$$

Based on this distribution, many useful quantities can be computed. The total inelastic cross section as a function of the impact parameter is obtained integrating the double differential interaction cross section for two colliding nuclei:

$$\frac{\mathrm{d}^2\sigma_{inel}^{AB}(b)}{\mathrm{d}b^2} = \sum_{n=1}^{\mathrm{AB}} P(n,b) = 1 - [1 - T_{AB}(\vec{b})\sigma_{inel}]^{AB} \tag{1.7}$$

$$\sigma_{inel}^{AB}(b) = \int_0^\infty 2\pi b\mathrm{d}b \left[1 - [1 - T_{AB}(\vec{b})\sigma_{inel}]^{AB}\right] \tag{1.8}$$

Then, the N_{coll} as a function of the impact parameter is derived from this expression summing all the possible numbers of collisions weighted by their own probability and using the definition of the mean of the binomial distribution:

$$N_{coll}(b) = \sum_{n=1}^{\mathrm{AB}} nP(n,b) = \mathrm{AB}T_{AB}(b)\sigma_{inel} \tag{1.9}$$

where the impact parameter vector $\vec{b}$ has been replaced with its norm as the direction of the vector plays a role only for polarised nuclei.

Similarly N_{part} is obtained by integrating over $\overrightarrow{s}$ the following relation:

$$N_{part}(b) = \int \mathrm{d}^2 s \left(\mathrm{A} T_A(\overrightarrow{s})[1-(1-T_B(\overrightarrow{b}-\overrightarrow{s})\sigma_{inel})^B] + \mathrm{B} T_B(\overrightarrow{b}-\overrightarrow{s})[1-(1-T_A(\overrightarrow{s})\sigma_{inel})^A] \right) \tag{1.10}$$

where the first term is the contribution of the projectile nucleus and the second term is the contribution of the target nucleus.

The optical form of the Glauber Model with the input of $\rho(\overrightarrow{s})$ and σ_{inel} allows to express N_{coll} and N_{part} as a function of the impact parameter $\overrightarrow{b}$. The main limitation in this model is the usage of continuous density functions and integrals for quantities that are discrete in nature and, thus, can fluctuate event by event. An alternative approach is the Glauber Monte Carlo Model, where the colliding nuclei geometry is generated by spawning their nucleons in the space according to their nuclear density functions. A random impact parameter b is then drawn from the distribution $\mathrm{d}\sigma/\mathrm{d}b{=}2\pi b$ derived from 1.7. Once the nuclei geometry and the impact parameter are generated, the collision between nuclei is treated as the superposition of single binary collisions between the nucleons. A binary collision occurs in these simulations when the condition on the distance between two nucleons $d \leq \sqrt{\sigma_{inel}/\pi}$ is satisfied. Within this method N_{coll} and N_{part} can be easily computed counting the number of wounded nucleons and the number of the collisions in the simulation. Moreover, the Monte Carlo Glauber simulation can be used as input for the impact parameter estimation in the heavy ion experiments, as will be shown in Chapter 3.

Figure 1.5 shows the results of the calculations performed with the two approaches. The geometrical quantities N_{coll} and N_{part} converges to the same values for the Glauber Monte Carlo and the Optical Glauber Model (right plot). On the other hand, the Optical Glauber Model gets the same σ_{inel}^{AA} of the Glauber Monte Carlo when σ_{inel} is smaller and the approximation of point-like scattering centres is valid.

1.3.2. Space time evolution of Heavy Ion collisions

A long lived and strongly interacting system is created when two ultrarelativistic atomic nuclei collide. The evolution of this system and the characterisation of its properties, like T and ϵ, in the different phases is one of the main goal of heavy ion experiments. Figure 1.6 summarises the current view of the key phases of relativistic heavy ion collisions [15]:

1. $t < 0$ fm/c: before the collision, the two colliding nuclei travel in the beam line. The nuclei are strongly Lorentz contracted, by a factor of 2700 at the LHC, in the laboratory reference frame at the ultrarelativistic energies;

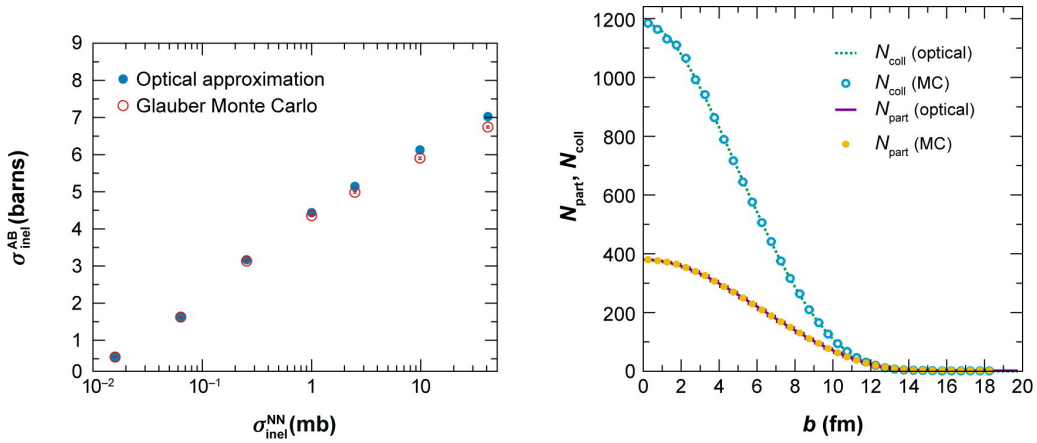

Figure 1.5.: (left) Total cross section calculated in the optical approximation and with a Glauber Monte Carlo as a function of σ_{inel}^{NN}; (right) N_{coll} and N_{part} as a function of the impact parameter, calculated in the optical approximation (lines) and with a Glauber Monte Carlo (markers).

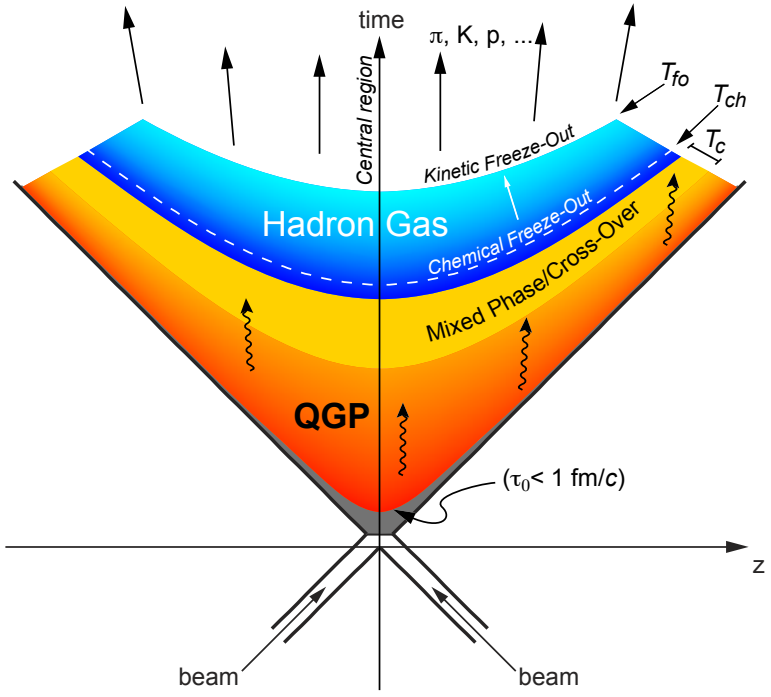

Figure 1.6.: Space-time evolution of the system created in a central collision in the mid-rapidity region.

2. t = 0 fm/c: collision time. The geometry of the collision can be described using the Glauber Model described in the previous section;

3. $0 < t \lesssim \tau_0 \sim$ 1fm/c: in the early collision stages hard processes occur between the partons and particles with either a large mass or large transverse momenta are created. Their creation involves large momentum transfer Q^2, therefore their production can be calculated with perturbative QCD. The typical time scale for such processes is 0.1 fm/c. This is called *pre-equilibrium* phase. In high energy collisions, the constituent partons of nuclei undergo several interactions, losing their energy in the mid-rapidity[4] region (y≈0) and then they escape at forward rapidities. The obtained system at mid-rapidity is a hot and interacting medium with vanishing baryon chemical potential. In heavy ion collisions at RHIC and LHC the energy density is such that the formation of the QGP state is expected. After a short strong parton rescattering phase, the obtained droplet of QGP matter reaches the equilibrium at his proper time τ_0;

4. $1 \lesssim t \lesssim 10$ fm/c: the thermalized system has thermal pressure which leads to collective expansion of the collision fireball. As a consequence, the QGP cools and its energy density decreases. The rapid expansion of the QGP droplet is usually modelled using the relativistic hydrodynamics [16] which provide useful insights to interpret the experimental data;

5. $10 \lesssim t \lesssim 15$ fm/c: the critical temperature between the two phases is reached and the hadronisation starts. The system gradually evolves into an interacting *hadron resonance gas*. In this phase, the expansion and contextual cooling of the system continue, as well as the elastic and inelastic interactions among the hadrons within the system. The moment when the momentum exchange between hadrons is not sufficient for inelastic interaction is called *chemical freeze-out* (T_{ch}). Since no other inelastic processes will take place, the relative abundances of different particle species are fixed after the chemical freezeout. The second landmark in the system evolution is the *kinetic freeze-out* (T_{fo} or T_{kin}), when also the elastic interactions among the hadrons ceased and the particle momenta are fixed;

6. $t \gtrsim 15$ fm/c: hadrons created in the collision escape the interaction region with no further interaction. This regime is also known as *free hadron stream*.

The particles produced in the collisions and escaped from the interaction region are detected by the experimental apparata. The technologies and methodologies implied in this last step will be presented in the Chapter 3. In the following, the most important probes used to study and characterise the Quark Gluon Plasma will be described.

[4] Rapidity is defined in Chapter 3 Sec. 3.2.

1.4. Probing the Quark Gluon Plasma

1.4.1. Soft probes

Hadrons p_{T} spectra

Low momentum hadrons, usually defined *soft hadrons*, represent the majority of the particles produced in a heavy ion collision ($\approx$ 95% for $p_{\mathrm{T}} < 1.5$ GeV/c). The study of the momentum spectra of identified particles gives important insights about the characteristics of the medium at the kinetic freeze-out. Assuming a Boltzmann-Gibbs distribution for the particle emission at the kinetic freeze-out, the particle spectra for each species i can be written as:

$$\frac{1}{m_{\mathrm{T}}}\frac{\mathrm{d}^2N_i}{\mathrm{d}m_{\mathrm{T}}\mathrm{d}y} \propto e^{-\beta m_{\mathrm{T}}} \tag{1.11}$$

where $m_{\mathrm{T}} = \sqrt{m^2 + p_{\mathrm{T}}^2}$ is the transverse mass. This formulation keeps into account only the thermal component of the spectra and predicts a common emission temperature β for all particle species, the so called m_{T} *scaling*, which successfully describes the spectra in pp collisions.

The measured p_{T} spectra of pions, kaons and protons are shown in Figure 1.7 for the most central Au-Au and Pb–Pb collisions at RHIC [17,18] and at the LHC [19], respectively. The measured spectra show a different slope (i.e. temperature) for different particle species, thus breaking the predicted m_{T} scaling. This behaviour can be interpreted adding a further component to the measured emission temperature for each particle species:

$$T_i = T_{kin} + \frac{1}{2}m_i\langle v_\perp\rangle^2 \tag{1.12}$$

where T_{kin} is the temperature of the medium at the kinetic freeze-out, while the additional terms is related to the kinetic energy acquired by the particles of species i due to the hydrodynamical collective expansion along the transverse plane. This phenomenon, called *radial flow*, modifies the production spectra pushing the mean transverse momentum, at the emission, to higher values proportionally to the particle species mass.

This can be qualitatively seen in Figure 1.7, where the slope for pions (soft spectrum) is steeper than the one for protons (hard spectrum). Moreover, the spectra measured at RHIC and at the LHC are obtained at two different energies, $\sqrt{s_{\mathrm{NN}}}$[5] = 200 GeV and 2.76 TeV

[5] nucleon-nucleon centre-of-mass energy

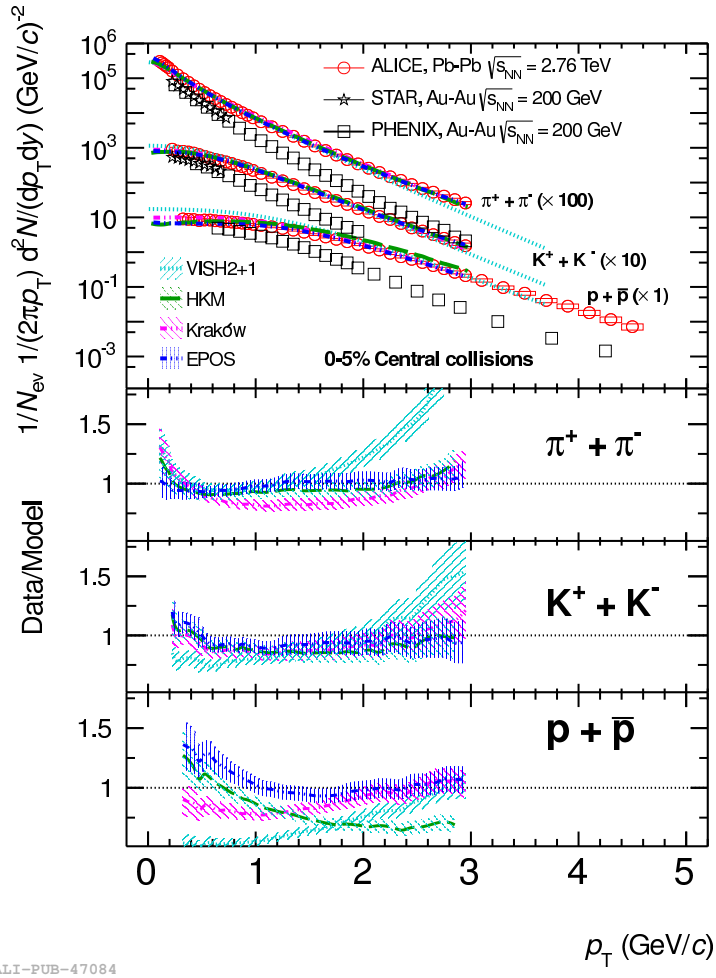

Figure 1.7.: Pion, kaon and proton p_T spectra in central (0–5%) Au-Ay collisions at $\sqrt{s_{NN}}$= 200 GeV at RHIC [17, 18] and in Pb–Pb collisions at $\sqrt{s_{NN}}$= 2.76 TeV at the LHC [19]. The data are fitted with a Blast-Wave model [20] (lines) and are compared with three additional hydrodynamical models predictions (shaded areas).

respectively. Thus it is possible to study the evolution of the particle spectra shape with the collision energy. The p_T spectra measured at lower energies show a profile softer than those measured at the LHC and this suggests a radial flow with stronger pressure gradients driving the hydrodynamical expansion in more energetics collisions. The comparison of the production spectra with two hydrodynamical models like HKM [21] and Krakow [22], strongly supports the interpretation of the slope modification with the presence of radial flow. Finally a simplified hydrodynamical model, corresponding to a Blast-Wave description [20], is usually fitted simultaneously to the measured spectra in order to extract the temperature T_{kin} and the mean radial velocity $\langle\beta_\perp\rangle$ of the particles at the kinetic freeze out. The results of these fit, presented in Figure 1.7, show a radial flow velocity $\langle\beta_\perp\rangle$ and a ki-

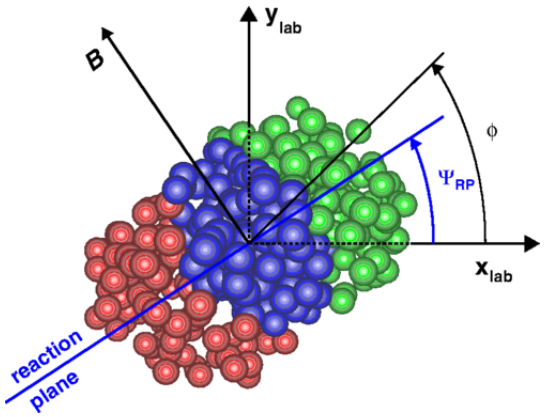

Figure 1.8.: Sketch of the transverse plane for a collision of two heavy ions. Particles are produced in the overlap region (blue nucleons). Ψ_{RP} is the azimuthal angle of the reaction plane and ϕ is the azimuthal emission angle of each particle.

netic freeze-out temperature T_{kin} larger at the LHC than those extracted at RHIC collision energies.

Anisotropic transverse flow

Another usual signature of the collective motions of particles created in heavy ion collision is the presence of azimuthal anisotropies in the particle production spectra. In particular, when considering two nuclei overlapping only partially, as shown in Figure 1.8, a correlation between the emission angles of the particles and the impact parameter is obtained.

This azimuthal anisotropies can be quantified by looking at the Fourier expansion in the azimuthal angle of the production spectra [23]:

$$\frac{\mathrm{d}N}{\mathrm{d}\phi} \propto 1 + 2\sum_{n=1}^{\infty} v_n \cos[n(\phi - \Psi_n)] \tag{1.13}$$

where Ψ_n is the angle of the reaction plane, ϕ is the particle azimuthal angle and v_n are the coefficients which quantify the magnitude of the anisotropy. The reaction plane is defined by the beam direction and the impact parameter vector. However this plane cannot be measured directly and the n^{th} order event planes are used for the calculation of the Fourier expansion. The typical almond shape of the overlap region between the colliding nuclei, in semicentral collisions, generates a pressure gradient along the reaction plane. This collective motion is called *elliptic flow* and it contributes to the v_2 coefficient of Eq. 1.13. The higher order Fourier coefficients, like v_3 (*triangular flow*) and v_4 (*quadrangular flow*),

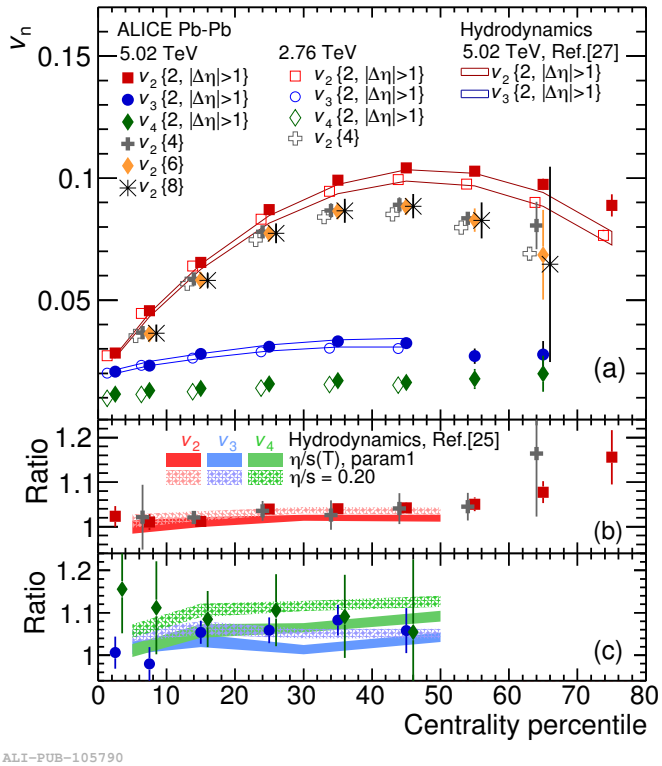

Figure 1.9.: Panel (a): v_n coefficients up to fourth order measured by the ALICE experiment at different energies as a function of the centrality percentile [24]. Panels (b) and (c): ratios between the measurements at 5.02 TeV and those at 2.76 TeV show good agreement with the unity. This suggests that the medium characteristics and the thermalisation dynamics do not change between the two energies. The results are also compared with hydrodynamical models (references in [24]) showing a good agreement with model using small η/s value.

are related to initial inhomogeneities of the colliding systems. Thus the measurements of these v_n coefficients is extremely important since they are related with the initial geometric condition and inhomogeneities through the properties of the medium, such as the shear viscosity over entropy η/s and the bulk viscosity over entropy ζ/s. The detailed study and comparison of the measured v_n with the models allows to unveil the characteristics of the medium and the dynamics of its thermalisation.

Figure 1.9 shows the v_n coefficients measured by the ALICE experiment at different energies in Pb–Pb collisions [24]. The value are compared with hydrodynamical models, which combine the initial spatial anisotropy and the hydrodynamical response. This comparison allows to inquire into the value of η/s and it is possible to state that the current v_n values are well described assuming a medium with small shear viscosity.

Strangeness enhancement

Unlike up (u) and down (d) quarks, strange (s) quarks are not present as valence in quarks in the initial state and they need to be produced during the collision. In the early stages of a high-energy nuclear collision, strangeness is produced in hard partonic scattering processes and the dominant mechanism at high p_{T} is the gluon fusion $gg \rightarrow s\bar{s}$. At low p_{T}, non perturbative processes dominate the production of strange hadrons, such as the string fragmentation model [25]. The production mechanisms of strangeness in hadron collisions are the reference for the predicted enhancement.

The strangeness enhancement was originally proposed [26] as a signature of the QGP formation in high-energy nuclear collisions. In particular the authors in [26] proposed this enhancement assuming a parton gas the medium created in the collision. They predicted the enhancement in heavy ion collision based on the lower Q-value for the production of strange partons than the one for strange hadrons production and on the less equilibration time required by strangeness in the partonic gas than in the hadronic one. These assumptions are still valid today, with the only main difference that the medium created in a heavy ion collision behaves like a liquid instead of a gas. Thus, the production of strange hadrons in heavy ion collisions provides a way to investigate the creation and the properties of the medium.

Strange particles are those consisting of at least one s ($\bar{s}$) quark, like the $\mathrm{K}^0_{\mathrm{s}}$. The baryons with strange quarks, like Λ (uds), Ξ^- (dss) and Ω^- (sss), are called *hyperons*. The production of these particles has been investigated since several years and according to the prediction [26] the enhancement in strange hadron production should increase with the collision energy. However, the abundances of strange particles measured in heavy ion collisions both at RHIC [27–29] and LHC [30, 31] energies do not show a significant dependence on the collision energy.

The production of strange hadrons in heavy ion collisions is actually an open question of the high energy nuclear physics and still further developments are ongoing. A possible hypothesis that has been proposed to explain this behaviour is the canonical suppression of strangeness production in small collision systems.

In small collision systems, like pp collisions, one strange hadron is created locally with another hadron with opposite strangeness inside the small collision volume at the same time. On the other hand, in heavy-ion collision the strangeness conservation needs to be satisfied only globally, because the larger phase space relaxes the local strangeness conservation. Hence, the concept of strangeness enhancement can be described using the language of statistical mechanics. The Grand Canonical ensemble limit is valid in the central

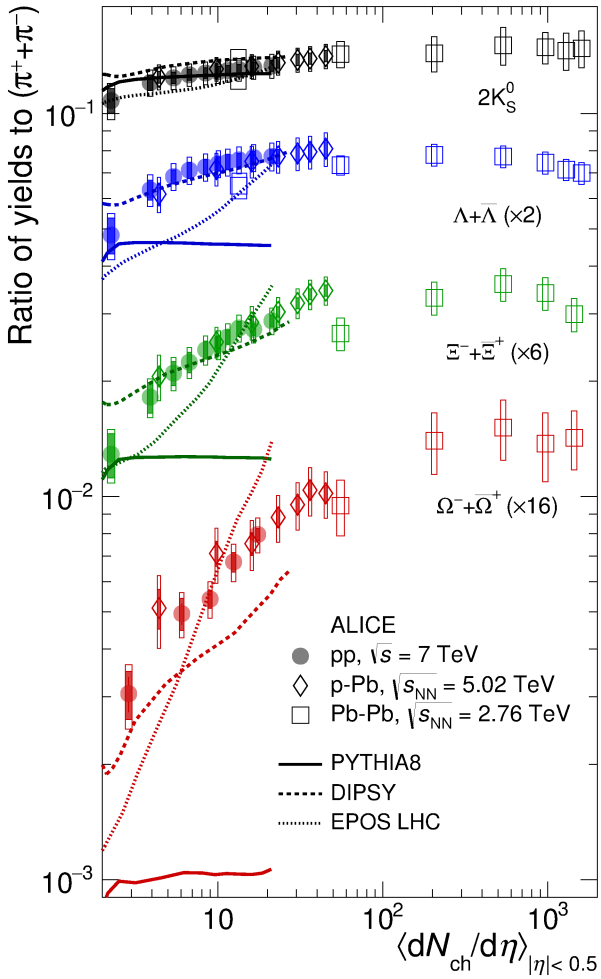

Figure 1.10.: p_T-integrated yield ratios to (π^++π^-) as a function of the charged particle multiplicity $\langle dN_{ch}/d\eta \rangle$ measured in $|y|$<0.5. The results obtained in pp, p–Pb and Pb–Pb collisions are compared to calculations from MC models [33–35]

heavy-ion collisions where a high particle multiplicity is present. On the other hand, the description of small collision systems, as pp collisions, requires a Canonical ensemble since the number of particle is locally conserved. Consequentely, any measured strangeness enhancement is really a phase space suppression in pp and p–Pb collisions that is removed in the heavy ion case [32]. The hadrons predicted to profit most from the strangeness redistribution within the medium are the multi-strange hadrons such as Ξ and Ω and their enhancements are expected to be more pronounced than those of Λ and K^0_s.

One of the most effective observables is the p_T-integrated strange hadron yields ratio to the p_T-integrated pion yields as a function of the charged particle multiplicity $\langle dN_{ch}/d\eta \rangle$. The ALICE collaboration results [36] for these ratios in Pb–Pb collisions at $\sqrt{s_{NN}}$= 2.76 TeV are shown in Figure 1.10 as open square markers for K^0_s (black), Λ (blue), Ξ (green)

and Ω (red). All the markers in the figure are scaled for visibility as indicated in the legend, however from a qualitative look at these ratios it is possible to see an ordering in the strangeness enhancement, as previously predicted. In addition, the same figure show the ratios measured also in pp collisions at $\sqrt{s}$ = 7 TeV, with full circle markers, and in p–Pb collisions at $\sqrt{s_{\mathrm{NN}}}$= 5.02 TeV, with open diamond markers, and the results show an intriguing trend. Indeed, the evolution of the strangeness enhancement increases as a function of $\langle \mathrm{d}N_{\mathrm{ch}}/\mathrm{d}\eta \rangle$ from low multiplicity pp to high multiplicity p–Pb collisions and reaches the values observed in Pb–Pb collisions. Actually it is not clear if the strangeness enhancement observed in pp collision is due to the onset of QGP in small systems, nevertheless the abundance of strangeness produced in high multiplicity pp collisions is similar to that one measured in Pb–Pb collisions, where the QGP is formed. This suggests a possible common underlying physics mechanism in the three collision systems, however a further experimental effort is needed in order to reach more precise measurements, which will allow us to understand this behaviour.

1.4.2. Hard probes

High momentum particles and heavy flavours

High momentum and heavy flavour (charm and beauty) quarks, can be created only at the very early stages of the collisions, when the high Q^2 processes occur and can be treated with the pQCD approach. Consequently, the hadrons with high momentum and/or containing heavy flavour quarks are crucial probes used to inquire into the mechanisms driving the parton propagation and the energy loss in the QGP. If we assume the collision between two nuclei as the superposition of uncorrelated nucleon-nucleon collisions, the observed production cross section for hard particles should be equal to the pp cross section scaled by the number of binary collisions N_{coll}. Thus, a useful observable is the *nuclear modification factor* defined as:

$$R_{AA} = \frac{1}{\langle N_{coll} \rangle} \frac{\mathrm{d}^2 N_{AA}/\mathrm{d}p_{\mathrm{T}}\mathrm{d}y}{\mathrm{d}^2 N_{pp}/\mathrm{d}p_{\mathrm{T}}\mathrm{d}y} \tag{1.14}$$

which should be equal to unity for hard processes. In the previous formula N_{AA} and N_{pp} are the yields measured in heavy ion (AA) and proton-proton (pp) collisions. The study of the p_{T} dependence of the nuclear modification factor could show deviations due to other effect not related to the presence of the QGP: the Cronin enhancement and the modification of the parton distribution function inside the neutron and the proton, mainly the nuclear shadowing. However, these *cold nuclear matter* effects can be factorised from the QGP in-

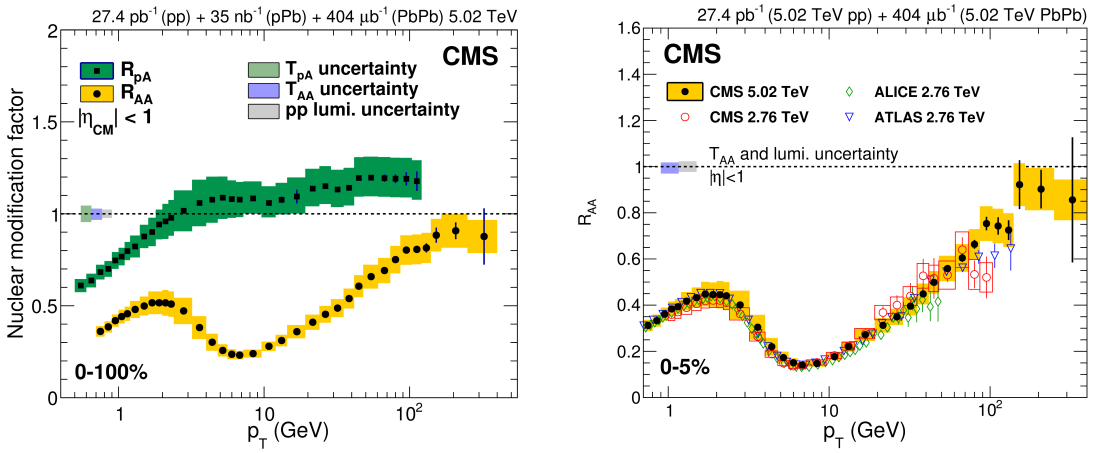

Figure 1.11.: (left): R_{AA} and R_{pA} of charged particles as a function of transverse momentum in p–Pb and Pb–Pb collisions at $\sqrt{s_{\mathrm{NN}}}$=5.02 TeV measured by the CMS experiment; (right): R_{AA} of charged particles as a function of transverse momentum in the most central (0–5%) Pb–Pb collisions at $\sqrt{s_{\mathrm{NN}}}$=2.76 TeV and 5.02 TeV measured by ALICE, ATLAS and CMS [37]. The coloured boxes refer to the systematics uncertainties of the measurement while the vertical bar are the statistical uncertainties.

duced ones, by studying them in pp and p–Pb collisions. Figure 1.11a shows the nuclear modification factor measured in p–Pb (R_{pA}) and Pb–Pb (R_{AA}) collisions by the CMS experiment [37]. The R_{pA} for hard particles ($p_{\mathrm{T}} \geq 3\,\mathrm{GeV}/c$) is close to one and even larger at very high transverse momenta. On the other hand, the R_{AA} shows a clear suppression of the production of hard particles for $p_{\mathrm{T}} \geq 3\,\mathrm{GeV}/c$. This suggests the presence of the energy loss of the partons in the hot and dense medium. At very high momenta, it grows again reaching one and this trend can be naively interpreted as an extreme fast parton which manage to escape the interaction regione before the medium formation. Figure 1.11b shows the R_{AA} for the most central Pb–Pb collisions (0–5%) at $\sqrt{s_{\mathrm{NN}}}$=2.76 TeV and 5.02 TeV measured by CMS, ATLAS and ALICE. From a comparison with the figure on the left, it is visible a higher suppression of the nuclear modification factor, hinting a higher energy loss in the medium created in the most central collision. On the other hand, the R_{AA} does not show major changes between the two energies.

The study of the heavy flavour is also extremely important since heavy flavour hadrons allow to tag and study the energy loss of a specific heavy quark. Moreover, the fragmentation functions of heavy quarks are such that a large fraction of the momentum carried by the original parton is transferred to the observed heavy flavour hadron. Thus, it is possible to study in details the energy loss effects for heavy flavour quarks as a function of their momentum. The contribution to this energy loss can be splitted in two components: the

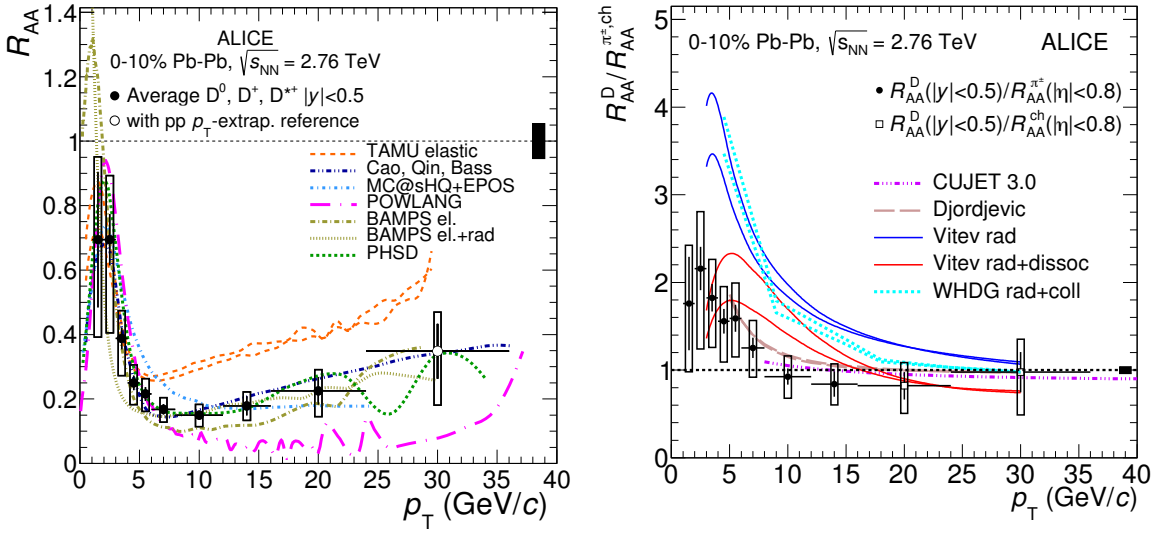

(a) **(b)**

Figure 1.12.: (left): R_{AA} of D mesons as a function of p_T in the 0–10% centrality class of Pb–Pb collisions at $\sqrt{s_{NN}}$=2.76 TeV measured by the ALICE experiment; (right): ratio of the R_{AA} of D mesons and the R_{AA} of charged pions and of charged particles. In both figures: the boxes refer to the systematic uncertainties of the measurement while the vertical bars represent the statistical uncertainties. The coloured lines correspond to different transport model predictions, see [38] for more details.

elastic scatterings with other partons (*collisional* energy loss) and the inelastic scattering (*radiative* energy loss).

Figure 1.12a shows the measurement of the R_{AA} of charmed mesons by the ALICE experiment [38]. From the comparison with the transport models for heavy partons in the medium[6], it is possible to state that the data favour those models including both collisional and radiative energy loss. Figure 1.12b, instead, shows the ratio between the nuclear modification factor of charmed meson R^D_{AA} and those of charged particles R^{ch}_{AA} or pions $R^{\pi^\pm}_{AA}$. The R_{AA} of D mesons and light-flavour hadrons are consistent for $p_T > 6$ GeV/ c, while the first one tends to be slightly higher than that of pions and charged hadrons for $p_T < 6$ GeV/c. This can be explained in terms of quark-mass dependent energy loss, where the energy loss of gluons in the medium is larger than the energy loss of the charm quark because of the larger coupling of gluons with the coloured medium. Also in these case, only the models including both the collisional and the radiative energy loss are able to reproduce the trend of the ratio.

[6]The details on the analyses as well as on the models can be found in [38] and references therein.

Quarkonia

One of the most important features of a deconfined state of quarks and gluons is the modification of the interaction potential between two quarks. Indeed this potential, that in the vacuum is parametrised as a Cornell potential [39], becomes a Yukawa potential inside the medium:

$$V(r) = -\frac{\alpha(r)}{r} e^{-r/r_D} \tag{1.15}$$

where the potential is modulated by an exponential driven by the attenuation length r_D, called *Debye radius*. This means that all the $q\bar{q}$ states with a radius larger than r_D cannot bind, as a consequence of the colour screening of the medium. The density of free colour charges in the plasma depends on the temperature ($\rho \propto T^3$) and this corresponds to the colour interaction attenuation with $r_D \sim 1/(gT)$, where g is the coupling constant of the interaction in the medium. As described in details in [40], the Debye length decreases with increasing temperature and this results in a sequential suppression of quarkonium states.

For this reason heavy flavour quarkonia states, $c\bar{c}$ and $b\bar{b}$ states, are good candidates to probe the temperature of the medium created in a heavy-ion collision. Indeed, the relative suppression of a particular quarkonium state, in heavy-ion collision with respect to pp collision, indicates that the temperature of the medium is such that the Debye radius is smaller than the binding radius of the investigated $q\bar{q}$ state.

The CMS collaboration studied the relative production yields of Y states [41] in pp and Pb–Pb collisions at the center-of-mass energy per nucleon pair of $\sqrt{s_{\mathrm{NN}}}$= 5.02 TeV, measuring the double ratios:

$$\frac{(\mathrm{Y(nS)/Y(1S)})_{\mathrm{Pb-Pb}}}{(\mathrm{Y(nS)/Y(1S)})_{\mathrm{pp}}} \tag{1.16}$$

where n can be 2 or 3. If there is not suppression of $q\bar{q}$ states due to the colour screening, then this ratio would be compatible with unity as the relative abundances of Y states depend only on the production cross section and the integrated luminosity. The centrality-integrated Y(2S) double ratio is $0.308 \pm 0.055(\mathrm{stat.}) \pm 0.019(\mathrm{syst.})$, which is well below 1, and, in addition, in the most central bin (0-5%) the Y(2S) signal is consistent with zero within one standard deviation. For the Y(3S), as shown in Figure 1.13, the suppression is even stronger from pp, Figure 1.13a, to Pb–Pb, Figure 1.13b, and the signal is compatible with zero in heavy ion collisions. Thus they extracted the Y(3S) double ratio confidence interval that is smaller than 0.26 at 95% CL. These results confirm the predicted sequential melting of quarkonia states.

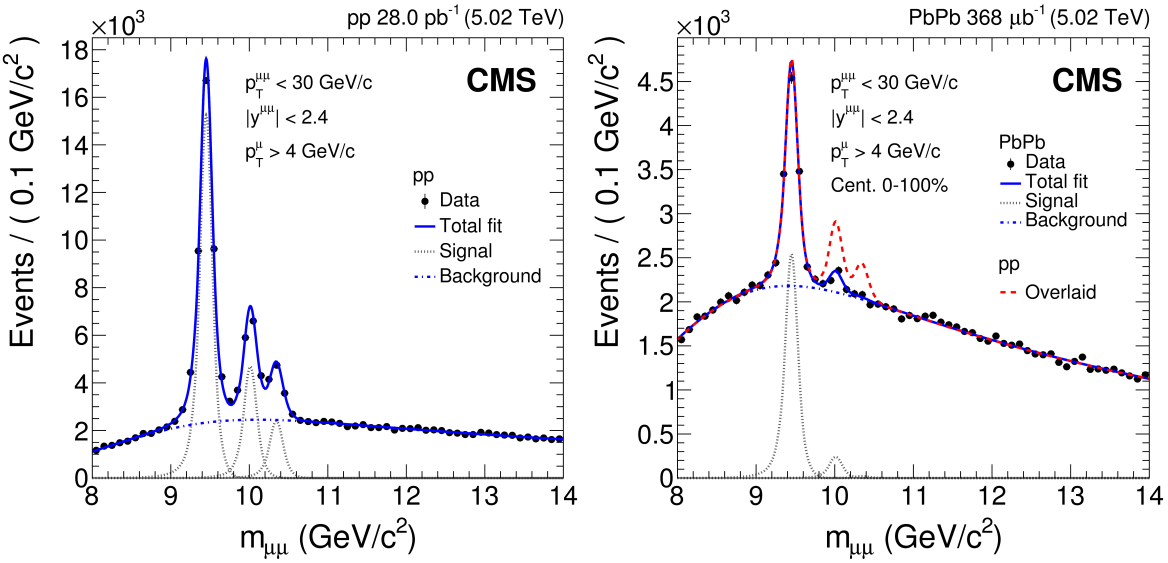

(a) pp collisions **(b)** Pb–Pb collisions

Figure 1.13.: Measured $\mu^+\mu^-$ invariant mass pairs in pp (left) and in Pb–Pb (right) collisions performed by the CMS experiment [41]. The three peaks corresponding to the Y(1S), Y(2S) and Y(3S) are clearly visible in pp collisions, while in Pb–Pb collisions a suppression is seen for 2S and 3S states.

However, the ALICE collaboration results on the J/ψ nuclear modification factor in Pb–Pb collisions at $\sqrt{s_{\mathrm{NN}}}$= 2.76 TeV [42] show a smaller suppression for the J/ψ state with respect to the observations at lower energies. These results can be interpreted with a later formation of J/ψ states either by recombination with other charm quarks in the medium or during the hadronisation, as shown in some predictions of statistical hadronisation model [43].

Chapter 2.

(Hyper-)nuclei production in Heavy Ion collisions

"I don't know anything, but I do know that everything is interesting if you go into it deeply enough"

— Richard Phillips Feynman, 1918–1988

High energy heavy ion collisions offer a unique way to investigate the behaviour of nuclear matter under extreme conditions of temperature and energy density. At the LHC energies, one of the remarkable features is the nearly equal abundance of matter and antimatter in the central rapidity region. It is believed that a similar symmetry existed in the initial stage of the Universe and it is extremely important, also for the cosmologists, to understand how this symmetry got lost in the evolution of the Universe, reaching the actual stage with no visible amounts of antimatter being present.

In relativistic heavy-ion collisions a huge number of particles carrying strangeness is produced. Strangeness can be found not only in elementary particles (i.e. K, Λ, Ξ, Ω), but also in composite objects, such as the hypernuclei.

This chapter will introduce hypernuclei, especially the hypertriton ($^{3}_{\Lambda}$H), starting from their definition, their characteristics and concluding with the introduction of the theoretical frameworks used to describe their production in heavy ion collisions. A special section will be dedicated to the introduction of the $^{3}_{\Lambda}$H lifetime puzzle.

2.1. Hypernuclei

Hypernuclei are bound nuclear systems of non-strange and strange baryons. The most studied are Λ-hypernuclei, where a nucleon of the nucleus is replaced by a Λ hyperon, and they are indicated with the usual notation of the nuclei ${}^{A}_{\Lambda}Z$ where A is the mass number and Z the number of proton. Other hypernuclei are investigated and they can contain two Λ (${}^{A}_{\Lambda\Lambda}Z$) [44] or heavier strange baryons like the Ξ (${}^{A}_{\Xi}Z$) [45].

The first observation of a hypernucleus is due to Danysz and Pniewski in 1953 [46], through the analysis of the events recorded by a stack of photographic emulsions exposed to the cosmic radiation at nearly 26 km from the Earth surface using a balloon. Since the first observation, there has been an increasing interest in searching for new hypernuclei and studying their structure.

In general, the study of the hypernuclei is important for two main reasons. On one hand, the studies on the hypernuclei structure [47] provide indications on the hyperon-baryon ($Y - N$) and hyperon-hyperon ($Y - Y$) strong interactions, which can not be determined from scattering experiments. In this way the nucleus is used as an "internal" laboratory offering the opportunity to study the properties of the hyperon interactions. On the other hand, the hypernuclear weak decay is a useful tool to inquire the strangeness-changing weak baryon interactions [48].

The studies and the results of the hypernuclear physics are also of interest for other fields such as the nuclear astrophysics. For instance, the $Y - N$ interaction plays a key role in understanding the structure of neutron stars. Indeed, the collapsed stellar core could be a kaonic condesate or consist of hyperons depending on the strength of this interaction [49].

At the beginning of the hypernuclear physics cosmic rays were used as source to study the hypernuclei. Then, from 1972 two-body reactions producing Λ on a nuclear target have been used. The three two-body reactions, widely used, that led to almost all the bulk of experimental results are [50]:

1. the "*Strangeness exchange*" reaction:

$$K^- + N \rightarrow \Lambda + \pi \tag{2.1}$$

   mainly used in the K^-+$n \rightarrow \Lambda + \pi^-$ charge states, since it is easier the spectroscopy of the π final state. The reaction can be interpreted as a transfer of the s-quark from the incident meson to the struck baryon.

2. the "*Associated production*" reaction:

$$\pi^+ + n \rightarrow \Lambda + K^+. \tag{2.2}$$

This reaction proceeds by the creation of $s\bar{s}$ pair by the incident meson.

3. the *electroproduction* of strangeness on protons in the very forward direction,

$$e + p \rightarrow e^{'} + \Lambda + K^+ \tag{2.3}$$

exploited quite recently. The virtual photons associated to the reaction can be regarded as quasi-real and the aforementioned reaction is often rewritten as a two-body photoproduction reaction:

$$\gamma + p \rightarrow \Lambda + K^+ \tag{2.4}$$

These reactions have been used in the last decades by many experiments which studied the spectroscopy of Λ-hypernuclei. Their results showed an important step forward in determining the energy levels of nearly all *p*-shell hypernuclei both by γ-ray spectroscopy from the decay of low-lying excited states and by missing-mass measurements with the magnetic spectrometers at KEK (SKS), JLab (Hall A and Hall C) and LNF-INFN (FINUDA) [50, 51].

2.1.1. Weak decay of hypernuclei

Λ-Hypernuclei can be produced in the ground states or in an excited state of the Λ-particle neutron-hole configuration. A Λ-hypernucleus in the ground state, which is the one investigated in heavy ion collision experiments, decays to non-strange nuclear systems through two different mechanisms: the mesonic (MWD) and the non-mesonic (NMWD) weak decay.

In the NMWD the Λ-hypernucleus decays through processes which involve a weak interaction of the Λ with one or more core nucleons. When the pion emitted in $\Lambda \rightarrow \pi$N reaction is virtual, it can be absorbed by the nuclear medium, resulting in a non-mesonic decay as:

$$\Lambda n \rightarrow nn, \quad \Lambda p \rightarrow np, \quad \Lambda NN \rightarrow nNN \tag{2.5}$$

where the first are defined as *one-nucleon induced decays*, with decay rates respectively Γ_n and Γ_p, while the last one is identified as *two-nucleon induced decays*, with decay rate Γ_2.

In the MWD the Λ hyperon decays into a nucleon and a pion inside the nuclear medium, following the weak decay mode in the free space:

$$\Lambda_{free} \rightarrow p + \pi^- \qquad (B.R. = 64.2\%) \tag{2.6}$$

$$\Lambda_{free} \rightarrow n + \pi^0 \qquad (B.R. = 35.8\%) \tag{2.7}$$

In MWD, light- and medium-A hypernuclei are converted to non-strange nuclei through the reactions:

$${}^{A}_{\Lambda}Z \rightarrow^{A} (Z+1) + \pi^- \qquad (\Gamma_{\pi^-}) \tag{2.8}$$

$${}^{A}_{\Lambda}Z \rightarrow^{A} Z + \pi^0 \qquad (\Gamma_{\pi^0}) \tag{2.9}$$

where the final nuclear states are note necessarily stable. The theory of hypernuclear MWD was introduced by Dalitz [52], based on a phenomenological Lagrangian which describes the elementary process in Eq. 2.6 and 2.7.

The total decay wdith of a Λ-hypernucleus $\Gamma_T({}^{A}_{\Lambda}Z)$ is obtained with the sum of the mesonic and non-mesonic decay widths:

$$\Gamma_T = \Gamma_{MWD} + \Gamma_{NMWD} \tag{2.10}$$

where the first term Γ_{MWD} contains the contribution of the charged and neutral decay of the Λ and the second Γ_{NMWD} can be expressed as the sum of the one-nucleon and two-nucleon induced decay widths.

Furthermore, the total decay width $\Gamma_T({}^{A}_{\Lambda}Z)$ can be expressed in terms of the hypernuclear lifetime by:

$$\Gamma_T({}^{A}_{\Lambda}Z) = \hbar/\tau({}^{A}_{\Lambda}Z) \tag{2.11}$$

where $\hbar$ is the reduced Planck constant equal to 6.582×10^{-16} eV $\cdot$ s/rad.

Among the different experimental observables, the hypernucleus lifetime τ can be measured with the highest accuracy, especially in experiments where the hypernucleus production is seen. It is an inclusive quantity which can be measured by detecting any of the

possible products of either mesonic or non-mesonic decays as a function of time and by fitting the observed distribution with an exponential law.

An interesting result, presented in [53], shows the mass number dependence of hypernuclear lifetime for A<60 obtained by different counter experiments at BNL and KEK. The data indicate that the lifetime is quite stable from light- to medium-A hypernuclei and is rather constant above A = 20 at nearly 210 ps, which corresponds to $\sim$ 80% of the free Λ lifetime. This smoothly decreasing trend has been interpreted as a sign of anticorrelation between the MWD and the NMWD modes: the MWD mode decrease because of the Pauli blocking effect and seems to be balanced by the NMWD decay mode. In addition, this suggests that light-A hypernuclei have a lifetime slightly below the free Λ lifetime.

In a recent review [54] a compilation of the light and medium mass hypernuclei lifetime is presented and the results are shown in Figure 2.1. All the measured values show a good agreement and seem to be aligned around a similar value, with the only exception of the ${}^{4}_{\Lambda}$He and of the ${}^{5}_{\Lambda}$He. The authors computed the weighted average of these lifetime values, excluding those of ${}^{4}_{\Lambda}$He and ${}^{5}_{\Lambda}$He, and obtained the result of 205.3 $\pm$ 3.7 ps (blue dashed line), which is 20% below the free Λ lifetime (black dashed line).

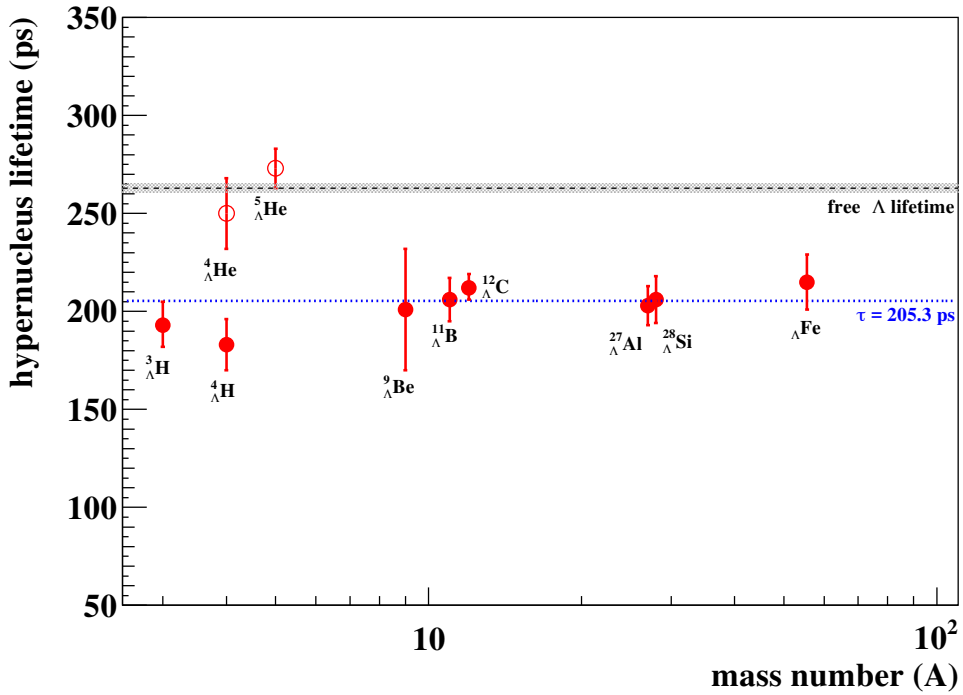

Figure 2.1.: Measured lifetime of light and medium-mass hypernuclei (x axis in logarithmic scale). The dashed black line is the free Λ lifetime and the dashed blue line is the weighted average of the measured values excluding the ${}^{4}_{\Lambda}$He and ${}^{5}_{\Lambda}$He results.

2.1.2. Hypertriton

The hypertriton ${}^{3}_{\Lambda}\mathrm{H}$ is the lightest Λ-hypernucleus. It is a loosely bound baryonic system composed by one proton, one neutron and one Λ and with a total binding energy [55]:

$$\mathrm{B}_{tot} = 2.35 \pm 0.05(stat.) \pm 0.04(syst.) MeV \tag{2.12}$$

It is also the weakest bound strange few-body hadronic system, since the Λ separation energy is only [55]:

$$\mathrm{B}_{\Lambda} = 0.13 \pm 0.05(stat.) \pm 0.04(syst.) MeV \tag{2.13}$$

It was discovered at the beginning of the hypernuclear physics by analising the events produced in the interaction of K^{-} both in flight and at rest with the nuclei of the sensitive layers of the visualizing detectors used in those years. Several Λ-hypernuclei, including the ${}^{3}_{\Lambda}\mathrm{H}$, have been found since the beginning of the hypernuclear physics, the anti-hypernucleus has been observed only seven years ago, with the discovery of the ${}^{3}_{\overline{\Lambda}}\overline{\mathrm{H}}$ in Au–Au collisions at $\sqrt{s_{\mathrm{NN}}}$= 200 GeV by the STAR Collaboration at RHIC [56].

The weak decay channels of the ${}^{3}_{\Lambda}\mathrm{H}$ are essentially mesonic (MWD):

$${}^{3}_{\Lambda}\mathrm{H} \rightarrow \pi^{-} + {}^{3}\mathrm{He} \qquad {}^{3}_{\Lambda}\mathrm{H} \rightarrow \pi^{0} + {}^{3}\mathrm{H} \tag{2.14}$$

$${}^{3}_{\Lambda}\mathrm{H} \rightarrow \pi^{-} + d + p \qquad {}^{3}_{\Lambda}\mathrm{H} \rightarrow \pi^{0} + d + n \tag{2.15}$$

$${}^{3}_{\Lambda}\mathrm{H} \rightarrow \pi^{-} + p + p + n \qquad {}^{3}_{\Lambda}\mathrm{H} \rightarrow \pi^{0} + p + n + n \tag{2.16}$$

The most recent evaluation of the B.R. of the ${}^{3}_{\Lambda}\mathrm{H}$ weak decay channels is presented in [57]. In particular in this reference the authors calculated the partial and total mesonic and non-mesonic decay rates, which are reported in Table 2.1.

These values led to a B.R. for the two and three body mesonic weak decay channel of 37% and 60%, respectively, considering both the charged and neutral modes, while the charged decay channels have a B.R. of 25% and 40%. These values will be used in this thesis as reference in the calculations that will involve the B.R.

Channel	Γ (sec^{-1})
Mesonic	
$^3He + \pi^-$ $^3H + \pi^0$	0.146×10^{10}
$d + p + \pi^-$ $d + n + \pi^0$	0.235×10^{10}
$p + p + n + \pi^-$ $p + n + n + \pi^0$	0.368×10^{8}
Non mesonic	
d + n	0.67×10^{7}
p + n + n	0.57×10^{8}
All channels	0.391×10^{10}

Table 2.1.: Total and partial mesonic and non mesonic decay rates of the $^3_\Lambda H$

2.1.3. $^3_\Lambda$H lifetime puzzle

The $^3_\Lambda H$ lifetime is one of the most important and challenging question of the hypernuclear physics. The very small value of B_Λ led to the hypothesis that the lifetime of the hypertriton $\tau(^3_\Lambda H)$ is equal or slightly below the free Λ lifetime $\tau(\Lambda) = 263.2 \pm 0.2$ ps [5].

Its measurement was done at the beginning with the visualizing techniques, which did not allow a direct time measurement. The main difficulty of this approach was related to the disentanglement of the events produced by K^- in flight or at rest, resulting in large systematic uncertainties. All the measurements performed with this techniques are based on small samples of events, sometimes less than 10, and this led to large statistical uncertainty, often exceeding 100%. The result reported in [58] is the unique based on a good sample of events, but the authors noticed a possible bias due to Coulomb dissociation of the loosely bound $^3_\Lambda H$ while going through the materials composing the emulsion.

Recently, the value of $\tau(^3_\Lambda H)$ has been measured by experiments which study ultrarelativistic heavy ion collisions, like STAR at BNL RHIC and ALICE at CERN LHC, or relativistic ion fragmentation, like HypHI at GSI SIS. The results reported by the three experiment, even though affected by large statistical and systematic uncertainties, are in agreement and significantly lower than the free Λ lifetime.

A detailed collection of the lifetime obtained with different techniques is reported in Table 2.2 taken from [54] and is also reported graphically in Figure 2.2, where the references on the markers are as defined in [54]. The red circles are the results from He bubble cham-

bers, the blue crosses those from the photographic emulsions and the green squares from counter experiments. The dashed lines and the shaded areas represent the weighted averages and their uncertainties calculated in [54] for the different class of experiment. For the emulsion series the average is of 203^{+40}_{-31} ps (blue dashed line), for the He bubble chamber is of 193^{+15}_{-13} ps (red dashed line) and for the combination of both the visualizing techniques is of 195^{+14}_{-13} ps. The weighted average of the results from heavy ion experiments is 185^{+28}_{-23} ps (green dashed line). All these weighted averages are comparable and shows a trend well below the free Λ lifetime.

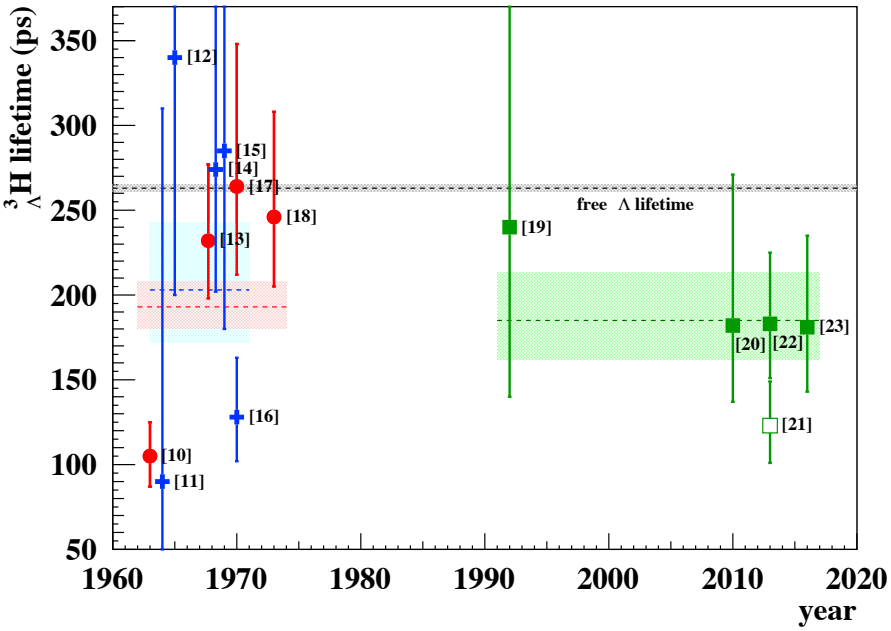

Figure 2.2.: Chronological synopsis of the experimental values on $^3_\Lambda$H lifetime taken from [54] and the reference on each marker can be find therein. Red circles are results from He bubble chambers, blue crosses from photographic emulsions and green squares from counter experiments.

However, the few existing theoretical calculations go in the direction of the hypothesis mentioned at the beginning of this section. The first approach to theoretical determination of $\tau(^3_\Lambda\mathrm{H})$ is due to Dalitz and Rayet; they obtained τ estimates in the range from 239.3-255.5 ps [71]. More recent calculations from Congleton [72] and Kamada [57] estimated a value of 232 ps and 256 ps, respectively.

The experimental values previously reported and the theoretical calculations of $\tau(^3_\Lambda\mathrm{H})$ represents the so called “lifetime puzzle". Thus, it is extremely important to measure the lifetime value with the highest precision possible, ideally 5%, in order to shed light on this question and solve this puzzle.

year	laboratory	beam	exp. method	lifetime (ps)	Reference
1963	LBL Bevatron	stopped K^-	He bubble chamber	105^{+20}_{-18}	[59]
1964	BNL AGS	K^-, 2.3-2.5 GeV/c	ph. emulsions	90^{+220}_{-40}	[60]
1965	BNL AGS and LBL Bevatron	K^-, 2.3 GeV/c K^- 790 MeV/c	ph. emulsions	340^{+820}_{-140}	[61]
1968	ANL ZGS	stopped K^-	He bubble chamber	232^{+45}_{-34}	[62]
1968	LBL Bevatron	K^- 1.1 GeV/c	ph. emulsions	274^{+110}_{-72}	[63]
1969	BNL AGS	K^- 1.1 GeV/c	ph. emulsions	285^{+127}_{-105}	[64]
1970	CERN PS	stopped K^-	ph. emulsions	128^{+35}_{-26}	[58]
1970	ANL ZGS	stopped K^-	He bubble chamber	264^{+84}_{-52}	[65]
1973	ANL ZGS	stopped K^-	He bubble chamber	246^{+62}_{-41}	[66]
1992	Dubna Synchrophasotron	He, Li ions 2.2-5 AGeV rHIc	counter experiment	240^{+170}_{-100}	[67]
2010	BNL RHIC	Au-Au $\sqrt{s_{NN}}$=200 GeV central urHIc	counter experiment	182^{+89}_{-45}	[56]
2013	BNL RHIC	Au-Au $\sqrt{s_{NN}}$=7.7-200 GeV central urHIc	counter experiment	123^{+26}_{-22}	[68]
2013	GSI SIS	Li ions 2 AGeV peripheral rHIc	counter experiment	183^{+42}_{-32}	[69]
2016	CERN LHC	Pb-Pb $\sqrt{s_{NN}}$=2.76 TeV central urHIc	counter experiment	181^{+54}_{-38}	[70]

Table 2.2.: Chronology of the lifetime measurements: year, laboratory, beam, experimental method, measured lifetime and publication Reference are given. rHIc stands for relativistic heavy-ions collisions, urHIc for ultra relativistic heavy-ions collisions.

2.2. Hypernuclei in heavy ion collisions

The production of light (anti-)(hyper-)nuclei in heavy ion collisions leads to a major puzzle: how these loosely bound objects could bind at the temperature reached in heavy ion collisions? While the experimental techniques used to measure the production spectra of ${}^{3}_{\Lambda}\mathrm{H}$ and ${}^{3}_{\Lambda}\overline{\mathrm{H}}$ are the main subject of this thesis, the following two sections are dedicated to a brief description of the major two classes of models that try to explain such a strange phenomenon: the Statistical Hadronisation Models (SHMs) and the Coalescence model [73].

2.2.1. Statistical Hadronisation Models

The analysis of particle production assessing the degree of thermalization of the particle source has been undertaken since many decades. The first to propose a statistical approach was Enrico Fermi in 1950 [74], who assumed that particles originated from an excited region occupy all available phase space. This was further developed by Hagedorn [75, 76], who noted that the hadronic mass spectrum has the asymptotic ($m \to \infty$) form:

$$\rho_H \sim exp[m/T_H] \tag{2.17}$$

where m is the mass of the hadron and T_H is the parameter, identified as temperature, which controls the slope of the mass spectrum.

The general idea behind these models, often called Thermal Models, is that the final state is composed by all the particle states compatible with the conservation laws imposed by the underlying theory of interaction, which in our scenario is the Standard Model of particle physics. The relative abundance of different particle states is set by the maximisation of the total phase space filled by the system, to which each particle species contributes according to its partition function. These models are particularly suited for the heavy ion collisions where the presence of an expanding medium that eventually reaches the thermal equilibrium seems appropriate for the statistical hadronisation approach.

As described in [77], the system created in a relativistic heavy ion collision is large enough to be modelled using the Grand Canonical ensemble. This formalism can be used since the experiments measure only the characteristics of a small portion of the system, like the central rapidity region in the case of the ALICE central detectors. This part of the phase space is in equilibrium with a thermal reservoir (the rest of the medium created in a heavy ion collision) and quantities like energy, baryon number, charge and isospin are conserved on average.

The parameters describing the equilibrium condition of a heavy ion collision in the Grand Canonical formalism include also the temperature T and the baryon chemical potential μ_B. The partition function of the system can be written as:

$$Z(T, V, \mu) = \mathrm{Tr}\left[e^{-\beta(H-\sum_i Q_i \mu_i)}\right] \tag{2.18}$$

with

$$\mu = \sum_i Q_i \mu_{Q_i} \qquad \text{and} \qquad \beta = \frac{1}{T} \tag{2.19}$$

where V is the volume of the system at equilibrium (also known as canonical volume), H is the Hamiltonian and μ_{Q_i} is the chemical potential associated to the conserved quantum number Q_i.

For a strongly interacting medium created in heavy ion collisions, the main conserved quantum numbers are the electric charge Q , the strangeness content of the system S and the baryon number B. The Hamiltonian H in the partition function is that one of a Hadron Resonance Gas since it is able to describe the behaviour of a strongly interacting medium reproducing over a wide temperature range the equation of state obtained with lQCD calculations before the transition to a deconfined state. The choice of the mesonic, baryonic and resonance states included in the Hamiltonian depends on the implementation of the model and it determines the maximum temperature that can be described accurately.

The total partition function Z of the system is the product of the partition functions Z_i of all the particle states in the Hadron Resonance Gas:

$$Z(T, V, \mu) = \prod_i Z_i(T, V, \mu_i) \qquad \rightarrow \qquad \mathrm{log}Z(T, V, \mu) = \sum_i \mathrm{log}Z_i(T, V, \mu_i) \tag{2.20}$$

where the Z_i functions, defined as

$$\mathrm{log}Z_i(T, V, \mu_i) = \frac{V g_i}{2\pi^2} \int_0^\infty \pm p^2 \mathrm{d}p \mathrm{log}\left(1 \pm \lambda_i(T, \mu_i) e^{-\beta\epsilon_i}\right) \tag{2.21}$$

are the Bose–Einstein (-) and Fermi–Dirac (+) partition functions for bosons and fermions, respectively. The g_i constant is the number of spin and isospin degenerate states for the species i and ϵ_i is the energy of one particle of the species i with momentum p ($\epsilon_i = \sqrt{p^2 + m_i^2}$). The dependence on the chemical potentials μ_i is encoded in the parameter λ_i, called *fugacity* and defined as:

$$\lambda_i(T, \mu_i) = e^{\beta(B_i\mu_B + S_i\mu_S + Q_i\mu_Q)} = e^{\beta\mu_i} \tag{2.22}$$

where B_i, S_i and Q_i are the baryon number, strangeness content and electric charge associated with the particle species and μ_B, μ_S and μ_Q are the corresponding chemical potentials. As described in [78], expanding the logarithm and integrating over the momentum, the partition function for the species i becomes:

$$\log Z_i(T,V,\mu_i) = \frac{VTg_i}{2\pi^2}\sum_{k=1}^{\infty}\frac{(\pm 1)^{k+1}}{k^2}\lambda_i^k m_i^2 K_2(\beta k m_i) \tag{2.23}$$

where the (+) is for bosons, the (-) for fermions and the K_2 is the second kind modified Bessel function of second order.

The average number of particle for the species i for a system described by the Gran Canonical ensemble, is defined as:

$$\langle N_i\rangle^{th}(T,V,\mu_i) = \frac{1}{\beta}\frac{\partial}{\partial\mu_i}\log Z_i(T,V,\mu_i) = \frac{VTg_i}{2\pi^2}\sum_{k=1}^{\infty}\frac{(\pm 1)^{k+1}}{k}\lambda_i^k m_i^2 K_2(\beta k m_i) \tag{2.24}$$

which does not fully describe the particle production measured in the heavy ion collisions. Indeed, for the measured yields the feed-down contribution from all the other particle species (resonances) j in the thermal system that can decay strongly in a final state containing particles of the species i should be considered:

$$\langle N_i\rangle(T,V,\mu) = \langle N_i\rangle^{th}(T,V,\mu_i) + \sum_j \Gamma_{j\to i}\langle N_j\rangle^{th}(T,V,\mu_j) \tag{2.25}$$

where $\Gamma_{j\to i}$ is the decay rate of the state j into the final state i.

The definition of particle yields, here introduced, is valid in the limit of a low density system, where the repulsion interaction between the hadrons constituting the systems is negligible. The treatment of these interactions, for instance introducing an eigenvolume for each particle state in the system as described in [78], is still matter of active theoretical research (especially for light (anti-)(hyper-)nuclei where it is difficult to neglect [79]). Nevertheless Eq 2.25 and 2.24 already indicate the crucial dependencies of the observed particle yields on the temperature T, volume V and the three chemical potentials (μ_B, μ_Q and μ_S).

In particular, two of these five parameters are constrained from the heavy ion collision conditions since no net strangeness is present in the colliding nuclei, thus $\mu_S = 0$, and μ_Q is fixed by the isospin asymmetry in the collision. The baryon chemical potential μ_B is not constrained as the “amount of baryonic number" transported in the equilibrium region varies with the energy of the collision. The dependence on the volume V of the system can

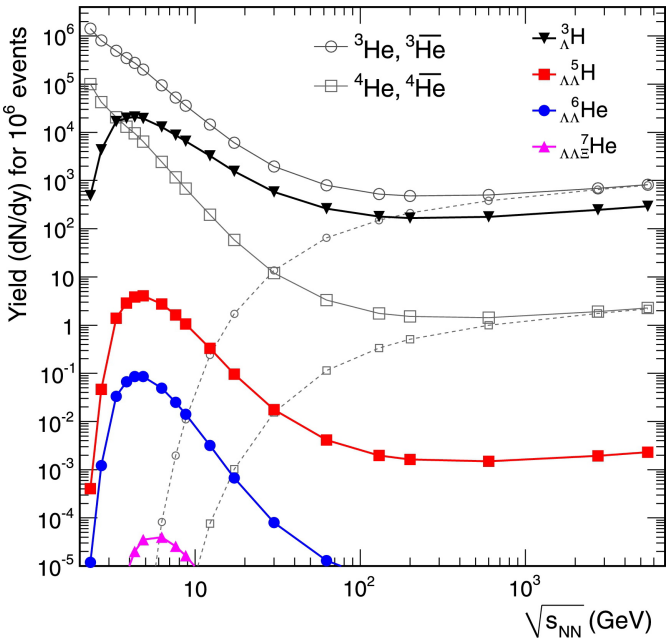

Figure 2.3.: Thermal model predictions for the production yields of different (anti-)(hyper-)nuclei as a function of the collision energy from [81]. At low collision energy there is a large difference between matter and anti-matter, which is due to the non-vanishing baryon chemical potential ($\mu_B \neq 0$). As the energy increases μ_B decreases and this difference vanishes.

be removed looking at ratio between the yields of different particle species, which therefore depends only on the temperature T of the system and on the baryon chemical potential μ_B.

There are some implementations of this model [80] that postulate the emission of some particle species (e.g. strange particle) out of the grand canonical equilibrium. These models introduce some additional phase space occupancy factors that are useful to describe systems where the suppression of the production rate for some particle species is observed.

Light nuclei and hypernuclei yields arise naturally in the thermal models when the chemical freeze-out temperature T_{chem} and the baryon chemical potential μ_B are set. A possible explanation on how the light nuclei can survive to the high temperature at the chemical freeze-out is given in [81], where the authors suggest the entropy density conservation of the system, after the chemical freeze-out, as the steering mechanism for the nuclei and hypernuclei production. Finally, from the fit of the particle abundances at lower energies, they predicted the yields of (anti-)(hyper-)nuclei at the LHC energy, as shown in Figure 2.3. The predictions for ^{3}He and ^{4}He are done both for matter (open marker and solid line) and antimatter (open marker and dashed line) and it is visible a large difference between them at low collision energy. This is due to the baryon chemical potential which

differs significantly from zero and, thus, the $e^{\beta B_i \mu_B}$ term in the particle yield favours matter over anti-matter. Then, as the energy increases, μ_B decreases and the difference vanishes.

The yields reported in the figure are predicted for 10^6 central collision events and the expectation of the $(^3_\Lambda\overline{\mathrm{H}})^3_\Lambda\mathrm{H}$ production yield per event is nearly 3×10^{-4}, considering only the production and not a single decay channel.

2.2.2. Coalescence Models

Another theoretical approach used to explain the measured light (hyper-)nuclei production in heavy ion collision is represented by the hadron coalescence models [73]. In these static models the (hyper-)nuclei are created at the kinetic freeze-out and there is no attempt to give a detailed description of the interactions that lead to their formation. The fundamental idea behind these predictions is that if A constituents are close enough in phase space at the kinematic freeze-out they can bind to form a nucleus or a hypernucleus. The coalescence models make a prediction about the momentum distribution of the produced light nuclei and hypernuclei as a function of the production spectra of the constituents. Historically, the coalescence formalism has been firstly developed for the light nuclei, such as deuteron and ^{3}He, and only recently has been extended to the hypernuclei production.

In 1961 Butler and Pearson [82] developed the first model to describe the deuteron formation in proton-nucleus collisions, using the proton and neutron invariant momentum spectra $\mathrm{E_i}\frac{\mathrm{d}^3N_\mathrm{i}}{\mathrm{d}p_\mathrm{i}^3}$. They took into account the *p-n* strong force and the nuclear optical potential to evaluate the deuteron invariant momentum spectrum as:

$$E_\mathrm{d}\frac{\mathrm{d}^3N_\mathrm{d}}{\mathrm{d}p_\mathrm{d}^3} = B_2\left(E_\mathrm{p}\frac{\mathrm{d}^3N_\mathrm{p}}{\mathrm{d}p_\mathrm{p}^3}\right)\cdot\left(E_\mathrm{n}\frac{\mathrm{d}^3N_\mathrm{n}}{\mathrm{d}p_\mathrm{n}^3}\right) \tag{2.26}$$

where B_2 is the coalescence parameter, which contains the dependence from the nucleon mass, the binding energy of the final state and the depth of the potential.

This model has been extended in 1963 by Schwarzchild and Zupancic [83] to describe the production of various light nuclei in nucleus-nucleus collisions. They proposed a formalism generalized for any nucleus of the species i with A nucleons:

$$E_i\frac{\mathrm{d}^3N_i}{\mathrm{d}p_i^3} = B_A\left(E_\mathrm{p}\frac{\mathrm{d}^3N_\mathrm{p}}{\mathrm{d}p_\mathrm{p}^3}\right)^A \tag{2.27}$$

where the proton spectrum is assumed to be identical to that one of the constituent neutron. One of the main reasons behind this generalization is that proton spectra are easier to mea-

sure in an experiment. In this formulation of the coalescence model the authors redefined the proportionality constant B_A. Indeed, they no longer considered it as related to the binding energy of the nucleus and to the nuclear optical potential of the target nucleus, since for violent nucleus-nucleus collisions the optical potential of the colliding nuclei is not a meaningful concept. The coalescence parameter B_A has been reinterpreted as a function of the radius p_0, that is the maximum distance at which coalescence can happen.

The simplest formulation of the coalescence models considers only the momentum space and not the space-time, thus the coalescence parameter can be expressed neglecting the nucleon spin, as:

$$B_A = \left(\frac{4}{3}\pi p_0^3\right)^{A-1} \frac{m_i}{m_p^A}. \tag{2.28}$$

where p_0 is the aforementioned radius and m_i and m_p are the nucleus and proton mass, respectively. This formulation, which foresees only a dependence of the coalescence parameter from p_0, it the most commonly used for the comparison with the data. Other extensions of the models predict a dependence on the geometry of the system. For instance, if one assumes that neutrons and protons are emitted in thermal and chemical equilibrium [84], in the limit of high temperature, their momenta spectra can be described with the Boltzmann-Gibbs distribution [1]:

$$E\frac{\mathrm{d}^3N}{\mathrm{d}p^3} = gV\frac{m_\mathrm{T}}{8\pi^3}e^{-\beta m_\mathrm{T}} \tag{2.29}$$

where g it the spin-isospin degeneracy of the nucleon and m_T it the transverse mass defined as $m_\mathrm{T} = \sqrt{m^2 + p_\mathrm{T}^2}$. Using this expression in the definition of the coalescence parameter, a dependence from the volume V of the emitting source becomes evident:

$$B_A = \frac{2J_A + 1}{2^A}\left(\frac{8\pi^3}{V}\right)^{A-1} \frac{m_{i\mathrm{T}}}{m_{p\mathrm{T}}^A} \tag{2.30}$$

where J_A is the total angular momentum of the nucleus and $m_{i\mathrm{T}}$ and $m_{p\mathrm{T}}$ are the transverse mass of the nucleus and of the proton, respectively. This formulation of the model predicts a smaller coalescence parameter, which means less probability to form a (hyper-)nucleus, for central collisions (bigger volume) than in peripheral collisions (smaller volume).

Recently the coalescence model approach has been extended to the hypernuclei production in heavy ion collision. In particular, since the introduction of the cascade model

[1] see Appendix B for the complete formula of Boltzmann-Gibbs distribution

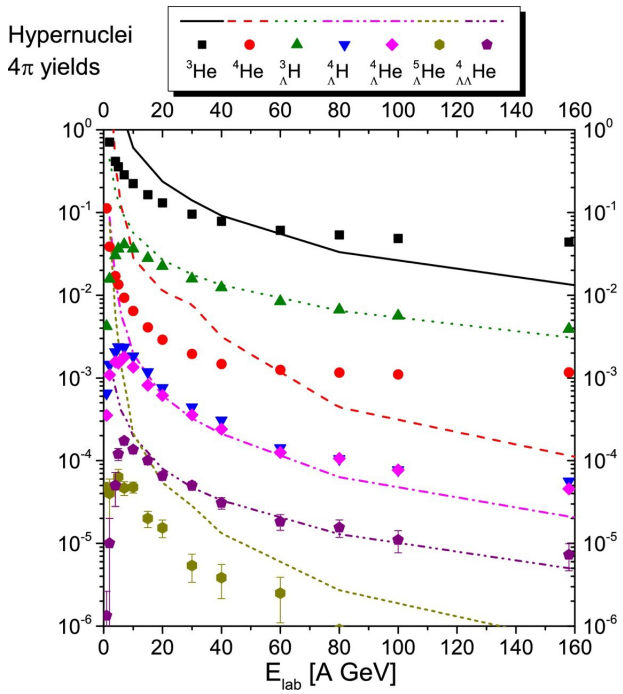

Figure 2.4.: Yield per event of different (hyper-)nuclei at midrapidity ($|y|<0.5$) for the central events (b<3.4 *fm*) of Pb–Pb/Au–Au collisions as a function of the collision energy. The symbols and the curves are the results of the Dubna Cascade Model [85].

calculation, which allow to take into account the interaction of particles at the initial stage of the collision. The advantage of using a cascade calculation is that many problems related to relativistic considerations, hydrodynamics and different kinematic distributions of protons and neutrons are taken into account in the dynamics of the cascade, and assumptions about the equilibrium properties and shapes of the system are not necessary.

Simulations of (anti-)(hyper-)nuclei production from cascade based coalescence models (e.g. Dubna Cascade Model, DCM [85]) have been performed in a wide range of momenta and energy in the center of mass. These calculations allow to have a prediction of (hyper-)nuclei production up to the top energy of the RHIC collider. Figure 2.4 shows the expected production yield of (hyper-)nuclei at mid-rapidity ($|y|$ <0.5) for central events (b < 3.4 *fm*) of Pb–Pb or Au–Au collisions as a function of energy.

The coalescence results depend on the parameters used in the model. To perform the calculations, the authors of [85] used for the Λ the same parameters of the nucleons. However the $Y-Y$ and $Y-N$ interactions are not well known and it is expected that some parameters should be different for these clusters.

Measurements of $(^{3}_{\overline{\Lambda}}\overline{\mathrm{H}})^{3}_{\Lambda}\mathrm{H}$ production yields at the LHC energy of $\sqrt{s_{\mathrm{NN}}}$= 5.02 TeV, which are the subject of this thesis, will help to understand if the coalescence is the process that governs the (anti-)(hyper-)nuclei production.

Chapter 3.

The ALICE experiment

"Dreaming is necessary, although in the dream reality should be glimpsed"
— Ayrton Senna, 1960–1994

The Large Hadron Collider (LHC) is the most powerful and complex accelerator ever built for particle physics research and can reach the high energy density and temperature required to melt the hadronic matter. Even though most of the LHC running time is devoted to the proton-proton physics which led to the discovery of the Higgs Boson [86, 87] and to the first observation of the double charmed baryon Ξ_{cc}^{++} [88], a significant part of the physics program is dedicated to the characterisation of the Quark-Gluon Plasma created in heavy-ion collisions.

3.1. The Large Hadron Collider

The Large Hadron Collider (LHC) is the last element of the accelerator complex at CERN (Figure 3.1), which is a succesion of machines that accelerate particles to increasingly higher energies. Each element in this chain boosts the energy of a beam of particles, before injecting it into the next machine. Protons and heavy ions are brought to their collision energies through different acceleration chains.

In particular, the choice of ions for the CERN heavy ion upgrade program was taken in the late 80s. The nucleus needed to be spherical so that the collision geometry would be simple. Moreover, it was favourable to have only one isotope in the injection chain for the acceleration of heavy nuclei. Thus, the spherical heavier nucleus of lead (^{208}Pb) was chosen for the SPS heavy ion program [89] and kept for the LHC ion beam project [90].

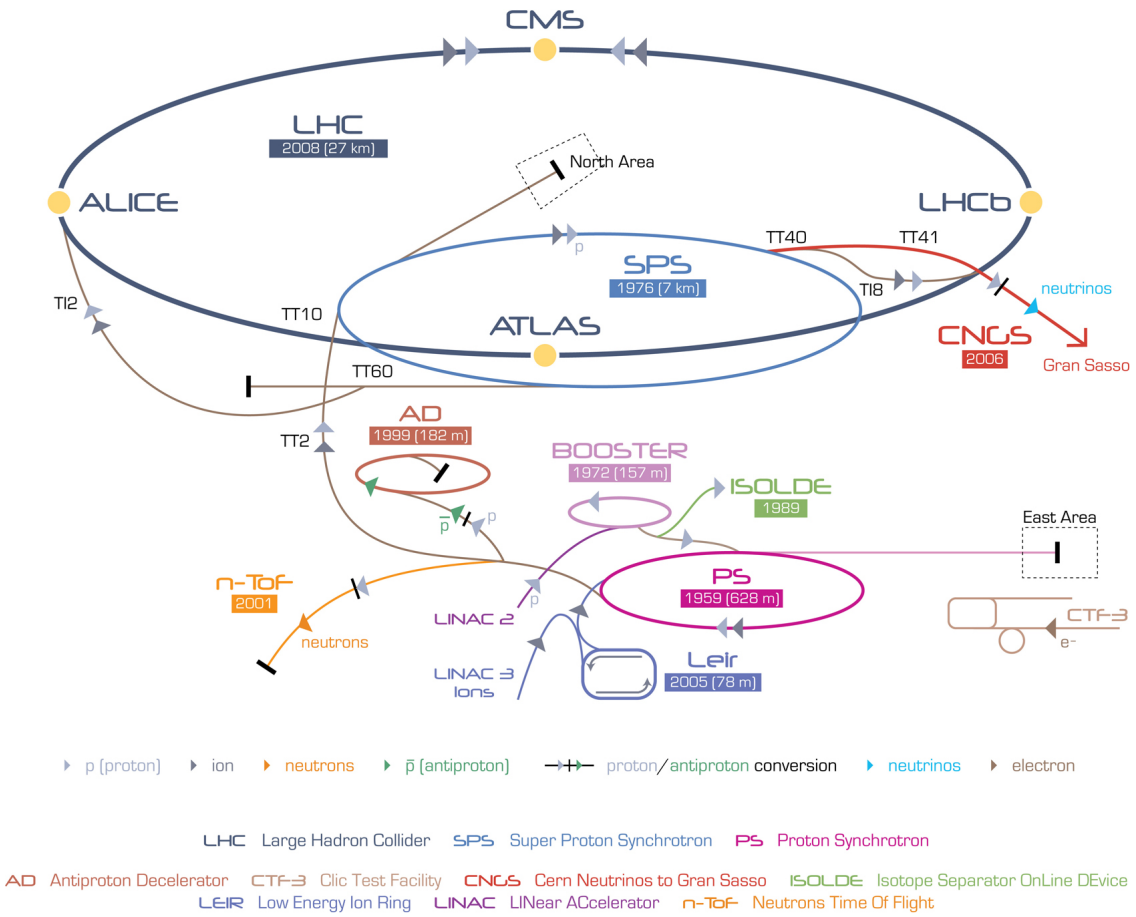

Figure 3.1.: The accelerator complex at CERN [91]

Protons are extracted from a source of hydrogen gas using an electric field to strip hydrogen atoms of their electron and then they are accelerated up to 50 MeV by LINAC 2. The beam is injected in the Proton Synchrotron Booster (PSB), which accelerates the protons up to 1.4 GeV and provides the beam bunches to the Proton Synchrotron (PS). The Proton Synchrotron pushes protons up to 25 GeV and then they are injected into the Super Proton Synchrotron (SPS), where they are accelerated up to 450 GeV before the injection in the LHC.

Lead ions are produced by heating up a small isotopically pure ^{208}Pb sample and then by ionising the gas obtained. The obtained ions enter the LINAC 3 that provides the ion beam at the energy of 4.5 MeV to the Low Energy Ion Ring (LEIR). The beam is split into 4 short bunches, which are further accelerated from 4.2 MeV to 72 MeV. The ion beam is then transferred from the LEIR to the PS and it follows the same acceleration steps previously described for the proton beams.

In the LHC two counterrotating beams are guided in separate vacuumfilled pipes by 1232 dipole magnets and focused by 392 quadrupole magnets. In particular these magnets are cooled down to 1.9 K to become superconductive and can reach the peak magnetic field value of 8.33 T. The beams are accelerated up to the energy of 6.5 TeV for protons and brought into collisions in the four interaction points corresponding to the four major LHC experiments. The top centre-of-mass energies reached at the LHC in the collisions are 13 TeV and 5.02 TeV per nucleon pair for pp and Pb–Pb collisions, respectively.

A crucial parameter for the experiments, along with the top energy, is the *luminosity* delivered by the collider. Indeed the number of events per second generated in the LHC collisions can be evaluated with the following formula [92–94]

$$R_{event} = L\sigma_{event} \tag{3.1}$$

where L is the machine istantaneous luminosity and σ_{event} is the cross section for the event under study. The istantaneous luminosity depends only on the beam parameters and can be written as

$$L = \frac{N_b N^2 f_{rev} \gamma}{4\pi\epsilon_n \beta^*} F, \tag{3.2}$$

where N_b is the number of bunches in the collider ring, N is the number of charges in each bunch, f_{rev} is the revolution frequency of the beam, γ is the relativistic factor, ϵ_n is the normalized emittance[1], F is a geometrical factor and β^* is the value of the amplitude function[2] at the interaction point (IP) where the luminosity is estimated. The geometrical luminosity reduction factor F is given by

$$F = \left[\sqrt{1 + \left(\frac{\sigma_z}{2\sigma_T}\theta_c\right)^2}\right]^{-1}, \tag{3.3}$$

where σ_z and σ_T are the root mean square (*rms*) of the longitudinal and transverse[3] size of the beam respectively and θ_c is the total crossing angle between the two beams at the IP. This small angle (about 300 μrad at the LHC), between the two beams at the IP, limits the istantaneous luminosity of the collider and is introduced to limit the long range electromagnetic interaction between the two beams.

[1] $\epsilon_n = \beta\gamma\epsilon$, where β and γ are the usual relativistic factors and the emittance ϵ is the spread of beam particles in the positionmomentum phase space.

[2] The amplitude function $\beta(s)$ describes the beam amplitude modulation due to the changing focusing strength.

[3] The transverse size of the beam $\sigma_T(s) = \sqrt{\epsilon\beta(s)}$ depends on the emittance and $\beta(s)$

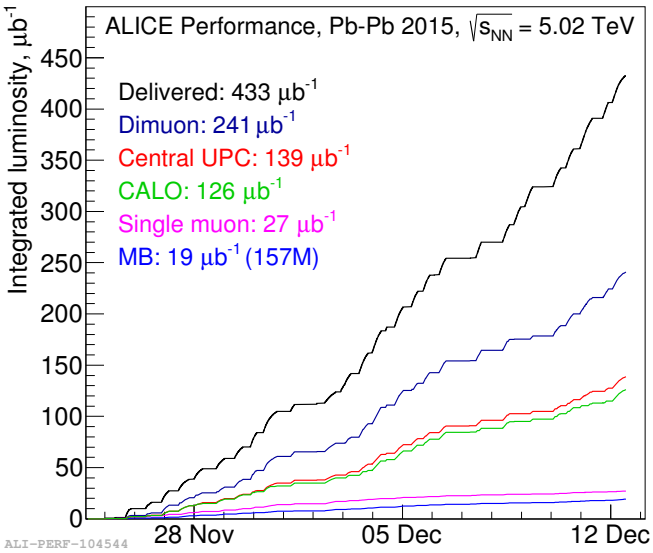

Figure 3.2.: ALICE delivered and integrated luminosity during the first Pb–Pb period in Run 2.

The two high-luminosity experiments installed at the LHC, ATLAS and CMS, and the low-luminosity experiment LHCb aim to a peak luminosity of $L = 10^{34}$ cm^{-2}s^{-1} and $L = 10^{32}$ cm^{-2}s^{-1} respectively in pp collisions. ALICE requires a peak luminosity of $L = 10^{27}$ cm^{-2}s^{-1} in Pb–Pb collisions. The high beam intensity required to achieve these luminosities excluded the possibility of a $p\overline{p}$ collider, since the production of anti–protons is much more complicated than the production of protons. The number of protons per bunch N is of the order of $\sim 10^{11}$ and the ring can store up to 2808 bunches with 25 ns spacing. The normalised emittance at the end of the acceleration in the LHC is 3.75 μm while the β^* depends on the IP. Figure 3.2 shows the delivered luminosity by the LHC (black line) and the integrated luminosities collected by ALICE, for different trigger configurations (colored lines), during the first Pb–Pb period in Run 2 at the end of 2015.

Finally, an important information for the physics analyses at collider experiments is the knowledge of the position where the collision between the two beams takes place, which is called *primary vertex*. The nominal position of the primary vertex is the origin of the coordinate reference frame of the experiment. Nevertheless, the position of the primary vertex varies around the nominal position due to the finite size of the bunches. Being $\sigma^{bunch}_{x,y,z}$ the *rms* of the bunch in the transverse and longitudinal direction, it can be shown that, assuming a gaussian profile of the bunches in the three directions, the *rms* of the vertex variation is

$$\sigma^{vertex}_{x,y,z} = \frac{\sigma^{bunch}_{x,y,z}}{\sqrt{2}}, \tag{3.4}$$

where the *rms* size of the bunch depends on the beam emittance and β^* [95] :

$$\sigma_{x,y,z}^{bunch} = \sqrt{\frac{\epsilon_{x,y,z}\beta^*}{\sqrt{\pi}}}. \tag{3.5}$$

The typical values of *sigma* at IP2, where the ALICE experiment is located, are $\sim$ 50 μm and $\sim$ 20 μm for $\sigma_{x,y}^{vertex}$, in pp and Pb–Pb collisions, respectively, and $\sim$ 5 cm for σ_{z}^{vertex} for both colliding systems.

3.2. ALICE setup

The ALICE experiment has been specifically designed and optimised for the study of the QCD matter created in high-energy heavy ion collisions. The main requirements for a heavy ion experiment are an efficient tracking system with a large acceptance and a good particle identification (PID) in a wide momentum range. At the time of ALICE design, the charged particles multiplicity per rapidity unit in central Pb–Pb collisions was predictied to range between 2000 and 8000 [96], and for this reason detectors with high granularity and low material budget have been adopted [97, 98].

The current layout of the ALICE experiment is shown in Figure 3.3 while Table 3.1 lists the position and the purpose of the ALICE sub-detectors.

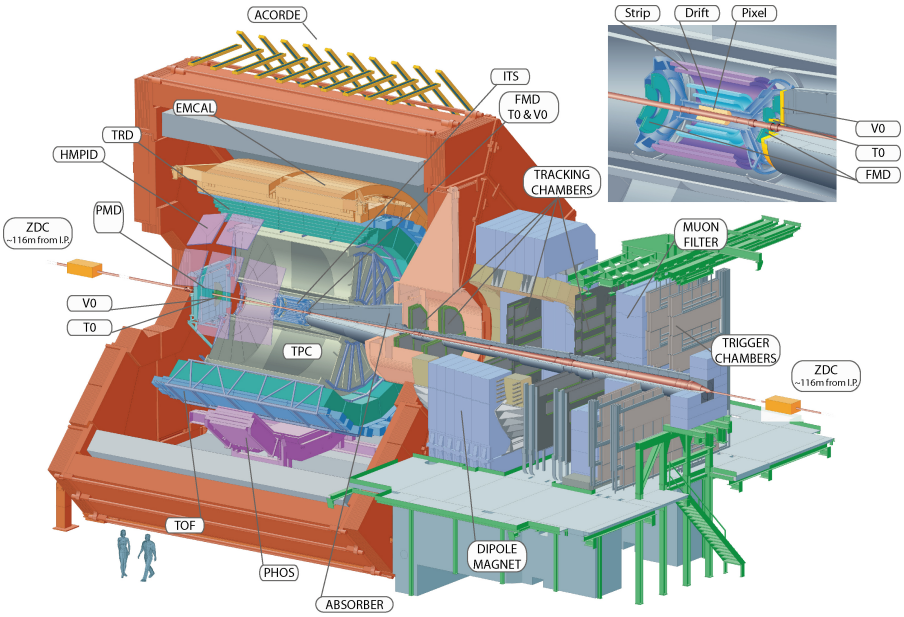

Figure 3.3.: The ALICE experimental setup and the red L3 solenoid magnet. The top right inset shows a zoom on the V0, T0, FMD and the ITS detectors.

	Acceptance			
Detector	*Polar*	*Azimuthal*	Position	Main purpose
SPD† *layer 1*	$\lvert\eta\rvert < 2.0$	full	r = 3.9 cm	tracking, vertex
SPD† *layer 2*	$\lvert\eta\rvert < 1.4$	full	r = 7.6 cm	tracking, vertex
SDD *layer 3*	$\lvert\eta\rvert < 0.9$	full	r = 15 cm	tracking, PID
SDD *layer 4*	$\lvert\eta\rvert < 0.9$	full	r = 23.9 cm	tracking, PID
SSD *layer 5*	$\lvert\eta\rvert < 1.0$	full	r = 38 cm	tracking, PID
SSD *layer 6*	$\lvert\eta\rvert < 1.0$	full	r = 43 cm	tracking, PID
TPC	$\lvert\eta\rvert < 0.9$	full	85 < r/cm < 247	tracking, PID
TRD†	$\lvert\eta\rvert < 0.8$	full	290 < r/cm < 368	tracking, $e^{\pm}$ id
TOF†	$\lvert\eta\rvert < 0.9$	full	370 < r/cm < 399	PID
PHOS†	$\lvert\eta\rvert < 0.12$	$220^\circ<\phi<320^\circ$	460 < r/cm < 478	photons
EMCal†	$\lvert\eta\rvert < 0.7$	$80^\circ<\phi<187^\circ$	460 < r/cm < 478	photons, jets
HMPID	$\lvert\eta\rvert < 0.6$	$1^\circ<\phi<59^\circ$	r = 490 cm	PID
ACORDE†	$\lvert\eta\rvert < 1.3$	$30^\circ<\phi<150^\circ$	r = 850 cm	cosmics
PMD	$2.3 < \eta < 3.9$	full	z = 367 cm	photons
FMD	$3.6 < \eta < 5.0$	full	z = 320 cm	charged particles
	$1.7 < \eta < 3.7$	full	z = 80 cm	charged particles
	$-3.4 < \eta < -1.7$	full	z = -70 cm	charged particles
V0 A†	$2.8 < \eta < 5.1$	full	z = 329 cm	charged particles
V0 C†	$-3.7 < \eta < -1.7$	full	z = -88 cm	charged particles
T0 A†	$4.6 < \eta < 4.9$	full	z = 370 cm	time, vertex
T0 C†	$-3.3 < \eta < -3.0$	full	z = -70 cm	time, vertex
ZDC†	$\lvert\eta\rvert > 8.8$	full	$z = \pm 113$ cm	forward neutrons
	$6.5 < \eta < 7.5$	$\lvert\phi\rvert<10^\circ$	$z = \pm 113$ cm	forward protons
	$4.8 < \eta < 5.7$	$\lvert 2\phi\rvert<32^\circ$	$z = \pm 113$ cm	photons
MCH	$-4.0 < \eta < -2.5$	full	-14.2 < z/m < -5.4	muon tracking
MTR†	$-4.0 < \eta < -2.5$	full	-17.1 < z/m < -16.1	muon trigger

Table 3.1.: Geometrical details and main purposes of the ALICE sub-detectors. This table has been taken and adapted from the description of the ALICE apparatus in [99]. The transverse (r) and longitudinal (z) coordinates as well as the acceptance (*polar* and *azimuthal*) are measured with respect to the ALICE coordinate reference frame, described in the text. When more than one position value is specified the detector is divided in two or several parts and the reported values are the minimum and maximum distances from the interaction point. The detectors marked with a dagger (†) are also used for triggering.

The ALICE coordinate system is a right-handed orthogonal Cartesian system with the origin settled at the nominal beams IP. The x axis of the reference frame is aligned with the horizontal accelerator plane and points to the centre of the LHC, while the y axis is perpendicular to the accelerator plane and points upward. As a consequence the z axis is parallel to the beam direction and its positive direction is defined by the chirality of the coordinate system. Finally, the azimuthal angle ϕ increases counter-clockwise starting from $\phi = 0$ for x axis looking towards the CMS side, and the polar angle θ increases from z (θ = 0) to -z ($\theta = \pi$). Two other variables, widely used in this thesis, need to be introduced: the rapidity y and the pseudo-rapidity η[4] . These variables are defined as

$$y = \frac{1}{2} ln \frac{E + p_z}{E - p_z} \tag{3.6}$$

$$\eta = \frac{1}{2} ln \frac{|p| + p_z}{|p| - p_z} = -ln \left[tan \left(\frac{\theta}{2} \right) \right] \tag{3.7}$$

where E and p_z are the particle energy and momentum along z axis respectively, while θ is the polar angle previously described.

Three main parts can be distinguished in the ALICE apparatus: the *central barrel*, the *muon spectrometer* and the *forward detectors*.

The *central barrel* consists of all the detectors located inside and outside the ALICE solenoid in the pseudo-rapidity range $|\eta| < 0.9$. The central barrel tracking detectors cover the full azimuthal acceptance and include, going from the IP to the outside, the Inner Tracking System (ITS), the Time Projection Chamber (TPC) and the Transition Radiation Detector (TRD). The central systems are embedded in a mild solenoidal magnetic field (B = 0.5 T), in order to extend the transverse momentum reach of the experiment down to 80 MeV/c. The magnetic field is produced by the warm resistive magnet previously used for the L3 experiment at LEP [100]. The resolution on the momentum depends also on the lever arm length of the tracking detectors L and on the resolution of track sagitta[5] measurement σ_s

$$\frac{\sigma_p}{p} \propto p \frac{\sigma_s}{BL^2}. \tag{3.8}$$

The ALICE experiment is able to reconstruct tracks of momenta up to $\sim$ 100 GeV/c as a consequence of the large radial coverage (3.9 $\leq$ r $\leq$ 368 cm), despite the low solenoidal magnetic field. The tracking detectors provide also the information for particle identification (PID), together with the Time Of Flight (TOF) detector and the High-Momentum

[4] In the high energy limit it can be shown that $lim_{\beta \to 1} \eta = y$.

[5] The sagitta is the distance from the center of the arc to the center of its base.

Particle Identification (HMPID). These detectors are used in most of the analyses (e.g. identified particle spectra, strange hadrons and hypernuclei production) thanks to their Particle Identification performances which will be described in Section 3.4.3. There are also an ElectroMagnetic Calorimeter (EMCal) and a Photon Spectrometer (PHOS) which do not have full azimuthal or pseudo-rapidity coverage in the central barrel region: they are dedicated to the physics of high p_{T} photons and jets. Finally, the central barrel is supplemented by an array of 60 large scintillators (ACORDE) which is placed on top of the ALICE solenoid. ACORDE is used to study the high-energy cosmic air showers in the energy range $10^{15} \div 10^{17}$ eV to determine the nature of primary cosmic rays [101], as well as for trigger and alignment purposes [102] .

The *muon spectrometer* is located in the -4 < η < -2.5 region and it allows the measurement of the complete spectrum of heavy-quark vector-mesons resonances, as well as the ϕ mesons, through their $\mu^+\mu^-$ decay channel. It consists of an absorber with small atomic number Z, a spectrometer with a dipole magnet, five tracking stations, four trigger stations and an iron absorber.

The *forward detectors* are located in the forward-backward pseudorapidity regions and as close as possible to the beam line. They are: the Forward Multiplicity Detector (FMD), made of silicon strips detectors, the Photon Multiplicity Detector (PMD) and the Zero Degree Calorimeters (ZDC) consisting of two hadronic calorimeters, for protons and neutrons, plus one electromagnetic calorimeter. In addition there are two trigger detectors located at each side of the interaction point: the V0, made of scintillator detectors, and the T0, composed by two arrays of Cherenkov counters.

In the following sections the sub-detectors used in the study of (anti-)hypertriton are described in detail.

3.2.1. Inner Tracking System

The Inner Tracking System (ITS) [96, 99] is a cylindrical silicon tracker and it is the central barrel detector closest to the interaction point. It is composed of six layers of silicon detectors, using three different technologies as can be seen in Figure 3.4. The radial position and the azimuthal and polar coverage of each layer are reported in Table 3.1.

The silicon pixel detectors (SPD) are the two innermost layers of the ITS and are fundamental for the determination of the primary vertex position as well as for the measurement of the impact parameter of secondary tracks originating from the weak decays of particles.

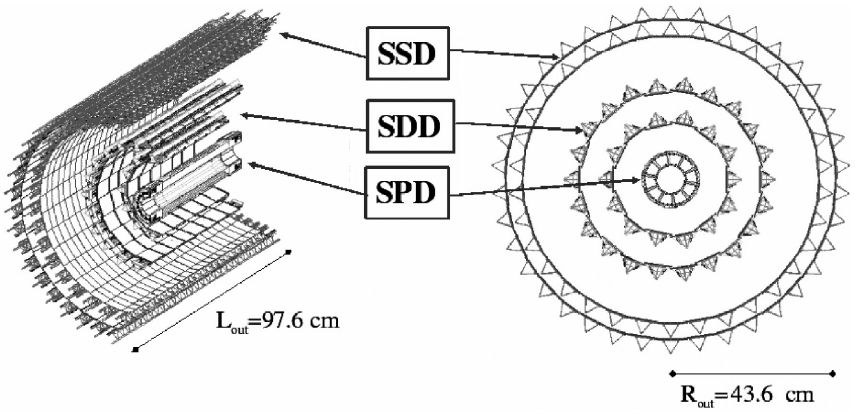

Figure 3.4.: Layout of the ALICE Inner Tracking System, which is equipped with three different subdetectors.

Parameter	SPD	SDD	SSD
Material budget per layer (%X_0)	1.14 - 1.14	1.13 - 1.26	0.83 - 0.86
Spatial resolution $r\phi$ (μm)	12	35	20
Spatial resolution z (μm)	100	25	830
Two track resolution $r\phi$ (μm)	100	200	300
Two track resolution z (μm)	850	600	2400
Active cell size (μm^2)	50×425	202×294	95×40000
Number of readout channels (k)	9835	133	2603

Table 3.2.: Details about the material budget and spatial resolution of the ITS subdetectors [96]. The material budget is reported for each single layer.

In addition, the SPD provides a quick trigger signal (*Fast-OR*), which contributes to the Level 0 trigger of the experiment.

The silicon drift detectors (SDD) are adopted on the third and fourth layers. The SDD uses the time necessary to electrons, produced by ionizing particle crossing the detector, to drift towards the collecting anodes in order to determine the position of the particle. The advantages of this detector are the high 2D resolution, as shown in Table 3.2 , with limited number of read-out channels and the low material budget.

The last two layers are equipped with double sided silicon strip detectors (SSD). The SSD provides a two dimensional measurement of the track position and it is crucial for the matching of the tracks from ITS to TPC, being the outermost layers of the silicon tracker system. The SSD, together with the SDD, provide also information about the energy loss of particles in their sensitive volume, extending the ALICE PID capabilities in the p_{T} region below 200 MeV/c.

The ITS allows the reconstruction of primary and secondary vertices with a resolution better than 100 μm and extends the tracking of the low p_{T} particles down to $p_{\mathrm{T}} = 80$ MeV/c, thanks to its high spatial resolution (Table 3.2) and low material budget. The total material budget of the ITS, keeping into account also the support structures and the thermal shields, is 7.18% $\mathrm{X/X_0}$.

3.2.2. Time Projection Chamber

The Time Projection Chamber (TPC), depicted in Figure 3.5, is a gas detector and it is the main tracking detector of the central barrel [103]. It provides charged particle momentum measurements with good two-track separation and it is also one of the main PID detectors as it provides the information about the specific energy loss of the particles in its volume in a momentum range larger than the other detectors (e.g. ITS). The total sensitive detector volume is 88 m^3 and it was filled with a mixture of Ne and $\mathrm{CO_2}$ during LHC Run 1 (2009-2012), while at the beginning of the LHC Run 2 (2015-2018) a mixture of Ar and $\mathrm{CO_2}$ has been used.

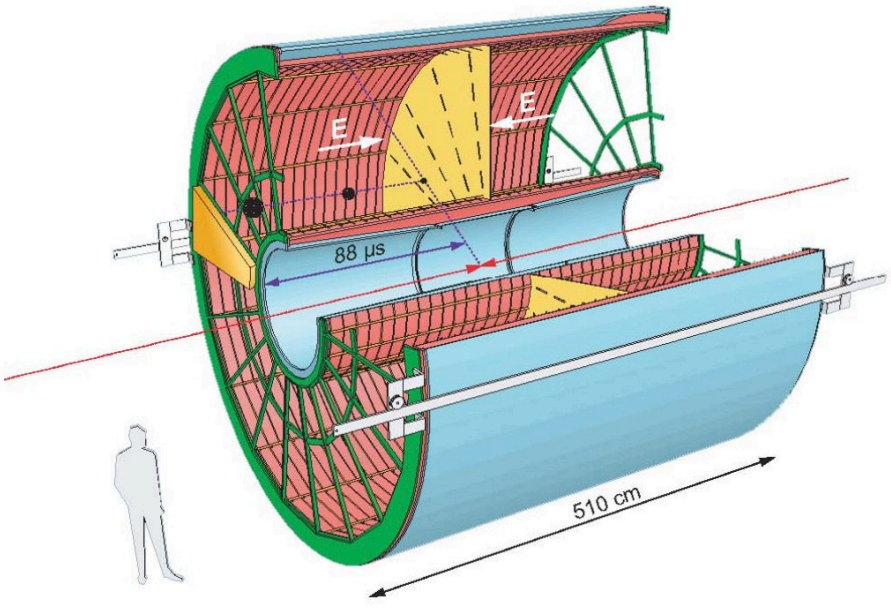

Figure 3.5.: Schematic layout of the ALICE Time Projection Chamber.

The total active length of 4.994 m is divided into two drift regions by the central high voltage (HV) catode. The drift voltage of -100 kV applied at the central electrode produces in a drift field of 400 V/m, pointing towards the central catode. A charged particle, crossing

the TPC, ionizes the gas creating free electrons and ions. The drift field separates the two charges and the electrons drift to the end-plates with a drift velocity of 2.65 cm/μs.

Each end-plate is equipped with 36 readout chambers, which are organized in 18 sectors, covering 20° in azimuth each. The readout chambers consist in a system of multi-wire proportional chambers (MWPC) with cathode pad read-out. Each sector is segmented by pads organized in rows and the longitudinal coordinate is given by the drift time. The pads in the inner readout chamber (IROC) are smaller than those in the outer readout chamber (OROC), 4 $\times$ 7.5 mm^2 and 6 $\times$ 15 mm^2 respectively. This choice has been done to cope with the predicted high multiplicity environment. Thanks to this segmentation, charged particles can be tracked and identified with up to 159 3-dimensional space points (TPC clusters), including also the specific energy loss information for the PID. The TPC radial position and acceptance are reported in Table 3.1.

3.2.3. Time Of Flight detector

The Time of Flight detector (TOF) is used to identify charged particles and light nuclei in the momentum interval 0.2$\div$4 GeV/c in the central pseudorapidity range ($|\eta| < 0.9$). The TOF has a cylindrical geometry and consists of a large area array of Multi-gap Resistive-Plate Chambers (MRPC) with a sensitive area of 7.4 $\times$ 120 cm^2 each and an intrinsic resolution of about $\sim$ 40 ps [96].

The precise determination of the event collision time, the so called t_0, represents an important ingredient for the TOF PID. It is determined by using the information from the T0 and TOF detectors as described in [104]. The time of flight of a particle is determined measuring the time between the event collision and the particle TOF hit cluster. The time of flight of the particle together with the momentum, obtained from the track curvature, allows to compute the particle β and, as a consequence, its mass.

3.2.4. T0

The T0 detector consists of two arrays of Cherenkov counters placed on both sides of the interaction point (Table 3.1). It is mainly used to determine the event collision time (t_0) with a resolution below 50 ps and independently from track and vertex reconstruction. The T0 information allows also the determination of the primary vertex position with a precision of $\pm$ 1.5 cm along the beam axis for each interaction and provides the Level 0 trigger when the position of the vertex falls in appropriate intervals. During the LHC Run 2 it is also used as the primary luminosity monitoring detector.

3.2.5. V0

The V0 [105] is a small angle detector consisting of two arrays of 64 scintillators counters (V0A and V0C[6]) distributed in 8 rings and they are installed on both sides of the ALICE interaction point (Table 3.1). The V0 detectors are used to define the minimum bias (MB) trigger in ALICE, which is a logical "*or*" between the signals of V0A, V0C and SPD. The signal of the V0 is also used to determine the centrality in p–Pb and Pb–Pb collisions and to reject the beam-gas interactions.

3.3. ALICE data-flow: from collisions to physics

3.3.1. Trigger system

The trigger system in ALICE is managed by the Central Trigger Processor (CTP) [106], which combines and synchronizes the signals from all the triggering detectors with the information on the LHC filling scheme and then checks if any of the trigger conditions is satisfied. It forms a decision for every bunch crossing and communicates it to all the detectors which need to be read out. A 3-level system has been adopted in ALICE to comply with the different readout times and trigger latencies of the detectors. The CTP evaluates the trigger inputs from the trigger detectors every machine clock cycle ($\sim$ 25 ns). The Level 0 trigger (L0) decision is taken $\sim$ 0.9 ns after the collision by using the fast detectors (SPD, V0, T0, EMCal, PHOS and muon trigger). The Level 1 trigger (L1) evaluates the event accepted in the L0 and makes a decision in $\sim$ 6.5 μs. The buffering of the event data in the detector front-end electronics is triggered by the L0 and L1 decisions. The Level 2 (L2) decision, taken after 100 μs, triggers the sending of the event to the Data Acquisition (DAQ) system [107] and to the High-Level Trigger system (HLT) [108].

3.3.2. Data acquisition

The Local Trigger Units (LTU) of each detector broadcasts the positive trigger decision and the data are pushed into the DAQ system by the detectors Front-End and Read-Out (FERO) electronics. The data produced by the detector electronics (*event fragments*) are transported to the Local Data Concentrator (LDCs) through a point-to-point optical connections with a capacity of 200 MB/s, the Detector Data Link (DDLs). The LDCs realize the first event-building, assembling the event fragments belonging to the same collision into a sub-event.

[6] A and C stand for ATLAS and CMS

The second step is realized by the Global Data Collectors (GDCs), where the sub-events are received (data rate up to 20 GB/s) and assembled, together with the HLT output, in the full event. When the event building in the GDC is completed, the data are buffered in a local disk pool waiting to be transferred to the CERN computing centre.

3.3.3. ALICE offline framework

The routine of Monte-Carlo simulations and the event reconstruction flow will be briefly described in this section.

Monte-Carlo simulations

The first step of Monte-Carlo simulations is the event generation. Since the physics program of ALICE includes the study of pp, pA and heavy-ion collisions, the simulation tools include generators for all the interaction topologies. The result of the event generation is the set of all stable and weakly decaying particles, that will be transported, with their starting kinematic parameters. The strongly decaying particles are usually handled at the generator level. The generated kinematic parameters are propagated, using a transport framework, through the experiment, whose geometry and material budget are precisely described in the ALICE software. It is possible to use three different transport codes in the simulation framework: GEANT3 [109], GEANT4 [110] and FLUKA [111]. These tools provide the information about the particle energy loss in the sensitive part of the detector, usually called *hits*. They also take into account the generation of secondary particles from the material (e.g. delta rays) and handle the weak decays of particles (e.g. K^0_S, Λ). The hits are then processed through the simulation of each detector response to produce the corresponding electronics signal, the *digits*. The digits are finally stored in the same detector raw data format used in the real data taking and reconstruction.

Event reconstruction

The ALICE event reconstruction flow starts from the raw data, collected or simulated, and is schematically shown in Figure 3.6 The first step of the event reconstruction is the clusterization, where the detector raw data are converted into *clusters*, through a set of algorithms which perform this reconstruction for each detector separately. All clusters are characterized by positions, signal amplitude and time. Other informations, like the energy lost by

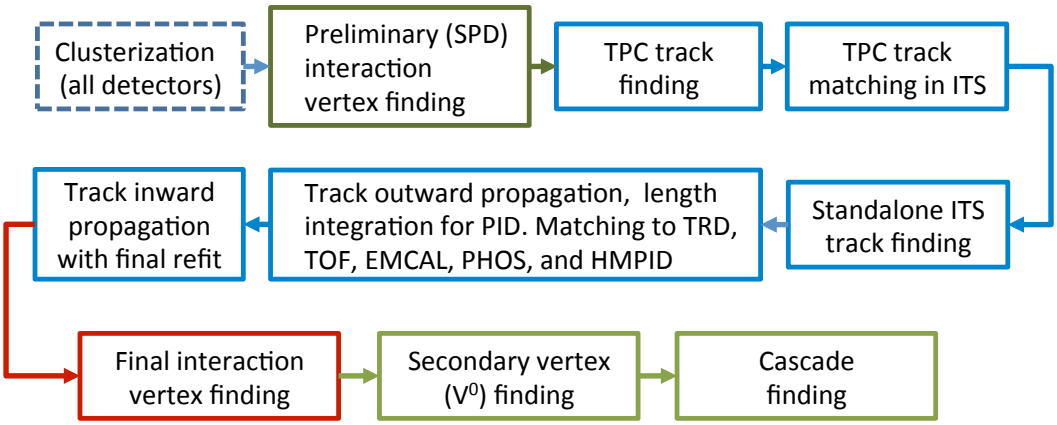

Figure 3.6.: Vertex and tracks reconstruction procedure in ALICE [99].

the particle, the time of flight and the Čerenkov angle, are attached to the clusters of the PID detectors allowing the identification of the tracked particles (Section 3.4.3).

The second step in the reconstruction flow is a preliminary estimation of the position of the primary vertex using clusters in the first two ITS layers (SPD). The first estimate of the primary vertex is important to speed-up the tracking algorithm searching good candidate tracks, even if the best and final estimation of the position of the interaction vertex is obtained using the full track information.

Subsequently, track finding and fitting are performed in TPC and ITS using the Kalman filter technique [112]. The tracks are reconstructed starting from the TPC which is the main tracking detector in ALICE. Then they are prolonged in the ITS. The found tracks are backward propagated searching for a possible match in the other central barrel detectors. Finally, the primary vertex can be determined using the fully reconstructed tracks.

The search for photon conversion and decays of strange hadrons as K^0_S, Λ, $\Xi^{\pm}$ and $\Omega^{\pm}$ is the last step of the event reconstruction chain. More details on the procedure and the performance of the different steps will be given in Section 3.4.

3.3.4. ALICE analysis framework

The analysis framework plays a crucial role as any detector for high energy physics experiment. The amount of data collected by the ALICE experiment during the last years is of the order of ten petabytes. Consequently, it requires a complete set of tools able to process

and analyse the reconstructed events in the most efficient way by optimising the available computing resources.

The reconstruction of the collected data, the analyses and the simulations are performed using the Worldwide LHC Computing Grid (WLCG) [113]. It is a federation of 170 computing centres in 42 countries, as of 2017, which has been designed to handle and process the data acquired by the LHC experiments. The computing centres are organised in 3 *tiers*. The first level (Tier 0) is constituted by the CERN computing centre and the computing centre at the Wigner Research Centre for Physics in Budapest. It hosts one replica and performs the first reconstruction of the raw data. A second replica of the raw and reconstructed data is stored in the Tier 1 centres, which are also involved in the re-processing of the data and in part of the reconstruction. Finally there are the Tier 2 centres where the Monte Carlo simulations and the processing of the analyses are performed.

The Alien (ALICE Environment) [114] grid middleware is the ALICE software infrastructure that allows, through the Alien user interface, the access to the collected and simulated data available everywhere on the grid. It is possible to launch the analysis tasks singularly on those data. Nevertheless, when more users are interested in analysing the same data sample, the access pattern is optimised by running together all the tasks of those users in the same jobs and this optimisation is called *analysis train*. It defines a standard analysis flow in the ALICE experiment and it ensures the reproducibility of the analyses.

The data of the ALICE experiment are stored in binary files using the ROOT framework data format. The ROOT framework [115] is also the core of the ALICE software environment introduced in 1998: *AliRoot*. Recently, the analysis related codes have been collected in a part of the ALICE offline framework denominated *AliPhysics*. The reconstructed events are stored in two different formats: the Event Summary Data (ESD) format, that is mainly used for calibration and detector performance studies, and the Analysis Object Data (AOD) format, which contains only the relevant information at the analysis level.

3.4. ALICE performance

A precise reconstruction of both momentum and origin of the particles produced in nucleus-nucleus collisions is one of the most challenging tasks in ALICE. The tracking and vertexing performances of the ALICE experiment as well as the method for the particle identification and the centrality determination will be briefly described in this section.

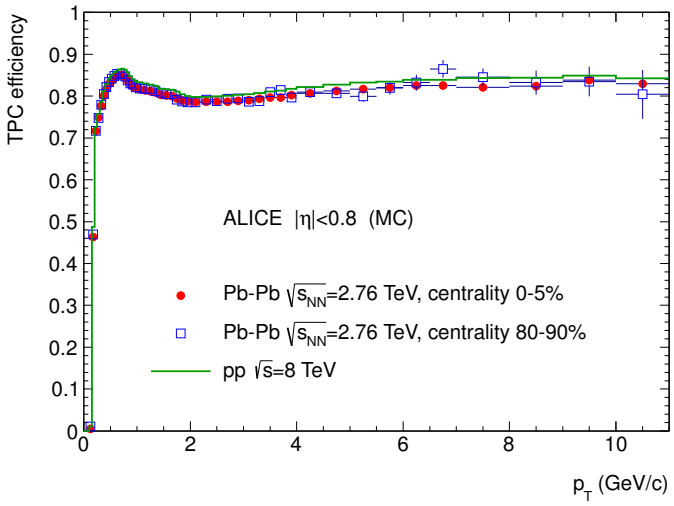

Figure 3.7.: TPC track reconstruction efficiency in pp (green line) collisions at $\sqrt{s}$ = 8 TeV and for central (red dots) and peripheral (blue open square) collisions Pb–Pb collisions at $\sqrt{s_{\mathrm{NN}}}$= 2.76 TeV. The efficiency does not depend on the detector occupancy.

3.4.1. Tracking

Track finding and fitting is performed in ALICE following the inward-outward-inward approach [116].

The first inward stage of the tracking algorithm starts building the track seeds at a large radius of the TPC. Track seeds are built first requiring two clusters and the vertex constraint, then with three clusters and without the vertex constraint. The seeds are propagated inward and, whenever a compatible cluster is found at each step of the propagation, the track parameters are updated using a Kalman filter [112]. Since clusters can be reused by different seeds, it is not uncommon to have two or more tracks sharing some clusters. If the fraction of shared clusters is above a predefined threshold (between 25% and 50%), a special algorithm rejects the candidate tracks with the worst parameters quality. Only the tracks with at least 20 clusters (out of a maximum of 159) and that miss no more than 50% of the expected clusters are accepted and propagated to the inner radius of the TPC. A preliminary particle identification is performed using the energy loss in the TPC gas. It is used for the most-probable-mass assignment that is important for the energy loss correction calculations in the following steps. Figure 3.7 shows the track reconstruction efficiency in the TPC. The drop for $p_{\mathrm{T}} \leq 0.5$ GeV/c is due to energy loss in the detector material and the shape at higher p_{T} is related to the loss of clusters in the dead zones of the TPC.

The reconstructed TPC tracks are propagated to the outermost layer of the ITS and the tracking algorithm in ITS proceeds with a procedure similar to that adopted and described

for the TPC. Starting from the second layer of SSD, the seeds are propagated inward and, whenever they do not find a compatible cluster in the extrapolation, a penalty factor to its χ^2 is added. Once the complete tree of prolongation candidates for each TPC track is built, the one with the highest quality is stored as ITS+TPC track in the reconstructed event.

The second stage of the tracking algorithm is the backward refit of the ITS+TPC tracks using the Kalman filter. At each outward step, the integrated track length and the expected time of flight for different particle species are updated, since they will be necessary for a correct TOF PID (Section 3.4.3). Once the track reaches the TRD, the algorithm attempts to match the track with the TRD tracklets, which are segments connecting the clusters in the TRD, and, if the matching is successful, updates the track parameters using the TRD tracklet informations. Then an attempt to extrapolate the track and match it to one of the TOF clusters is performed. The track length integration and time of flight calculation are stopped at this stage. A further extrapolation is performed to match the track with other external central barrel detectors as HMPID, PHOS and EMCal.

At the final stage of the track reconstruction, all the tracks are propagated from the TRD back to the innermost ITS layer. In each detector (TRD, TPC and ITS) the tracks are refitted using the information of all attached clusters. The corresponding *refit flag* is switched on, when each refit is done successfully. At this stage the track's position, direction, inverse curvature and its associate covariance matrix are determined. Figure 3.8a shows the $1/p_{\mathrm{T}}$ resolution for standalone TPC and ITS+TPC tracks which is related to the p_{T} resolution by the formula:

$$\frac{\sigma_{p_{\mathrm{T}}}}{p_{\mathrm{T}}} = \frac{\sigma_{1/p_{\mathrm{T}}}}{1/p_{\mathrm{T}}} \tag{3.9}$$

Tracks can be reconstructed with a resolution between 1% and 10% in the momentum range from 0.1 to 100 GeV/c. The effect of constraining the tracks to the primary vertex is shown as well and considering, for instance, TPC standalone tracks the resolution is reduced from 6% to 2% at low p_{T} by this requirements.

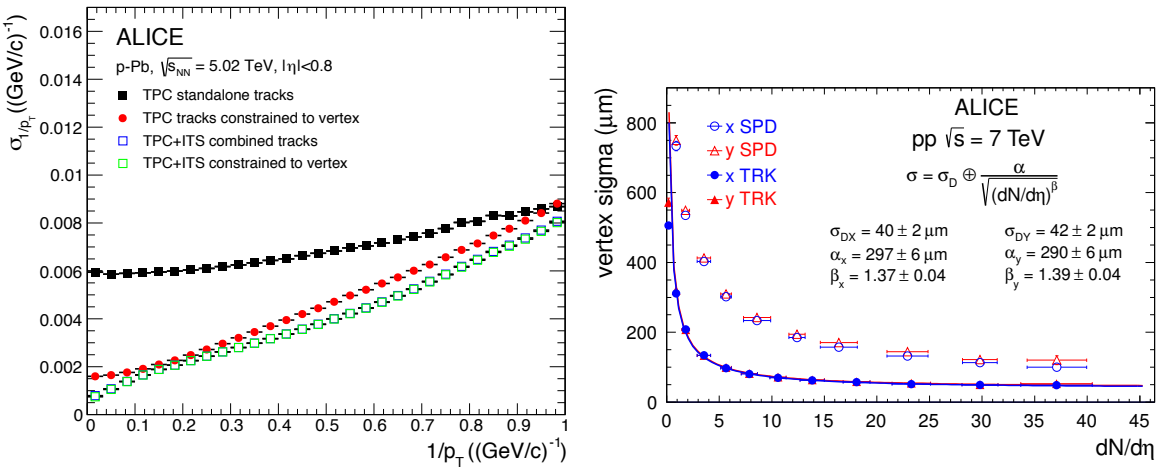

(a) **(b)**

Figure 3.8.: Panel (a): p_T resolution for standalone TPC (black and red markers) and ITS+TPC (blue and green open squares) tracks with and without constraint to primary vertex in p–Pb collisions. Panel (b): Vertex resolution in the transverse plane using only the SPD clusters (open markers) or the full track informations (full markers).

3.4.2. Vertexing

Primary vertex reconstruction

A first estimation of the interaction vertex is performed by using the clusters on the two layers of SPD. The algorithm builds a set of segments, called *tracklets*, using the clusters on the SPD layers which are inside a fixed azimuthal window. Then a dedicated task computes the point in the space minimising the distance from all the tracklets. The obtained space point is the interaction vertex estimation. At least two tracklets are required for a 3D reconstruction of the primary vertex position.

Despite the fact that this fast reconstruction is required in the first stage of the tracking algorithm, the most precise determination of the primary vertex position is obtained by using the full reconstructed track informations, as shown in Figure 3.8b. The full reconstructed tracks, obtained at the end of the tracking procedure, are propagated to the nominal beam line and the tracks too far from it are excluded from the vertex computation.

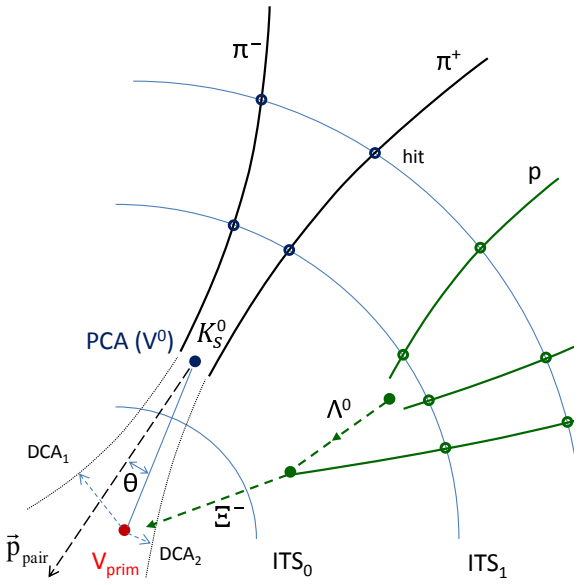

Figure 3.9.: Sketch of the secondary vertex reconstruction using the V^0 topology, with K_S^0 and Ξ^- decays as an example. The solid lines represent the reconstructed secondary track particles, while the dashed lines are the extrapolation to the primary vertex of the mother particle.

Secondary vertex reconstruction

Once the tracks and the primary vertex have been reconstructed, the event reconstruction procedure searches for photon conversions and secondary vertices from particle decays as depicted in Figure 3.9.

The reconstruction of a secondary vertex from decays of neutral particles and with a V-shaped track topology of the daughters, V^0 topology, is performed with the V^0 finder algorithm. The V^0 finder algorithm is implemented in the ALICE software and performed with two different procedures, the *offline* and the *on-the-fly*. The basic principle is the combination of two tracks with opposite sign, which are close in the space and presumably come from the decay of one mother particle. The properties of the combined tracks as well as of the resulting mother momentum are requested to pass some quality selection criteria before being stored as V^0 candidate.

The offline V^0 finder is executed after the tracks have been reconstructed and the full track information have already been consolidated. This algorithm can also be re-run offline, once the reconstruction is done, applying different selection criteria.

The on-the-fly V^0 finder, instead, is already operated during the track fitting. It reconstructs the candidate V^0 using the full cluster informations and not only the reconstructed

tracks, as done in the offline alternative. The tracks are reconstructed for a second time starting from the clusters and the on-the-fly V^0 finder checks if the χ^2 for a track matching with the primary vertex is above a minimal value. In case of a large χ^2, the track is assumed to originate from a secondary vertex. It is combined with a candidate of opposite sign, taken from the track hypothesis tree, which is a list of all secondary tracks satisfying the aforementioned criteria. Finally the tracks are re-fitted with the assumption to come from the secondary vertex candidate.

The on-the-fly finder applies a selection called causality cut which reduces the combinatorial background by requiring that there are not clusters before the candidate V^0 position. In addition, the V^0 tracks and secondary vertex candidates need to fullfil some conditions, which are similar to the offline V^0 finder but less tight. The selections applied during the V^0 reconstruction process are [99] :

- the minimum *Distance of Closest Approach* (DCA) of each candidate track to the primary vertex;
- the maximum distance between the two tracks at the candidate secondary vertex;
- the minimum *Cosine of the Pointing Angle* ($\cos(\theta_{pointing})$), represented by θ in Figure 3.9.

The usage of the clusters in the algorithm has the advantage of having direct access to the local characteristics of the helix describing the trajectory. This means that, in the refit step, it includes the material budget in the reconstruction of the particle track, which allows a proper correction for the energy loss in the dead zones of the apparatus, leading to the correct momentum of the daughters tracks at the decay vertex. For this reason the on-the-fly V^0 finder has a better invariant mass and geometric resolution than the offline finder and it has been used for the analysis of the hypertriton.

The reconstruction of the decay vertex with more than two daughters can only be performed offline once the full track reconstruction is done. The approach is similar to the offline V^0 finder. The candidate tracks are selected through geometrical selections and the secondary vertex is the point of closest approach to the selected set of tracks. Then the tracks parameters need to be propagated to the candidate secondary vertex for a more precise computation of the invariant mass.

3.4.3. Particle Identification

One of the characteristics that distinguish the ALICE experiment from the other LHC experiments is the Particle Identification capability with high resolution by combing the informa-

tion of different detectors according to p_{T} range to be investigated. Those used in the analyses for the charged hadron identification are the ITS, the TPC, the TOF and the HMPID. The ITS and the TPC provide information on the specific energy loss of the tracked charged particles. The TOF detector measures the time of flight and the HMPID, a ring-imaging Čerenkov detector, gives the $\beta = v/c$ of the particle from the measurement of the Čerenkov angle. The hadron identification is performed in a wide momentum range (0.1-10 GeV/c) through the combination of all these kinds of informations. More details are given on those detectors useful for the identification and reconstruction of the hypernuclei.

TPC particle identification

The TPC measures the charge deposited on up to 159 padrows and then a truncated mean $\mathrm{d}E/\mathrm{d}x$ is calculated. Particle identification is performed by measuring simultaneously the specific energy loss ($\mathrm{d}E/\mathrm{d}x$) and the momentum of each particle traversing the detector gas. The energy loss as a function of the momentum in TPC has been parametrized with a function originally proposed by the ALEPH collaboration [117]:

$$f(\beta\gamma) = \frac{P_1}{\beta^{P_4}} \left(P_2 - \beta^{P_4} - ln \left(P_3 + \frac{1}{(\beta\gamma)^{P_5}} \right) \right) \tag{3.10}$$

where β is the particle velocity, γ is the Lorentz factor and P_{1-5} are the fit parameters, which are obtained from a fit to the experimental data. Alternatively the response functions have been parametrized using splines as shown in Figure 3.10a , which are provided by the ALICE analysis framework.

At low momenta ($p \leq 1$ GeV/c) particles can be identified on a track-by-track basis, selecting a fiducial band around the expected energy loss for the particle of interest. The amplitude of this region is expressed in terms of number of σ, where σ is the $\mathrm{d}E/\mathrm{d}x$ resolution obtained with a Gaussian fit to the energy loss distribution at each momentum interval. The $\mathrm{d}E/\mathrm{d}x$ resolution is about 5.2% in pp collisions and 6% in Pb–Pb collisions. Thanks to the good resolution it is also possible to apply the aforementioned method in the relativistic rise region, where the relative contribution of different particle species is extracted through an unfolding procedure of the $\mathrm{d}E/\mathrm{d}x$ contribution.

Moreover, it is possible to identify light nuclei like ^{3}He and ^{4}He [118] track-by-track up to 6 GeV/c, thanks to the dependence of the specific energy loss on the charge of the particle ($\propto \mathrm{Z}^2$).

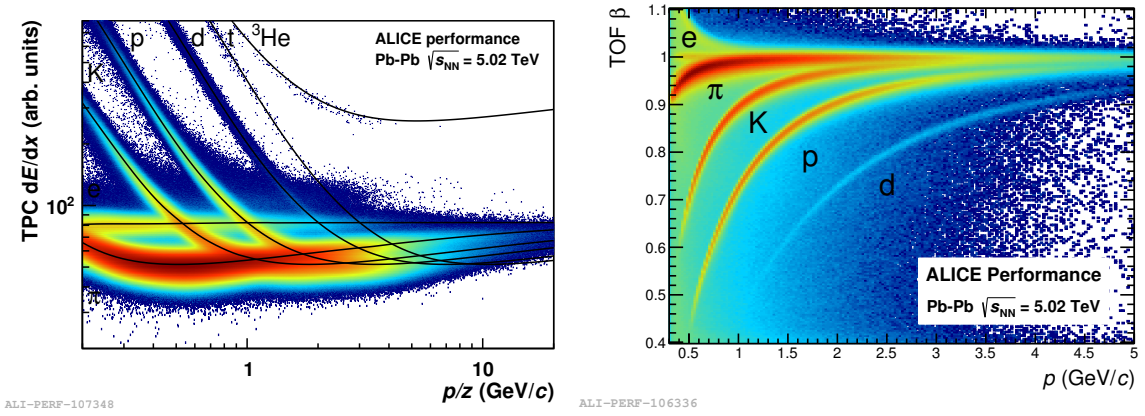

(a) (b)

Figure 3.10.: Panel (a): specific energy loss as a function of the rigidity for particles traversing the TPC gas in Pb–Pb collisions at $\sqrt{s_{\rm NN}}$= 5.02 TeV. The black lines represent the expected detector response for different particles. Panel (b): measured β of the particles in Pb–Pb collisions at $\sqrt{s_{\rm NN}}$= 5.02 TeV as a function of the track momentum.

TOF particle identification

The ALICE TOF, described in Section 3.2.3, is able to identify pions with a momentum of 1 GeV/c in Pb–Pb collisions, in the 0–70% centrality range, with a resolution of 80 ps. This value keeps into account the intrinsic detector resolution, the contribution from electronics and calibration, the tracking and momentum resolution and the uncertainty on the start time of the event. More details on the determination of the start time of the collision can be found in [104]. Thanks to its excellent time resolution the TOF detector provides the information for PID in the intermediate momentum range, up to 2.5 GeV/c for pions and kaons, 4 GeV/c for protons and 5 GeV/c for deuterons.

Using the time of flight t_{TOF} and the integrated track length L it is possible to compute the particle β with the classical formula:

$$\beta c = \frac{t_{TOF}}{L} \tag{3.11}$$

Figure 3.10b shows the measured particle β as a function of the momentum estimated in the tracking procedure. It is visible the mismatch background, which is due to tracks incorrectly matched to TOF clusters. This background is an effect related to the TOF occupancy and it is preminent in Pb–Pb collisions while negligible in p–Pb and pp collisions, as it was shown in [99]. It is possible to distinguish, on top of the mismatch background, the bands corresponding to the different particle species. The parameterization of the TOF β as a

function of track momentum is used for the particle idenfication on a track-by-track basis as previously explained in Section 3.4.3.

3.4.4. Centrality determination in Pb–Pb collisions

The geometry of heavy-ion collisions is characterized by the impact parameter vector b connecting the centers of the two colliding nuclei in the plane transverse to the beams. However this quantity cannot be measured directly. Consequently the centrality of the collision is estimated using the particle multiplicities (N_{ch}) and the energy deposit in the ZDCs (E_{ZDC}) and they are correlated to the value of the impact parameter using the Glauber Model [14]. In literature the centrality of nuclear collisions is expressed as a percentage of the total hadronic interaction cross section σ_{AA}:

$$c(b) = \frac{\int_0^b \frac{d\sigma}{db^{'}} db^{'}}{\int_0^\infty \frac{d\sigma}{db^{'}} db^{'}} = \frac{1}{\sigma_{AA}} \int_0^b \frac{d\sigma}{db^{'}} db^{'} \tag{3.12}$$

Assuming a monotonic dependence of both the charged particle multiplicity and the energy deposit at zero degrees on the overlap volume, the centrality can be expressed as:

$$c(b) \approx \frac{1}{\sigma_{AA}} \int_{N_{ch}}^\infty \frac{d\sigma}{dN_{ch}^{'}} dN_{ch}^{'} \approx \frac{1}{\sigma_{AA}} \int_0^{E_{ZDC}} \frac{d\sigma}{dE_{ZDC}^{'}} dE_{ZDC}^{'} \tag{3.13}$$

The total cross section can be replaced with the number of observed events n under the same assumption:

$$c(b) \approx \frac{1}{N_{ev}} \int_{N_{ch}}^\infty \frac{dn}{dN_{ch}^{'}} dN_{ch}^{'} \approx \frac{1}{N_{ev}} \int_0^{E_{ZDC}} \frac{dn}{dE_{ZDC}^{'}} dE_{ZDC}^{'} \tag{3.14}$$

The assumption holds only for central collisions $c \leq 50\%$ for the ZDC energy measurement, because nuclear fragments emitted in peripheral collisions may be deflected out of the acceptance of the ZDCs, leading to low signals indistinguishable from those seen in central collisions. The ambiguity can be solved by correlating the ZDC signal with the energy deposit in the ZEM.

The centrality determination [119] via particle multiplicity is usually performed with the V0 detectors as shown in Figure 3.11a. The distribution of the sum of V0A and V0C amplitudes is fitted with a parameterisation based on a Glauber Monte Carlo in order to connect the experimental quantity with the impact parameter of the collision. This parameterisation requires the number of participant nucleons N_{part} and the number of bi-

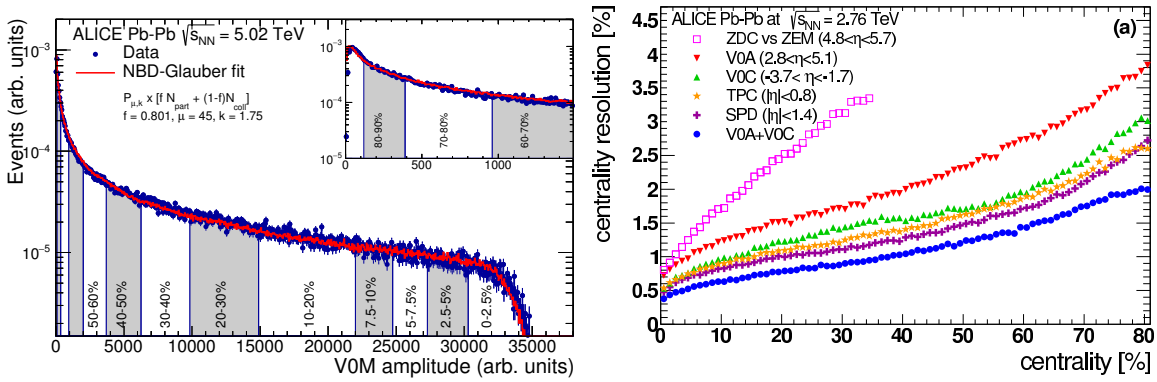

Figure 3.11.: Panel (a): distribution of the V0A+V0C amplitude. The centrality intervals are determined integrating the distribution following 3.14 model. The red line shows the fit with the Glauder-NBD model and the inset shows a magnified version of the most peripheral region. Panel (b): centrality resolution for all the estimators available in the ALICE experiment.

nary collisions N_{coll}, which are generated with the Glauber model. The particles produced per nucleon-nucleon collision is parametrised by a Negative Binomial Distribution (NBD-Glauber fit):

$$P_{\mu,k}(n) = \frac{\Gamma(n+k)}{\Gamma(n+1)\Gamma(k)} \cdot \frac{(\mu/k)^n}{(\mu/k+1)^{n+k}} \tag{3.15}$$

which gives the probability of measuring n hits per emitting source, where μ is the mean multiplicity per source and k is the width.

The same procedure can be performed by using the distribution of the number of clusters on the second SPD layer or on the distribution of the number of TPC tracks. The resolution on the centrality determination has been evaluated for different estimators and it shows a dependence on the rapidity coverage of the used detector, as shown in Figure 3.11b . The best centrality estimator is obtained combining the V0A and V0C, which is called V0M and is represented in Figure 3.11a, with a resolution ranging from 0.5% for central collisions to 2% for the peripheral ones.

Chapter 4.

Reconstruction of ${}^{3}_{\Lambda}\mathrm{H}$ and ${}^{\overline{3}}_{\overline{\Lambda}}\overline{\mathrm{H}}$ in ALICE

"Begin at the beginning, and go on till you come to the end: then stop."
— Lewis Carroll, 1832–1898

Relativistic heavy ion collisions offer a unique opportunity to shed light on the characteristics of the QGP and the study of the ${}^{3}_{\Lambda}\mathrm{H}$ production plays a key role, as highlighted in Chapter 2. The starting point for all the measurements, which will be presented in the following, is the identification of the $({}^{3}_{\overline{\Lambda}}\overline{\mathrm{H}})^{3}_{\Lambda}\mathrm{H}$ candidates. This chapter is dedicated to the analysis procedure adopted to reconstruct the $({}^{3}_{\overline{\Lambda}}\overline{\mathrm{H}})^{3}_{\Lambda}\mathrm{H}$ in Pb–Pb collision with the ALICE experiment as well as the performance studies performed using some dedicated MC productions.

4.1. Data and Monte Carlo sample

The analysis presented in this thesis is based on the data set of Pb–Pb collisions at $\sqrt{s_{\mathrm{NN}}}$= 5.02 TeV collected in 2015. The collisions in the LHC were delivered at different interaction rates: the low interaction rate (300-400 Hz) and the high interaction rate (1-7.5 kHz). The events were acquired when a coincidence of signals for both sides of the V0 detector was found, the so called *Minimum Bias* trigger (MB). Moreover, the time information of the V0 scintillator arrays paired with the same information of the ZDC is used to reject offline events triggered by the interaction of the beams with the residual gas in the LHC vacuum pipe. Since many analyses in the ALICE experiment require a large amount of statistics, also events with an incomplete TPC acceptance were collected and are used in this analysis. The sample of collected data consists of nearly 154x10^{6} minimum bias events.

Monte Carlo productions			
Anchor period	b (fm)	Injected particles per event (+ charge coniugate)	Events
Pb–Pb $\sqrt{s_{\mathrm{NN}}}$= 5.02 TeV	0-5	10x (H^2,H^3,He^3,He^4); 40x ${}^{3}_{\Lambda}\mathrm{H}$; 20x (${}^{4}_{\Lambda}\mathrm{H}$, ${}^{3}_{\Lambda}\mathrm{He}$)	112112
	5-11		439760
	11-15		355740
Pb–Pb $\sqrt{s_{\mathrm{NN}}}$= 5.02 TeV	11-15	injection as above, +4.5% material budget	444,300
	11-15	injection as above, -4.5% material budget	444,240

Table 4.1.: Details about the MC productions used in this analysis. The particles are injected on top of each HIJING event and the injection scheme is the same for all the productions. The number of injected particles has to be multiplied by 2 to count also the respective charge conjugate states. The impact parameter (b) is extracted from a flat distribution with the limits reported in the table.

The Monte Carlo (MC) sample, used to study the cuts applied in the analysis and to compute the efficiency and acceptance corrections, was generated using the HIJING event generator [120]. The data taking conditions are accounted in the MC by reproducing the configuration of the different detectors in the runs used for the analysis. Since the HIJING event generator used to simulate a Pb–Pb collision does not include any (anti-)(hyper-)nucleus, an *ad-hoc* generator was used to inject them on top of each HIJING event. The kinematics of the injected hypernuclei is chosen randomly, since their production spectra in heavy ion collisions are barely or completely unknown. The transverse momentum p_{T} is picked from a flat distribution in the range between 0 and 10 GeV/c, the azimuthal angle ϕ from a flat distribution between 0 and 2π radians and the rapidity from a flat distribution in the range $|y|<1$.

The MC simulation of a full Pb–Pb event, from the generation of the kinematics of the particles up to the final event reconstruction, is extremely expensive in terms of computing resources ($\sim$ one hour for one central Pb–Pb event on the ALICE Grid). Thus, only a fraction of the total collected statistics is simulated and reconstructed in the MC samples. The centrality of the simulated event is determined by the impact parameter (b), which is extracted randomly from a flat distribution. The b_{min} and b_{max} of the distribution have been chosen to match the edges of the centrality distribution of the real data. In order to optimise the computing resources usage, the MC production anchored to the 2015 Pb–Pb data is divided in three different sub-samples corresponding to three different b intervals. These three MC productions corresponds to the 0-10%, 10-50% and 50-90% V0M centrality intervals. The anchor period and the b intervals used in each sub-sample as well as the number of injected particles in each HIJING event are reported in Table 4.1.

Two additional MC samples have been produced to evaluate the systematics effect of the uncertainty on the material budget determination in ALICE. The material budget is increased and decreased of 4.5% with respect to the nominal amount in the MC samples, as reported in Table 4.1. These variations have been driven by the results obtained from the photon conversion analyses performed in ALICE[1]. Since the uncertainty on the material budget determination is independent from the collision centrality, only the most peripheral collisions ($b\rightarrow$ 11-15 fm), which require less computing resources, have been simulated.

4.2. Event selection

The collected events are further selected offline to reduce possible biases from particular data taking conditions. All the events are required to be minimum bias trigger, as already mentioned. Events with the primary vertex outside the fiducial region of $\pm$ 10 cm in the beam direction from the nominal interaction point are rejected ($|V_z| \leq 10$ cm). These selections are the standard ones used in the analysis of Pb–Pb events, which guarantee a symmetric acceptance and the rejection of beam-gas events.

An important consequence of the high interaction rate in 2015 data taking, is the presence of *pile-up* in triggered events. These events contain more than one primary collision vertex. The first selection applied to remove the pile-up is on the number of primary vertices reconstructed with SPD with more than n contributors. The number of contributors is the number of SPD tracklets[2] used to estimate the vertex position. The choice of the n parameter depends on the multiplicity of the events and it is driven by the multiplicity dependence of false positive pile-up tagging of previous analyses. It is set to 3 for events with less than 20 tracklets, to 5 for events with more than 50 tracklets and to 4 for the remaining events. This selection based on the SPD vertex finding can remove the pile-up of collisions occurring either in the same bunch crossing[3] or out of bunch within the SPD readout time (300 ns). Nevertheless, the aforementioned criterion is not able to resolve and remove collisions spaced by less than 8 mm along the beam axis. These pile-up collisions are merged and treated as a single one.

The second selection criterion used to reduce the pile-up background is based on the correlation between different centrality estimators. The correlation, reported in Figure 4.1a, between the centrality estimator V0M, based on the V0 detectors, and CL0, based on the

[1] ALICE Collaboration, paper in preparation.

[2] See Chapter 3 Sec. 3.4.2 for the definition.

[3] The bunch crossing is defined as the instant when the two LHC beams cross at the ALICE interaction point. The time windows separating two bunch crossings are always multiple of 25 ns, that is the period of the LHC clock.

Event selection criteria		
Variable	Selection	Effect
$\lvert V_z \rvert$	≤ 10 cm	uniform acceptance
Trigger	Minimum bias	
Multiple SPD vertices	reject with more than n contributors	pile-up rej.
$\lvert$ V0M - CL0 $\rvert$	$\leq 5\sigma$	pile-up rej.
$\lvert$ V0M - $n^{SPD}_{tracklets}$ $\rvert$	$\leq 5\sigma$	pile-up rej.
$\lvert \Delta V_z \rvert$	$\leq 20\sigma_{tracks}$, $\leq 10\sigma_{SPD}$	pile-up rej.
$\lvert \Delta V_z \rvert$	≤ 0.2 cm	pile-up rej.

Table 4.2.: List of the event selections applied to the data sample used in this analysis. More details are given in the text.

SPD clusters, shows some outliers which are interpreted as events with residual pile-up. The correlation has been parametrized and the obtained correlation function allows to compute the expected V0M percentile corresponding to a given value of CL0. Consequentely, the outliers can be removed with a 5σ selection on the aforementioned correlation, where σ is the resolution of the correlation distribution. Figure 4.1a and Figure 4.1b show the correlation between the V0M and CL0 centrality estimators before and after the event selection. It is possible to see how the selection cleans the correlation plot, removing the outliers. Another possibility is to remove the outliers in the correlation, shown in Figure 4.1c, between the V0M centrality estimator and the number of SPD tracklets. In this case, it is possible to see how the selection on the correlation V0M-CL0 removes also the outliers in the correlation between tracklets and V0M, as shown in Figure 4.1c and Figure 4.1d.

The last selection used to further reject the pile-up background is based on the position of the reconstructed primary vertex. High multiplicity events can contain two piled-up central collisions and in such conditions the vertex finding algorithm based on the reconstructed tracks fails to find the correct primary vertex. For this reason, the distribution of the z coordinate of the primary vertices shows some spikes and a large difference is visible between the reconstructed vertex position obtained with the SPD based method and the track based vertex finding algorithm (ΔV_z) as shown in Figure 4.2a. These discrepancies are ruled out using the resolution on the primary vertex reconstructed with tracks σ_{track} and SPD σ_{SPD}, and selecting only events where ΔV_z is less than $20\sigma_{track}$ and $10\sigma_{SPD}$. Furthermore the ΔV_z is required to be less than 0.2 cm. The effect of these selections is shown in Figure 4.2b. The event selections previously described and used in this analysis are summarized in Table 4.2.

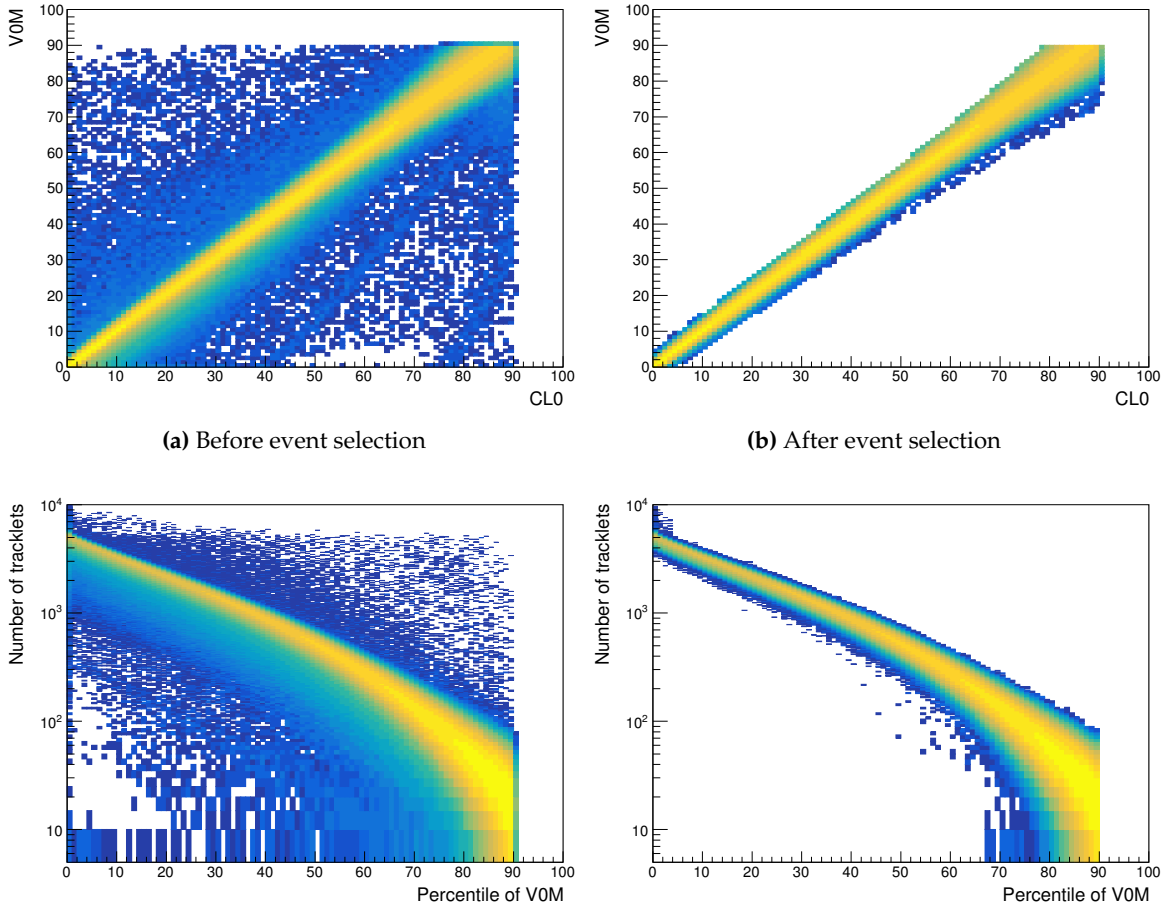

(a) Before event selection

(b) After event selection

(c) Before event selection

(d) After event selection

Figure 4.1.: Top: (a) correlation between the CL0 and V0M centrality estimators before event selection; (b) correlation between the CL0 and V0M centrality estimators after event selection. Bottom: (a) correlation between the number of SPD tracklets and the V0M estimator before event selection; (b) correlation between the number of SPD tracklets and the V0M estimator after event selection;

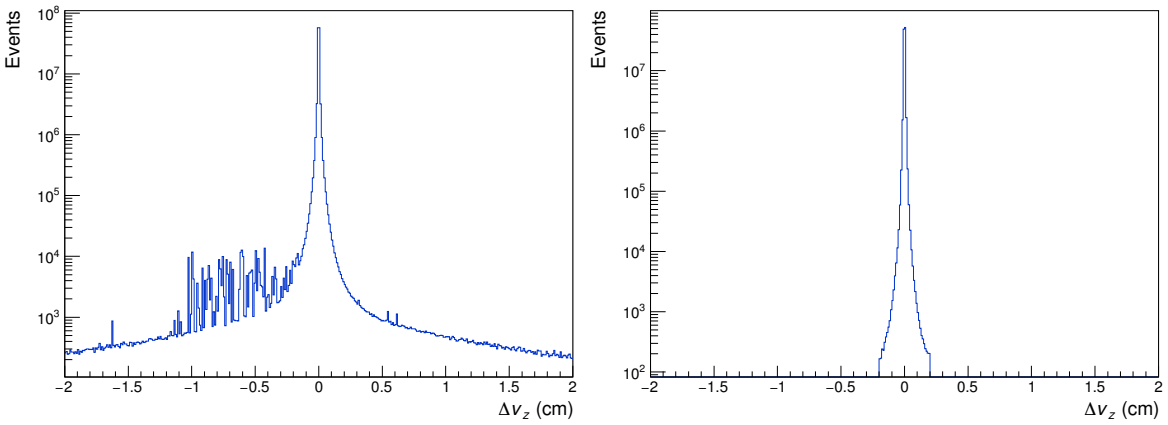

(a) Before event selection

(b) After event selection

Figure 4.2.: Distribution of the distance between the primary vertex reconstructed with the tracks based and the SPD tracklets only vertex finding algorithm. The left plot shows the distribution before the event selection while the right plot shows the same distribution after the event selection.

4.2.1. Selected data sample

After the offline event selection, the data sample consists of nearly 104 million Pb–Pb collisions at $\sqrt{s_{\mathrm{NN}}}$= 5.02 TeV. The centrality percentile distribution for the 2015 data, which were collected with a minimum bias trigger, is flat in the range 0-90%, as shown in Figure 4.3.

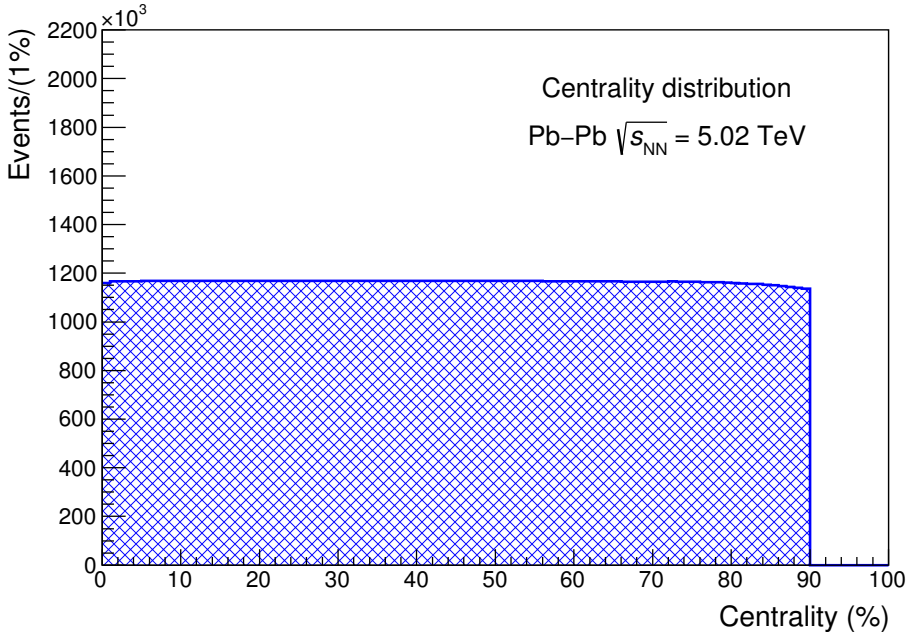

Figure 4.3.: V0M centrality percentile distribution for the 2015 data sample for the events satisfying the event selection criteria. Increasing the percentile means decreasing the collision centrality. The centrality estimation and the V0M definition were briefly discussed in Sec.3.4.4.

The whole collected statistics will be used for the $(^{3}_{\Lambda}\overline{\mathrm{H}})^{3}_{\Lambda}\mathrm{H}$ lifetime measurement. With the available numbers and based on the idea to improve the published results [70], the 2015 data sample has been divided in 3 centrality intervals for the study of $(^{3}_{\Lambda}\overline{\mathrm{H}})^{3}_{\Lambda}\mathrm{H}$ production yields: 0-10%, 10-30%, 30-50%. Moreover, since the ${}^{3}\mathrm{He}$ spectra[4] have been measured in three different centrality classes (0-10%, 10-40%, 40-90%), the $(^{3}_{\Lambda}\overline{\mathrm{H}})^{3}_{\Lambda}\mathrm{H}$ production spectra have been measured using the events in the 10-40% centrality interval and this will allow the calculation of variables useful for the comparison with the theoretical models: the ${}^{3}\mathrm{He}/^{3}_{\Lambda}\mathrm{H}$ ratio and the S_3 parameter.

The centrality classes are used to classify the collisions and are related to the overlap of the colliding nuclei, as presented in Chapter 1 and 3. Consequently, each centrality class is

[4] ALICE Collaboration work in progress.

Centrality class observables						
Centrality	b_{min} (fm)	b_{max} (fm)	$\langle \mathrm{d}N_{ch}/\mathrm{d}\eta \rangle$	$\langle N_{part} \rangle$	Events	Analysis
0 - 10%	0.00	4.96	1765 $\pm$ 52	359 $\pm$ 4	11.6 $\times$ 10^6	
10 - 30%	4.96	8.59	983 $\pm$ 25	226 $\pm$ 4	23.4 $\times$ 10^6	$\mathrm{d}N/\mathrm{d}y$
30 - 50%	8.59	11.1	415 $\pm$ 14	108.6 $\pm$ 2	23.4 $\times$ 10^6	
10 - 40%	4.96	9.92	826 $\pm$ 22	194 $\pm$ 3	35 $\times$ 10^6	p_{T} spectra
0 - 90%	0.00	15.0	-	-	104.8 $\times$ 10^6	lifetime

Table 4.3.: Centrality classes used in the analysis with their corresponding average values of the minimum (b_{min}) and maximum (b_{max}) impact parameter, the charged particles multiplicity ($\langle \mathrm{d}N_{ch}/\mathrm{d}\eta \rangle$) and the number of participating nucleons (N_{part}). These values are taken from [121, 122]. The last two columns report the total selected events and the measurement for each centrality class.

characterized by global event observables, as the number of participating nucleons (N_{part}) and the average charged particles multiplicity ($\langle \mathrm{d}N_{ch}/\mathrm{d}\eta \rangle$), which are related to the collision geometry. The relation of these observables with the centrality collision has been studied in detail by ALICE and the results are published in [121, 122]. Table 4.3 reports the most relevant event observables for the centralities used in this thesis. The values of (N_{part}) and $\mathrm{d}N_{ch}/\mathrm{d}\eta \rangle$) are obtained with an average of the published results, following the same procedure adopted for other analyses in the collaboration, while b_{min} and b_{max} are obtained with the NBD-Glauber fit to the centrality distribution, which has been introduced in Chapter 3 Sec.3.4.4. Moreover, the number of events for each centrality class is reported and will be used in the analysis of the production yields and spectra.

4.3. Hypertriton reconstruction

The aim of the analyses presented in this thesis is the study of the production of the $({}^{3}_{\Lambda}\overline{\mathrm{H}})^{3}_{\Lambda}\mathrm{H}$ and the measurement of its lifetime via the 2 body charged mesonic decay channels:

$$ {}^{3}_{\Lambda}\mathrm{H} \longrightarrow {}^{3}\mathrm{He} + \pi^{-} \tag{4.1} $$

$$ {}^{3}_{\Lambda}\overline{\mathrm{H}} \longrightarrow {}^{3}\overline{\mathrm{He}} + \pi^{+} \tag{4.2} $$

Once the events are selected, the second step for all the analyses is the identification of $({}^{3}_{\Lambda}\overline{\mathrm{H}})^{3}_{\Lambda}\mathrm{H}$ candidates.

on-the-fly V^0 finder	
Variable	Value
track DCA_{PV}	> 1 mm
DCA_{tracks} at V^0	< 1.5 cm
$\cos(\theta_{pointing})$	> 0.9

Table 4.4.: List of the selections applied to the V^0 candidate obtained with the on-the-fly V^0 finder algorithm during the global reconstruction of the 2015 Pb–Pb collisions raw data.

The method used for the reconstruction of the $({}^{3}_{\Lambda}\overline{\mathrm{H}})^{3}_{\Lambda}\mathrm{H}$ decay vertex is the on-the-fly V^0 finder algorithm. As already mentioned, this algorithm runs only during the global reconstruction of the raw data. Since it is applied while the track is reconstructed, the track properties can be used, i.e. the full material and the magnetic field are known while the tracks are propagated, which is the main difference with respect to the offline algorithms. In order to reduce the combinatorial background already during the reconstruction, each V^0 candidate is selected by applying a set of loose cuts[5]. In Table 4.4 the loose selections, applied during the global reconstruction of 2015 Pb–Pb collisions, are reported.

The V^0 candidates, which overcome these selections, are added to the V^0 candidates list in the output of the reconstruction. Then specific selections are applied on the candidates at the analysis level. In the following, the selections of the daughter tracks and of the $({}^{3}_{\Lambda}\overline{\mathrm{H}})^{3}_{\Lambda}\mathrm{H}$ decay vertex are presented. A detailed study on the MC sample has been performed. First of all to check the correct identification and reconstruction of the $({}^{3}_{\Lambda}\overline{\mathrm{H}})^{3}_{\Lambda}\mathrm{H}$, since it is a charged particle and not neutral as expected in a candidate V^0. Then also to tune the selections to be applied to the real data.

4.3.1. (Anti-)${}^{3}_{\Lambda}\mathrm{H}$ candidates selection and PID

The identification of the $({}^{3}_{\Lambda}\overline{\mathrm{H}})^{3}_{\Lambda}\mathrm{H}$ candidates starts with the selection of the daughter tracks.

In order to use only the geometrical region where the ALICE experiment is able to perform a full tracking and to provide the best possible PID information, only tracks in the pseudorapidity region $|\eta| < 0.9$ are selected in these analyses. This requirements is mainly related to the TPC acceptance, since it is the main used detector. Moreover, to guarantee a track momentum resolution better than 5% and a TPC $\mathrm{d}E/\mathrm{d}x$ resolution of 6%, the selected tracks are required to have at least 70 clusters in the TPC. The refit steps,

[5] See Chapter 3 Sec. 3.4.2 for details on these selections.

Track selection criteria	
Variable	Selection
$\mid \eta \mid$	≤ 0.9
$\mathrm{n}_{TPCclusters}$	> 70
TPC refit	TRUE
$\chi^2/\mathrm{n}_{TPCclusters}$	≤ 5
Kink topology	reject

Table 4.5.: Summary of the track selections applied in the analyses of the 2015 data sample.

which are the last part of the global tracking algorithm (see Sec. 3.4.1), are also performed in the reconstruction of the V^0 daughter tracks. Then the selected tracks are required to overcome successfully the TPC refit. In addition, the χ^2 per TPC clusters is computed in the track fitting procedure and is required to be less than 5. Finally the daughter tracks reconstructed as kink topology are rejected. Indeed this topology is defined for weak decay with a neutral daughter particle (e.g. $\mathrm{K}^{\pm} \rightarrow \mu^{\pm} + \nu_{\mu}$). The aforementioned track selection criteria are applied to all the analyses presented in this thesis and Table 4.5 summarises them.

The following step is the identification of the daughter particles and it is performed using the TPC information on the specific energy loss. The most commonly used discriminating variable for PID is the nσ variable, defined as the deviation of the measured signal from that expected for a species, in terms of detector resolution:

$$n\sigma = \frac{S_{measured} - S^{i}_{expected}}{\sigma^{i}_{expected}} \tag{4.3}$$

In Eq. 4.3, $S_{measured}$ is the measured signal for the candidate track, $S^{i}_{expected}$ is the expected signal for the species i and $\sigma^{i}_{expected}$ is the expected detector resolution for the same species i.

Figure 4.4 shows the specific energy loss for particles in the TPC active volume and the expected signal for pion (red line) and ^{3}He (black line), which are parameterized using the splines and are used in this thesis. The TPC response functions are parametrized for every data taking period and then included in the ALICE Offline framework, in order to be used for all the analyses.

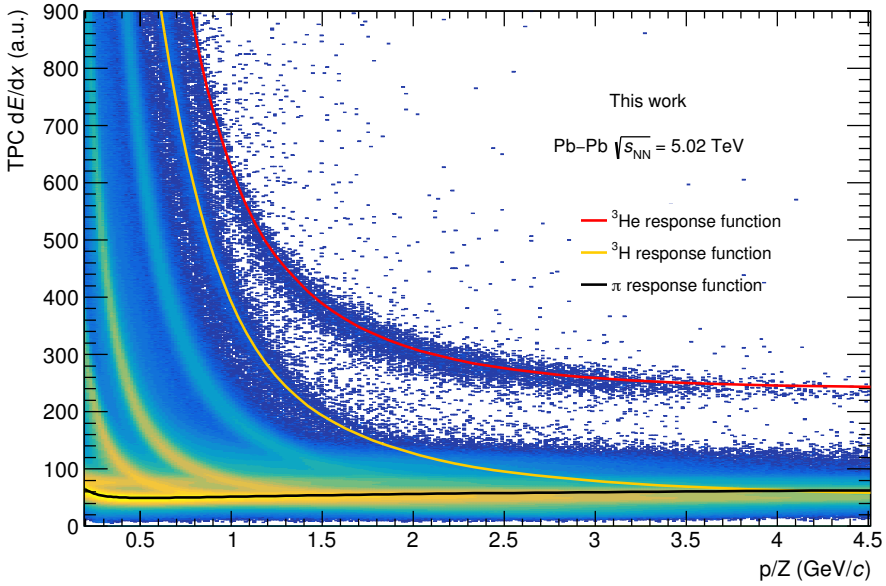

Figure 4.4.: Specific energy loss in the TPC active volume as a function of the particle rigidity in Pb–Pb collisions for the 2015 data sample. The solid lines represent the expected TPC response for pion (red) and ^{3}He (black).

The particle identification is performed track-by-track and applying a selection on the nσ variable, as reported in Table 5.7. Pions are identified requiring a nσ within ± 3 with respect to the expected π energy loss in the TPC given the momentum of the particle. Due to the contamination from kaons and protons the identification of pions can be performed up to $\sim$ 1 GeV/c. At higher momenta the identification track-by-track is less trivial and could be improved requiring the matching with other PID detectors. However, the requirements of the identification in other detectors would reduce the final efficiency for the ${}^{3}_{\Lambda}\mathrm{H}$ reconstruction. For these reasons, a study of the p_{T} distribution of the pions produced in the ${}^{3}_{\Lambda}\mathrm{H}$ decay has been performed using MC events. The result is shown in Figure 4.5a

Particle Identification		
Species	Variable	Selection
π	$\lvert \mathrm{n}\sigma_{\pi} \rvert$	≤ 3
^{3}He	$\lvert \mathrm{n}\sigma_{^3\mathrm{He}} \rvert$	≤ 3
	$\mathrm{n}\sigma_{^3\mathrm{H}}$	> 0

Table 4.6.: Selection applied for the identification of candidate π and ^{3}He using the specific energy loss in the TPC active volume.

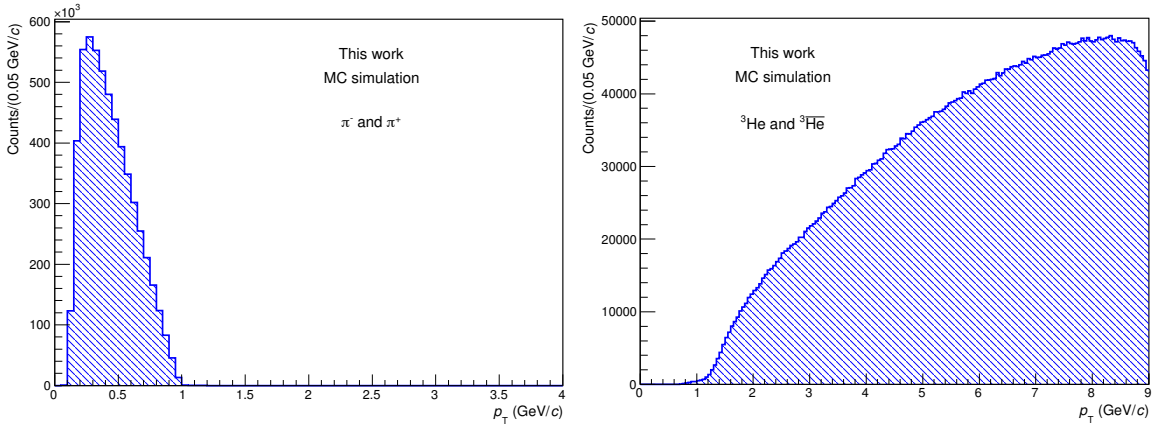

(a) π^- and π^+ **(b)** ${}^3\mathrm{He}$ and ${}^{3}\overline{\mathrm{He}}$

Figure 4.5.: Transverse momentum distribution of pions (left) and ${}^3\mathrm{He}$ (right) from the $({}^{\overline{3}}_{\overline{\Lambda}}\overline{\mathrm{H}})^{3}_{\Lambda}\mathrm{H}$ decay. The distribution are obtained from the MC production.

where the maximum p_{T} for a π daughter is $\sim$ 1 GeV/c. Consequently the candidate pions are required to have a p_{T} lying in the 0.2 –1.2 GeV/c interval and the identification can be performed only with the TPC information.

Conversely, for the ${}^3\mathrm{He}$, that has charge $z = 2e$, the TPC can provide a clean identification up to high momenta. The explanation is given by the Bethe-Bloch [5][6] formula for the specific energy loss, that depends on the square of z. Thus the ${}^3\mathrm{He}$ is well separated from all the particle species with $z = 1e$ in a large momentum range. The only known species that could contaminate the ${}^3\mathrm{He}$ signal in the TPC is the ${}^4\mathrm{He}$, but since its expected production rate is approximately 100 times smaller than the expected production of ${}^{3}_{\Lambda}\mathrm{H}$, it can be neglected in the present analysis work. In the low rigidity region, instead, the specific energy loss of the ${}^3\mathrm{He}$ becomes similar to the one of the ${}^3\mathrm{H}$. As a consequence, the candidate ${}^3\mathrm{He}$ are required to have the nσ within ± 3 with respect to the expected ${}^3\mathrm{He}$ TPC signal and the nσ with respect to the expected ${}^3\mathrm{H}$ TPC signal larger than 0. Furthermore, the p_{T} distribution of ${}^3\mathrm{He}$ coming from the ${}^{3}_{\Lambda}\mathrm{H}$ decay, shown in Figure 4.5b, suggests a selection on the minimum p_{T} of the ${}^3\mathrm{He}$ at $\sim$ 1.2 GeV/c. However, other analyses on nuclei production [123], performed in the ALICE Collaboration, showed that a large fraction of nuclei produced by secondary interaction has p_{T} smaller than 1.7-1.8 GeV/c. For this reason, the candidate ${}^3\mathrm{He}$ are required to have p_{T} greater than 1.8 GeV/c.

[6] See the section "Experimental Methods and Colliders - *Passage of particles through matter*" of the PDG.

4.3.2. Decay vertex selection

The last set of selections to identify $({}^{3}_{\Lambda}\overline{\mathrm{H}})^{3}_{\Lambda}\mathrm{H}$ candidates is performed on the reconstructed decay vertex. Indeed, the variables related to the topology and kinematics of the $({}^{3}_{\Lambda}\overline{\mathrm{H}})^{3}_{\Lambda}\mathrm{H}$ candidate are evaluated during the decay vertex reconstruction. Thus it is possible to apply selections on these observables in order to maximize the $({}^{3}_{\Lambda}\overline{\mathrm{H}})^{3}_{\Lambda}\mathrm{H}$ signal and reject the combinatorial background. The latter is due to primaries π and ${}^{3}\mathrm{He}$ which do not come from the $({}^{3}_{\Lambda}\overline{\mathrm{H}})^{3}_{\Lambda}\mathrm{H}$ decay and, however, satisfy the selections applied in the on-the-fly V^{0} finder algorithm (Table 4.4). A detailed study, using MC events, will allow to understand which additional selections can be required to further reduce the background.

Figure 4.6 shows a pictorial sketch of the ${}^{3}_{\Lambda}\mathrm{H}$ two body decay and the topological observables used for the candidates selection.

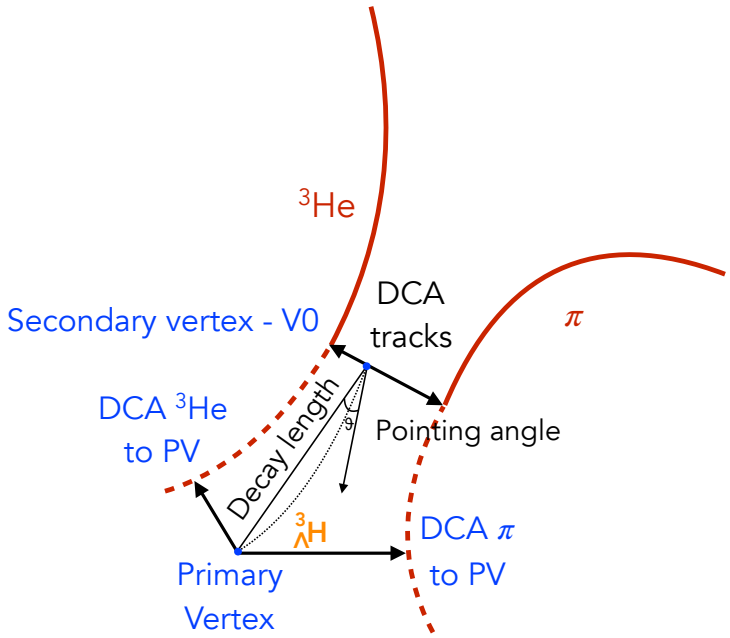

Figure 4.6.: Pictorical sketch of the ${}^{3}_{\Lambda}\mathrm{H}$ two body decay. The observables which have been used to reduce the combinatorial background are reported on the figure.

The set of topological cuts include the distance of closest approach to the primary vertex for each candidate DCA^{i}_{PV}, which can be used to reject primary pions and ${}^{3}\mathrm{He}$, and the distance of closest approach between the two daughters tracks at the secondary vertex DCA_{tracks}. Then, one of the most effective cuts for the rejection of the combinatorial background is the cosine of the pointing angle $\cos(\theta_{pointing})$. $\theta_{pointing}$ is the angle between the

total momentum vector of the daughter pair and the straight line connecting the primary and secondary vertices.

The decay length is shown in Figure 4.6 with a solid straight line and represents the distance covered between the primary and secondary vertices. This observable is used to evaluate the lifetime of the candidate *c*t, which gives another topological cut. The definition of *c*t is:

$$ct = \frac{ML}{p} \tag{4.4}$$

where M is the nominal mass of the ${}^{3}_{\Lambda}$H (M = 2.991 GeV/c^2), L is the measured decay distance and p is the total momentum of the ${}^{3}_{\Lambda}$H candidate. In particular, the decay distance is defined as:

$$L = \sqrt{(x_{SV} - x_{PV})^2 + (y_{SV} - y_{PV})^2 + (z_{SV} - z_{PV})^2} \tag{4.5}$$

where (x_{PV}, y_{PV}, z_{PV}) and (x_{SV}, y_{SV}, z_{SV}) are the coordinate of the primary and secondary vertex, respectively. For electrically neutral particles, the track length is the straight line between the production and the decay vertex. But for charged particles produced in the collision, the decay distance is equivalent to the helix segment length because of the presence of the solenoidal magnetic field of L3. The definition of the length of the helix segment is:

$$\text{Helix length} = \sqrt{(\text{Ark length})^2 + (z_{SV} - z_{PV})^2} \tag{4.6}$$

with

$$\text{Ark length} = 2R \cdot arcsin\left(\sqrt{\frac{(x_{SV} - x_{PV})^2 + (y_{SV} - y_{PV})^2}{2R}}\right) \tag{4.7}$$

where R is the curvature radius of the charge track, defined as:

$$R = \frac{p_{\mathrm{T}}}{qB} = \frac{p_{\mathrm{T}}}{B} \cdot \frac{10}{3} \tag{4.8}$$

where p_{T} is given in GeV/c, B in Tesla and R in metre. For two candidates with p_{T} equal to 2 and 10 GeV/c, the corresponding curvature radii are $\sim$13 m and $\sim$67 m, respectively.

The correlation between the length measured with the helix and straight line approach has been studied and the result is shown in Figure 4.7a. The dashed orange line corresponds to the ideal case where the two lengths are exactly the same and it is visible that

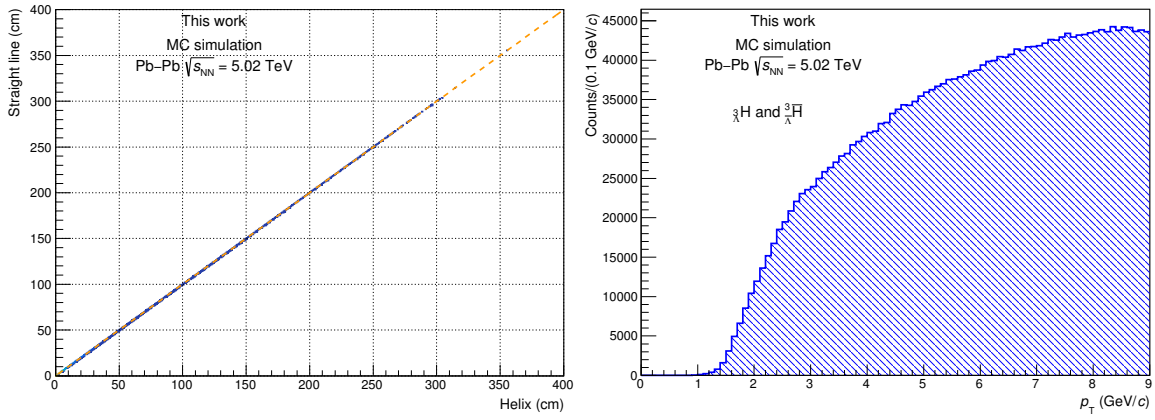

(a) **(b)**

Figure 4.7.: (Left) Helix *vs* straight line length (cm) for ${}^{3}_{\Lambda}\mathrm{H}$ candidates. The dashed orange line corresponds to equal lengths. (Right) p_{T} distribution of the reconstructed ${}^{3}_{\Lambda}\mathrm{H}$ obtained using MC events.

there are no differences between the two approaches. As a consequence the decay distance can be evaluated following Eq. 4.5.

Two additional observables related to the kinematics of the $({}^{3}_{\Lambda}\overline{\mathrm{H}})^{3}_{\Lambda}\mathrm{H}$ candidate are used in the selection criteria: the rapidity y and the transverse momentum p_{T}.

In order to measure the ${}^{3}_{\Lambda}\mathrm{H}$ production yield and spectrum in the mid-rapidity region, the candidates are required to have $|y|<0.5$. For the lifetime measurement, instead, the requirements is $|y|<0.8$ and it will be explained in Chapter 6.

The transverse momentum of the candidate ${}^{3}_{\Lambda}\mathrm{H}$ is required to be larger than 2 GeV/c. Figure 4.7b shows the p_{T} distribution of $({}^{3}_{\Lambda}\overline{\mathrm{H}})^{3}_{\Lambda}\mathrm{H}$ reconstructed in the MC production and few of them are reconstructed in the p_{T} region below 2 GeV/c. On the other hand, that p_{T} range is largely contaminated by candidate obtained pairing pions and ${}^{3}\mathrm{He}$ from secondary interaction. Moreover, this selection has the advantage to exclude the transverse momentum range where the reconstructed p_{T} is affected by the mis-assignment of the mass hypothesis to the ${}^{3}\mathrm{He}$ candidate. Indeed, during the track fitting step of the reconstruction, the mass hypothesis of the tracked particle is used to keep into account the particle energy loss while traversing the material. The mass hypothesis is chosen among the particle whose expected $\mathrm{d}E/\mathrm{d}x$ is compatible with the one measured with the track. However, during the reconstruction the selection on the expected energy loss is loose ($|\mathrm{n}\sigma| < 15$). As a consequence, some ${}^{3}\mathrm{He}$ candidate can be reconstructed with the mass hypothesis of α or ${}^{3}\mathrm{H}$ and this lead to an imprecise reconstruction of the ${}^{3}\mathrm{He}$ momentum for $p_{\mathrm{T}} \leq 1.8$ GeV/c. Fig-

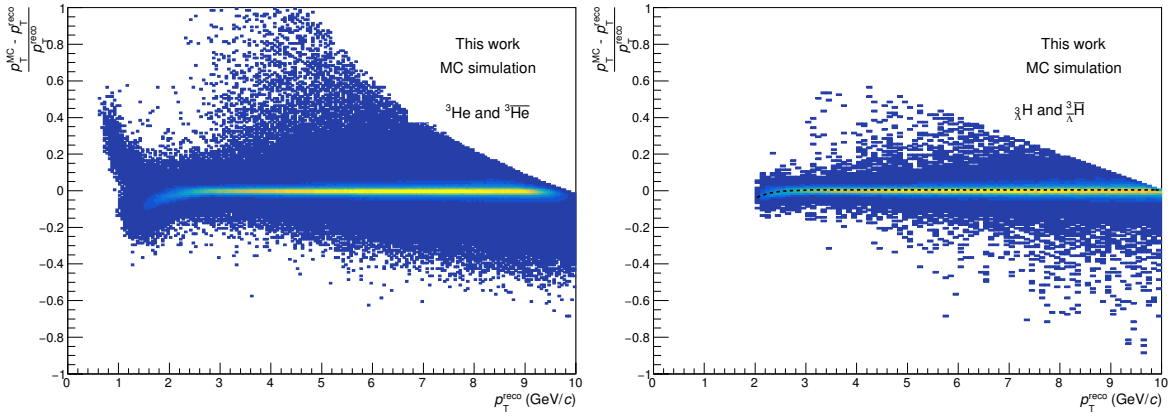

(a) **(b)**

Figure 4.8.: Relative difference between generated (p_{T}^{MC}) and reconstructed (p_{T}^{reco}) transverse momentum as a function of p_{T}^{reco} for ^{3}He (left) and ${}^{3}_{\Lambda}\mathrm{H}$ (right). The dashed black line on the right plot corresponds to the correction applied to the reconstructed $({}^{3}_{\Lambda}\overline{\mathrm{H}})^{3}_{\Lambda}\mathrm{H}$ p_{T}.

ure 4.8a shows the relative difference between the generated p_{T}^{MC} and reconstructed p_{T}^{reco} transverse momentum of the ^{3}He and there are large deviations due to the different mass hypothesis. The effect on the reconstructed p_{T} of the ${}^{3}_{\Lambda}\mathrm{H}$ is mainly in the low p_{T} region but is strongly suppressed with the aforementioned selection on the ^{3}He p_{T}. Figure 4.8b shows the relative difference for the $({}^{3}_{\Lambda}\overline{\mathrm{H}})^{3}_{\Lambda}\mathrm{H}$ transverse momentum. The candidate ^{3}He daughter are selected as previously mentioned and there is a small relative difference of $\sim$ 2-3% between 2 and 2.2 GeV/c. To recover the missed momentum fraction, a fit to the distribution has been performed with the following formula:

$$f(p_{\mathrm{T}}^{reco}) = a - b \cdot exp(-c \cdot p_{\mathrm{T}}^{reco}) \tag{4.9}$$

and the resulting parameterisation has been used to apply a track-by-track correction to the reconstructed $({}^{3}_{\Lambda}\overline{\mathrm{H}})^{3}_{\Lambda}\mathrm{H}$ transverse momentum.

Monte Carlo studies

The analyses presented in this thesis use the on-the-fly V^0 finder algorithm, which was developed for the reconstruction of neutral particle decays. For this reason, preliminary studies on the MC sample have been performed to check the reconstruction of the ${}^{3}_{\Lambda}\mathrm{H}$ and the effect of the selection criteria previously introduced.

MC preliminary study						
	Set 1	Set 2	Set 3	Set 4	Set 5	Set 6
DCA^{π}_{PV} (cm)	≥ 0.4	≥ 0.2	≥ 0.1	≥ 0.1	≥ 0.2	≥ 0.4
ct (cm)		> 1			> 0.5	
$\text{DCA}_{^3\text{He},\pi}$ (cm)	$< 0.7, 0.3, 0.1$					
$\cos(\theta_{pointing})$	$> 0.94, 0.99, 0.995$					

Table 4.7.: Sets of different selection criteria tested on the MC production. More details in the text.

Baseline selections which have already been studied and tuned properly are the event selections, the track selections, the particle identification and the p_{T} ranges for the reconstructed decay products and ($^{3}_{\Lambda}\overline{\text{H}}$)hypertriton.

The focus of these preliminary studies is on the DCA between the daughters tracks $\text{DCA}_{^3\text{He},\pi}$, the DCA of the π track to the primary vertex DCA^{π}_{PV}, the cosine of the pointing angle $\cos(\theta_{pointing})$ and the lifetime ct. In addition all the studies have been done for the two rapidity ranges $|y| < 0.5$ and $|y| < 0.8$.

Table 4.7 summarises the different set of cuts that have been tested on the MC sample. Each set corresponds to a different cut on the DCA^{π}_{PV} and ct (e.g. Set 1 $\rightarrow$ $\text{DCA}^{\pi}_{PV} \geq 0.4$, $ct > 1$). Then the $\text{DCA}_{^3\text{He},\pi}$ and the $\cos(\theta_{pointing})$ have been varied for each set. As a result, several invariant mass distributions have been obtained for $^{3}_{\Lambda}$H and $^{3}_{\Lambda}\overline{\text{H}}$ corresponding to a different configuration of the cuts. Figure 4.9 and 4.10 show the invariant mass distribution for the $^{3}_{\Lambda}$H and $^{3}_{\Lambda}\overline{\text{H}}$, respectively, selected with the cuts denominated as Set 2. The values of $\text{DCA}_{^3\text{He},\pi}$ and $\cos(\theta_{pointing})$ are reported on top of each panel. Moving from left to right the variation is done on the $\text{DCA}_{^3\text{He},\pi}$ while from top to bottom on the cosine($\theta_{pointing}$). The fitting function is the sum of a gaussian and pol3 for the signal and the background contribution, respectively.

The observables used to study the effect of the applied selection criteria are the signal over background ratio S/B and the significance $\text{S}/\sqrt{\text{S}+\text{B}}$, where S and B are the signal and background counts, respectively. They are obtained integrating the corresponding function in the mass window $\pm 3\sigma$ with respect to the mean value from the gaussian distribution. The values of S/B and significance in these studies are directly related to the injection scheme of the MC production. However, the trends of these observables can give a hint on the effect of the different cuts in terms of signal enhancement.

Figure 4.11a and 4.11b show the trend of the significance for the $^{3}_{\Lambda}$H and $^{3}_{\Lambda}\overline{\text{H}}$ as a function of the different $\text{DCA}_{^3\text{He},\pi}$ selections. Moreover, the different markers correspond to

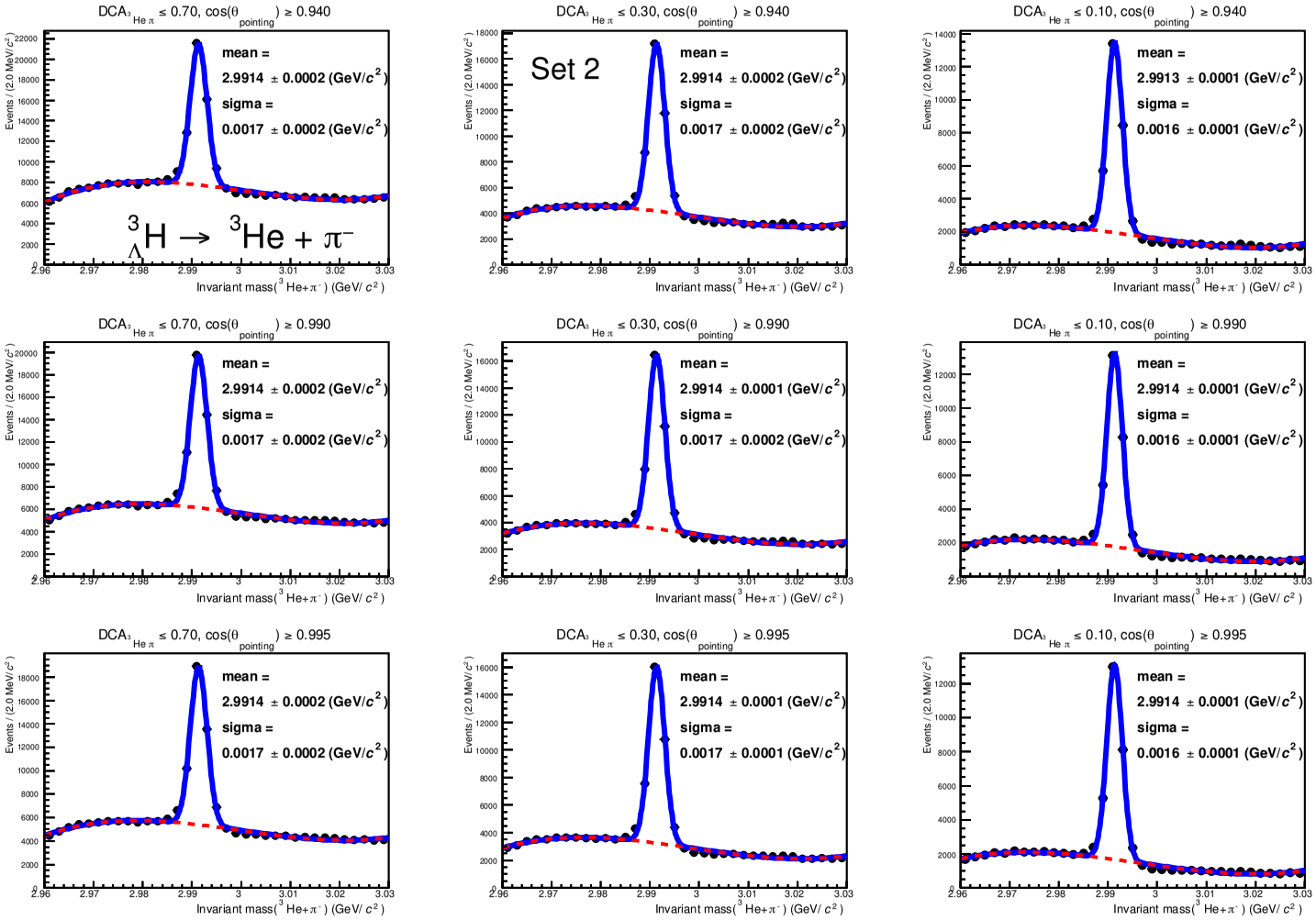

Figure 4.9.: ${}^{3}_{\Lambda}\mathrm{H}$ invariant mass distributions from cut variation study. Fixed cuts are $\mathrm{DCA}^{\pi}_{PV} > 0.2$ cm, $c\tau > 1$ cm and $|y| < 0.5$. Variations of the $\mathrm{DCA}_{^3\mathrm{He},\pi}$ and of the $\cos(\theta_{pointing})$ are reported on top of each plot. Fit are performed using a function sum of a gaussian (signal) and a pol3 (background).

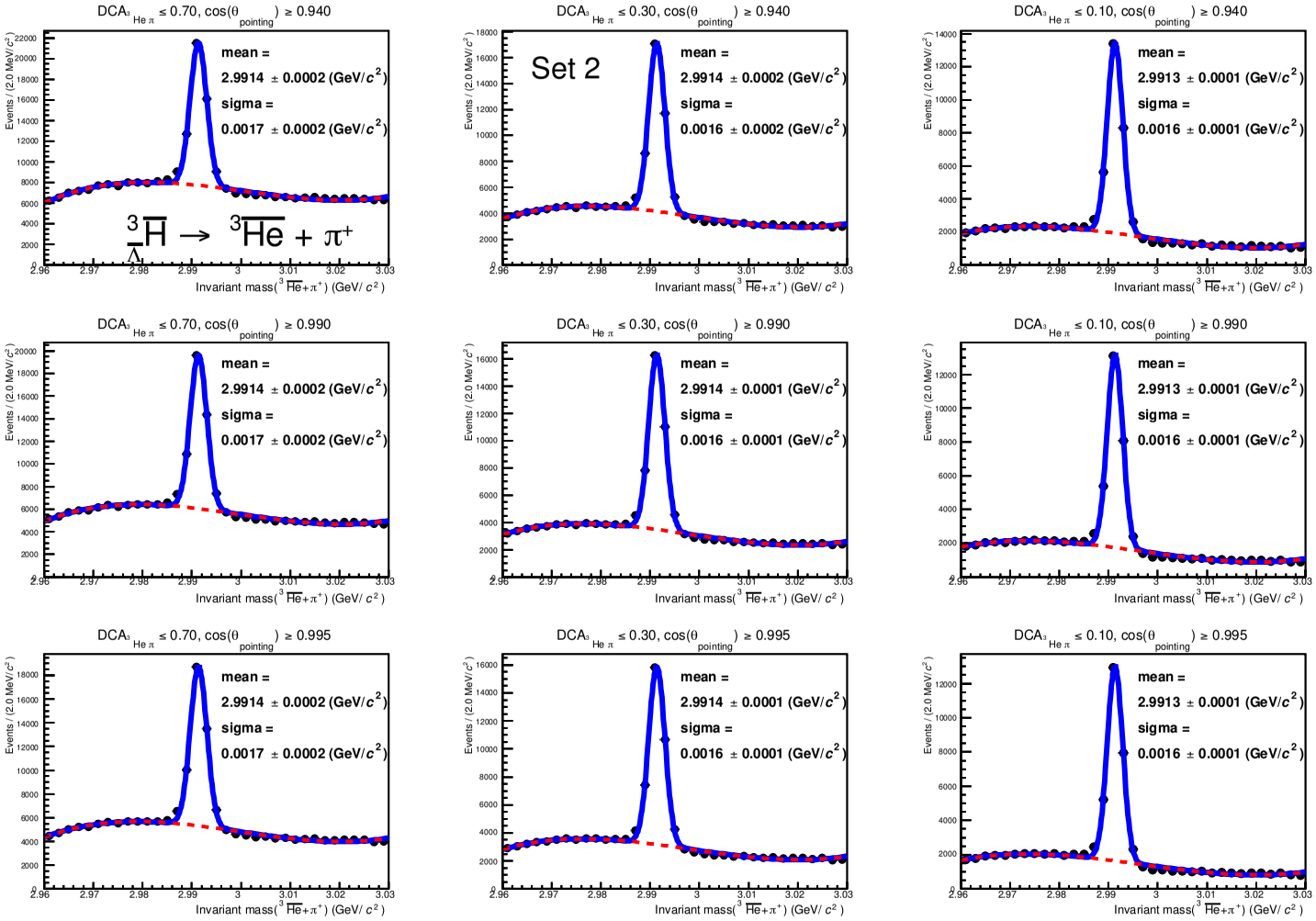

Figure 4.10.: ${}^{3}_{\Lambda}\overline{\mathrm{H}}$ invariant mass distributions from cut variation study. Fixed cuts are $\mathrm{DCA}^{\pi}_{PV} > 0.2$ cm, $ct > 1$ cm and $|y| < 0.5$. Variations of the $\mathrm{DCA}_{^{3}\mathrm{He},\pi}$ and of the $\cos(\theta_{pointing})$ are reported on top of each plot. Fit are performed using a function sum of a gaussian (signal) and a pol3 (background).

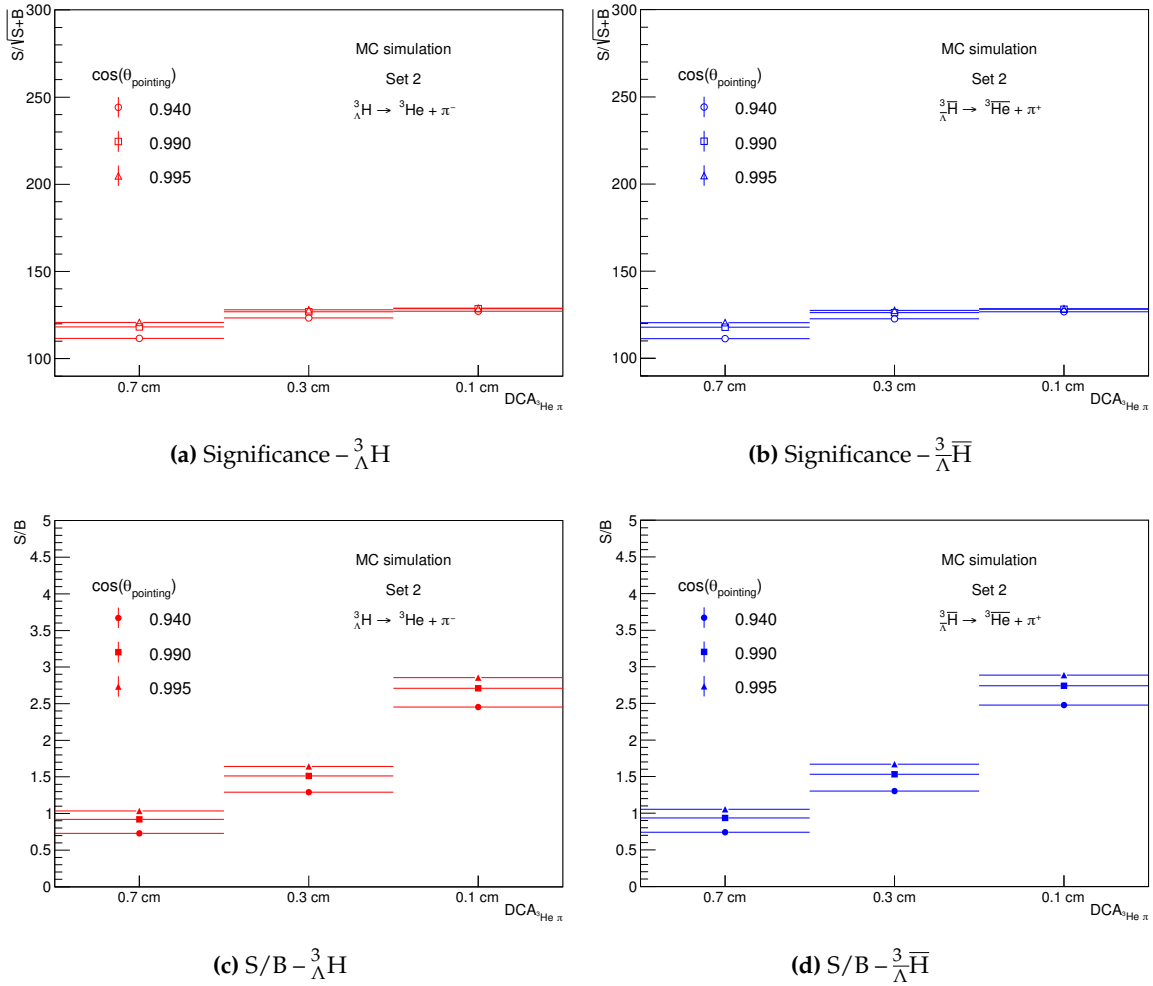

(a) Significance – ${}^{3}_{\Lambda}\mathrm{H}$

(b) Significance – ${}^{3}_{\Lambda}\overline{\mathrm{H}}$

(c) S/B – ${}^{3}_{\Lambda}\mathrm{H}$

(d) S/B – ${}^{3}_{\Lambda}\overline{\mathrm{H}}$

Figure 4.11.: Trend of the Significance (top) and S/B ratio (bottom) for ${}^{3}_{\Lambda}\mathrm{H}$ (left) and ${}^{3}_{\Lambda}\overline{\mathrm{H}}$ (right) reconstructed and selected with cuts of Set 2.

a different cut on the $\cos(\theta_{pointing})$, as reported in the legend. The significance slightly increases while tightening the selection on the DCA between the daughters tracks. The effect of the variation of the $\cos(\theta_{pointing})$ is visible for $\mathrm{DCA}_{^3\mathrm{He},\pi}$ = 0.7 cm and it becomes less effective for smaller DCA values. Similarly, Figure 4.11c and 4.11d show the trend of the signal over background ratio for the different selections on $\mathrm{DCA}_{^3\mathrm{He},\pi}$ and cosine$(\theta_{pointing})$. In this case a stronger selection on the tracks DCA increases the S/B and the same effect is also visible when tightening the cut on the cosine$(\theta_{pointing})$.

Other sets of cuts have been studied, following Table 4.7. The invariant mass distributions, the S/B ratios and the significance for the different set of cuts are reported for completeness in the Appendix A.

These preliminary studies show that the $\mathrm{DCA}_{^3\mathrm{He},\pi}$ and cosine($\theta_{pointing}$) are the two most effective cuts to select $({}^{3}_{\Lambda}\overline{\mathrm{H}})^{3}_{\Lambda}\mathrm{H}$ candidates. Also the selection on the minimum ct goes in the direction of reducing the combinatorial background, even if mildly with respect to previous two cuts. On the other hand the DCA^{π}_{PV} does not bring to variations in the S/B and the significance trends. However this cut will be tested for the analysis of the production yields in the most central collisions, where a large fraction of primaries pions are created.

The choice of the set of cuts, used as starting point for the selection criteria on the real data, is based on these studies and considering that a tigher a cut will have lower reconstruction efficiency. For this reason the Set 2 with $\mathrm{DCA}_{^3\mathrm{He},\pi} > 0.7$ cm and cosine($\theta_{pointing}$) > 0.995 has been chosen as reference for the selection criteria on the real data. The significance of this set of cuts is close to those of the other configurations. However it corresponds a higher reconstruction efficiency since these selections are less strong compared to the other possible combinations. These cuts are used as a starting point for the selection to be applied to the real data and can be further tuned in the different analyses.

Chapter 5.

Study of ${}^{3}_{\Lambda}\mathrm{H}$ and ${}^{3}_{\Lambda}\overline{\mathrm{H}}$ production in Pb–Pb collisions in the two body decay

"The gratification comes in doing, not in the results"
— James Dean, 1931–1955

The production of the $({}^{3}_{\Lambda}\overline{\mathrm{H}})^{3}_{\Lambda}\mathrm{H}$ in heavy ion collisions is mainly described by two different approaches: the thermal production from the thermalized medium at the chemical freeze-out and the coalescence of nucleons and strange particles at the kinetic freeze-out. These two categories of models are based on the characteristics of the medium created in the collision. Therefore, the study of the production as a function of the collision centrality is crucial for testing and constraining the model predictions. In this chapter the determination of the production yields per rapidity $\mathrm{d}N/\mathrm{d}y$ is presented for three different centrality classes (0–10%, 10–30%, 30–50%). Moreover, the available statistics in the 10–40% centrality class allows the measurement of the $({}^{3}_{\Lambda}\overline{\mathrm{H}})^{3}_{\Lambda}\mathrm{H}$ transverse momentum spectra, which is also motivated by the transverse momentum spectra of ${}^{3}\mathrm{He}$ done in the same centrality class by the ALICE Collaboration. The analyses presented in this Chapter are performed using the data sample of Pb–Pb collisions at $\sqrt{s_{\mathrm{NN}}}$= 5.02 TeV collected by the ALICE experiment in 2015.

5.1. Production yields

The details of the analysis method adopted for the measurements of ${}^{3}_{\Lambda}\mathrm{H}$ and ${}^{3}_{\Lambda}\overline{\mathrm{H}}$ production yields in three centrality classes are presented, which are selected based on the available collected statistics.

5.1.1. Raw yields extraction *vs* centrality

The candidates ${}^{3}_{\Lambda}\mathrm{H}$ and ${}^{3}_{\Lambda}\overline{\mathrm{H}}$, used in the determination of the raw yield, are chosen separately applying the selection criteria described in the previous chapter. Table 5.1 reports the set of cuts applied in this analysis for the three centrality classes. The requirements have been determined after an accurate MC study of the effect of the different selection critera. Only in the 0–10% centrality class, pion tracks are required to have a DCA to the primary vertex DCA^{π}_{PV} larger than 0.2 cm. The reason for this additional selection in the most central collisions is related to the large number of primary pions ($\sim$ 2000) produced in those collisions.

Candidate selections			
	0–10%	10–30%	30–50%
π p_{T} (GeV/c)	0.2-1.2	0.2-1.2	0.2-1.2
${}^{3}\mathrm{He}$ p_{T} (GeV/c)	≥ 1.8	≥ 1.8	≥ 1.8
DCA^{π}_{PV} (cm)	≥ 0.2	-	-
DCA_{tracks} (cm)	< 0.7	< 0.7	< 0.7
ct (cm)	> 2	> 2	> 2
$\cos(\theta_{pointing})$	≥ 0.995	≥ 0.995	≥ 0.995
$\lvert y \rvert$	≤ 0.5	≤ 0.5	≤ 0.5

Table 5.1.: Set of cuts applied for the selection of ${}^{3}_{\Lambda}\mathrm{H}$ and ${}^{3}_{\Lambda}\overline{\mathrm{H}}$ candidates in the three centrality classes.

The invariant mass distributions for the candidates selected with the aforementioned criteria are reported in Figure 5.1, on the left for the ${}^{3}_{\Lambda}\mathrm{H}$ and on the right for the ${}^{3}_{\Lambda}\overline{\mathrm{H}}$. The distributions are also divided in the three centrality class 0–10% (top), 10–30% (middle) and 30–50% (bottom). The fitting function used for the signal extraction is the sum of two probability density functions, a Gaussian for the signal and a second degree polynomial for the background and it is drawn with a blue curve. The parameters of the background component are determined with a fit to the sidebands distribution, which corresponds to the [-9σ,-4σ] and [+4σ,+9σ] intervals from the mean of the Gaussian, and is represented with a red dashed line. The sidebands are chosen in order to be far from the region where the signal is expected and to fit the combinatorial background only. The normalization of the fit function is kept into account with two parameters N_{sig} and N_{bkg}, which corresponds to the signal and background counts, respectively. The fit function is defined as:

$$\mathrm{p.d.f.}(m) = \mathrm{N}_{sig} \cdot \mathrm{p.d.f.}_{sig}(m|\mu,\sigma) + \mathrm{N}_{bkg} \cdot \mathrm{p.d.f.}_{bkg}(m|a_i) \tag{5.1}$$

where m is the invariant mass, μ and σ are the mean and width of the Gaussian, respectively, while a_i are the parameters of the polynomial.

In the centrality class 30–50% the statistics is very low, by a factor 3 compared to the 0–10% class, and the signal extraction depends on the outcome of the fit to the distribution. For this reason, a first fit is performed on the invariant mass distribution obtained from the sum of matter and anti-matter. The σ of the Gaussian is evaluated from the result of the fit. Then the signal extraction of matter and anti-matter separately is performed fixing the σ of the fitting function to the previously found value.

The mean (μ) and the width (σ) of the Gaussian distribution are evaluated in the fit procedure and the first one is compared, for all the three centrality classes, with the experimental mass value of the $({}^{3}_{\Lambda}\overline{\mathrm{H}})^{3}_{\Lambda}\mathrm{H}$ measured by the ALICE [70] and STAR [56] experiments. Figure 5.2a and 5.2b show this comparison for ${}^{3}_{\Lambda}\mathrm{H}$ (a) and ${}^{3}_{\Lambda}\overline{\mathrm{H}}$ (b), respectively, and all the mean values are in agreement within the uncertainties with the other experimental results.

The mean values from the ${}^{3}_{\Lambda}\overline{\mathrm{H}}$ invariant mass fit in the three analysed centralities are comparable and the same can be observed for the ${}^{3}_{\Lambda}\mathrm{H}$. On the other hand the ${}^{3}_{\Lambda}\overline{\mathrm{H}}$ mass is slightly higher than the one of the ${}^{3}_{\Lambda}\mathrm{H}$, even if in agreement with previous experimental values. Still more important is the comparison between the σ which will be used to estimate the raw yields and are compatible between matter and antimatter in the different centralities.

The counts of signal S (raw yield) and background B are obtained from the integral of the respective component of the fitting function in the range $\pm 3\sigma$ with respect to the mean value of the Gaussian. Thus it is possible to calculate the S/B and the significance $\mathrm{S}/\sqrt{\mathrm{S}+\mathrm{B}}$ for the signal extracted. The increase of the signal over background ratio (S/B) from the 0–10% to the 30–50% in due to the reduction of the combinatorial background as can be also seen in Figure 5.1. Indeed, the combinatorial background is expected to scale also with the charged particle multiplicity, which decreases going from central to peripheral collisions. A summary of the fit results and signal extraction for ${}^{3}_{\Lambda}\mathrm{H}$ and ${}^{3}_{\Lambda}\overline{\mathrm{H}}$ in the three analysed centrality classes is reported in Table 5.2 and 5.3, respectively.

As a general rule, the raw yield estimate is statistically significant if the significance is larger than 3, which corresponds to the 99.7% of the integral of a Gaussian probability density function (p.d.f.). However the signals extracted for ${}^{3}_{\Lambda}\mathrm{H}$ in the 10–30% and 30–50% centrality classes are slightly below the threshold, precisely 4% and 11% off the 3σ. As a crosscheck, the signals are extracted from the merged invariant mass distributions of matter and anti-matter and are compared with the sum of the obtained raw yields. The outcome of the check is that in both cases the significance is larger than 3 and the raw yields of 88

$\pm$ 21 in 10–30% and 46 $\pm$ 16 in 30–50% are compatible with sum of the signals extracted separately. Thus, also the raw yields of the ${}^{3}_{\Lambda}\mathrm{H}$ in 10–30% and 30–50% are used to study the production in the semi-central collisions, despite their significances.

${}^{3}_{\Lambda}\mathrm{H}$			
	0–10%	10–30%	30–50%
mean (GeV/c^2)	2.9911 $\pm$ 0.0007	2.9916 $\pm$ 0.0009	2.9901 $\pm$ 0.0009
width (GeV/c^2)	0.0023 $\pm$ 0.0005	0.0027 $\pm$ 0.0003	0.0021 $\pm$ 0.0007
χ^2/NDF	1.60	1.36	0.89
S/B	0.22	0.19	0.42
Significance (3σ)	3.34	2.88	2.65
Raw yield	72 $\pm$ 16	50 $\pm$ 13	29 $\pm$ 8

Table 5.2.: From top: mean, width, χ^2/NDF, S/B and significance obtained from the fit to the ${}^{3}_{\Lambda}\mathrm{H}$ invariant mass distributions in the three centrality classes. Raw yields are obtained as the integral of the signal function in $\pm 3\sigma$ with respect to the mean value.

${}^{3}_{\Lambda}\overline{\mathrm{H}}$			
	0–10%	10–30%	30–50%
mean (GeV/c^2)	2.9923 $\pm$ 0.0009	2.9929 $\pm$ 0.0007	2.9923 $\pm$ 0.0007
width (GeV/c^2)	0.0029 $\pm$ 0.0008	0.0027 $\pm$ 0.0005	0.0021 $\pm$ 0.0005
χ^2/NDF	1.38	1.26	1.93
S/B	0.26	0.26	0.85
Significance (3σ)	3.33	3.07	3.40
Raw yield	57 $\pm$ 12	48 $\pm$ 12	26 $\pm$ 7

Table 5.3.: From top: mean, width, χ^2/NDF, S/B and significance obtained from the fit to the ${}^{3}_{\Lambda}\overline{\mathrm{H}}$ invariant mass distributions in the three centrality classes. Raw yields are obtained as the integral of the signal function in $\pm 3\sigma$ with respect to the mean value.

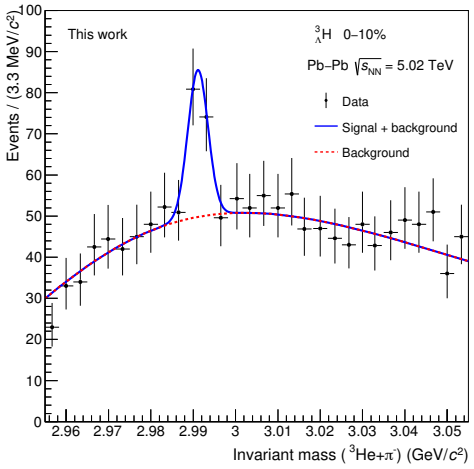

(a) ${}^{3}_{\Lambda}\mathrm{H}$ 0–10%

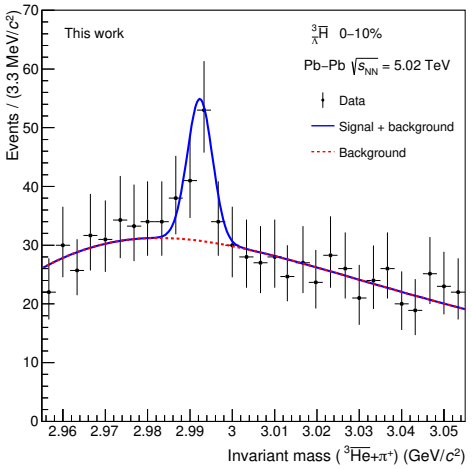

(b) ${}^{3}_{\Lambda}\overline{\mathrm{H}}$ 0–10%

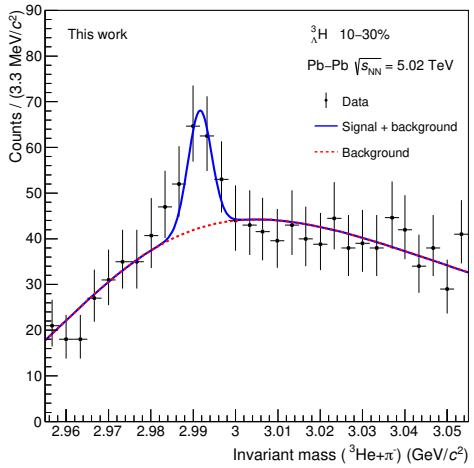

(c) ${}^{3}_{\Lambda}\mathrm{H}$ 10–30%

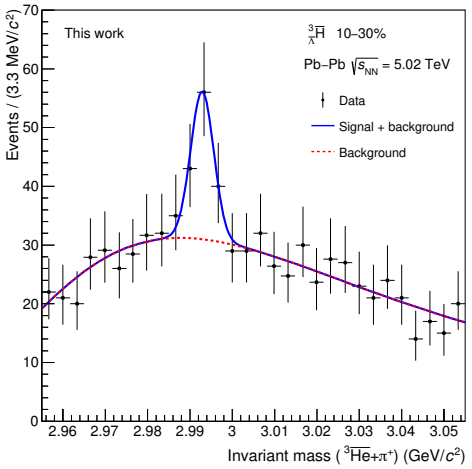

(d) ${}^{3}_{\Lambda}\overline{\mathrm{H}}$ 10–30%

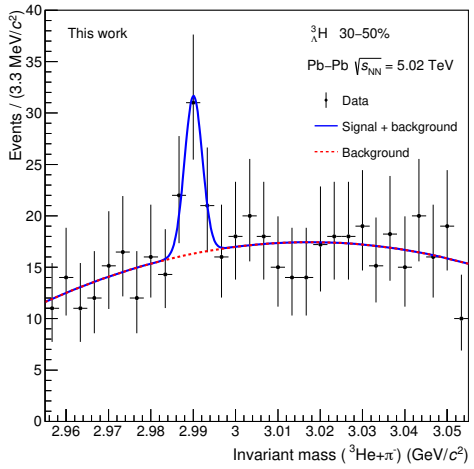

(e) ${}^{3}_{\Lambda}\mathrm{H}$ 30–50%

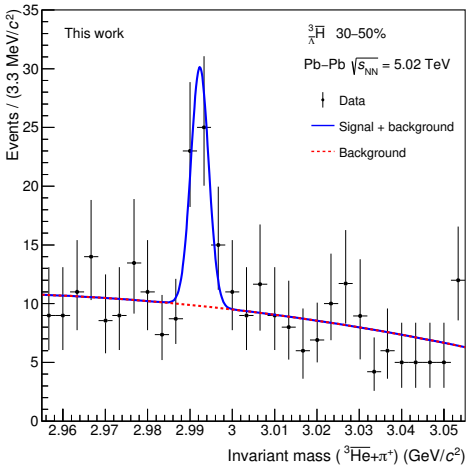

(f) ${}^{3}_{\Lambda}\overline{\mathrm{H}}$ 30–50%

Figure 5.1.: Invariant mass distributions of ${}^{3}_{\Lambda}\mathrm{H}$ (left) and ${}^{3}_{\Lambda}\overline{\mathrm{H}}$ (right) in the 0–10% (top), 10–30%(middle) and 30–50% (bottom) centrality class. The blue curve is the fit function, sum of signal background (Gaussian + pol2), and the red dashed line is the background component.

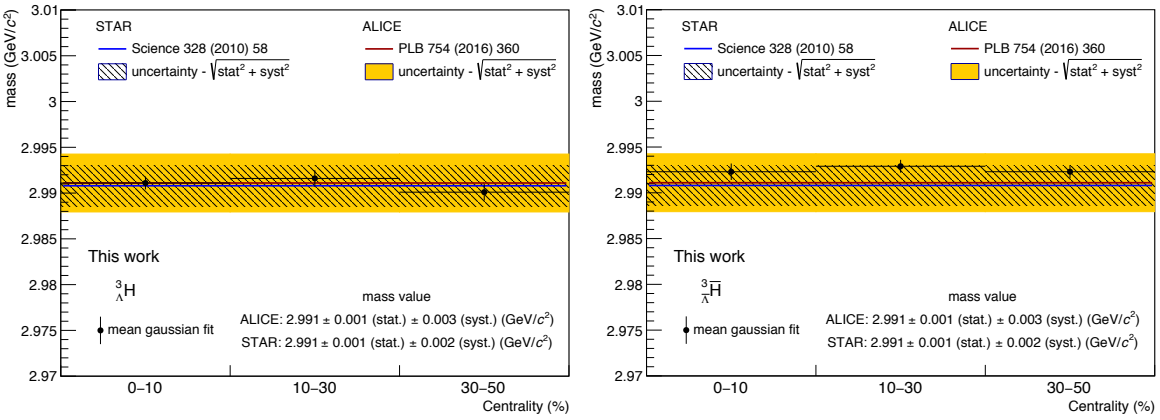

(a) ${}^{3}_{\Lambda}\mathrm{H}$ **(b)** ${}^{3}_{\Lambda}\overline{\mathrm{H}}$

Figure 5.2.: Mean values with their uncertainties obtained from the fit to the ${}^{3}_{\Lambda}\mathrm{H}$ (a) and ${}^{3}_{\Lambda}\overline{\mathrm{H}}$ (b) invariant mass distributions compared with the experimental mass value measured by STAR [56] and ALICE [70].

5.1.2. Efficiency correction

The measured raw yields are biased by inefficiencies in the ALICE detectors. For instance, the active area of the experiment is not hermetic by design (e.g. sector edges of the TPC) or, sometimes, parts of the detectors might be switched off during some periods of the data taking periods (e.g. TPC readout chambers excluded during some runs because unstable).

It is possible to correct for the finite efficiency and acceptance using a MC simulation where the full geometry and the real data taking conditions are reproduced. The MC production used for this analysis has been described in detail in Chapter 4. The number of particles crossing the detectors and their kinematics observables are known when using a MC simulation and the efficiency $\times$ acceptance can be computed as:

$$Efficiency \times Acceptance(p_{\mathrm{T}}) = \frac{\mathrm{N}_{rec}(p_{\mathrm{T}})}{\mathrm{N}_{gen}(p_{\mathrm{T}})} \tag{5.2}$$

where N_{gen} is the number of $(\overline{{}^{3}_{\Lambda}\mathrm{H}})^{3}_{\Lambda}\mathrm{H}$ generated in the azimuthal region $0 \leq \phi < 2\pi$ and in the rapidity range $|y|<0.5$, while N_{rec} is the number of $(\overline{{}^{3}_{\Lambda}\mathrm{H}})^{3}_{\Lambda}\mathrm{H}$ that satisfies the selection criteria summarised in Table 5.1. The efficiency $\times$ acceptance is evaluated for ${}^{3}_{\Lambda}\mathrm{H}$ and ${}^{3}_{\Lambda}\overline{\mathrm{H}}$ separately as a function of the transverse momentum and it is shown in Figure 5.3a and 5.3b. The distributions are obtained in the centrality classes used in the analysis to check if the different occupancies of the detector play a role in the reconstruction performance. Moreover they are evaluated in narrow p_{T} intervals to take into account the dependence

on the transverse momentum of the particles. In particular, the efficiency for the candidates reconstruction in 0–10% lower since there is the additional cut on the DCA^{π}_{PV}.

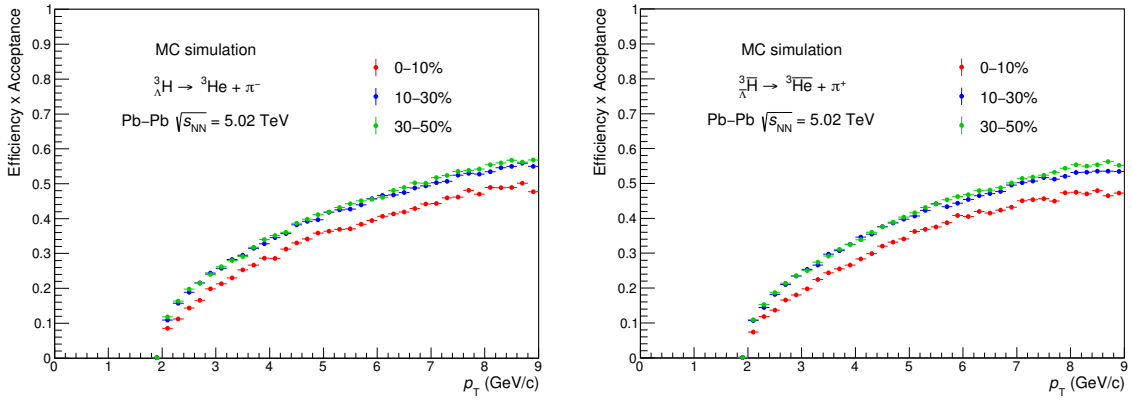

(a) ${}^{3}_{\Lambda}\mathrm{H}$ **(b)** ${}^{3}_{\Lambda}\overline{\mathrm{H}}$

Figure 5.3.: Efficiency $\times$ acceptance as a function of p_{T} for ${}^{3}_{\Lambda}\mathrm{H}$ (a) and ${}^{3}_{\Lambda}\overline{\mathrm{H}}$ (b) in the three centrality classe 0–10% (red), 10–30% (blue) and 30–50% (green).

Since the extracted ${}^{3}_{\Lambda}\mathrm{H}$ and ${}^{3}_{\Lambda}\overline{\mathrm{H}}$ raw yields are p_{T}-integrated in the range 2-9 GeV/c (see Table 5.1), the efficiency correction estimate has to be provided also p_{T}-integrated in the same interval. Practically, it is obtained as a weighted average of the efficiency $\times$ acceptance distribution from 2 to 9 GeV/c following:

$$Efficiency \times Acceptance = \frac{\sum_{p_{\mathrm{T}}=2}^{9} w_{p_{\mathrm{T}}} \cdot \epsilon(p_{\mathrm{T}})}{\sum_{p_{\mathrm{T}}=2}^{9} w_{p_{\mathrm{T}}}} \tag{5.3}$$

where $\epsilon(p_{\mathrm{T}})$ is the efficiency for a given p_{T}, as in Eq.5.2, while the weight $w_{p_{\mathrm{T}}}$ is taken from the Blast-Wave [20] distributions[1] of the ${}^{3}\mathrm{He}$ [124], shown in Figure 5.4. The reason for this choice is related to the fact that the ${}^{3}\mathrm{He}$ mass is much closer to that one of the ${}^{3}_{\Lambda}\mathrm{H}$ than the other light hadrons (e.g. π, K, p). In particular the ${}^{3}\mathrm{He}$ Blast-Wave distributions are obtained in the 0–10% (blue), 10–40% (red) and 40–90% (green) centrality classes and are used in the average computation of the $({}^{3}_{\Lambda}\overline{\mathrm{H}})^{3}_{\Lambda}\mathrm{H}$ efficiencies in 0–10%, 10–30% and 30–50%, respectively.

The efficiency $\times$ acceptance values, obtained from the weighted average, are reported in Table 5.4 and are used to correct the raw yields previously extracted of the ${}^{3}_{\Lambda}\mathrm{H}$ and the ${}^{3}_{\Lambda}\overline{\mathrm{H}}$ reported in Table 5.2 and 5.3.

[1] More details on the Blast-Wave distribution in Appendix B.

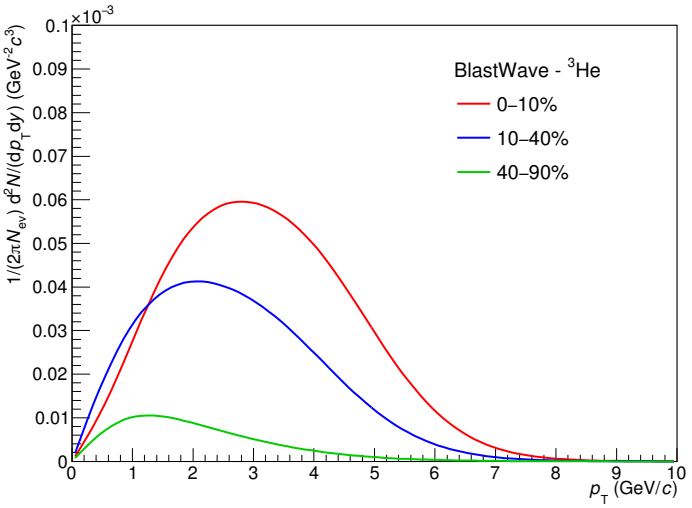

Figure 5.4.: Blast-Wave distributions from the analysis of the ^{3}He production in three centrality classes 0–10% (blue), 10–40% (red) and 40–90% (green) [124].

Efficiency × Acceptance			
	0–10%	10–30%	30–50%
${}^{3}_{\Lambda}\mathrm{H}$	25.3 %	27.6 %	25.4 %
${}^{3}_{\Lambda}\overline{\mathrm{H}}$	24.5 %	27.1 %	24.7 %

Table 5.4.: Efficiency × acceptance for ${}^{3}_{\Lambda}\mathrm{H}$ (top) and ${}^{3}_{\Lambda}\overline{\mathrm{H}}$ (bottom) in the three centrality classes. More details on their evaluation in the text.

5.1.3. Absorption correction

GEANT3 is the transport code used in the MC productions used to finalize the analysis of this thesis and it does not take into account the interaction of ${}^{3}_{\Lambda}\mathrm{H}$ and ${}^{3}_{\Lambda}\overline{\mathrm{H}}$ with the material. This can be deduced from the efficiency distributions of ${}^{3}_{\Lambda}\mathrm{H}$ and ${}^{3}_{\Lambda}\overline{\mathrm{H}}$ in Figure 5.3a and 5.3b, which have the same trend and magnitude.

In order to estimate the correction for the absorption of ${}^{3}_{\Lambda}\mathrm{H}$ and ${}^{3}_{\Lambda}\overline{\mathrm{H}}$ an empirical approach has been adopted and the key elements for this evaluation are the absorption probabilities of $({}^{3}_{\Lambda}\overline{\mathrm{H}})^{3}_{\Lambda}\mathrm{H}$ and of $({}^{3}\overline{\mathrm{He}})^{3}\mathrm{He}$. In this analysis, as already done for the published results [70], the absorption indicates all those interactions which do not allow the $({}^{3}_{\Lambda}\overline{\mathrm{H}})^{3}_{\Lambda}\mathrm{H}$ and its daughters to reach the TPC and, thus, to be identified.

Since the interaction cross section for (anti-)nuclei is barely known and is missing for the (anti-)hypernuclei, the starting point for this calculation is the absorption probability

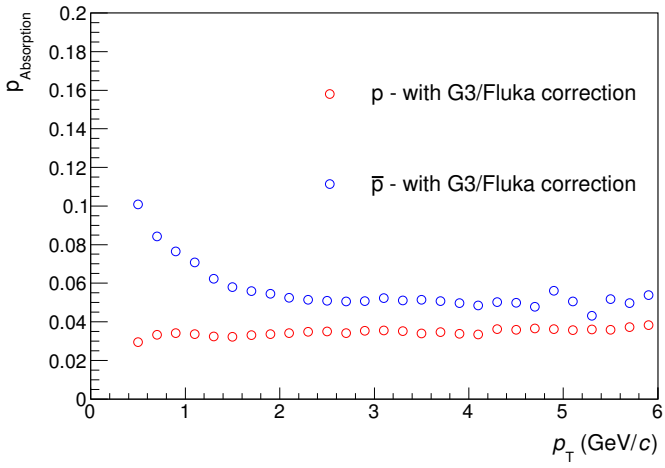

Figure 5.5.: Absorption probability of protons (red) and anti-protons (blue) from [125]

of p and $\overline{\mathrm{p}}$ measured by the ALICE Collaboration [125]. Figure 5.5 shows the fractions of protons (red) and anti-protons (blue) which do not reach the TPC ($\mathrm{p}_{Absorption}$) and they are computed using a MC simulation using GEANT3 with the Fluka correction. The latter one is a correction applied to the parameterisation of the inelastic cross section for p-A and $\overline{\mathrm{p}}$-A interaction, in the MC simulation. Indeed, in [126], it is shown that GEANT3 significantly overestimates the measured inelastic cross-sections, while FLUKA describes the data very well. Thus, the FLUKA results are used to account for the difference p and $\overline{\mathrm{p}}$ cross sections. More details can be found in [126]. The probability of a proton to be absorbed can be written as:

$$\mathrm{p}_{Absorption} = 1 - e^{-n_0 \sigma L} \tag{5.4}$$

where n_0 is the number of scattering center proportional to the density of the target, σ is the interaction cross-section of the projectile on the target and L is the path length of the projectile. In the probabilities reported in Figure 5.5 L is equal to the distance between the primary vertex (PV) and the TPC wall (TPC) that is 80 cm. Thus, it can be evaluated the absorption probability for p and $\overline{\mathrm{p}}$ as a function of the distance from the primary vertex, as shown in Figure 5.6a and 5.6b. They are evaluated for p (a) and $\overline{\mathrm{p}}$ (b) dividing the distance of 80 cm in intervals with width ΔL = 1 cm and assigning, for each ΔL and each p_{T}, 1/80 of the total absorption probability previously shown (Figure 5.5). The material density ρ, taken from the results on the photon conversion analysis performed in ALICE [127], is also included in the calculation. These two dimensional distributions are used as baseline for the next steps.

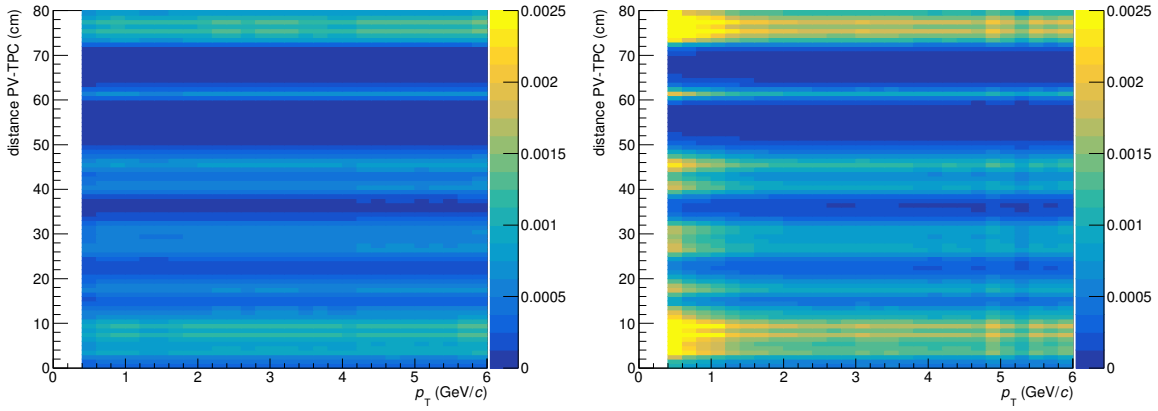

(a) Proton **(b)** Anti-Proton

Figure 5.6.: Absorption probability as a function of the distance between the primary vertex and the TPC for protons (a) and anti-protons (b).

The absorption probability of the $({}^{3}\overline{\mathrm{He}})^{3}\mathrm{He}$ is calculated from that one of the $(\overline{\mathrm{p}})\mathrm{p}$ and assuming the same distribution for protons and neutrons. Thus the probability to absorb the ${}^{3}\mathrm{He}$ can be written as:

$$\mathrm{p}_{Absorption,{}^{3}\mathrm{He}} = 1 - \mathrm{p}^{3}_{NotAbsorption,\mathrm{p}} \tag{5.5}$$

where $\mathrm{p}_{NotAbsorption,\mathrm{p}}$ is defined as 1 - $\mathrm{p}_{Absorption,\mathrm{p}}$, according to the definition of binomial distribution, and $\mathrm{p}_{Absorption,\mathrm{p}}$ is the proton absorption probability (Eq. 5.4).

The evaluation of the absorption probability for the $({}^{3}_{\Lambda}\overline{\mathrm{H}})^{3}_{\Lambda}\mathrm{H}$ is performed adopting a similar approach, but, in this case, to take into account the small Λ separation energy, the ${}^{3}_{\Lambda}\mathrm{H}$ cross-section is increased by 50% with respect to the one of the ${}^{3}\mathrm{He}$. This choice was already done in the published result [70] and it is based on the calculation of the ${}^{3}_{\Lambda}\mathrm{H}$ absorption cross-section on ${}^{238}\mathrm{U}$ [128] and its ratio with the extrapolated ${}^{3}\mathrm{He}$ cross-section [129] on the same target. The probability can be written as:

$$\mathrm{p}_{Absorption,{}^{3}_{\Lambda}\mathrm{H}} = 1 - e^{-1.5 n_0 \sigma_{{}^{3}\mathrm{He}} L} \tag{5.6}$$

The absorption probabilities of the ${}^{3}\mathrm{He}$ and the ${}^{3}_{\Lambda}\mathrm{H}$ are finally used to compute the probability not to observe an $({}^{3}_{\Lambda}\overline{\mathrm{H}})^{3}_{\Lambda}\mathrm{H}$ in the path between the primary vertex and the TPC inner wall. This probability is defined as:

$$\mathrm{p}^{(PV-TPC)}_{NotObserve_{{}^{3}_{\Lambda}\mathrm{H}}} = \mathrm{p}^{(PV-SV)}_{Absorption_{{}^{3}_{\Lambda}\mathrm{H}}} + \left(1 - \mathrm{p}^{(PV-SV)}_{Absorption_{{}^{3}_{\Lambda}\mathrm{H}}}\right) \cdot \mathrm{p}^{(SV-TPC)}_{Absorption_{{}^{3}\mathrm{He}}} \tag{5.7}$$

where (PV-SV) is the distance between the primary vertex and the decay vertex, while (SV-TPC) is the distance between the decay vertex and the TPC inner wall. Finally the probability to observe the ${}^{3}_{\Lambda}\mathrm{H}$, which is used as correction factor for the absorption, is obtained as:

$$\mathrm{p}^{(PV-TPC)}_{Observe_{{}^{3}_{\Lambda}\mathrm{H}}} = \left(1 - \mathrm{p}^{(PV-TPC)}_{NotObserve_{{}^{3}_{\Lambda}\mathrm{H}}}\right) \tag{5.8}$$

The probability to observe an $({}^{\overline{3}}_{\overline{\Lambda}}\overline{\mathrm{H}})^{3}_{\Lambda}\mathrm{H}$ depends on the distance between the primary vertex and the decay vertex (PV-SV), as can be deduced from Eq. 5.7. Thus, the probability has been evaluated for different distances (PV-SV) and the two extreme cases, corresponding to PV-SV = 1 cm and PV-SV = 79 cm, are shown in Figure 5.7a and 5.7b for the ${}^{3}_{\Lambda}\mathrm{H}$ and the ${}^{\overline{3}}_{\overline{\Lambda}}\overline{\mathrm{H}}$, respectively. The black curve corresponds to a decay vertex inside the beam pipe (PV-SV = 1 cm), while the blue curve corresponds to an $({}^{\overline{3}}_{\overline{\Lambda}}\overline{\mathrm{H}})^{3}_{\Lambda}\mathrm{H}$ which travels without decaying through the whole ITS (PV-SV = 79 cm). The absorption correction used in the analyses is assessed with an average between the two limiting cases and corresponds to the orange curve in Figure 5.7.

The probability to observe an ${}^{\overline{3}}_{\overline{\Lambda}}\overline{\mathrm{H}}$ increases from 0.65, at low p_{T}, to a constant value around 0.80 at high p_{T}, while the same probability for the ${}^{3}_{\Lambda}\mathrm{H}$ is flat around 0.85. The probability for p_{T} below 0.4 GeV/c is 1 both for matter and anti-matter and is due to the fact that the absorption probability for p and $\overline{\mathrm{p}}$ is unmeasured in that range. However, this low p_{T} range is not relevant for the transverse momentum ranges considered in this thesis. Indeed the candidates $({}^{\overline{3}}_{\overline{\Lambda}}\overline{\mathrm{H}})^{3}_{\Lambda}\mathrm{H}$ are selected between 2 and 9 GeV/c and this means to use the absorption correction in the $(\overline{\mathrm{p}})\mathrm{p}$ p_{T} range from 0.65 to 3 GeV/c, assuming the proton p_{T} as one third of the ${}^{3}_{\Lambda}\mathrm{H}$ p_{T}.

Thanks to the probability to observe a ${}^{3}_{\Lambda}\mathrm{H}$ and an ${}^{\overline{3}}_{\overline{\Lambda}}\overline{\mathrm{H}}$, just obtained, the correction factor can be calculated. In particular, since the production yields are extracted p_{T}-integrated in the range 2-9 GeV/c, the absorption correction is evaluated with a weighted average of the distributions in the corresponding proton p_{T} range previously discussed. The weights are taken from the ${}^{3}\mathrm{He}$ Blast-Wave already introduced in Sec. 5.1.2 and have been used following the same approach adopted in the efficiency calculation. The results of the weighted average are reported, for the three centrality classes of this analysis, in Table 5.5. These values are used to correct for the absorption by dividing the measured raw yields for the corresponding correction factor.

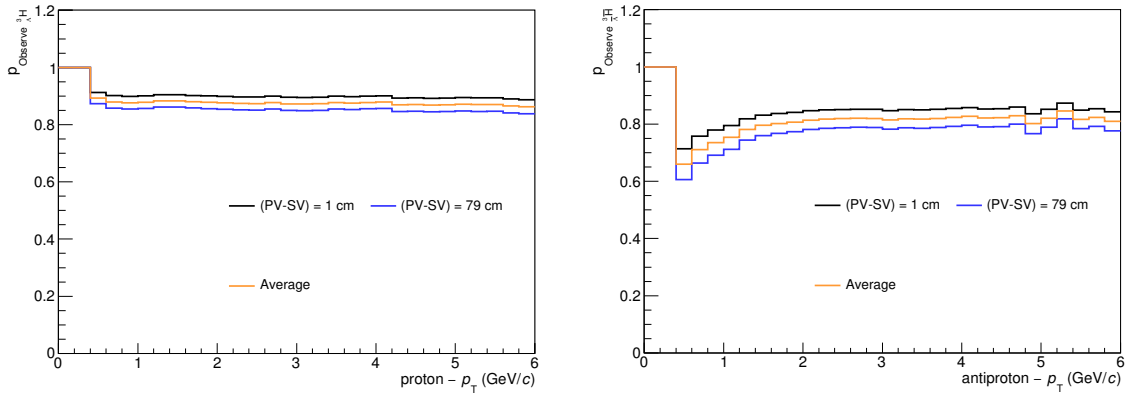

(a) ${}^{3}_{\Lambda}\mathrm{H}$ **(b)** ${}^{3}_{\Lambda}\overline{\mathrm{H}}$

Figure 5.7.: Probability to observe a ${}^{3}_{\Lambda}\mathrm{H}$ (a) and an ${}^{3}_{\Lambda}\overline{\mathrm{H}}$ (b) as a function of the $(\overline{\mathrm{p}})\mathrm{p}$ p_{T}. The black and blue curves correspond to a distance between primary and secondary vertices of 1 cm and 79 cm respectively. The orange curve is the average between the two distributions and it is the final correction.

Absorption correction			
	0–10%	10–30%	30–50%
${}^{3}_{\Lambda}\mathrm{H}$	87.96 %	87.95 %	87.91 %
${}^{3}_{\Lambda}\overline{\mathrm{H}}$	76.2 %	75.4 %	74.4 %

Table 5.5.: Probability to observe the ${}^{3}_{\Lambda}\mathrm{H}$ (top) and the ${}^{3}_{\Lambda}\overline{\mathrm{H}}$ (bottom) in the three centrality classes. More details on their evaluation in the text.

5.1.4. Systematics uncertainties

The accurate study of the systematic uncertainties is a fundamental part, especially in this analysis where the combinatorial background is very large and, thus, the applied selections could introduce systematic effects The main sources and the corresponding checks can be classified in four groups:

1. the absorption correction, done by varying the assumption on the $({}^{3}_{\Lambda}\overline{\mathrm{H}})^{3}_{\Lambda}\mathrm{H}$ cross-section and using the $\mathrm{p}_{Observe}$ distributions of different (PV-SV) distance;

2. the efficiency $\times$ acceptance, performed with different weights and taking into account the uncertainty on the material budget;

3. the selections criteria for the candidates and on the method adopted for the raw yield extraction;

4. the unknown $^{3}_{\Lambda}$H p_{T}-shape for the extrapolation of the yield in the unmeasured p_{T} regions.

These sources of systematic uncertainties are common to all the analyses presented in this thesis. Thus they will described in detail in this section, while in the following sections the results on the checks will be discussed.

The absorption correction is obtained with an empirical approach and it is based on two main assumptions, as described in Sec 5.1.3. The systematic uncertainty related to the usage of an average correction is evaluated using the probability to observe an $(^{\overline{3}}_{\overline{\Lambda}}\overline{\mathrm{H}})^{3}_{\Lambda}$H which decays in one case in the beam pipe (PV-SV = 1 cm) and in the other case close to the TPC (PV-SV = 79 cm). The raw yields are corrected separately with these two probabilities and the semi-difference between the corrected yields is taken as systematic uncertainty in each centrality class. This leads to the uncertainty of 4.5% for the $^{3}_{\Lambda}$H, independently of centralities, while the $^{\overline{3}}_{\overline{\Lambda}}\overline{\mathrm{H}}$ uncertainty slightly increases from 7 % to 7.5 % from the most central (0–10%) to the semi-central (30–50%) collisions.

The check on the assumption on the $^{3}_{\Lambda}$H cross-section value is performed in a similar way. In one case the correction is evaluated without rescaling the ^{3}He cross-section, $\sigma_{^{3}_{\Lambda}\mathrm{H}} = 1 \cdot \sigma_{^{3}\mathrm{He}}$, and in the other one the cross-section is increased by a factor 2, $\sigma_{^{3}_{\Lambda}\mathrm{H}} = 2 \cdot \sigma_{^{3}\mathrm{He}}$. The raw yields are corrected with these two probabilities separately and the systematic uncertainty in each centrality class is assessed with semi-difference between the corrected yields. The result is a constant uncertainty of 4.5 % for the $^{3}_{\Lambda}$H, while it goes from 7.3 % to 7.75 % for the $^{\overline{3}}_{\overline{\Lambda}}\overline{\mathrm{H}}$.

Another important check for the $(^{\overline{3}}_{\overline{\Lambda}}\overline{\mathrm{H}})^{3}_{\Lambda}$H analyses is on the efficiency calculation. As already explained, a weighted average is performed to obtain the efficiency $\times$ acceptance values and the check is performed using different distribution as weights. In particular, the Blast-Wave from π-K-p production analysis [130], the Boltzmann and the $\mathrm{m_T}$-exponential distributions from ^{3}He analysis [124] are those used for the systematic uncertainty estimate. In addition, since the ^{3}He Blast-Wave are not in the same centrality classes of this analysis and the $^{3}_{\Lambda}$H efficiency in the 30–50% used as weights the ^{3}He Blast-Wave in 40–90 %, it is tried to calculate this efficiency with the ^{3}He Blast-Wave in 10–40 % in the systematic studies. The weighted average is calculated using these distributions and the raw yields are corrected with the obtained values. The rms of the corrected yields distribution is taken as systematic uncertainty and it decreases from 3 % to 1 % from the most central to the semi-central collisions.

The second check on the efficiency is performed in order to inquire into possible discrepancies in the evaluated reconstruction efficiency when changing the material budget

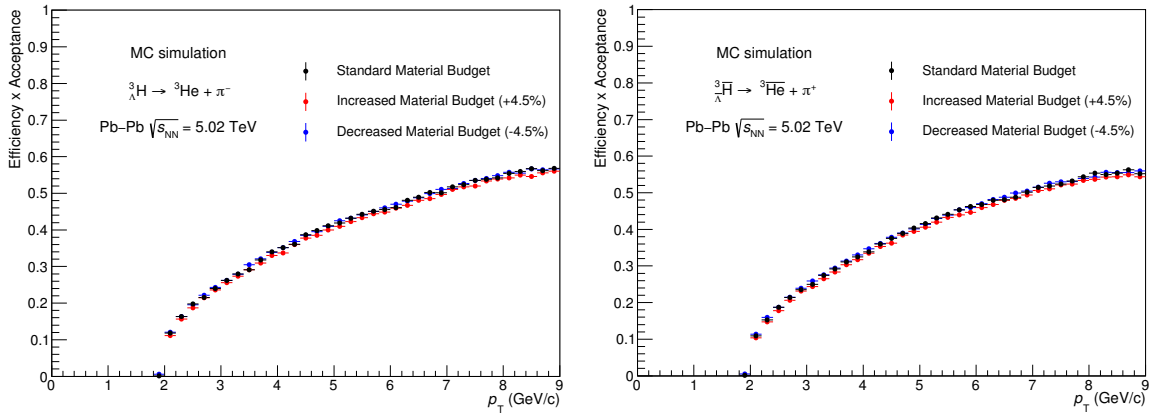

(a) ${}^{3}_{\Lambda}\mathrm{H}$ **(b)** ${}^{3}_{\Lambda}\overline{\mathrm{H}}$

Figure 5.8.: Study of the effect of the material budget variation in the estimation of the efficiency × acceptance for ${}^{3}_{\Lambda}\mathrm{H}$ (a) and ${}^{3}_{\Lambda}\overline{\mathrm{H}}$ (b).

estimation in the apparatus. This requires the usage of the MC productions introduced in Chapter 4 Sec. 4.1, where the material budget has been increased and decreased by 4.5% respectively. The efficiency × acceptance evaluated with these simulations are shown in Figure 5.8 and are compared with the results from MC simulation adopting the standard material budget. A trend with the material budget can be observed in each p_{T} interval, especially at low p_{T}. Reducing the material budget has the consequence of reducing the multiple scattering, thus increasing the tracks reconstruction efficiency (blue marker), while the decrease of the efficiency is related to the increased material budget. The variations in the efficiency × acceptance induced by changing in the material budget distribution are supposed to follow a uniform distribution and, for this reason, the systematic uncertainty is estimated as:

$$\sigma_{MB}(p_{\mathrm{T}}) = \frac{\epsilon_{max}(p_{\mathrm{T}}) - \epsilon_{min}(p_{\mathrm{T}})}{\sqrt{12}} \tag{5.9}$$

where ϵ_{max} and ϵ_{min} are the maximum and minimum efficiency in each p_{T} interval. This uncertainty estimation lies between 0.5% and 0.8% in the analysed p_{T} range both for ${}^{3}_{\Lambda}\mathrm{H}$ and ${}^{3}_{\Lambda}\overline{\mathrm{H}}$ and it has been chosen to assign a systematic uncertainty due to the not perfect knowledge of the material budget of 1% in each p_{T} bin.

The variation of the selection criteria, like topological cuts and PID, applied to the candidates is is the analysis approach used to investigate possible systematic effects related to the signal extraction. The variations of the topological and PID cuts with respect to the nominal ones (Table 5.1 and Table 5.7) are reported in Table 5.6 and in Table 5.7.

Candidate selection variations - systematics						
	Set 1	Set 2	Set 2	Set 4	Set 5	Set 6
${}^{3}\mathrm{He}$ p_{T} (GeV/c) $\geq$	1.7	1.8	1.6	1.9	1.9	1.8
DCA_{tracks} (cm) <	0.6	0.5	0.6	0.5	0.7	0.5
$\cos(\theta_{pointing}) \geq$	0.997	0.992	0.995	0.992	0.997	0.997

Table 5.6.: Set of cuts applied in the study of the systematics uncertainty related to the selection criteria of ${}^{3}_{\Lambda}\mathrm{H}$ and ${}^{3}_{\Lambda}\overline{\mathrm{H}}$ candidates.

PID selection variations - systematics						
		Set 1	Set 2	Set 2	Set 4	Set 5
π	$\lvert \mathrm{n}\sigma_{\pi} \rvert \leq$	3	3	3	3	2
${}^{3}\mathrm{He}$	$\lvert \mathrm{n}\sigma_{{}^{3}\mathrm{He}} \rvert \leq$	3	3	2	2	3
	$\mathrm{n}\sigma_{{}^{3}\mathrm{H}} >$	3	6	6	3	0

Table 5.7.: Set of nσ cuts applied in the study of the systematics uncertainty related to the PID of ${}^{3}_{\Lambda}\mathrm{H}$ and ${}^{3}_{\Lambda}\overline{\mathrm{H}}$ daughters.

For each of these selection variations the analysis is repeated *ab initio* for all centrality classes. Since the variation of the selection criteria modifies the sample of $({}^{3}_{\Lambda}\overline{\mathrm{H}})^{3}_{\Lambda}\mathrm{H}$ candidates, only the statistically significant variations of the final results have to be included in the systematic uncertainty. For this reason, a general prescription in ALICE is to compare the results obtained by changing the selection with the result obtained with the nominal selection and to include the cut and PID among the systematic uncertainties only if the difference is larger than 2σ. This method is usually called *Barlow criterion* from Roger Barlow's paper [131], where the variable used for the test $\Delta\mathrm{Y}/\sigma_{\Delta}$ is introduced. Following this principle, the significance of the difference between the results is evaluated for all the variations both for matter and anti-matter and they are reported in Figure 5.9. All the results exhibit a difference which does not exceed the $\pm 2\sigma$ (dashed lines) and, for this reason, both the cut and PID selection criteria are not included among the sources of systematic uncertaintities.

Considering the raw yield extraction, another check is performed on the function used for the background estimate. The analyses are repeated using two different functions for the background, the Landau and the third degree polynomial and, also in this case, the results are compared with those obtained with the nominal function. Nevertheless, also this check is not included in the sources of systematic uncertainties because the Barlow test results are below the 2σ threshold.

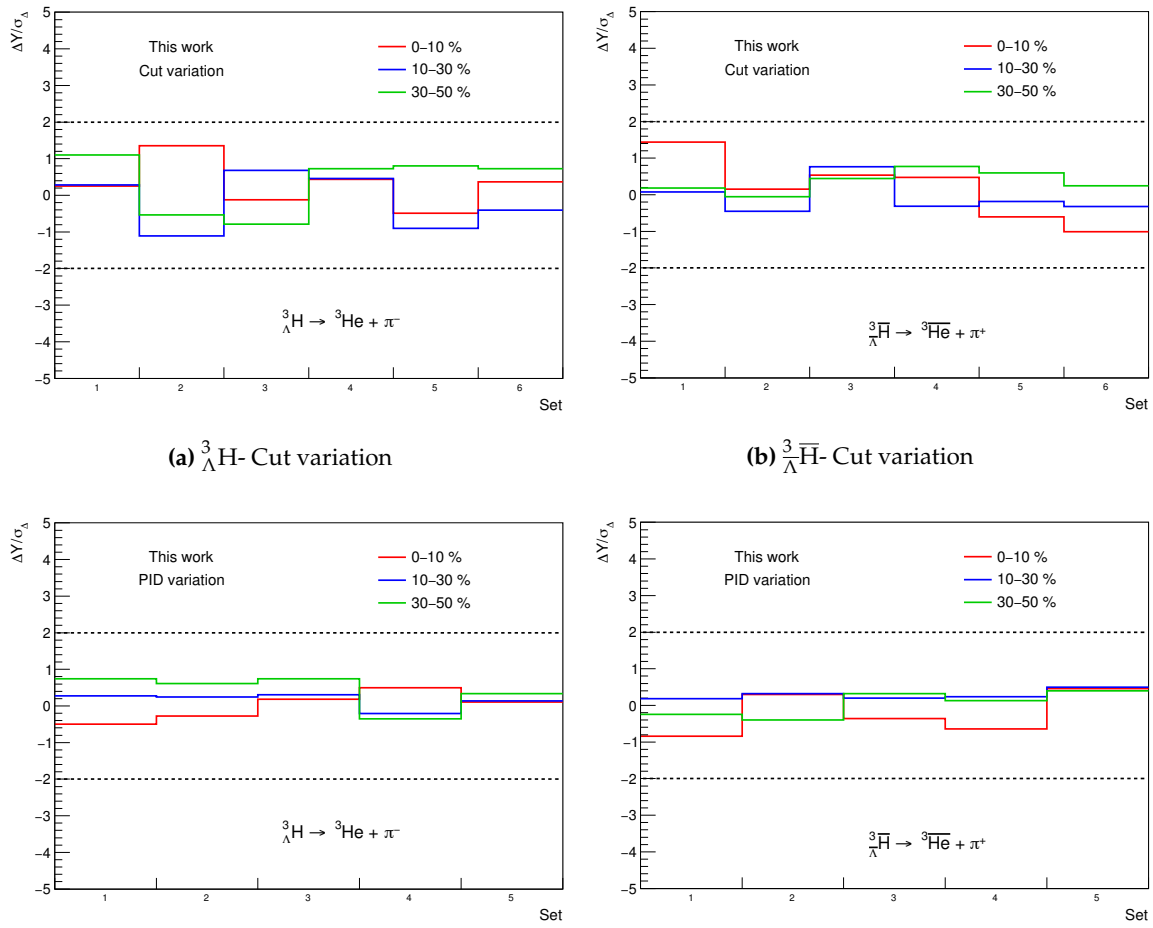

(a) ${}^{3}_{\Lambda}\mathrm{H}$- Cut variation

(b) ${}^{3}_{\Lambda}\overline{\mathrm{H}}$- Cut variation

(c) ${}^{3}_{\Lambda}\mathrm{H}$- PID variation

(d) ${}^{3}_{\Lambda}\overline{\mathrm{H}}$- PID variation

Figure 5.9.: Significance of the difference between the results obtained with nominal selections and those obtained with cuts (top) and PID (bottom) variations. The dashed line at ± 2 corresponds to the minimal threshold required in the *Barlow criterion* to include the variation in the systematic uncertainties.

The measured raw yields are obtained by selecting candidates ${}^{3}_{\Lambda}\mathrm{H}$ and ${}^{3}_{\Lambda}\overline{\mathrm{H}}$ in the p_{T} range 2-9 GeV/c. However the final production yields will be p_{T} integrated and the missing fraction is obtained from the integral of the Blast-Wave, that is the distribution used to describe the production spectra of light particles in heavy-ion collisions. In particular, the correction factor is the ratio between the integral of the distribution in the measured range (2-9 GeV/c) and the integral over the full p_{T} range. The raw yield is then divided for this value to include the missing fraction. Consequently, the distribution is the key element in this correction and the unknown p_{T}-shape in the unmeasured regions is a source of systematic uncertainties. The check is usually performed using different distributions to fit the p_{T} spectra, but in this case only the yields are available. For this reason the systematic

uncertainty is taken from the analysis on the p_{T} production spectra of $({}^{3}_{\Lambda}\overline{\mathrm{H}})^{3}_{\Lambda}\mathrm{H}$, which will be described in Sec. 5.2. In particular details on the evaluation of this source of systematic will be given in Sec. 5.2.4. The value of this uncertainty is 6.7 % for ${}^{3}_{\Lambda}\mathrm{H}$ and 6.5 % for ${}^{3}_{\Lambda}\overline{\mathrm{H}}$ in all centrality classes.

Finally, the last systematic effect is common to all the analyses in ALICE and is related to the tracking efficiency. Indeed it is not known to which extent the simulation reproduces the reality and the efficiency calculation can be a source of systematic uncertainty. This effect has been measured in the analysis of transverse momentum spectra of primary charged particles [132] in Pb–Pb collisions and the result is an uncertainty of 3.5 % on each single track. Since in the reconstruction of the $({}^{3}_{\Lambda}\overline{\mathrm{H}})^{3}_{\Lambda}\mathrm{H}$ two daughters tracks are used and in order to be conservative, the systematic uncertainty is assessed at 7 %.

In Table 5.8 the uncertainties, related to systematic effects previously described, are reported for ${}^{3}_{\Lambda}\mathrm{H}$ (left) and ${}^{3}_{\Lambda}\overline{\mathrm{H}}$ (right) in all centrality classes. The total systematic uncertainties assigned to the final corrected yield is obtained with a sum in quadrature of the single sources, assuming all of them as uncorrelated.

Systematic uncertainties						
Source	${}^{3}_{\Lambda}\mathrm{H}$			${}^{3}_{\Lambda}\overline{\mathrm{H}}$		
	0–10%	10–30%	30–50%	0–10%	10–30%	30–50%
Cross-section	4.48%	4.48%	4.5%	7%	7.28%	7.5%
Average absorption correction	4.49%	4.5%	4.51%	7.3%	7.5%	7.75%
Efficiency weights	3.1%	2.7%	1.6%	3.2%	2.8%	1.6%
Material budget		1%			1%	
Unknown p_{T}-shape		6.7%			6.5%	
Single track efficiency		7%			7%	
Total	12%	11.9%	11.7%	14.3%	14.4%	14.5%

Table 5.8.: Summary of the systematic uncertainties in the production yields analysis. The total uncertainty assigned in each centrality class is the sum in quadrature of the single sources.

The aforementioned corrections and the systematic uncertainties will be used in the calculation of the production yields of ${}^{3}_{\Lambda}\mathrm{H}$ and ${}^{3}_{\Lambda}\overline{\mathrm{H}}$ in the 2 body decay channel in three centrality classes.

5.2. p_{T} production spectra

The second part of the production analysis concerns the measurement of the p_{T} spectrum of ${}^{3}_{\Lambda}\mathrm{H}$ and ${}^{3}_{\Lambda}\overline{\mathrm{H}}$. Due to the available statistics in semi-central events, the study of the production p_{T} spectra is performed in the 10–40% centrality class. The steps followed to obtain the final result are the same previously described for the measurement of the corrected yields and, for this reason, only the outcomes from each steps are presented in the following.

5.2.1. Raw yields extraction *vs* p_{T}

The raw yields are measured as a function of the p_{T} and they are obtained from the invariant mass distributions of the ${}^{3}_{\Lambda}\mathrm{H}$ and ${}^{3}_{\Lambda}\overline{\mathrm{H}}$. In particular, the p_{T} intervals selected for this analysis are 2-3, 3-4, 4-5 and 5-9 GeV/c. The candidates $({}^{3}_{\Lambda}\overline{\mathrm{H}})^{3}_{\Lambda}\mathrm{H}$ are selected applying the selection criteria previously described and reported in Table 5.9. In this second part of the analysis the candidates are split in narrow p_{T} intervals and this means a lower signal in each of them if compared with the p_{T} integrated analysis (Sec 5.1.1). Thus, in order to increase the statistics, especially in the first p_{T} interval, the selection on the minimum ${}^{3}\mathrm{He}$ p_{T} is of 1.6 GeV/c. On the other hand, the cut on the DCA_{tracks} and on the $\cos(\theta_{pointing})$ are restricted to 0.6 and 0.997 respectively to further reduce the combinatorial background.

Candidate selections		
	${}^{3}_{\Lambda}\mathrm{H}$	${}^{3}_{\Lambda}\overline{\mathrm{H}}$
π p_{T} (GeV/c)	0.2-1.2	0.2-1.2
${}^{3}\mathrm{He}$ p_{T} (GeV/c)	≥ 1.6	≥ 1.6
DCA_{tracks} (cm)	< 0.6	< 0.6
ct (cm)	> 2	> 2
$\cos(\theta_{pointing})$	≥ 0.997	≥ 0.997
$\lvert y \rvert$	≤ 0.5	≤ 0.5

Table 5.9.: Set of cuts applied for the selection of ${}^{3}_{\Lambda}\mathrm{H}$ and ${}^{3}_{\Lambda}\overline{\mathrm{H}}$ candidates in different p_{T} intervals in the 10–40% centrality class.

The invariant mass distribution of the candidates ${}^{3}_{\Lambda}\mathrm{H}$ and ${}^{3}_{\Lambda}\overline{\mathrm{H}}$ in the four p_{T} intervals are shown in Figure 5.10 and 5.11, respectively. The distribution of the ${}^{3}_{\Lambda}\mathrm{H}$ in the 2-3 GeV/c shows a higher combinatorial background if compared to the others. It is mainly due to the contamination of secondary ${}^{3}\mathrm{He}$ produced by knock-out with the material which dominates the low p_{T} region.

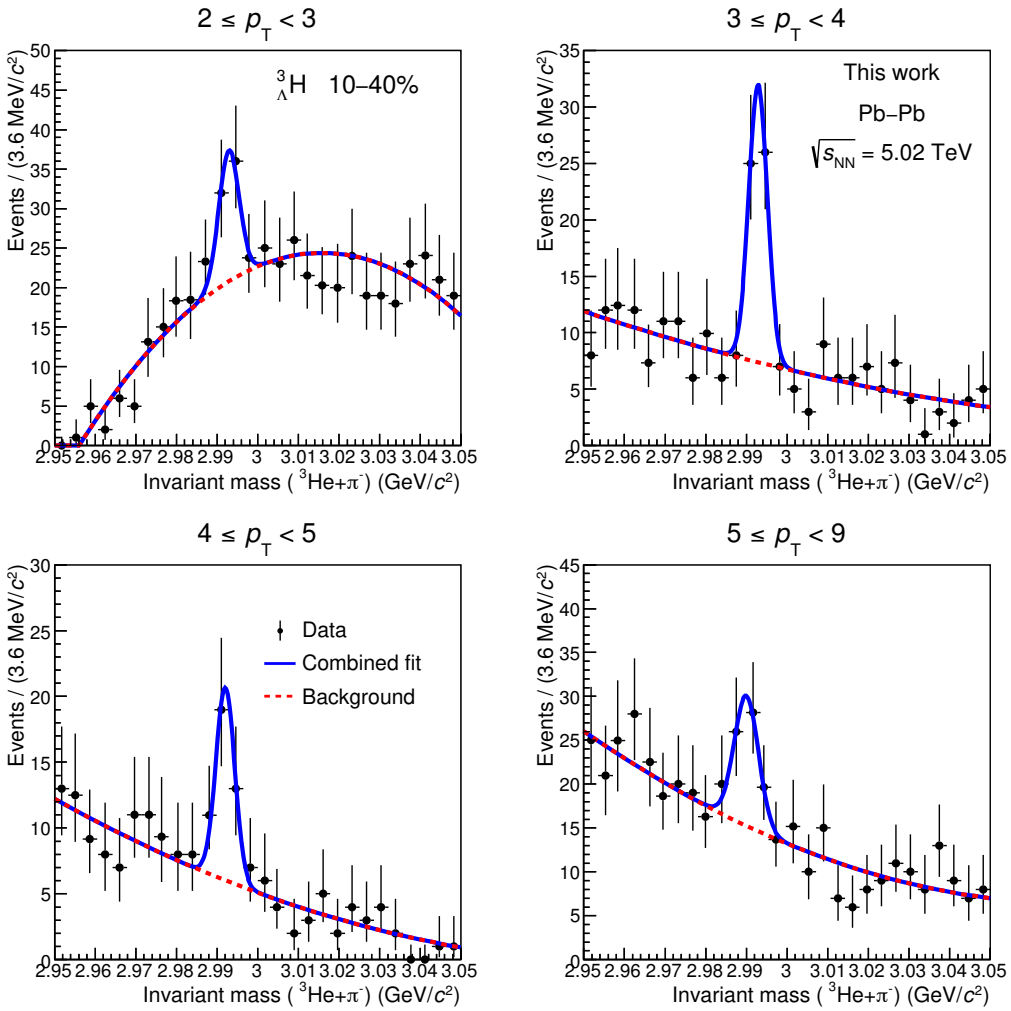

Figure 5.10.: ${}^{3}_{\Lambda}\mathrm{H}$ invariant mass distributions in the four p_{T} intervals. The blue curve is the fitting function and the red dashed curve is the background component.

The raw yield extraction is performed with a fit to the distribution using a combined function (blue curve), that is the sum of a Gaussian for the signal and a second degree polynomial (dashed red curve) for the background. As already introduced in Eq. 5.1, the normalization is kept into account with N_{sig} and N_{bkg}, which represent the raw signal and background counts.

The fit is performed separately for the ${}^{3}_{\Lambda}\mathrm{H}$ and the ${}^{3}_{\Lambda}\overline{\mathrm{H}}$ for the first three p_{T} bins (2-3, 3-4, 4-5 GeV/c). In the last p_{T} interval, instead, the raw yield extraction is performed in two steps because of the low statistics. A first fit is performed to the invariant mass distribution obtained with the sum of ${}^{3}_{\Lambda}\mathrm{H}$ and ${}^{3}_{\Lambda}\overline{\mathrm{H}}$ and the σ from the fit result is used in the second

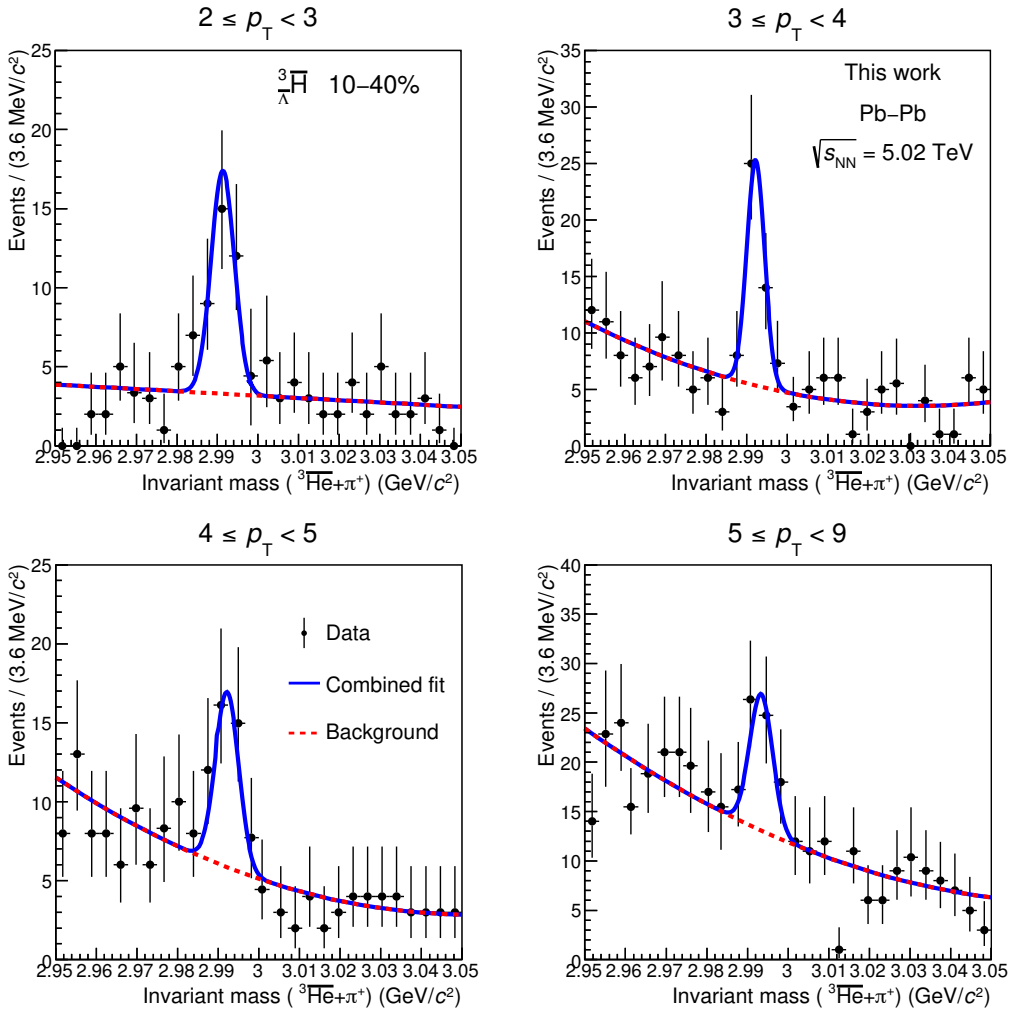

Figure 5.11.: ${}^{3}_{\Lambda}\overline{\mathrm{H}}$ invariant mass distributions in the four p_{T} intervals. The blue curve is the fitting function and the red dashed curve is the background component.

step. Indeed, the fit for the raw yield extraction is performed separately for matter and anti-matter, having fixed the width of the Gaussian to the σ previously found.

The mean values (μ) of the Gaussian obtained from the fits are compared to the experimental mass value measured by ALICE [70] and STAR [56], as shown in Figure 5.12a and Figure 5.12b. The results of the fit as well as the S/B ratio and the significance of the extracted raw yields are reported in Table 5.10 for the ${}^{3}_{\Lambda}\mathrm{H}$ and in Table 5.11 for the ${}^{3}_{\Lambda}\overline{\mathrm{H}}$ for the different p_{T} intervals. The raw yields (S) and the background counts (B) are obtained from the integral, of the respective components of the fitting function, in the invariant mass range $\mu \pm 3\sigma$.

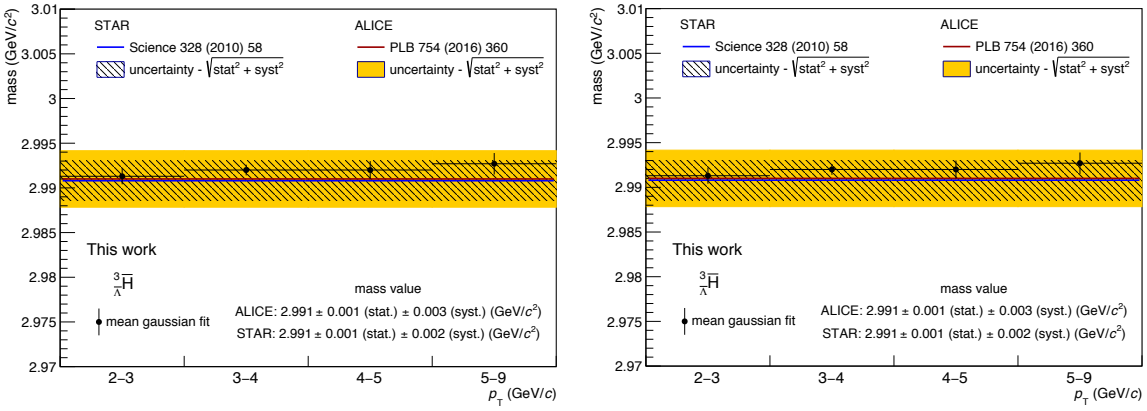

(a) ${}^{3}_{\Lambda}\mathrm{H}$ **(b)** ${}^{3}_{\Lambda}\overline{\mathrm{H}}$

Figure 5.12.: Mean values with their uncertainties obtained from the fit to the ${}^{3}_{\Lambda}\mathrm{H}$ (a) and ${}^{3}_{\Lambda}\overline{\mathrm{H}}$ (b) invariant mass distributions compared with the experimental mass value measured by STAR [56] and ALICE [70].

	${}^{3}_{\Lambda}\mathbf{H}$			
p_{T} (GeV/c)	2-3	3-4	4-5	5-9
mean (GeV/c^2)	2.9929 ± 0.0008	2.9928 ± 0.0005	2.9921 ± 0.0007	2.9902 ± 0.0008
width (GeV/c^2)	0.0025 ± 0.0003	0.0023 ± 0.0004	0.0023 ± 0.0003	0.0029 ± 0.0008
χ^2/NDF	1.74	2.00	1.08	1.09
S/B	0.51	1.80	1.29	0.44
Significance (3σ)	3.11	4.95	3.54	2.69
Raw yield	30 ± 9	30 ± 7	22 ± 6	23 ± 7

Table 5.10.: Results of the fit to the ${}^{3}_{\Lambda}\mathrm{H}$ invariant mass distributions in the four p_{T} intervals. Raw yields are obtained as the integral of the signal function in $\pm 3\sigma$ with respect to the mean value.

5.2.2. Efficiency correction

The efficiency × acceptance distribution is evaluated, as previously described in Sec. 5.1.2, with the ratio of the number of reconstructed $({}^{3}_{\Lambda}\overline{\mathrm{H}})^{3}_{\Lambda}\mathrm{H}$ which satisfies the selections of Table 5.9 and the number of generated $({}^{3}_{\Lambda}\overline{\mathrm{H}})^{3}_{\Lambda}\mathrm{H}$ in the rapidity range $|y| < 0.5$. The distributions are reported with open markers in Figure 5.13a and 5.13b for the ${}^{3}_{\Lambda}\mathrm{H}$ and ${}^{3}_{\Lambda}\overline{\mathrm{H}}$ respectively.

The efficiency × acceptance in the p_{T} intervals used in the analysis is obtained with a weighted average of the distributions in the same p_{T} ranges. The weights are taken from the Blast-Wave distribution obtained from the ${}^{3}\mathrm{He}$ production analysis and the result of

	${}^{3}_{\Lambda}\overline{\mathrm{H}}$			
p_{T} (GeV/c)	2-3	3-4	4-5	5-9
mean (GeV/c^2)	2.9913 $\pm$ 0.0009	2.9922 $\pm$ 0.0006	2.9922 $\pm$ 0.0010	2.9931 $\pm$ 0.0015
width (GeV/c^2)	0.0028 $\pm$ 0.0006	0.0023 $\pm$ 0.0006	0.0028 $\pm$ 0.0005	0.0029 $\pm$ 0.0008
χ^2/NDF	1.87	1.89	1.03	2.86
S/B	1.94	1.73	0.99	0.44
Significance (3σ)	4.26	4.24	3.31	2.45
Raw yield	20 $\pm$ 7	22 $\pm$ 7	21 $\pm$ 6	24 $\pm$ 8

Table 5.11.: Results of the fit to the ${}^{3}_{\Lambda}\overline{\mathrm{H}}$ invariant mass distributions in the four p_{T} intervals. Raw yields are obtained as the integral of the signal function in $\pm 3\sigma$ with respect to the mean value.

the weighted average are reported as histogram in Figure 5.13a and 5.13b. In addition the values of the efficiency in the p_{T} intervals and for the ${}^{3}_{\Lambda}\mathrm{H}$ and the ${}^{3}_{\Lambda}\overline{\mathrm{H}}$ are reported in Table 5.12.

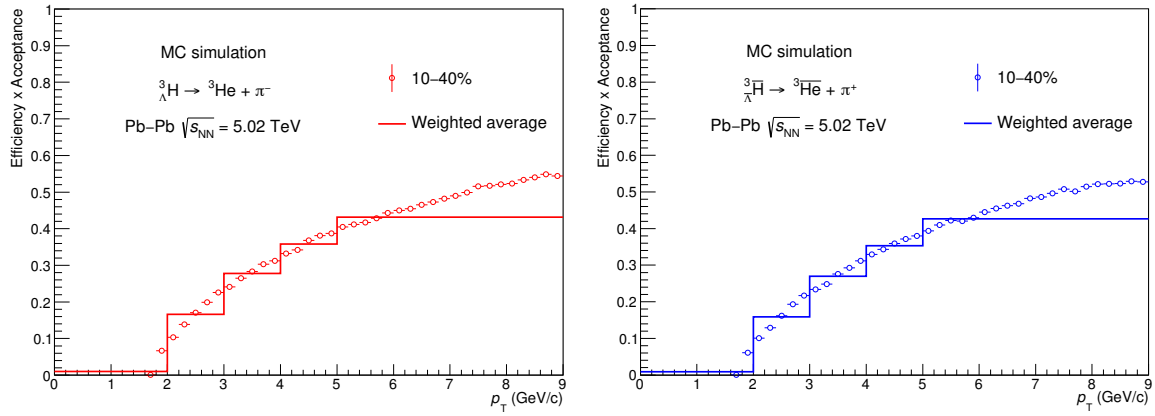

(a) ${}^{3}_{\Lambda}\mathrm{H}$ **(b)** ${}^{3}_{\Lambda}\overline{\mathrm{H}}$

Figure 5.13.: Efficiency $\times$ acceptance distribution (open markers) for the ${}^{3}_{\Lambda}\mathrm{H}$ (a) and the ${}^{3}_{\Lambda}\overline{\mathrm{H}}$ (b). The line represents the efficiency in the p_{T} intervals of this analysis obtained with a weighted average of the distribution.

5.2.3. Absorption correction

The evaluation of the absorption correction is the procedure described in detail in Sec. 5.1.3. In particular, the distribution of the probability to observe $\mathrm{p}_{Observe}$ the ${}^{3}_{\Lambda}\mathrm{H}$ (Figure 5.7a) and

Efficiency × Acceptance				
p_{T} (GeV/c)	2-3	3-4	4-5	5-9
${}^{3}_{\Lambda}\mathrm{H}$	16.6%	27.8%	35.8%	43.1%
${}^{3}_{\Lambda}\overline{\mathrm{H}}$	15.9%	26.9%	35.3%	42.6%

Table 5.12.: Efficiency × acceptance for the ${}^{3}_{\Lambda}\mathrm{H}$ and the ${}^{3}_{\Lambda}\overline{\mathrm{H}}$ obtained with a weighted average in the four analyzed p_{T} intervals.

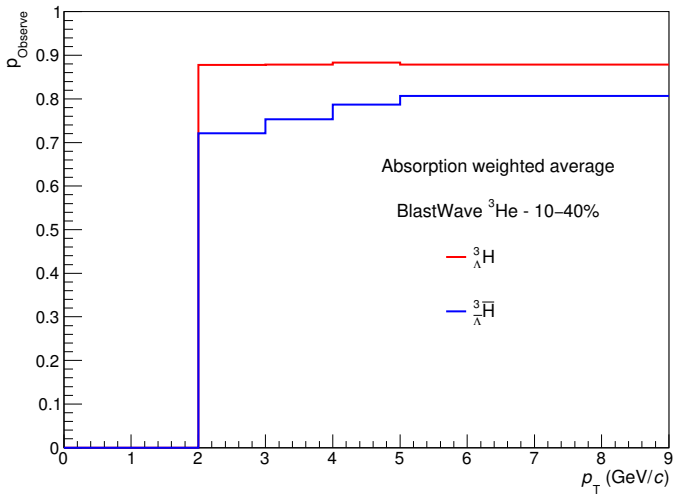

Figure 5.14.: Distribution of the probability to observe the ${}^{3}_{\Lambda}\mathrm{H}$ (red) and the ${}^{3}_{\Lambda}\overline{\mathrm{H}}$ (blue). The values in the p_{T} intervals of this analysis are obtained with a weighted average.

the ${}^{3}_{\Lambda}\overline{\mathrm{H}}$ (Figure 5.7b) are used to evaluate the absorption probability in the p_{T} intervals of this analysis. It is important to remember that these distributions are evaluated as a function of the $(\overline{\mathrm{p}})\mathrm{p}$ p_{T}. Thus, in order to find the corresponding p_{T} interval in these distributions one has to keep in mind that $p_{\mathrm{T}} = p_{\mathrm{T}}^{{}^{3}_{\Lambda}\mathrm{H}}/3$ (e.g. 2-3 $\rightarrow$ 0.66-1 GeV/c).

The probability to observe the $({}^{3}_{\Lambda}\overline{\mathrm{H}})^{3}_{\Lambda}\mathrm{H}$ in the four p_{T} ranges is obtained as weighted average of the distributions, using the ^{3}He Blast-Wave distribution as weight and the results are shown in Figure 5.14. The red line is the probability to observe the ${}^{3}_{\Lambda}\mathrm{H}$, while the blue line is the same probability for the ${}^{3}_{\Lambda}\overline{\mathrm{H}}$. The rise of the distribution of the ${}^{3}_{\Lambda}\overline{\mathrm{H}}$ corresponds to a higher absorption in the low p_{T} region, while this effect is constant for the ${}^{3}_{\Lambda}\mathrm{H}$ as a function of p_{T}. In addition the values of the absorption correction factor are reported in Table 5.13.

Absorption correction				
p_{T} (GeV/c)	2-3	3-4	4-5	5-9
${}^{3}_{\Lambda}\mathrm{H}$	87.8%	87.8%	88.3%	87.8%
${}^{3}_{\Lambda}\overline{\mathrm{H}}$	72.3%	75.3%	78.7%	80.6%

Table 5.13.: Probability to observe the ${}^{3}_{\Lambda}\mathrm{H}$ and the ${}^{3}_{\Lambda}\overline{\mathrm{H}}$ obtained with a weighted average in the four p_{T} intervals.

5.2.4. Systematics uncertainties

The sources of the systematic uncertainty that have been checked in the analysis of the p_{T} production spectra analysis are the same previously introduced and described in detail for the production yields as a function of the collision centrality (see Sec. 5.1.4). The main difference is that in this case the systematics are assessed on the yields in the different p_{T} intervals, while previously they were evaluated directly on the integrated yield. The results of the checks on the different contribution together with the total systematic uncertainty are shown in Figure 5.15a and 5.15b.

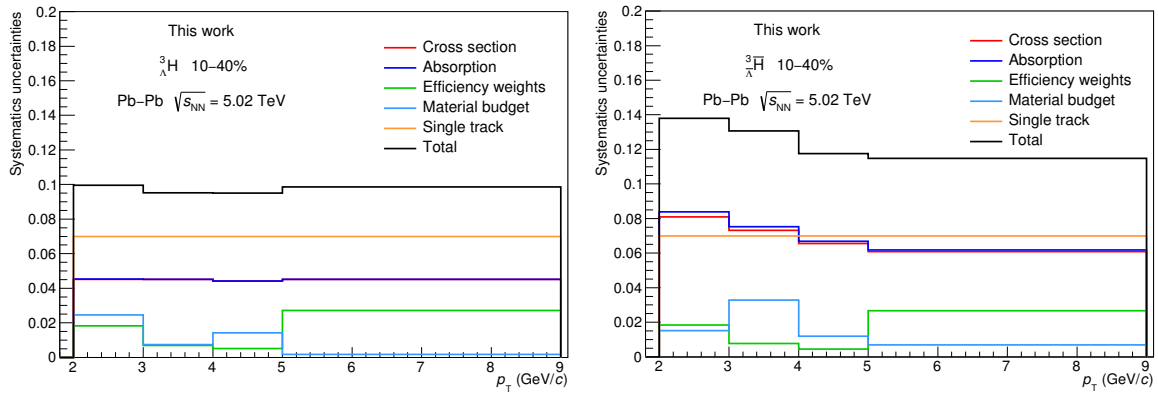

(a) ${}^{3}_{\Lambda}\mathrm{H}$ **(b)** ${}^{3}_{\Lambda}\overline{\mathrm{H}}$

Figure 5.15.: Systematic uncertainties for the ${}^{3}_{\Lambda}\mathrm{H}$ (a) and the ${}^{3}_{\Lambda}\overline{\mathrm{H}}$ (b) as a function of p_{T}. The colored lines are the systematic uncertainties of the single sources, while the black line is the total uncertainty in each p_{T} interval.

The contribution of the absorption correction in the systematic uncertainty is related to the usage of an average correction and to the scale factor applied in the $\sigma_{{}^{3}_{\Lambda}\mathrm{H}}$. The checks give a flat uncertainty at $\sim$4.5 % for the ${}^{3}_{\Lambda}\mathrm{H}$ as a function of p_{T}, while for the ${}^{3}_{\Lambda}\overline{\mathrm{H}}$ it decreases from $\sim$8.3 % at low p_{T} to $\sim$6 % at high p_{T} for both sources. In Figure 5.15a the contribution

of the cross section (red line) and of the absorption (blue line) are overlapped because of they are similar, thus only the blue line is visible.

The systematic uncertainties on the efficiency calculation are evaluated firstly by changing the distributions used as weight in the average and this gives an uncertainty from 0.4 % to 2.6 % both for the ${}^{3}_{\Lambda}$H and the ${}^{3}_{\Lambda}\overline{\mathrm{H}}$. In particular, as shown in Figure 5.15, the higher uncertainty is in the 5-9 p_{T} interval and this is due to the weighted average computation in that range. Indeed, the $({}^{3}_{\Lambda}\overline{\mathrm{H}})^{3}_{\Lambda}$H efficiency distribution is almost flat from 5 to 9 GeV/c, while the weights distribution have large variation from one to another. Thus, the effect of using different functions as weights is a larger systematic uncertainty in that p_{T} interval.

The effect of the uncertainty on the material budget used in the simulation is studied, as already described, using two MC productions with the material budget varied of $\pm 4.5\%$ with respect to the nominal one. Following what previously done and using Eq.5.9 the systematic uncertainty is 1 % for both particle and anti-particle in all the p_{T} ranges.

The criteria applied for the candidates selection are another source inspected in this analysis. The different set of cuts and PID requirements, previously introduced and reported in Tables 5.6 and 5.7, are tested and the Barlow criterion is also used to select variations with a significance larger than 2σ if compared with the value obtained with the nominal cuts. In this case the variable introduced in the Barlow criterion $\Delta\mathrm{Y}/\sigma_{\Delta}$ is calculated for the yield variation in each single p_{T} interval. Figures 5.16a and 5.16b show the trend of the Barlow variable for the different set of cuts and for the different p_{T} intervals, represented with four different colored lines. The same distributions are also studied for the variation on the PID selections and they are reported in Figure 5.16c and 5.16d. The result shows that the variations induced by changing the cuts are within the threshold of ± 2 used in the application of the Barlow criterion. Thus these systematic uncertainties are not included in the total systematic uncertainty. Moreover, the same result is obtained also for the test on the fitting function used for the yield extraction. Indeed, the distribution used for the background component are replaced with a Landau and a third degree polynomial and in both cases the variations are not significantly large to be included in the systematic uncertainties.

The effect related to the single track efficiency has already been introduced in Sec 5.1.4 and, as previously done, the uncertainty is assessed as twice the single tracking efficiency systematic uncertainty (3.5% from [132]), which means 7 % for all p_{T} intervals.

Finally, the unknown p_{T}-shape is an important source of uncertainty. Indeed, the p_{T} spectra are measured in a limited region from to 2 to 9 GeV/c and the integrated yield is obtained with a fit to the measured spectra. As a consequence, the choice of the fit

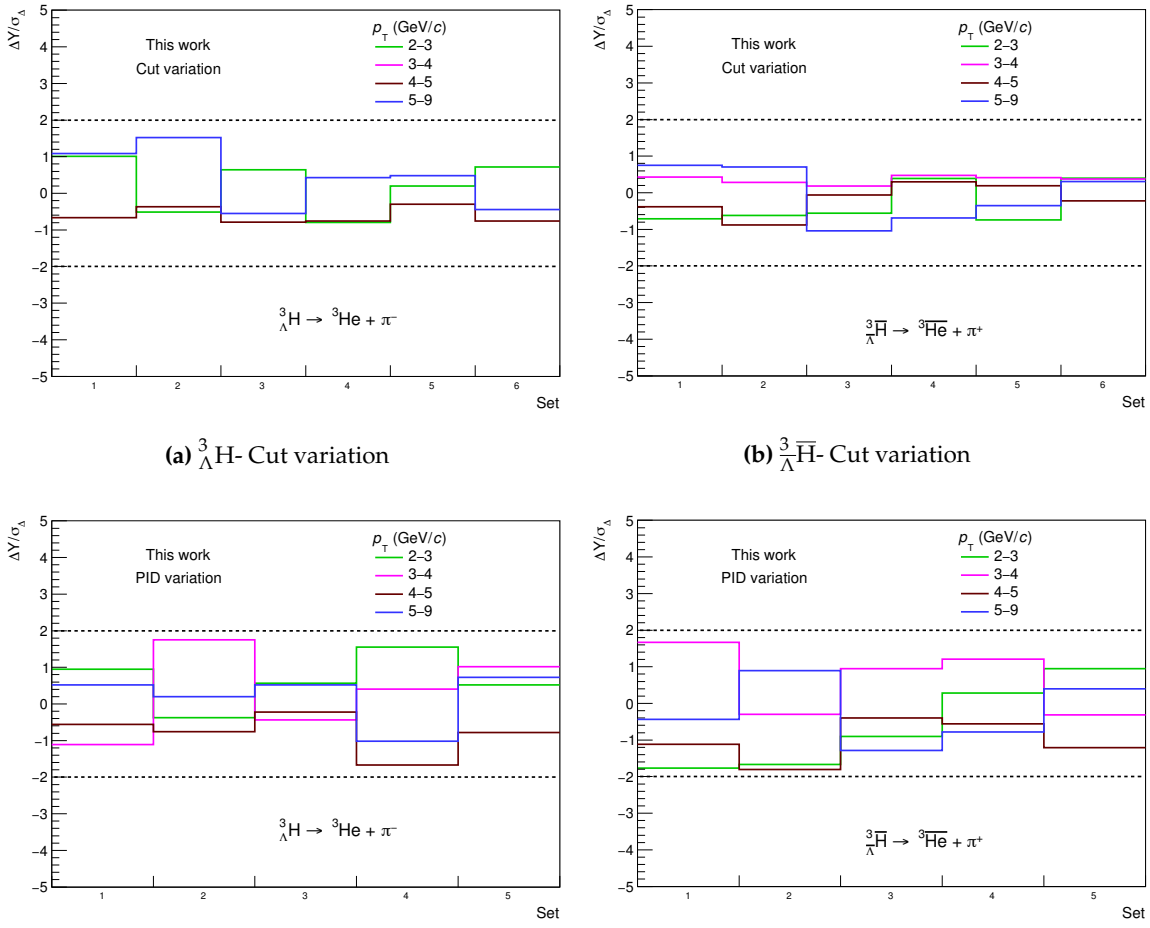

(a) ${}^{3}_{\Lambda}\mathrm{H}$- Cut variation

(b) ${}^{3}_{\Lambda}\overline{\mathrm{H}}$- Cut variation

(c) ${}^{3}_{\Lambda}\mathrm{H}$- PID variation

(d) ${}^{3}_{\Lambda}\overline{\mathrm{H}}$- PID variation

Figure 5.16.: Significance of the difference between the results obtained with nominal selections and those obtained with cuts (top) and PID (bottom) variations. The dashed line at ± 2 corresponds to the minimal threshold required in the *Barlow criterion* to include the variation in the systematic uncertainties.

function plays a crucial role. As it will be shown in Chapter 7, where the results are presented and compared with the theoretical models, the Blast-Wave distribution is used to describe the p_{T} spectra of particles produced in heavy-ion collisions. To check the effect of this choice and to evaluate a systematic uncertainty, the fit is repeated using different distributions: the Blast-Wave distribution with parameters extracted from π,K,p analysis, the Boltzmann function, the $\mathrm{m_T}$-exponential, the simple exponential, the Bose-Einstein and the Fermi-Dirac distributions [2]. When using the Blast-Wave as a fit function the parameters are fixed to those obtained in previous analysis and the reason is that the number of yields

[2] More details on these distributions in Appendix B

in the p_{T} spectra is lower than the number of parameters. For the other functions, instead, a fit with free parameters is performed. However, in order to be more conservative for this estimation, the uncertainty is assessed taking the semi-difference of the maximum and minimum values of the integrals of the distributions in the unmeasured p_{T} regions. This lead to a 6.7% for the ${}^{3}_{\Lambda}\mathrm{H}$ and a 6.5% ${}^{3}_{\Lambda}\overline{\mathrm{H}}$. These uncertainties are directly obtained on the integrated yield, so they will be added only to the total systematic on the integrated yield. Moreover, as previously anticipated, these uncertainties are also assigned to the production yields analysis described in Sec. 5.1.

Systematic uncertainties								
Source	${}^{3}_{\Lambda}\mathrm{H}$				${}^{3}_{\Lambda}\overline{\mathrm{H}}$			
p_{T} GeV/c	2–3	3–4	4–5	5–9	2–3	3–4	4–5	5–9
Cross-section	4.50%	4.51%	4.41%	4.50%	8.1%	7.3%	6.5%	6.1%
Average absorption correction	4.52%	4.52%	4.42%	4.52%	8.3%	7.5%	6.7%	6.2%
Efficiency weights	1.83%	0.7%	0.5%	2.7%	1.83%	0.8%	0.4%	2.6 %
Material budget	1%				1%			
Single track efficiency	7%				7%			
Unknown p_{T}-shape (*on integrated yield*)	6.7%				6.5%			
Total	9.96%	9.52%	9.5%	9.85%	13.8%	13.1%	11.7%	11.4%

Table 5.14.: Summary of the systematic uncertainties in the production yields analysis. The total uncertainty assigned in each p_{T} interval, except the Unknown p_{T}-shape, is the sum in quadrature of the single sources.

The values of the systematic uncertainties in each p_{T} interval are reported in Table 5.14 and the total systematic uncertainty is the sum in quadrature of the single sources. Only the systematic due to the unknown p_{T}-shape is excluded in the total uncertainty of the single p_{T} bin, as it is measured and assigned directly to the integrated yield.

5.3. Corrected yields and spectra

In this section the corrected $\mathrm{d}N/\mathrm{d}y$ in the three centrality classes and the corrected p_{T} spectra are reported. The discussion and the comparison with theoretical models will be presented in Chapter 7.

The $({}^{3}_{\Lambda}\overline{\mathrm{H}})^{3}_{\Lambda}\mathrm{H}$ $\mathrm{d}N/\mathrm{d}y$ are obtained with the following formula:

$$\frac{\mathrm{d}N}{\mathrm{d}y} = \frac{1}{N_{\mathrm{ev}}} \frac{f_{\mathrm{missing}}}{\epsilon \cdot f_{\mathrm{absorption}}} \frac{\mathrm{d}N_{\mathrm{raw}}}{\mathrm{d}y} \tag{5.10}$$

where N_{ev} is the total number of events analysed in each centrality class, ϵ is the acceptance $\times$ efficiency correction, $f_{\mathrm{absorption}}$ is the absorption correction and f_{missing} is the estimated fraction of the total yields in the unmeasured p_{T} regions, since the raw yields are measured in the 2-9 GeV/c interval. The results are reported in Table 5.15

Yields *vs* centrality		
	$\mathrm{d}N/\mathrm{d}y \times$ B.R. $\times 10^{-5}$	
	${}^{3}_{\Lambda}\mathrm{H}$	${}^{3}_{\Lambda}\overline{\mathrm{H}}$
0–10%	$3.50 \pm 0.77(\mathrm{stat.}) \pm 0.42(\mathrm{syst.})$	$3.32 \pm 0.70(\mathrm{stat.}) \pm 0.48(\mathrm{syst.})$
10–30%	$1.31 \pm 0.33(\mathrm{stat.}) \pm 0.17(\mathrm{syst.})$	$1.49 \pm 0.36(\mathrm{stat.}) \pm 0.23(\mathrm{syst.})$
30–50%	$0.83 \pm 0.23(\mathrm{stat.}) \pm 0.10(\mathrm{syst.})$	$0.91 \pm 0.25(\mathrm{stat.}) \pm 0.13(\mathrm{syst.})$

Table 5.15.: Integrated yields per rapidity unit $\mathrm{d}N/\mathrm{d}y$ times the B.R. of the 2 body decay channel, for the ${}^{3}_{\Lambda}\mathrm{H}$ and ${}^{3}_{\Lambda}\overline{\mathrm{H}}$ in the centrality classes analysed of the Pb–Pb collisions at $\sqrt{s_{\mathrm{NN}}}$= 5.02 TeV.

Similarly the $({}^{3}_{\Lambda}\overline{\mathrm{H}})^{3}_{\Lambda}\mathrm{H}$ spectrum is obtained with the following relation:

$$\frac{1}{N_{\mathrm{ev}}} \frac{\mathrm{d}^2N}{\mathrm{d}p_{\mathrm{T}}\mathrm{d}y} = \frac{1}{N_{\mathrm{ev}}} \frac{1}{\epsilon \cdot f_{\mathrm{absorption}}} \frac{\mathrm{d}N_{\mathrm{raw}}}{\mathrm{d}p_{\mathrm{T}}} \tag{5.11}$$

where N_{ev} is the total number of events analysed in the 10–40%, ϵ is the efficiency $\times$ acceptance correction and $f_{\mathrm{absorption}}$ is the absorption correction. The corrected p_{T} spectra of the ${}^{3}_{\Lambda}\mathrm{H}$ (red) and ${}^{3}_{\Lambda}\overline{\mathrm{H}}$ (blue) are shown in Figure 5.17. The ${}^{3}_{\Lambda}\overline{\mathrm{H}}$ p_{T} spectrum is shifted by 0.2 GeV/c for visibility

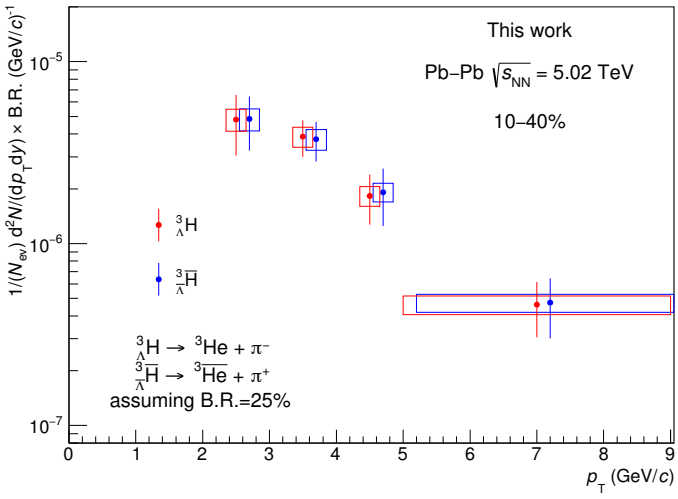

Figure 5.17.: p_{T} spectrum of the ${}^{3}_{\Lambda}\mathrm{H}$ (red) and the ${}^{3}_{\Lambda}\overline{\mathrm{H}}$ (blue) measured in the 10–40% centrality class of Pb–Pb collisions at $\sqrt{s_{\mathrm{NN}}}$= 5.02 TeV.

Chapter 6.

$^{3}_{\Lambda}$H and $^{3}_{\Lambda}\overline{\mathrm{H}}$ lifetime measurement in Pb–Pb collisions

"Omnia aliena sunt tempus tantum nostrum est"
— Lucio Anneo Seneca, 4 (B.C.)– 65

The puzzle on the hypertriton lifetime has been introduced in Chapter 2 and, consequentely, the result of this measurement is extremely important. The hypertriton lifetime is determined with the $^{3}_{\Lambda}$H and $^{3}_{\Lambda}\overline{\mathrm{H}}$ candidates selected in the 2015 statistics of Pb–Pb collisions at $\sqrt{s_{\mathrm{NN}}}$= 5.02 TeV. In particular, assuming the lifetime to be independent of the collision centrality, the events are selected in the 0–90% centrality range and correspond to the total minimum bias events collected by the ALICE experiment.

In this chapter, the different analysis steps as well as the final results are described in details. Two different methods are used to measure the hypertriton lifetime via two body decay channel. The first one is called "dN/dct *spectrum*" and consists in the exponential fit to the corrected yields distribution as a function of ct, as it will be introduced in Sec. 6.1. This is a standard approach and it was used by the ALICE experiment to measure the lifetime in Pb–Pb collisions at $\sqrt{s_{\mathrm{NN}}}$= 2.76 TeV, leading to the result of $\tau = 181^{+54}_{-39}$ (stat.) $\pm$ 33 (syst.) ps [70].

The second method, instead, consists in the unbinned fit to the ct distribution and the lifetime value is obtained with a maximum likelihood estimation, as it will be described in Sec. 6.2.

The first estimate of the $^{3}_{\Lambda}$H lifetime via three body decay channel is obtained with the analysis of the same data sample used for the two body decay channel and will be presented in Sec. 6.4.

Finally, the measured lifetime values will be discussed and compared in Sec.6.5 with all the other experimental results available in literature.

6.1. dN/d(ct) spectrum

The method consists in dividing the selected candidates $^{3}_{\Lambda}$H and $^{3}_{\Lambda}\overline{\mathrm{H}}$ into different ct intervals, extracting the signal, correcting it by means of the efficiency and finally fit the corrected dN/dct spectrum with an exponential function.

6.1.1. Raw yields extraction *vs* ct

The starting point are the raw yields measured as a function of ct and they are obtained from the invariant mass distribution of the $^{3}_{\Lambda}$H and $^{3}_{\Lambda}\overline{\mathrm{H}}$. These candidates are selected by applying the selection criteria introduced in Chapter 4 and reported in Table 6.1. The cuts are the same previously used in the analysis for the measurement of the production yield dN/dy in Sec. 5.1.1 with the exception of the rapidity cut. Previously the corrected production yields were required to be normalized to the rapidity unit, while the lifetime does not depend on the rapidity of the $^{3}_{\Lambda}$H. As a consequence, the candidates are required to lie in the rapidity range $|y| \leq 0.8$, in order to increase the number of selected $^{3}_{\Lambda}$H and $^{3}_{\Lambda}\overline{\mathrm{H}}$.

Candidate selections	
$^{3}_{\Lambda}\mathrm{H} + ^{3}_{\Lambda}\overline{\mathrm{H}}$	
π p_{T} (GeV/c)	0.2-1.2
^{3}He p_{T} (GeV/c)	≥ 1.8
DCA$_{tracks}$ (cm)	< 0.7
ct (cm)	> 2
cos($\theta_{pointing}$)	≥ 0.995
p_{T} (GeV/c)	2–9
$\lvert y \rvert$	≤ 0.8

Table 6.1.: Set of cuts applied for the selection of $^{3}_{\Lambda}$H and $^{3}_{\Lambda}\overline{\mathrm{H}}$ candidates in the different ct intervals. The events are selected in the centrality range 0–90%.

The available candidates are divided in five ct intervals (2-4, 4-7, 7-10, 10-15, 15-28 cm) and the corresponding invariant mass distributions are shown in Figure 6.1. The fitting

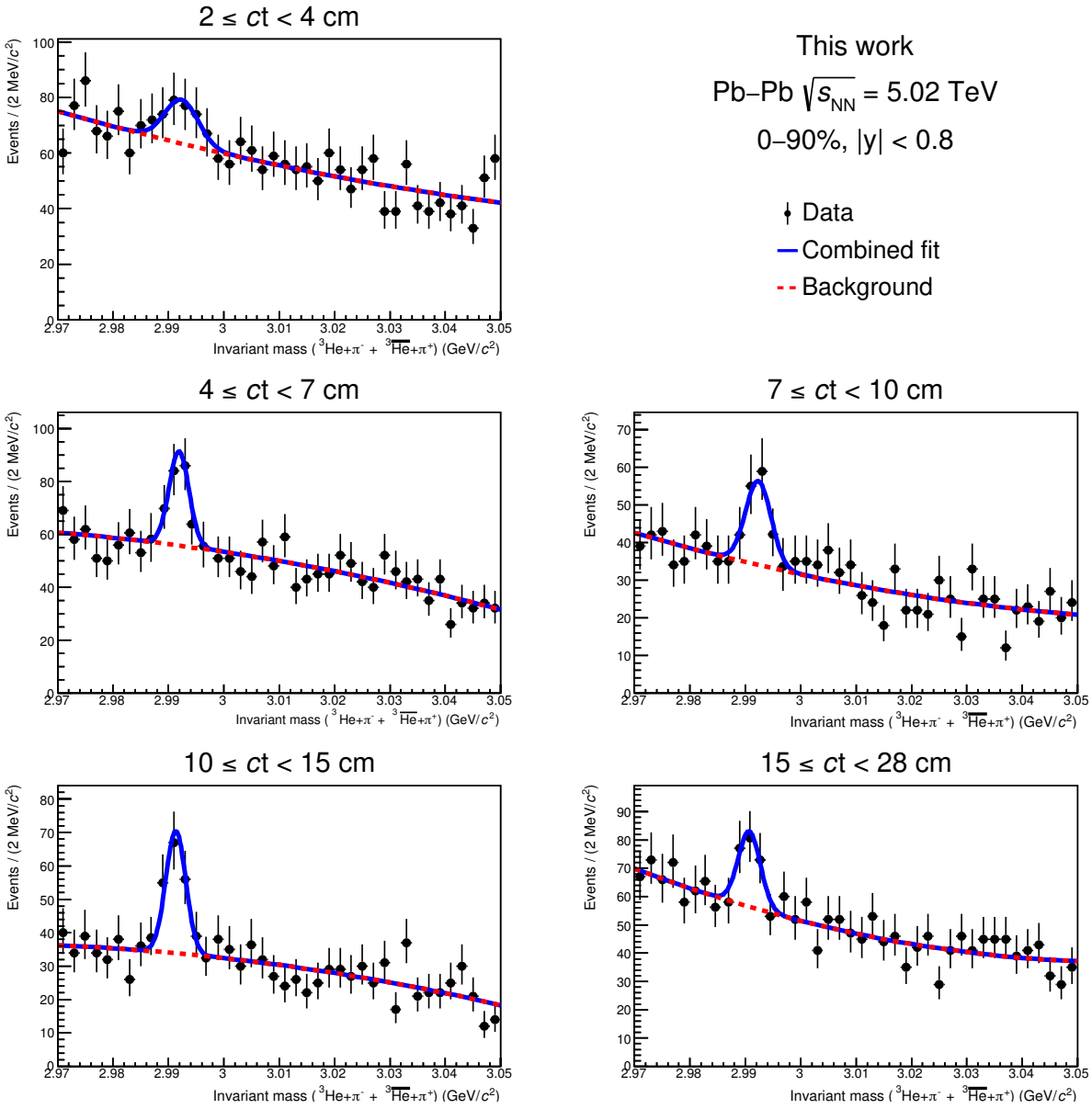

Figure 6.1.: $^{3}_{\Lambda}$H and $^{3}_{\Lambda}\overline{\text{H}}$ invariant mass distribution in 5 ct intervals, with superimposed the fit function (blue line), used to extract the raw yields, and the background component (red dashed line).

function (blue line) is the sum of a Gaussian for the signal and a second degree polynomial for the background (red dashed line) and the normalization is kept into account with N_{sig} and N_{bkg} (see Sec. 5.1.1 Eq. 5.1), which represents the raw signal and background counts. The raw yields are obtained as the integral of the Gaussian in the range $\pm 3\sigma$ scaled for the measured N_{sig}.

The result of the fit in the five ct intervals is reported in Table 6.2. In particular, the first ct bin shows a high background contribution in the invariant mass distribution and this gives a significance lower than 3. Since this would be the first corrected yield of the ct spectrum and, at the same time, the other four ct intervals have a significance larger than 3, it has been decided not to include the 2–4 ct bin in the dN/d(ct).

$^{3}_{\Lambda}$H + $^{3}_{\Lambda}\overline{\mathrm{H}}$					
ct (cm)	2–4	4–7	7–10	10–15	15–28
mean (GeV/c^2)	2.9923 $\pm$ 0.0014	2.9919 $\pm$ 0.0005	2.9920 $\pm$ 0.0006	2.9913 $\pm$ 0.0005	2.9909 $\pm$ 0.0006
width (GeV/c^2)	0.0029 $\pm$ 0.0012	0.0018 $\pm$ 0.0008	0.0021 $\pm$ 0.0006	0.0018 $\pm$ 0.0007	0.0020 $\pm$ 0.0005
χ^2/NDF	1.05	1.38	1.43	1.68	1.06
S/B	0.11	0.26	0.29	0.44	0.19
Significance (3σ)	2.39	3.98	3.77	4.86	3.08
Raw yield	–	73 $\pm$ 17	68 $\pm$ 13	80 $\pm$ 16	59 $\pm$ 16

Table 6.2.: Results of the fit to the $^{3}_{\Lambda}$H invariant mass distributions in the ct intervals . Raw yields are obtained as the integral of the signal function in $\pm 3\sigma$ with respect to the mean value.

Moreover, as done in the production analyses, the measured invariant mass in the different ct intervals is compared with the experimental values measured by the ALICE collaboration [70] and the STAR collaboration [56]. The result of this comparison is shown in Figure 6.2, where the two lines are the experimental mass values measured by ALICE (red line) and STAR (blue line). The two bands correspond to the uncertainties on the mass values, obtained by summing in quadrature the statistical and systematics uncertainties.

6.1.2. Absorption correction

It has already been pointed out that GEANT3 does not take into account any interaction of $^{3}_{\Lambda}$H and $^{3}_{\Lambda}\overline{\mathrm{H}}$ with the material and the approach followed to evaluate the corresponding correction has been described in Chapter 5. In particular, the correction is the probability to observe a $(^{3}_{\Lambda}\overline{\mathrm{H}})^{3}_{\Lambda}$H as a function of the transverse momentum.

Nevertheless, this analysis is performed as a function of ct and the correction has to be included in the corrected spectrum. For this reason a new approach has been developed and is used, the so called "*two-dimensional correction*". The input data in this approach are the probability to observe the $(^{3}_{\Lambda}\overline{\mathrm{H}})^{3}_{\Lambda}$H, previously shown in Figure 5.7, and the number of reconstructed $(^{3}_{\Lambda}\overline{\mathrm{H}})^{3}_{\Lambda}$H as a function of p_{T} and ct, that is the two-dimensional distribution.

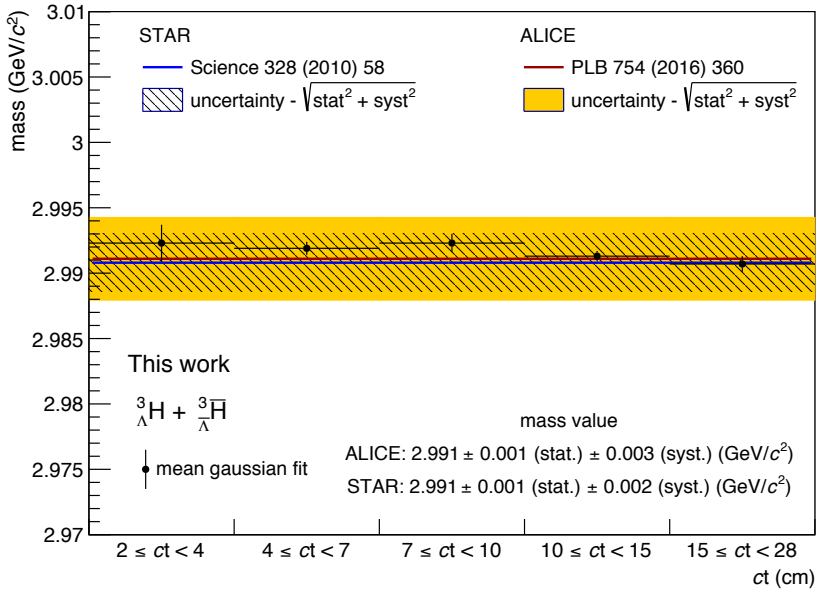

Figure 6.2.: Comparison of the measured mass (black markers) with two experimental reference values measured by ALICE [70] (red line) and STAR [56] (blue line). The bands are the sum in quadrature of statistical and systematics uncertainties.

Then, the entries of each cell in the two-dimensional distribution are corrected with the $\text{p}_{Observe}$ of the corresponding p_{T} following:

$$N^{rec}_{corrected\ for\ absorption}(c\text{t}, p_{\text{T}}) = N^{rec}(c\text{t}, p_{\text{T}}) \cdot \text{p}_{Observe}(p_{\text{T}}^{proton}) \tag{6.1}$$

where one has always to keep in mind that $p_{\text{T}}{}^{proton} = p_{\text{T}}^{^{3}_{\Lambda}\text{H}}/3$.

Figure 6.3 shows a pictorical sketch of the two-dimensional correction approach. The left plot is the probability to observe a $^{3}_{\Lambda}$H as a function of the proton p_{T}, as described in Chapter 5 Sec. 5.1.3, while the right grid represents the two-dimensional distribution of the number of reconstructed $^{3}_{\Lambda}$H as a function of p_{T} and ct. After the correction is applied, the two-dimensional distribution is projected on the ct axis obtaining the number of reconstructed $^{3}_{\Lambda}$H as a function of ct, $\text{N}_{rec}(c\text{t})$. The main difference with respect to the analyses described in Chapter 5, is that the absorption correction is included in the $\text{N}_{rec}(c\text{t})$ used for the efficiency evaluation, while previously it was applied separately to the raw yields in the different p_{T} intervals.

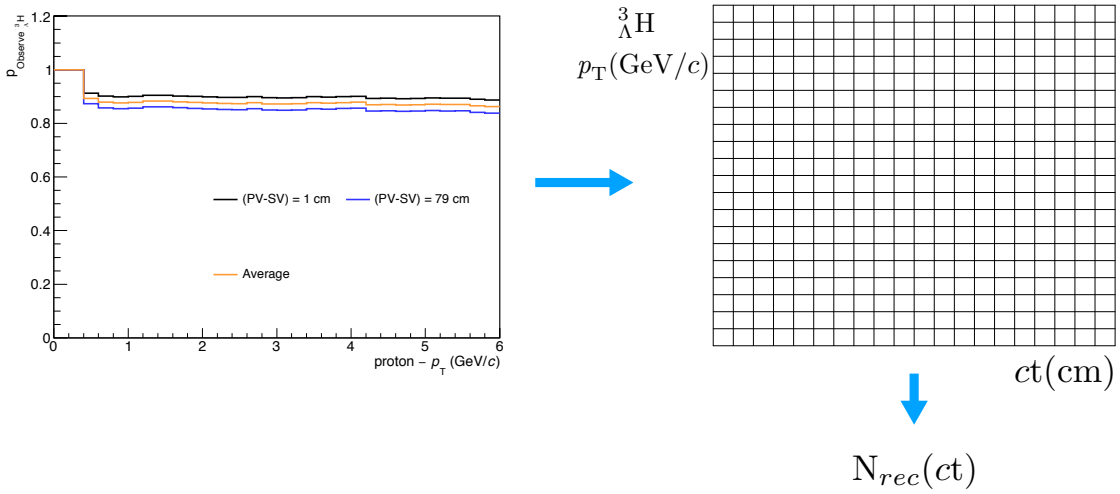

Figure 6.3.: Sketch of the "*two-dimensional approach*" adopted for the correction for absorption in the lifetime analysis.

6.1.3. Efficiency correction

The inefficiencies in the ALICE detectors affect also the raw yields measured as a function of ct, both in the two and three body decay analyses. Thus the correction for the finite efficiency and acceptance is evaluated, as previously described, using a MC simulation and with the following formula:

$$Efficiency \times Acceptance(c\mathrm{t}) = \frac{\mathrm{N}_{rec}(c\mathrm{t})}{\mathrm{N}_{gen}(c\mathrm{t})} \tag{6.2}$$

where N_{gen} is the number of $^{3}_{\Lambda}\overline{\mathrm{H}}$ and $^{3}_{\Lambda}$H generated in the azimuthal region $0 \leq \phi < 2\pi$ and in the rapidity range $|y| < 0.8$, while N_{rec} is the number of $^{3}_{\Lambda}\overline{\mathrm{H}}$ and $^{3}_{\Lambda}$H that satisfy the selection criteria summarised in Table 6.1 and corrected for the absorption, as described in the previous section.

The efficiency $\times$ acceptance is computed using the same ct bins which are used in the raw yields extraction. Figure 6.4 shows the efficiency $\times$ acceptance as a function of ct for $^{3}_{\Lambda}$H (red) and $^{3}_{\Lambda}\overline{\mathrm{H}}$ (blue) separately and for the sum of the two (black).

Efficiency × acceptance				
ct (cm)	4–7	7–10	10–15	15–28
$^{3}_{\Lambda}\text{H} + ^{3}_{\Lambda}\overline{\text{H}}$	31.9 %	32.7 %	35 %	37.3 %

Table 6.3.: Efficiency × acceptance for $^{3}_{\Lambda}$H and $^{3}_{\Lambda}\overline{\text{H}}$ in the four ct intervals.

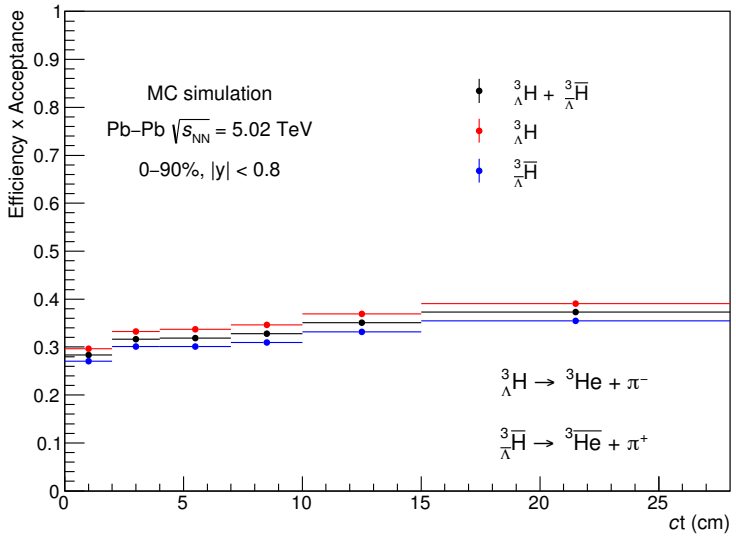

Figure 6.4.: Efficiency × acceptance as a function of ct for $^{3}_{\Lambda}$H (red), $^{3}_{\Lambda}\overline{\text{H}}$ (blue) and $^{3}_{\Lambda}\text{H} + ^{3}_{\Lambda}\overline{\text{H}}$ (black). The same ct intervals selected for the raw yields extraction are used.

The efficiency for the $^{3}_{\Lambda}$H is slightly higher than the one for the $^{3}_{\Lambda}\overline{\text{H}}$ and this is due to the application of the absorption correction, which is larger for the antimatter than for the matter. However, the efficiency used to correct the $\mathrm{d}N/\mathrm{d}(c\mathrm{t})$ spectrum is the one represented with black markers, where the number of reconstructed $^{3}_{\Lambda}$H and $^{3}_{\Lambda}\overline{\text{H}}$ are evaluated separately in order to apply the corresponding absorption correction. Then, they are summed ($^{3}_{\Lambda}\text{H} + ^{3}_{\Lambda}\overline{\text{H}}$) and divided for the total number of generated $^{3}_{\Lambda}$H and $^{3}_{\Lambda}\overline{\text{H}}$, obtaining the efficiency distribution. The values of the efficiency in the ct intervals used for the $\mathrm{d}N/\mathrm{d}(c\mathrm{t})$ spectrum are reported in Table 6.3.

6.1.4. Systematics uncertainties

Also in the analysis for the lifetime measurement is important to check if and how the results are affected by systematics uncertainties. The main sources are similar to those intro-

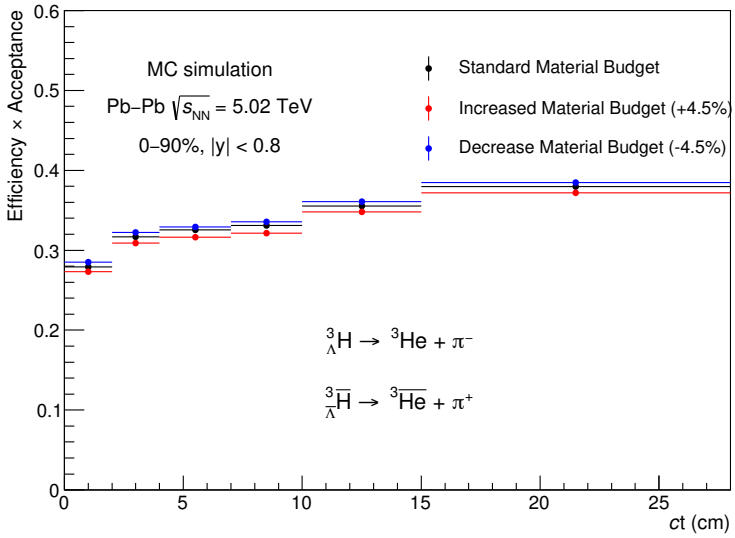

Figure 6.5.: Efficiency $\times$ acceptance as a function of ct for $^{3}_{\Lambda}$H and $^{3}_{\Lambda}\overline{\mathrm{H}}$ using the MC simulation with nominal (black), increased (red) and decreased (blue) material budget.

duced in Sec. 5.1.4 with the only exclusion of those related to p_{T}-shape. The corresponding evaluation can be classified in three groups:

1. the absorption correction, done by varying the assumption on the $(^{3}_{\Lambda}\overline{\mathrm{H}})^{3}_{\Lambda}$H cross-section and using the $\mathrm{p}_{Observe}$ distributions of different (PV-SV) distance;

2. the efficiency $\times$ acceptance, performed taking into account the uncertainty on the material budget;

3. the selections criteria for the candidates and on the raw yield extraction;

The absorption correction, described in Sec. 5.1.3, is the average between the two limiting cases of an $^{3}_{\Lambda}$H which decays in the beam pipe (PV-SV = 1 cm) and close to the TPC (PV-SV = 79 cm). The systematic from this assumption is evaluated by using the $\mathrm{p}_{Observe}$ of the two extreme cases, instead of the average. The efficiency $\times$ acceptance is evaluated in the two different cases and the systematics is assigned as the semi-difference between the two efficiencies, leading to an uncertainty of $\sim$ 3.6% for all ct intervals.

The other source which leads to systematic uncertainty is the scale factor applied in the $\sigma_{^{3}_{\Lambda}\mathrm{H}} = 1.5 \cdot \sigma_{^{3}\mathrm{He}}$. As previously done, the systematic is evaluated by varying the scale factor to 1 and to 2. The efficiency is calculated in these two cases and the systematic uncertainty is the semi-difference between the two cases, which leads to a $\sim$ 3.5% for all ct intervals.

The second source of systematic is related to possible discrepancies in the evaluated reconstruction efficiency due to the uncertainty on the material budget. This check is done using two MC productions already introduced in Chapter 4 Sec. 4.1, where the material budget has been increased and decreased by 4.5%, respectively. The efficiencies are evaluated with these simulations and they are shown in Figure 6.5, together with the efficiency obtained with the standard material budget. A trend with the material budget is visible in each ct interval, as already observed as a function of p_{T}. The variations in the efficiency $\times$ acceptance induced by changing the material distribution are supposed to follow a uniform distribution and, for this reason, the uncertainty is estimated as the RMS of a flat distribution. The uncertainty estimation lies between 0.7% and 0.9% in the analysed ct range and it has been decided to assign a systematic uncertainty for the material budget of 1% in each ct bin.

The selection criteria, like topological cuts and PID, applied to the candidates could induce systematic effects on the signal extraction. Thus, these selections have been varied, as reported in Table 6.4 for the cuts and Table 6.5 for the PID.

Candidate selection variations - systematics									
	Set 0	Set 1	Set 2	Set 3	Set 4	Set 5	Set 6	Set 7	Set 8
^{3}He p_{T} (GeV/c) $\geq$	1.8	1.8	1.8	1.6	1.6	1.6	1.9	1.9	1.9
DCA$_{tracks}$ (cm) <	0.7	0.5	0.8	0.7	0.5	0.8	0.5	0.7	0.8
cos($\theta_{pointing}$) $\geq$	0.995	0.997	0.992	0.992	0.997	0.992	0.995	0.997	0.992

Table 6.4.: Different sets of cuts used to study the systematics from candidates selection criteria

PID variations - systematics										
		Set 0	Set 1	Set 2	Set 3	Set 4	Set 5	Set 6	Set 7	Set 8
π	$\lvert n\sigma_{\pi} \rvert \leq$	3	2	2	2	2	2	2	3	3
^{3}He	$\lvert n\sigma_{^{3}\text{He}} \rvert \leq$	3	3	3	2.5	2	2	4	4	4
	$n\sigma_{^{3}\text{H}} >$	0	0	3	3	3	6	6	6	3

Table 6.5.: Different sets of number of σs used to identify the $^{3}_{\Lambda}$H and $^{3}_{\Lambda}\overline{\text{H}}$ daughters

For each of these selections the complete analysis is repeated *ab initio*. The result of each analysis is compared with the one of the reference analysis and, also in this case, the Barlow criterion is applied. As previously introduced in Chapter 5 Sec. 5.1.4, the variable used in the test $\Delta Y/\sigma_{\Delta}$ is evaluated for each set of cuts and only those variations with a significance larger than 2 are included in the systematic uncertainties. Figure 6.6a and 6.6b

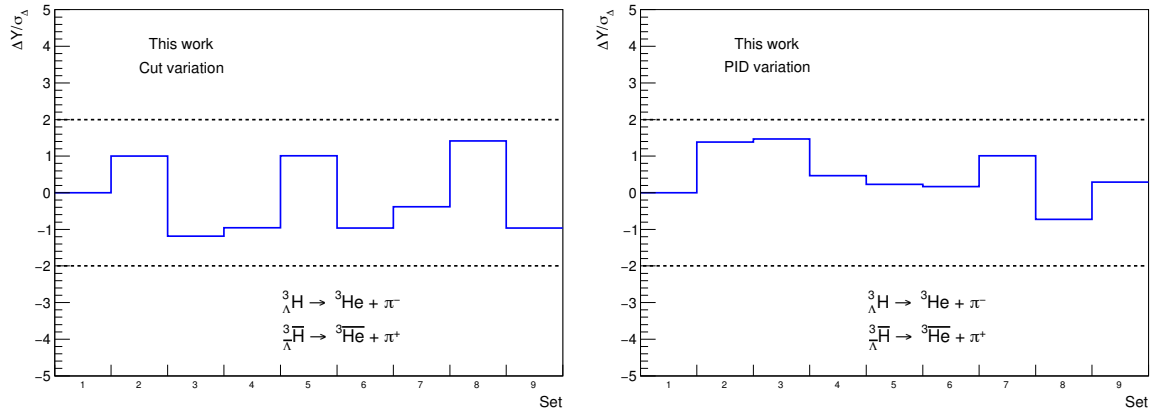

(a) Cut variation **(b)** PID

Figure 6.6.: Significance of the difference between the results obtained with nominal selections and those obtained with cuts (left) and PID (right) variations. The dashed line at ± 2 corresponds to the minimal threshold required in the *Barlow criterion* to include the variation in the systematic uncertainties.

show the results of the Barlow test variable for the different set of cuts and PID selections, respectively. The variations have a significance below the threshold ($\pm$ 2) and for this reason they are not included in the systematic uncertainties.

Finally, the last systematic effect on the tracking efficiency is related to the fact that it is not known to which extent the simulation reproduces the reality. Thus the efficiency calculation can be a source of systematic uncertainty. As already described in the previous Chapter, this effect has been estimated by the ALICE experiment in Pb–Pb collisions and the resulting uncertainty is 3.5% on each single track. Since the $^{3}_{\Lambda}$H has two daughters tracks and in order to be conservative, the systematic uncertainty is assessed at 7%.

The total systematic uncertainty in each ct bin is assigned with the sum in quadrature of the single contributions. The summary of the systematic uncertainties is reported in Table 6.6 and is shown in Figure 6.7.

These systematics uncertainties are assigned to the yields in the different ct bins and then they have to be propagated to the lifetime value τ, as will be described in Sec. 6.3

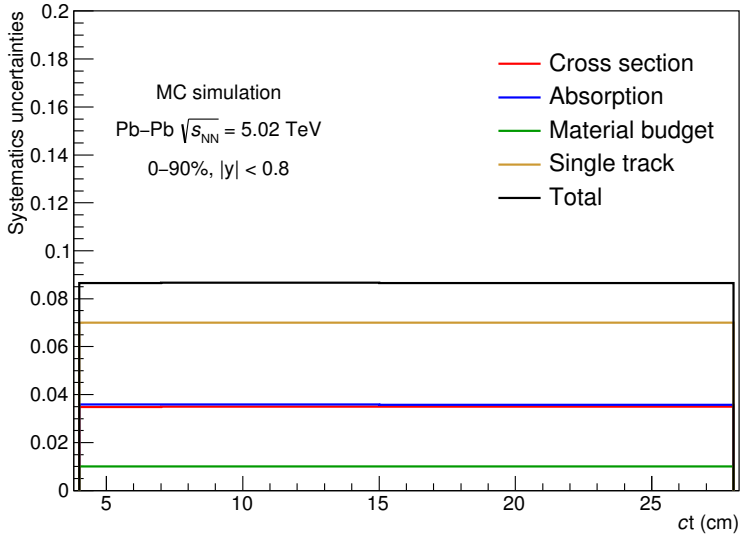

Figure 6.7.: Systematic uncertainties as a function of *c*t. The colored lines are the the single sources contribution, while the black lines is the total uncertainty in each *c*t interval, sum in quadrature of the single ones.

Systematic uncertainties				
Source	*c*t (cm)			
	4–7	7–10	10–15	15–28
Cross-section	3.49%	3.50%	3.49%	3.49%
Average absorption correction	3.58%	3.59%	3.58%	3.58%
Material budget	1%			
Single track efficiency	7%			
Total	8.7%	8.8%	8.7%	8.8%

Table 6.6.: Summary of the systematic uncertainties in the *c*t intervals used in the lifetime analysis. The total uncertainty assigned in each *c*t interval is the sum in quadrature of the single sources.

6.2. Unbinned fit

The second approach used to measure the $(^{3}_{\Lambda}\overline{\text{H}})^{3}_{\Lambda}\text{H}$ lifetime is the unbinned fit to the two-dimensional distribution as a function of the *invariant mass* and of the *c*t. The procedure can be divided in three steps:

- fit to the *c*t-integrated invariant mass distribution;

- tuning the function for the uncorrelated *c*t background;
- fit to the *c*t distribution.

In the following, the different steps will be described, highlighting the important aspects of each of them. The statistical tools used for this method are provided by the ROOT [115] and ROOFIT [133] software packages.

This method was tested re-performing the analysis on the data sample of Pb–Pb collisions at $\sqrt{s_{\text{NN}}}$= 2.76 TeV collected in 2011. The lifetime measured with the new method is $\tau = 182^{+44}_{-36} \pm 35$ ps [134] which is in agreement with the published results [70] on the same dataset, that is $\tau = 181^{+54}_{-39} \pm 33$ ps.

6.2.1. Invariant mass distribution

The starting point is the selection of the $^{3}_{\Lambda}$H and $^{3}_{\Lambda}\overline{\text{H}}$ candidates done by applying the same cuts previously introduced and reported in Table 6.1. The resulting two-dimensional distribution of the selected candidates is shown in Figure 6.8

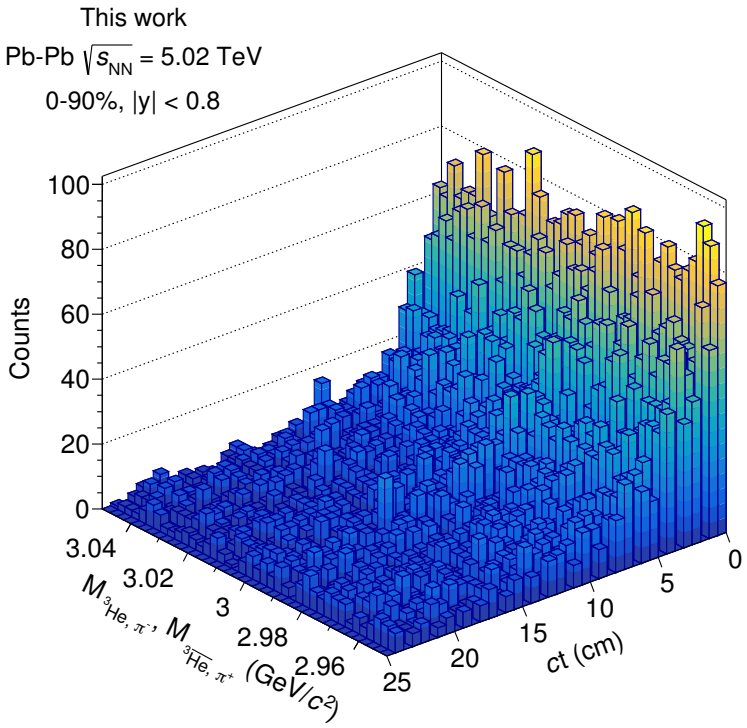

Figure 6.8.: Two-dimensional distribution of the $^{3}_{\Lambda}$H and $^{3}_{\Lambda}\overline{\text{H}}$ selected candidates.

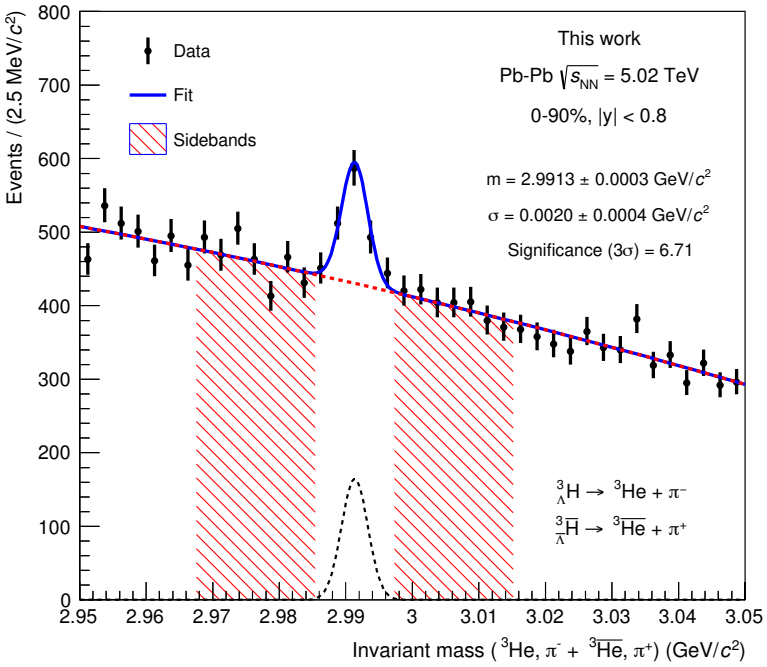

Figure 6.9.: $^{3}_{\Lambda}$H and $^{3}_{\Lambda}\overline{\text{H}}$ invariant mass distribution with superimposed the total fit function (blue line), the background (red dashed line) and the signal (black dashed line) components. The central white region is the signal range, defined as (-3σ,+3σ), while the red lined regions are the sidebands, defined as (-9σ,-3σ) and (+3σ,+9σ).

The fit to the *c*t-integrated invariant mass distribution is performed with a probability density function (p.d.f.) that is:

$$\text{p.d.f.}(m) = \text{N}_{sig} \cdot \text{p.d.f.}_{sig}(m|\mu,\sigma) + \text{N}_{bkg} \cdot \text{p.d.f.}_{bkg}(m|a_i) \tag{6.3}$$

where p.d.f.$_{sig}$ is the Gaussian for the signal and p.d.f.$_{bkg}$ is a second degree polynomial for the background, while N$_{sig}$ and N$_{bkg}$ are the normalization factors of the two p.d.f.. From the fit function the σ and the mean value μ of the Gaussian are extracted and they allow us to define two regions: the *signal* region, defined as $\mu \pm 3\sigma$, and two *sidebands*, defined as (-9σ, -3σ) and (+3σ, +9σ) with respect to the mean value. Then, N$_{sig}$ and N$_{bkg}$ are rescaled for the integral of the corresponding p.d.f. in the signal region, obtaining the signal and background counts in the aforementioned region.

Figure 6.9 shows the invariant mass distribution integrated in the analysed *c*t range. The blue line represents the total p.d.f. (Eq. 6.3) used in the fit, while the red and black dashed lines are the background and the signal components, respectively. The mass extracted from the fit is 2.9913 $\pm$ 0.0003 GeV/c^2 and it is in agreement with experimental

values measured by the ALICE [70] and the STAR [56] experiments. Moreover, the σ of the Gaussian is 0.0020 ± 0.0004 GeV/c^2, which is compatible with the width measured in the different ct intervals of the previous analysis (see Sec. 6.1.1). The central white area corresponds to the signal region which goes from 2.9853 to 2.9973 GeV/c^2, while the two red lined areas are the sidebands, which correspond to the ranges 2.9733–2.9853 GeV/c^2 on the left and 2.9973–3.0093 GeV/c^2 on the right.

6.2.2. Background tuning

The second step of the procedure consists in fitting the ct distribution of the background in the sidebands. The uncorrelated ct background is considered before performing the fit in the signal region for the lifetime estimate and assuming that it follows the same distribution also therein.

The background is modeled with a function which is the sum of two exponential p.d.f.:

$$\text{p.d.f.}_{Tot,Bkg}(c\text{t}) = \text{p.d.f.}_{Bkg,1}(c\text{t}) + \text{p.d.f.}_{Bkg,2}(c\text{t}) \tag{6.4}$$

with

$$\text{p.d.f.}_{Bkg,1}(c\text{t}) = \text{N}_{Bkg,1} \cdot e^{-\frac{\text{t}}{\tau_{b1}}} \qquad \text{p.d.f.}_{Bkg,2}(c\text{t}) = \text{N}_{Bkg,2} \cdot e^{-\frac{\text{t}}{\tau_{b2}}} \tag{6.5}$$

where $\text{N}_{Bkg,1}$ and $\text{N}_{Bkg,2}$ are the normalization constants to take in account the background counts in the sidebands, while τ_{b1} and τ_{b2} are the time constants of the two exponential functions. The results of the fit in the sidebands is shown in Figure 6.10, where the black histogram represents the fit function $\text{p.d.f.}_{Tot,Bkg}$ while the red markers is the ct distribution in the sidebands. The ROOFIT package allows to perform a simultaneous fit to this distribution in the two regions used for the background parameterization and the result of the fit, namely τ_{b1} and τ_{b2}, is used to describe the background in the signal region.

6.2.3. Signal ct distribution

The lifetime estimate is done by performing the unbinned fit to the ct distribution in the signal region. In this case the total p.d.f. used for the fit is the sum of the two background exponentials (Eq. 6.5) normalized to the background counts in the signal range N_{bkg}, and the exponential p.d.f. for the signal, defined as:

$$\text{p.d.f.}_{Signal}(c\text{t}) = \text{N}_{sig} \cdot e^{-\frac{c\text{t}}{c\tau}} \tag{6.6}$$

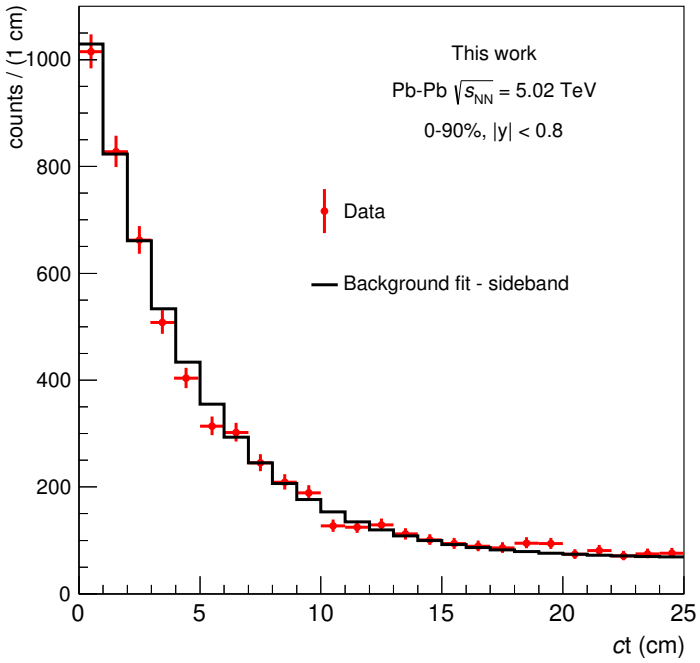

Figure 6.10.: *c*t distribution of the uncorrelated background in the sidebands. The black histogram represents the fit function used to model the background.

where τ is the $^{3}_{\Lambda}$H lifetime to be estimated and N_{sig} are the signal counts obtained from the fit to the invariant mass and normalized to the integral of the fit function in the signal range.

The signal p.d.f. needs to be corrected for the efficiency $\times$ acceptance of the detector before performing the fit. The efficiency for the $^{3}_{\Lambda}$H and $^{3}_{\Lambda}\overline{\text{H}}$ reconstruction is evaluated following the same procedure discussed in Sec. 6.1.3. In particular, the absorption correction is included in the efficiency distribution as explained therein. However, since the *c*t distribution is unbinned, the efficiency $\times$ acceptance correction can not be applied to correct the data but it can be used to scale the p.d.f.$_{Signal}(c\text{t})$. Indeed, the observed decay signal p.d.f. can be seen as the product of the p.d.f.$_{Signal}(c\text{t})$ and the efficiency function. For this reason, the efficiency $\times$ acceptance distribution, shown in Figure 6.11, is parametrized with the following piecewise polynomial:

$$Efficiency \times Acceptance(c\text{t}) = \begin{cases} p_0 + p_1 e^{p_2 \cdot c\text{t}}, & c\text{t} < 4.8 \text{ cm} \\ p_3 + p_4 \cdot c\text{t}, & c\text{t} \geq 4.8 \text{ cm} \end{cases} \tag{6.7}$$

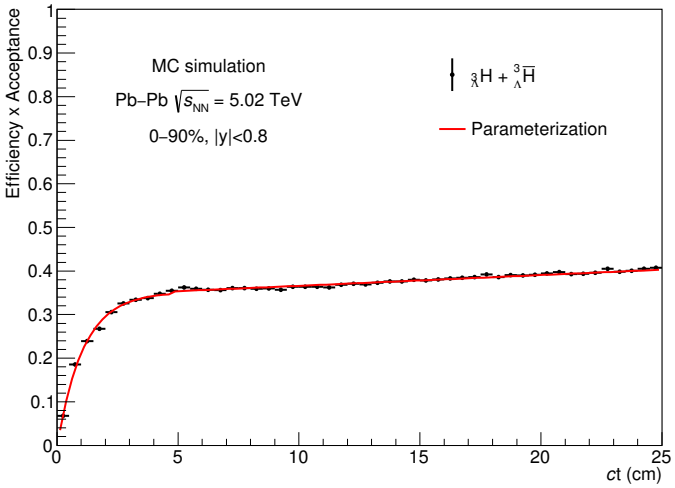

Figure 6.11.: Efficiency $\times$ acceptance as a function of ct for $^{3}_{\Lambda}$H and $^{3}_{\Lambda}\overline{\text{H}}$ with superimposed the piecewise polynomial parameterization (red line) defined in Eq. 6.7 and used for the correction.

Several different functions have been tried, however they exhibited a common behaviour by returning negative values for small values of ct, thus not reproducing properly the efficiency $\times$ acceptance. This issue has been solved using a piecewise polynomial, where the anchor point at 4.8 cm, obtained after several trials, guarantees the continuity between the two pieces.

Then, the p.d.f.$_{Signal}(c\text{t})$ is corrected with this parameterization, obtaining:

$$\text{p.d.f.}^{Observed}_{Signal}(c\text{t}) = \text{p.d.f.}_{Signal}(c\text{t}) \cdot Efficiency \times Acceptance(c\text{t}) \tag{6.8}$$

where p.d.f.$^{Observed}_{Signal}(c\text{t})$ is the signal component used in the total fit function for the lifetime estimate.

Finally, after tuning the background p.d.f. and correcting the signal p.d.f., the unbinned maximum-likelihood estimate (MLE) fit to the ct distribution is performed in the signal range.

The result of the fit is shown in Figure 6.12 and 6.13. Figure 6.12 shows the ct distribution (red markers) in the signal region, the total p.d.f. and the observed p.d.f.$_{Signal}$ used in the unbinned fit, represented with a black and a blue histogram, respectively. The total p.d.f. well describes the ct distribution as also indicated by the χ^2/NDF = 1.003. The drop of the blue histogram for ct < 2 cm is due to the convolution of the p.d.f.$_{Signal}$ with the efficiency $\times$ acceptance, which is low for small ct and then it increases. Figure 6.13 shows

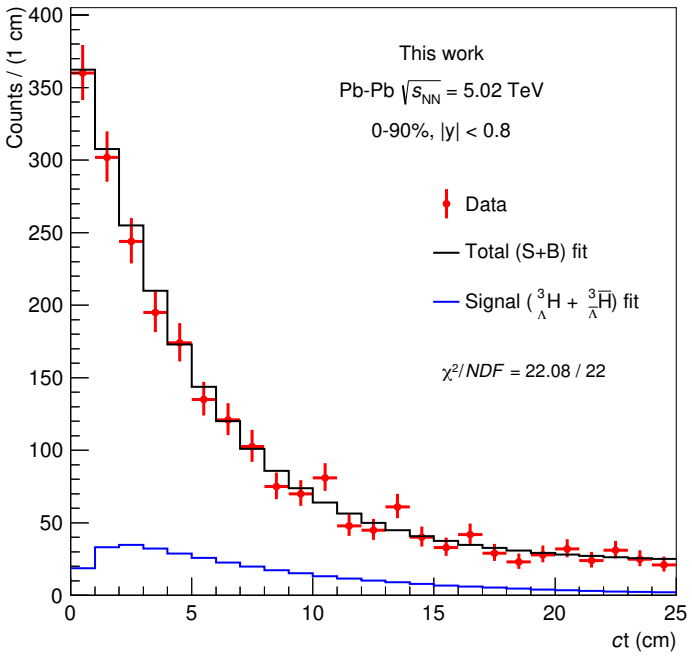

Figure 6.12.: ct distribution (red markers) in the signal region with superimposed the total fit function, as a black histogram, and the exponential distribution of the $^{3}_{\Lambda}$H and $^{3}_{\Lambda}\overline{\text{H}}$ signal as a blue histogram.

the three-dimensional representation of the unbinned fit procedure. Indeed, the "invariant mass vs ct" distribution of the candidates $^{3}_{\Lambda}$H and $^{3}_{\Lambda}\overline{\text{H}}$, is covered with a cyan surface which is the product of the p.d.f. used for the invariant mass and the ct distribution fits. Looking the ct distribution at the $^{3}_{\Lambda}$H mass, it is visible an enhancement of the surface, that is the exponential p.d.f. of the signal.

The lifetime value as well as the method used for the statistical uncertainty estimate will be presented and discussed in Sec. 6.3, together with the result from the analysis of the $\mathrm{d}N/\mathrm{d}(c\mathrm{t})$.

6.2.4. Systematic uncertainties

The possible sources of systematic uncertainties for the analysis performed with the unbinned fit method, are the same previously introduced in Sec. 6.1.4. The same approach for the evaluation of the different sources is adopted also here, the only major difference is that in this case the uncertainty is evaluated directly on the lifetime value τ.

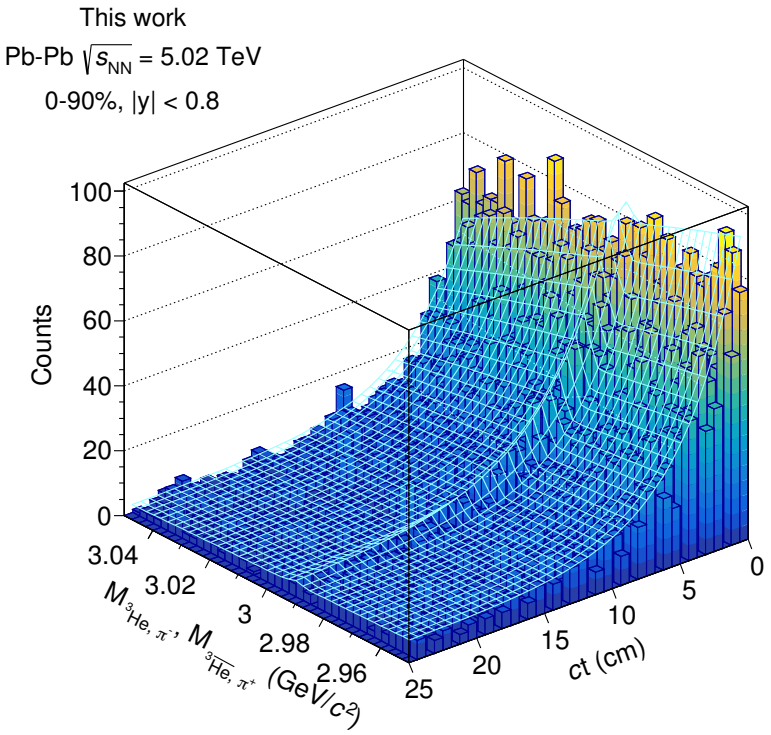

Figure 6.13.: three-dimensional representation of the unbinned fit result. The cyan surface is the product of the p.d.f. used for the invariant mass and the *c*t distribution fits.

The absorption has two main sources related to the scale factor used in the $\sigma_{^3_\Lambda\text{H}}$ and to the fact that an average $\text{p}_{Observe}$ between two limiting cases have been used. As already shown, these assumptions are varied using different scale factors, for the first source, and using the $\text{p}_{Observe}$ evaluated for different distances between primary and secondary vertex. The results of these checks lead to an uncertainty of 3.4% and 3.5% for the two absorption sources, respectively.

The second source is due to possible discrepancies in the evaluated reconstruction efficiency due to the uncertainty on the material budget which is evaluated with two dedicated MC simulations. Thus, the uncertainty is assessed as the RMS of a flat distribution (see Sec. 6.1.4) and it lies between 0.6% and 0.9% in the analysed *c*t range. Consequently, it has been decided to assign a systematic uncertainty of 1% for the material budget to the lifetime value.

The topological cuts and the PID selections criteria are also investigated as possible source of systematic uncertainty. These selections have been varied following the same variations reported in Table 6.4 for the cuts and 6.5 for the PID. For each of these set of cuts

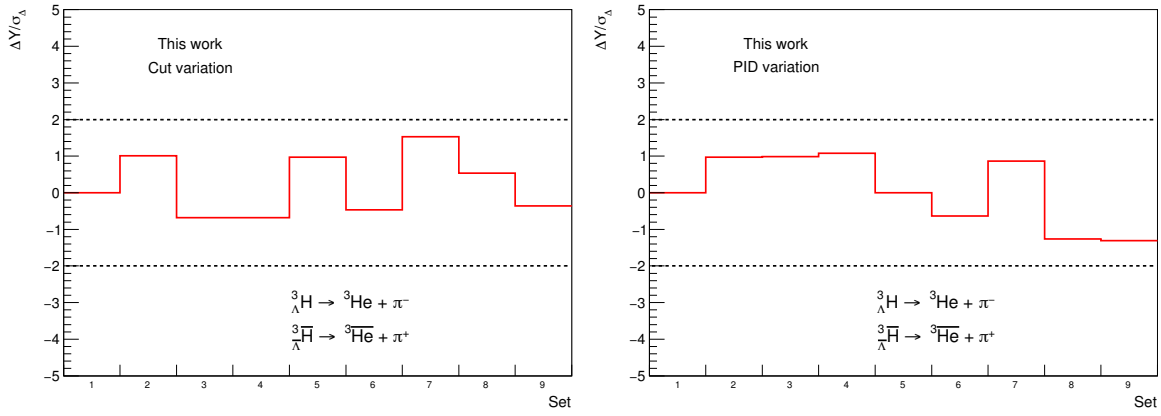

(a) Cut variation **(b)** PID

Figure 6.14.: Significance of the difference between the results obtained with nominal selections and those obtained with cuts (left) and PID (right) variations. The dashed line at ± 2 corresponds to the minimal threshold required in the *Barlow criterion* to include the variation in the systematic uncertainties.

the lifetime value is evaluated repeating the analysis from the beginning. As already done in the other analysis, the Barlow criterion is applied in order to include in the systematic uncertainties only those variations with a significance larger than 2. Figure 6.14 shows the trend of $\Delta Y/\sigma_{\Delta}$, which is the variable used in the test, for the variations of the topological cuts (left) and PID requirements (right). All these variations have a significance below 2 and for this reason the topological cuts and the PID are not included in the systematic uncertaintites.

The last systematic effect being investigated is due to the tracking efficiency. As already anticipated, this effect has been estimated by the ALICE experiment in Pb–Pb collisions and the resulting uncertainty is 3.5% on each single track and, since the $^{3}_{\Lambda}$H has two daughters tracks, it has been decided to assign a systematic uncertainty of 7% following a conservative approach.

The summary of the systematic uncertainty of each source are reported in Table 6.7 and the total uncertainty is the sum in quadrature of the single sources. It is important to keep in mind that the uncertainties have been evaluated directly on the lifetime, thus the total uncertainty is immediately propagated as a percentage of the measured lifetime τ.

Systematic uncertainties - Unbinned fit	
Cross-section	3.49%
Average absorption correction	3.58%
Material budget	1%
Single track efficiency	7%
Total	9%

Table 6.7.: Summary of the systematic uncertainties evaluated on the lifetime value τ with the unbinned fit method. The total uncertainty is the sum in quadrature of the single sources.

6.3. Lifetime estimate via 2 body decay channel

The lifetime value has been measured with two different approach in this thesis and in the following the results are presented and compared with the available τ values in literature.

The outcome of the first method is the corrected $\mathrm{d}N/\mathrm{d}(c\mathrm{t})$ spectrum, obtained with the following formula:

$$\frac{\mathrm{d}N}{\mathrm{d}(c\mathrm{t})} = \frac{1}{\epsilon \times \alpha} \cdot \frac{1}{\Delta c\mathrm{t}} \cdot N_{raw}(c\mathrm{t}) \tag{6.9}$$

where N_{raw} is the raw yield in each ct interval, $\epsilon \times \alpha$ is the efficiency $\times$ acceptance shown in Figure 6.4 and Δct is the width of the ct interval. The corrected spectrum is expected to follow the exponential distribution:

$$N(c\mathrm{t}) = \mathrm{N}_0 \cdot e^{-\frac{c\mathrm{t}}{c\tau}} \tag{6.10}$$

where N_0 is the normalization parameter and τ is the expected $^{3}_{\Lambda}$H lifetime.

The result of the exponential fit to the $\mathrm{d}N/\mathrm{d}(c\mathrm{t})$ spectrum is shown in Figure 6.15, where the blue marker is the corrected yield with its statistical uncertainty, the box is the systematic uncertainty and the red line is the exponential fit function. The fit is performed using only the statistical uncertainties, since the systematic contribution on the lifetime value has already been studied in Sec. 6.1.4, and the result is:

$$c\tau = 7.25^{+1.02}_{-1.13}(stat.) \pm 0.59(syst.)(cm) \tag{6.11}$$

$$\tau = 242^{+34}_{-38}(stat.) \pm 20(syst.)(ps) \tag{6.12}$$

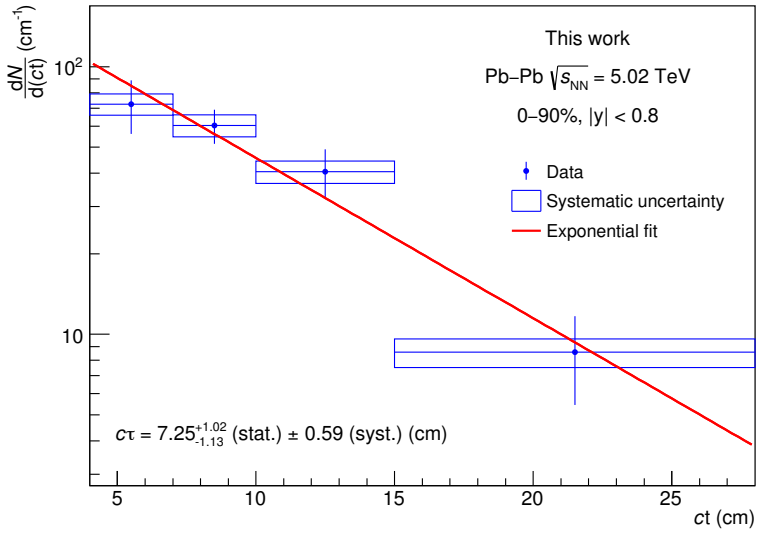

Figure 6.15.: dN/d(ct) spectrum with statistical (bar) and systematic (box) uncertainties. The red line corresponds to the exponential fit performed to estimate the lifetime value.

The method, used for this evaluation, consists, first of all, in shifting the dN/d(ct) spectrum according to the systematic uncertainty on each yield and it is based on the conservative assumption that the uncertainties are anti-correlated. The applied shifts to the single yields are reported in Table 6.8 and, in this way, two different dN/d(ct) spectra are obtained.

dN/d(ct) shifts				
ct (cm)	4–7	7–10	10–15	15–28
Hard spectrum	$+1\sigma_{syst.}$	$+0.5\sigma_{syst.}$	$-0.5\sigma_{syst.}$	$-1\sigma_{syst.}$
Soft spectrum	$-1\sigma_{syst.}$	$-0.5\sigma_{syst.}$	$+0.5\sigma_{syst.}$	$+1\sigma_{syst.}$

Table 6.8.: Applied shifts to the corrected yields in each ct bin. The two resulting “hard" and “soft" spectra are used for the evaluation of the systematics on the lifetime value τ. More details in the text.

Figure 6.16 shows the “hard" and “soft" spectra, respectively as red and green markers, together with the nominal spectra of this analysis, represented with blue markers. The boxes are only the systematic uncertainties on the corrected yields and the colored lines are the corresponding exponential fits to the aforementioned spectra. The measured lifetime values in the two cases are τ_{hard} = 220 $\pm$ 19 ps and τ_{soft} = 261 $\pm$ 23 ps. The systematic

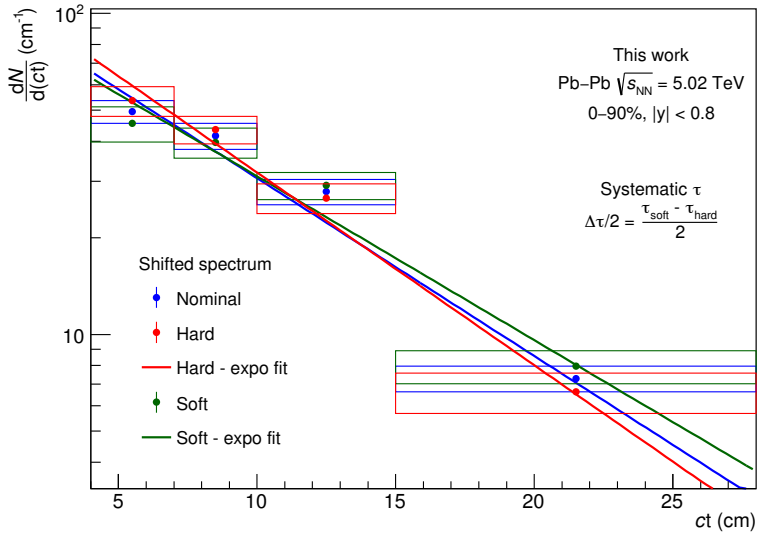

Figure 6.16.: "Hard" (red) and "soft" (green) dN/d(ct) spectra obtained by shifting the yields as explained in the text. The nominal spectrum is represented with blue markers. The boxes are only the systematic uncertainties of each yield and the colored lines are the exponential fit to the two shifted spectra.

uncertainty of τ is assessed as the semi-difference between the two cases, (τ_{soft} - τ_{hard})/2 = 20.5 ps, which corresponds to the 8.5% of the lifetime value.

The second estimate of the ($^{3}_{\Lambda}\overline{\text{H}}$)$^{3}_{\Lambda}$H lifetime is performed with the unbinned fit method. As previously described, the lifetime τ is evaluate using the maximum-likelihood estimate in the fit procedure. The statistical uncertainty is assessed by providing the interval of the estimated τ and the corresponding confidence level. The method implemented in the software package and used in this case is the Neyman interval construction [135]. It uses a test based on the likelihood ratio $\lambda(c\text{t}\,|\,\tau) = L(c\text{t}\,|\,\tau)/L(c\text{t}\,|\,\hat{\tau})$, where $\hat{\tau}$ is measured value and the ratio is evaluated for different values of τ. Then, the Wilks theorem [136] allows to construct a relation between the interval with confidence level 1-α and the 1-α quantile of the χ^2 distribution:

$$-2ln\lambda(c\text{t}|\tau) \leq \chi^2_{1-\alpha} \tag{6.13}$$

where, for instance, the confidence level of 68% corresponds to $\chi^2_{1-\alpha} \approx 1$ in case of a one dimensional problem.

The result of the lifetime estimate is shown in Figure 6.17 where the interval corresponding to the confidence level of 68% on the lifetime estimate is also indicated. In this case the interval is selected for $\chi^2_{1-\alpha} \approx 0.5$ since -$ln\lambda(c\text{t}\,|\,\tau)$ is used in the test.

The result obtained from the unbinned fit method is:

$$c\tau = 7.20^{+1.20}_{-0.93}(stat.) \pm 0.66(syst.)(cm) \tag{6.14}$$

$$\tau = 240^{+40}_{-31}(stat.) \pm 22(syst.)(ps) \tag{6.15}$$

The lifetime values estimated with the two methods are in agreement within 1σ, whether considering the statistical and systematic uncertainties singularly or summing them in quadrature.

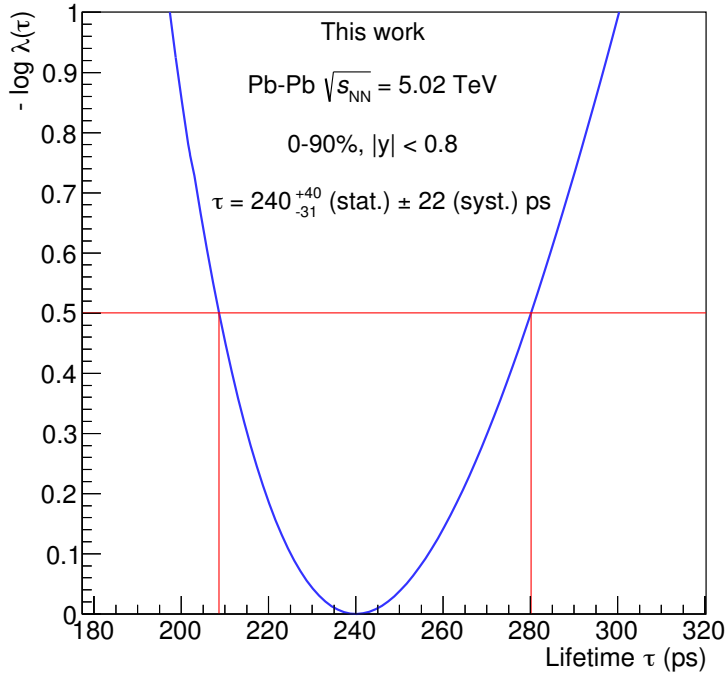

Figure 6.17.: Lifetime value τ from the unbinned maximum-likelihood estimate fit to the ct distribution. The statistical uncertainty is evaluated for a confidence level of 68% with the log-likelihood ratio, which corresponds to $-ln\lambda(c\text{t} \mid \tau) \approx 0.5$

6.4. $^{3}_{\Lambda}$H lifetime determination via 3 body decay

The statistics available from the 2015 Pb–Pb collisions at $\sqrt{s_{\text{NN}}}$= 5.02 TeV allows to measure the lifetime of the $^{3}_{\Lambda}$H via its 3 body decay channel:

$$^{3}_{\Lambda}\text{H} \longrightarrow \text{d} + \text{p} + \pi^{-} \tag{6.16}$$

$$^{3}_{\Lambda}\overline{\text{H}} \longrightarrow \overline{\text{d}} + \overline{\text{p}} + \pi^{+} \tag{6.17}$$

The 3 body decay channel of the $^{3}_{\Lambda}$H has a branching ratio of 40% [57], which is a 60% higher than the one for the 2 body decay channel, which is of 25% [57]. This suggests that the reconstruction of the $^{3}_{\Lambda}$H in this channel could be favorite with respect to all the other decay channels. The main difficulty is related to the identification of the three daughters, as it will be shown, and for this reason this analysis requires a large number of events.

In the following section the first estimate of the lifetime via the 3 body decay channel as well as the procedure will be described. The analysis presented in this thesis is still ongoing and the result shown is a first estimate, corresponding to half of the statistics used for the 2 body decay analysis

6.4.1. Event and track selection

The events used in this analysis are selected with the same criteria previously described in Sec. 4.2 and applied in the analysis of the 2 body decay channel. These selections are reported in Table 4.2 and, as already mentioned, allows to have uniform acceptance distribution and to reject pile-up events. The total number of minimum bias events used in this analysis is 50×10^{6}, which corresponds to half of the statistics previously used.

The second step is the selection of the tracks that will be used for the reconstruction of the secondary decay vertex and they are reported in Table 6.9. The cut on the minimum number of TPC clusters $\text{n}_{TPCclusters}$ and on the maximum $\chi^2/\text{n}_{TPCclusters}$ are tighter than those in Table 4.5. This is due to the fact that in this case the decay vertex is reconstructed using the tracks obtained from the global tracking procedure and not using a dedicated algorithm, like the on-the-fly V^0 finder, thus a higher quality track is required.

The last step in the track selection is the identification of the pion, proton and deuteron candidates. The PID is done using the specific energy loss $\text{d}E/\text{d}x$ information in the TPC

Track selection criteria	
Variable	Selection
$\lvert\eta\rvert$	≤ 0.9
$n_{TPCclusters}$	> 80
TPC refit	TRUE
$\chi^2/n_{TPCclusters}$	≤ 4
Kink topology	reject

Table 6.9.: Summary of the track selections applied in the analysis of the $^{3}_{\Lambda}$H in the 3 body decay channel in the 2015 data sample.

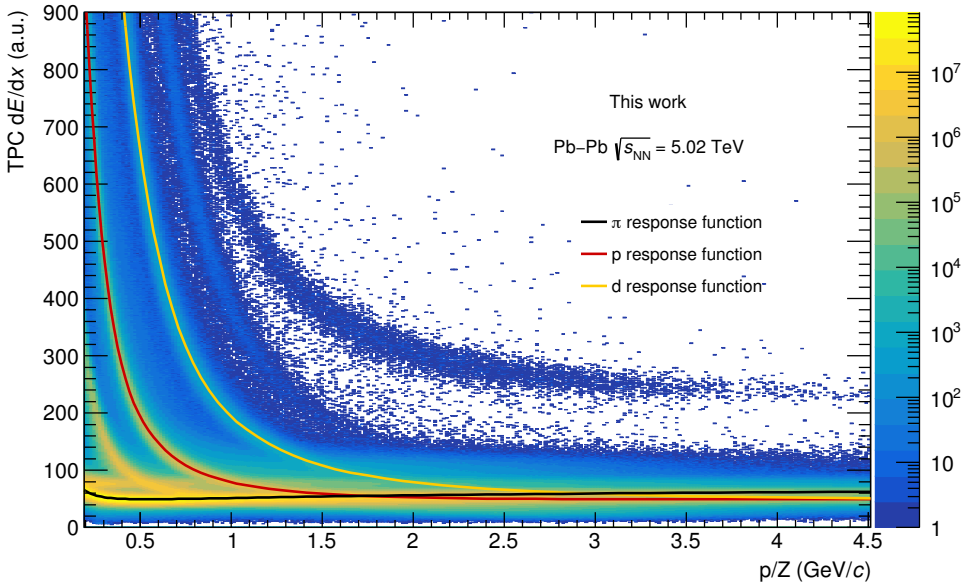

Figure 6.18.: Specific energy loss in the TPC active volume as a function of the particle rigidity in Pb–Pb collisions for the 2015 data sample. The solid lines represent the expected TPC response for pion (black), proton (red) and deuteron (orange).

and it is performed track-by-track, applying a selection on the nσ variable (see Eq.4.3) as reported in Table 6.10.

Figure 6.18 shows the specific energy loss for particles traversing the TPC active volume and the expected signal for pion (black line), proton (red line) and deuteron (orange line) used in this work. In this case all the daughter tracks have $z = 1e$ and this, as previously mentioned, makes their identification more challenging than in the 2 body decay analysis. Indeed, recalling the Bethe-Bloch formula, the specific energy loss depends on the square

Particle Identification		
Species	Variable	Selection
π	$\lvert \text{n}\sigma_{\pi} \rvert$	≤ 3
p	$\lvert \text{n}\sigma_{p} \rvert$	≤ 3
d	$\lvert \text{n}\sigma_{d} \rvert$	≤ 3

Table 6.10.: Selection applied for the identification of candidate π, p and d using the specific energy loss in the TPC active volume.

of z which is the same for all the daughters tracks. Thus, after a given momentum value, which is different for each species, the specific energy loss is similar to that of the other particles with the same z (e.g. K) and this produces a higher combinatorial background if compared with the 2 body analysis, where one daughter is well separated thanks to its $z = 2e$.

In order to reduce this background a dedicated selection is applied to the identified pion candidates, as reported in Table 6.11 . Indeed this particle species is largely primarly produced in the heavy ion collision over large p_{T} range, from 0.1 GeV/c to 12 GeV/c, while, as already highlighted for the 2 body decay topology, pions from the $^{3}_{\Lambda}$H decay do not exceed 1 GeV/c, thus the maximum p_{T} is required to be 1.2 GeV/c. In addition, the pion candidate is required to have distance of closest approach to the primary vertex larger than 0.1 cm.

π selection criteria	
Variable	Selection
$\text{n}_{TPCclusters}$	> 100
p_{T} (GeV/c)	0.2–1.2
DCA^{π}_{PV} (cm)	> 0.1

Table 6.11.: Summary of the track selections applied to pions in the analysis of the $^{3}_{\Lambda}$H in the 3 body decay channel in the 2015 data sample.

p_{T} selection	
Variable	Selection
proton p_{T} (GeV/c)	> 0.4
deuteron p_{T} (GeV/c)	> 1

Table 6.12.: Summary of the p_{T} selections applied to the candidate protons and deuterons in the analysis of the $^{3}_{\Lambda}$H in the 3 body decay channel in the 2015 data sample.

A selection on the p_{T} range of protons and deuterons is also applied, as reported in Table 6.12, driven by the MC simulation, shown in Figure 6.19a and 6.19b, respectively for p and d. The protons are required to have a p_{T} larger than 0.4 GeV/c and the deuterons larger than 1 GeV/c. These selections are also based on the results of the analysis of the primary

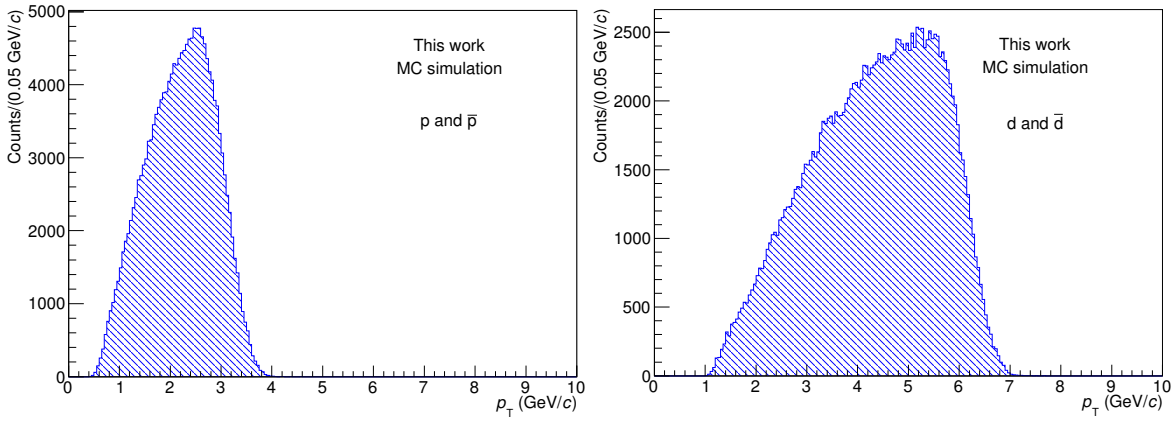

(a) p and $\overline{\text{p}}$ **(b)** d and $\overline{\text{d}}$

Figure 6.19.: Transverse momentum distribution of protons (a) and deuterons (b) from the $(^{3}_{\Lambda}\overline{\text{H}})^{3}_{\Lambda}$H decay. The distributions are obtained from the MC production.

p_{T} spectra of these particles [19, 137] , where it is shown that the p_{T} regions excluded with this cut are dominated by primary produced protons and deuterons.

6.4.2. Decay vertex reconstruction and selection

The selected candidate tracks are used to reconstruct the $(^{3}_{\Lambda}\overline{\text{H}})^{3}_{\Lambda}$H decay vertex and its topology is depicted in Figure 6.20, where the variables used for the vertex selection and the background reduction are reported.

The three tracks are required to have DCA from each other below a given threshold, in order to select a triplet of candidates which are close enough in space. In particular the $\text{DCA}_{d,p}$ is required to be lower than 0.1 cm while the $\text{DCA}_{d,\pi}$ and the $\text{DCA}_{p,\pi}$ are required to be smaller than 0.2 cm. The pion is expected to carry less momentum than the other two daughters, thus have a smaller curvature radius. For this reason the cut on the DCA between the pion and the other two tracks is larger.

An additional selection on the angle between two tracks has been studied using the MC simulation and then applied in the analysis. Indeed, the three daughters are boosted close to the direction of the $^{3}_{\Lambda}$H and thus the angular distribution of one track to the other is studied on the MC simulation selecting only those deuterons, protons and pions coming from the $(^{3}_{\Lambda}\overline{\text{H}})^{3}_{\Lambda}$H decay. The results are shown in Figure 6.21 and the selections applied are $\alpha_{d,\pi} < 0.4$ rad and $\beta_{p,\pi} < 0.5$ rad.

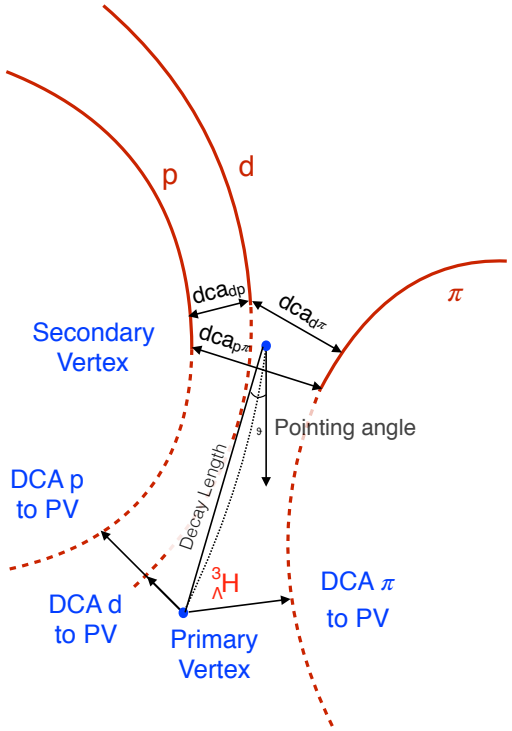

Figure 6.20.: Pictorical sketch of the $^{3}_{\Lambda}$H three body decay. The observables used to reduce the combinatorial background are reported on the figure.

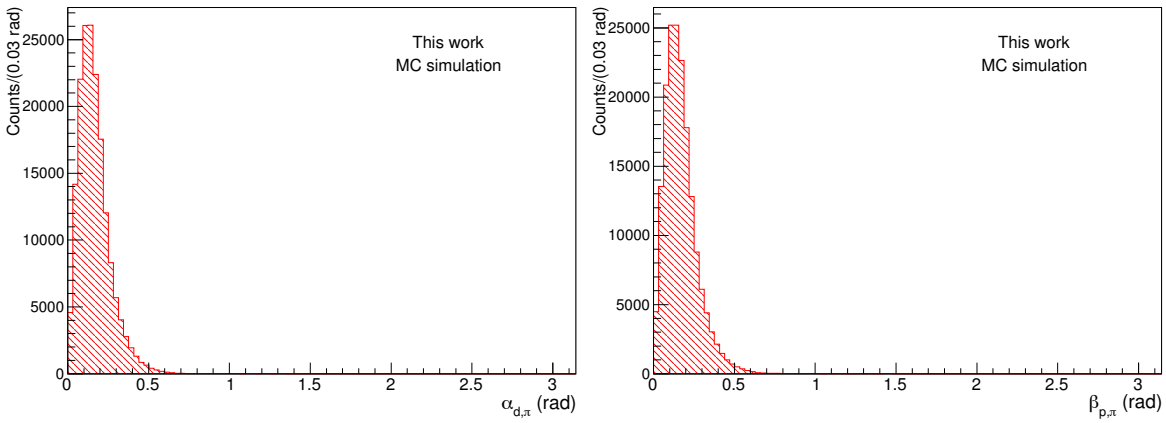

(a) angle deuteron-pion **(b)** angle proton-pion

Figure 6.21.: Distribution of the angle between deuteron and pion $\alpha_{d,\pi}$ (a) and between proton and pion $\beta_{p,\pi}$ (b) candidates coming from the $^{3}_{\Lambda}$H decay using the MC simulation.

After this selection, reported in Table 6.13, the decay vertex is reconstructed with an algorithm that estimates its position as the centre of gravity of the triangle formed by the three DCA between the tracks, pictorically represented as the blue point in Figure 6.20.

Track triplet selection	
Variable	Selection
$\text{DCA}_{d,p}$ (cm)	< 0.1
$\text{DCA}_{d,\pi}$ (cm)	< 0.2
$\text{DCA}_{p,\pi}$ (cm)	< 0.2
$\alpha_{d,\pi}$ (rad)	< 0.4
$\beta_{p,\pi}$ (rad)	< 0.5

Table 6.13.: Summary of the selections applied to select the triplet of tracks used to reconstruct and identify the secondary decay vertex.

6.4.3. Raw yields extraction *vs* *c*t

The raw yields as a function of *c*t are the starting point for the measurement of the lifetime and they are obtained, first of all, selecting the candidates reconstructed $(^{3}_{\Lambda}\overline{\text{H}})^{3}_{\Lambda}\text{H}$ with the cuts reported in Table 6.14.

Candidate selection	
Variable	Selection
DCA^{d}_{SV} (cm)	< 0.05
DCA^{p}_{SV} (cm)	< 0.05
DCA^{π}_{SV} (cm)	< 0.05
$\cos(\theta_{pointing})$	≥ 0.998
p_{T} (GeV/c)	2-9
ct (cm)	> 2 cm
$\lvert y \rvert$	≤ 0.8
$\Delta\text{L}/\sigma_{\Delta\text{L}}$	> 3

Table 6.14.: Summary of the selections applied to candidate $(^{3}_{\Lambda}\overline{\text{H}})^{3}_{\Lambda}\text{H}$ to extract the raw yields.

The first three cuts listed in the table are applied to the DCA of each track to the reconstructed secondary vertex which is required to be smaller than 0.05 cm. In the bottom part of the table the selections on the candidate $(^{3}_{\Lambda}\overline{\text{H}})^{3}_{\Lambda}\text{H}$ are listed. They have already been introduced for the analysis of the lifetime through the 2 body decay channel, with the exception of the last one $\Delta\text{L}/\sigma_{\Delta\text{L}}$ which is called *normalized decay distance*. It is largely used in the analyses for the jets reconstruction and can be defined as the significance of the reconstructed decay distance. Indeed, ΔL is evaluated as the geometrical distance be-

tween primary and secondary vertices and $\sigma_{\Delta L}$ is its uncertainty, which depends on the reconstruction resolution of the two vertices.

The selected candidates are divided in four ct bins 4-4.5, 4.5-5, 5-6 and 6-15 cm, covering almost the same range of the dN/d(ct) spectrum obtained for the 2 body decay analysis, and the raw yields are extracted from a fit to the invariant mass distributions, shown in Figure 6.22. The fit function (blue line) is the sum of a Gaussian for the signal and a third degree polynomial for the background (red dashed line) and the normalization is kept into account with N_{sig} and N_{bkg}, which represents the raw signal and background counts. The raw yields are obtained as the integral of the Gaussian in the range $\pm$ 3σ scaled for the measured N_{sig}.

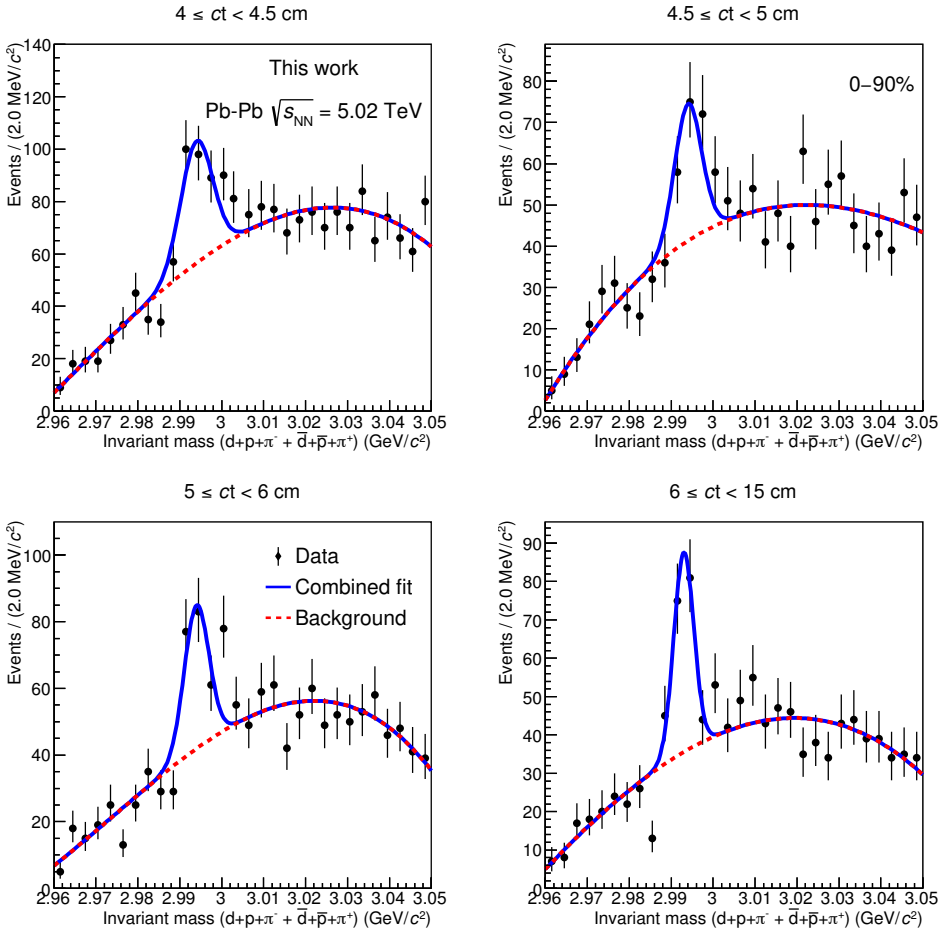

Figure 6.22.: $^{3}_{\Lambda}$H and $^{3}_{\Lambda}\overline{\text{H}}$ invariant mass distribution in 4 ct intervals, with superimposed the fit function (blue line), used to extract the raw yields, and the background component (red dashed line).

The results of the fit are reported in Table 6.15 together with the estimated raw yields.

	$^3_\Lambda$H + $^3_\Lambda\overline{\text{H}}$			
ct (cm)	4–4.5	4.5–5	5–6	6–15
mean (GeV/c^2)	2.993 ± 0.0009	2.9928 ± 0.0009	2.9928 ± 0.0007	2.9927 ± 0.0008
width (GeV/c^2)	0.0036 ± 0.0015	0.0032 ± 0.0009	0.0028 ± 0.0007	0.0025 ± 0.0005
χ^2/NDF	2.07	1.41	1.43	1.68
S/B	0.34	0.33	0.43	0.61
Significance (3σ)	6.1	4.7	5.6	6.2
Raw yield	148 ± 29	89 ± 21	105 ± 25	103 ± 18

Table 6.15.: Results of the fit to the $^3_\Lambda$H + $^3_\Lambda\overline{\text{H}}$ invariant mass distributions in the ct intervals . Raw yields are obtained as the integral of the signal function in $\pm 3\sigma$ with respect to the mean value.

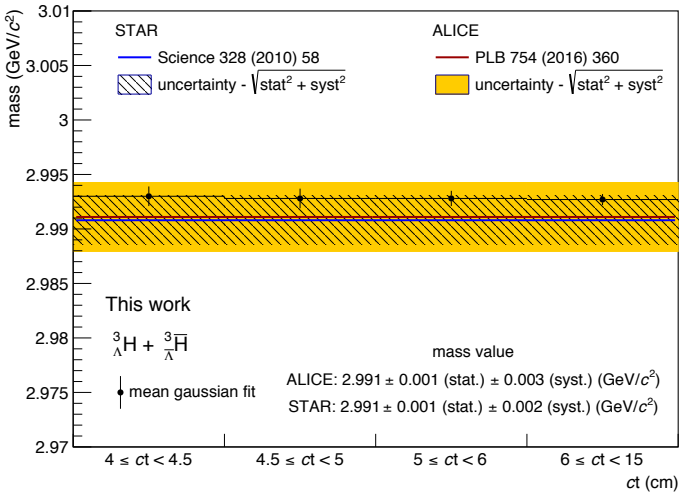

Figure 6.23.: Comparison of the measured mass (black markers) with two experimental reference values measured by ALICE [70] (red line) and STAR [56] (blue line). The bands are the sum in quadrature of statistical and systematics uncertainties

Both the mean values μ and the width σ are slightly higher compared to those obtained from the two body decay analysis even if by few MeV and this might be related to the reduced statistics used in this estimate. The mass values are also compared to those measured by ALICE [70] and STAR [56] and they are higher with respect even though in agreement within the uncertainties, as shown in Figure 6.23. It is important to keep in mind that these results are obtained with half of the available statistics and that they will be improved when the full statistics will be analysed. Moreover a detailed study of the combinatorial

background distribution will be performed in the future in order to have a clear selection of the signal. However a first attempt to estimate the lifetime of the $^{3}_{\Lambda}$H via the 3 body decay channel is presented in the next section.

6.4.4. Lifetime estimate via 3 body decay channel

The raw yields are corrected for the efficiency evaluated in the same way as it is done for the 2 body decay channel, then a fit with an exponential function is performed to estimate the lifetime value τ. Figure 6.24 shows the dN/d(ct) with the exponential fit (red line) used to estimate the lifetime.

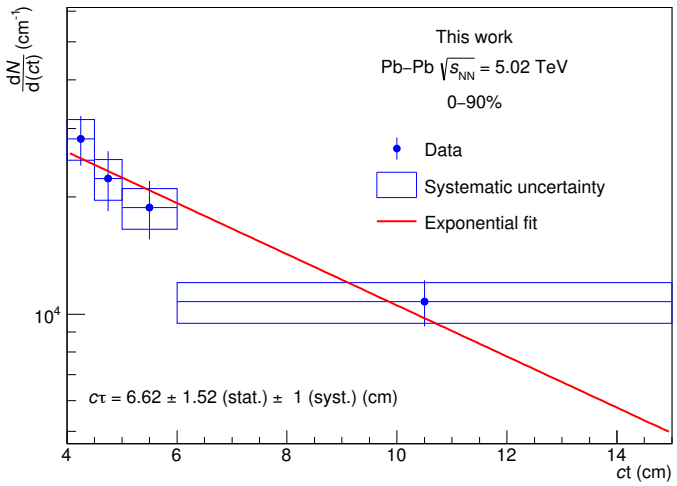

Figure 6.24.: dN/d(ct) spectrum with statistical (bar) and systematic (box) uncertainties. The systematic uncertainty is estimated increasing by 35% that one obtained from the two body decay analysis. The red line is to the exponential fit done for the lifetime estimate.

Since the analysis is still in progress, the systematic uncertainties as well as the absorption correction are still to be studied and quantified. Nevertheless, in order to have a complete comparison with the results obtained from the analysis of the two body decay channel, the systematic uncertainty is assessed by increasing of 35% the same uncertainty obtained for the dN/d(ct) spectrum in Sec. 6.1.4. Finally the propagation of this uncertainty to the τ value is performed as done in the aforementioned section, assuming the uncertainties as anticorrelated. The result of the fit is:

$$c\tau = 6.62 \pm 1.52(stat.) \pm 1(syst.)(cm) \tag{6.18}$$

$$\tau = 220 \pm 50(stat.) \pm 27(syst.)(ps) \tag{6.19}$$

6.5. Lifetime results

The lifetime values τ obtained from the analysis of the 2 body, with two methods, and the 3 body decay channels are all in agreement. In particular, the value of τ_{3body} is compatible with those of τ_{2body} even considering only the statistical uncertainty for the 2 body result. This is a fundamental remark that indicates that the lifetime does not depend on the analysed decay channel, as expected, and, moreover, confirms the accuracy of the method used for the lifetime estimate. The usage of the full data sample of Pb–Pb collisions at $\sqrt{s_{\text{NN}}}$= 5.02 TeV for the lifetime determination via 3 body decay channel will lead to an improved precision on the final result by reducing the statistical uncertainty.

At the moment, results for the $^{3}_{\Lambda}$H lifetime determined via 3 body decay channel are not present in literature. There is only a preliminary result by the STAR Collaboration [138], where they report a lifetime value of 142^{+24}_{-21}(stat.) $\pm$ 31(syst.) ps, combining the 2 and 3 decay channel results, which is lower than the results of this thesis and 50% below the expected free Λ lifetime. Thus, it is still more important the estimate of the lifetime via 3 body decay channel by analysing the data sample of the 2015 Pb–Pb collisions. The aim is to perform the measurement with the two methods used and described for the analysis of the 2 body decay channel.

The values of τ_{2body} and τ_{3body} are compared with previous experimental results in Figure 6.25. It is the compilation of the lifetime values available in literature (black markers) with the addition of three results obtained in this thesis. The free Λ lifetime (azure dashed line) as reported by the Particle Data Group [5] and the average of the $^{3}_{\Lambda}$H and $^{3}_{\Lambda}\overline{\text{H}}$ lifetime (green line and yellow band) results [139] available in literature, which is of $\tau = 216^{+19}_{-16}$ ps, are also shown in the figure.

The lifetime evaluated in this work are comparable with the results from experiment using visualizing techniques and also with their weighted average of $\tau_{visualtec.} = 195^{+14}_{-13}$ ps as reported in [54] [1].

The comparison with the published results [56, 69, 70] from heavy ion experiments, reported also in Table 6.16, shows that the measured τ_{2body} and τ_{3body}, presented in this thesis, higher and closer to the free Λ lifetime but still in agreement within the uncertainties with those lifetime values.

The results reported in Table 6.16 show that, at the moment, the precision is especially limited by the statistical uncertainty. However, this source of uncertainty can be reduced

[1] see also Chap. 2 Sec. 2.1.3

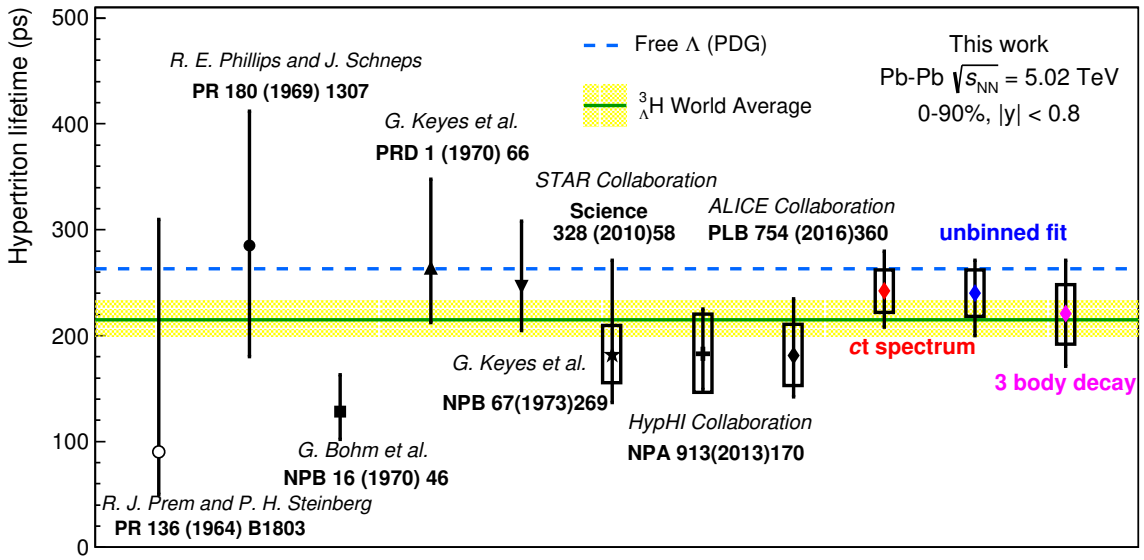

Figure 6.25.: First estimate of the lifetime values via three body decay analysis (magenta diamond) compared with the results of this thesis and with those published. The band represents the average of the published $^{3}_{\Lambda}$H lifetime measurements (τ = 216^{+19}_{-16} ps), while the dashed line is the lifetime of Λ from the Particle Data Group.

$^{3}_{\Lambda}$H lifetime from heavy ion experiments						
	STAR	HypHI	ALICE 2.76 TeV	ALICE 2body 5.02 TeV		ALICE 3body 5.02 TeV
τ (ps)	182	183	181	242	240	220
stat. uncert. (ps)	$^{+89}_{-45}$	$^{+42}_{-32}$	$^{+54}_{-39}$	$^{+34}_{-38}$	$^{+40}_{-31}$	± 50
σ_{stat}/τ	$^{+0.48}_{-0.25}$	$^{+0.23}_{-0.17}$	$^{+0.30}_{-0.22}$	$^{+0.14}_{-0.16}$	$^{+0.16}_{-0.13}$	± 0.23
syst. uncert. (ps)	± 27	± 37	± 33	± 20	± 22	± 27
σ_{syst}/τ	± 0.15	± 0.20	± 0.18	± 0.08	± 0.09	± 0.13

Table 6.16.: $^{3}_{\Lambda}$H lifetime values measures in heavy ion experiments. The published results as well as the statistical and systematic uncertainties are reported taken from [56, 69, 70]. The uncertainties are also reported as percentage of the measured lifetime.

by increasing the sample of events to be used for the analysis. The results of this thesis already go in this direction, since the 2015 Pb–Pb data sample is almost 2.5 times higher than 2011 Pb–Pb data sample analysed for the result published in [70], and the statistical uncertainty has been reduced.

On the other hand, the systematic uncertainties, which at the moment are lower than the statistical ones, might be the main limitation for the future measurements. Indeed, the main sources of systematic uncertainty are the single track efficiency and the absorption. The first one can be improved by studying to which extent the $^{3}_{\Lambda}$H reconstruction is reproduced in the MC simulations. The second source, instead, requires further developments, both from the theoretical and experimental point of view, to better describe and estimate the absorption of light (hyper-)nuclei produced in heavy ion collisions.

The results presented in this thesis might be improved with the data sample of Pb–Pb collisions that will be collected at the end of 2018, which will allow to perform the analysis on a larger amount of events. Moreover, after the LHC Long Shutdown foreseen between 2019-2021, the ALICE experiment will have completed its upgrade program, which mainly consists in the replacement of the ITS [140] with a new one and in the upgrade of the TPC [141]. The goal of the upgrade project is to reconstruct tracks and vertices with higher precision, which will allow to reduce the combinatorial background and, thus, get more precise results.

The heavy ion experiments are one of the available class of experiment where the lifetime of the $^{3}_{\Lambda}$H can be measured. One of the main advantages is the large number of events collected in a short time, which are analyzed. However two disadvantages are the large combinatorial background especially in the most central collisions and the fact that they are not able to see the production of the $^{3}_{\Lambda}$H but only the decay products. This can be done in fix target experiment, where the $^{3}_{\Lambda}$H can be tagged when is produced and thus it can be performed a pure time measurement. From this point of view the results from the experiment carried on in J-PARC, JLab, GSI (HypHI) and MAMI are of extreme interest in order to shed light on the puzzle of the $^{3}_{\Lambda}$H lifetime.

Chapter 7.

Final results

"Success is going from failure to failure without losing enthusiasm"
— Sir Winston L.S. Churchill, 1874–1965

In this chapter the measurements of the ${}^{3}_{\Lambda}\mathrm{H}$ and ${}^{3}_{\Lambda}\overline{\mathrm{H}}$ yields and spectra in Pb–Pb collisions at $\sqrt{s_{\mathrm{NN}}}$= 5.02 TeV will be shown and discussed. The results obtained from the analyses described in Chapter 5 will be compared with those from other analyses and with the predictions of theoretical models. Finally the coalescence parameter and the thermal fits will be shown to provide insight into the production mechanism of the ${}^{3}_{\Lambda}\mathrm{H}$ in heavy ion collisions.

7.1. Production yields and spectra

7.1.1. p_{T} spectra

By combining the information of the signal extraction and the corrections described in Chapter 5 Sec. 5.2 , the production spectra of the $({}^{3}_{\Lambda}\overline{\mathrm{H}})^{3}_{\Lambda}\mathrm{H}$ in 10–40% are evaluated as:

$$\frac{1}{N_{\mathrm{ev}}}\frac{\mathrm{d}^2N}{\mathrm{d}p_{\mathrm{T}}\mathrm{d}y} = \frac{1}{N_{\mathrm{ev}}}\frac{1}{\epsilon \cdot f_{\mathrm{absorption}}}\frac{\mathrm{d}N_{\mathrm{raw}}}{\mathrm{d}p_{\mathrm{T}}} \tag{7.1}$$

where N_{ev} is the total number of analysed events, ϵ is the efficiency $\times$ acceptance correction, $f_{\mathrm{absorption}}$ is the absorption correction and N_{raw} is the raw yield in each p_{T} interval. Figures 7.1 and 7.2 show the corrected p_{T} spectrum for the ${}^{3}_{\Lambda}\mathrm{H}$ and ${}^{3}_{\Lambda}\overline{\mathrm{H}}$, respectively, measured for the first time in semi-central collisions (10–40%). The corrected yields are drawn at the corresponding p_{T} value obtained from the evaluation of the mean p_{T} assuming a

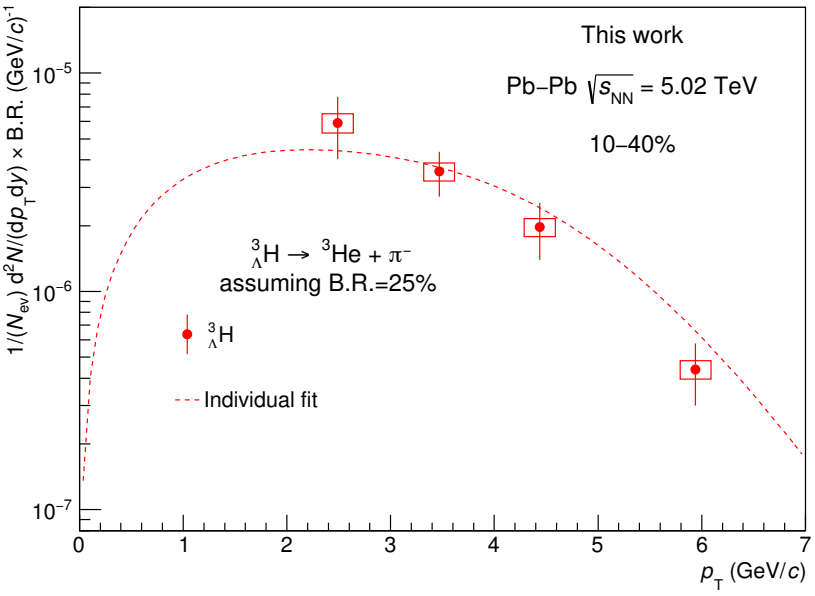

Figure 7.1.: $^3_\Lambda$H transverse momentum spectrum measured in the centrality class 10–40% and in the rapidity range $|y| < 0.5$. The dotted line is the Blast-Wave function with fixed ^{3}He parameters.

Blast-Wave [20] distribution of the transverse momentum in each interval. The reason for this approach is related to the fact that the p_T intervals of the spectrum are not small enough to assume a flat p_T distribution and the Blast-Wave distribution is assumed, since it well describes the spectra of lighter particles [19] and nuclei [137] in heavy ion collisions.

In order to measure the total yield per rapidity unit dN/dy in the 10–40% centrality class, the $^3_\Lambda$H and $^3_\Lambda\overline{\text{H}}$ spectra were fitted with the Blast-Wave function, represented with a dotted line in Figure 7.1 and 7.2. This function describes the measured spectra assuming a thermal production of particles from an expanding source:

$$\frac{1}{p_T}\frac{dN}{dp_T} \propto \int_0^R r dr m_T I_0\left(\frac{p_T sinh\rho}{T_{kin}}\right) K_1\left(\frac{m_T cosh\rho}{T_{kin}}\right) \tag{7.2}$$

where m_T is the transverse mass defined as $m_T = \sqrt{m^2 + p_T^2}$, I_0 and K_1 are the modified Bessel functions, r is the distance from the centre of the expanding system, R is the limiting radius of the system expansion, T_{kin} is the temperature of the kinetic freeze-out and ρ is the velocity profile. The velocity profile can be expressed in terms of the transverse expansion

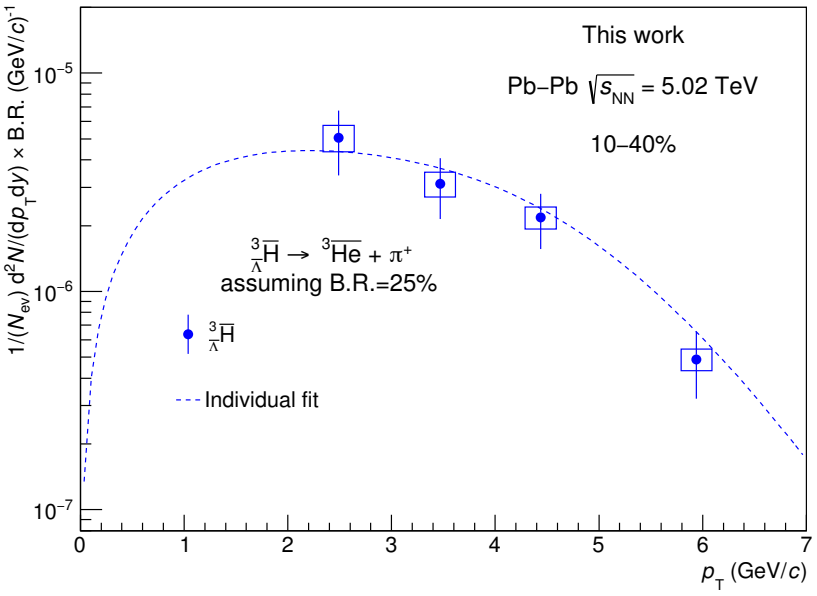

Figure 7.2.: $^3_{\Lambda}\overline{H}$ transverse momentum spectrum measured in the centrality class 10–40% and in the rapidity range $|y| < 0.5$. The dotted line is the Blast-Wave function with fixed ^{3}He parameters.

velocity at the system surface, β_S, and an exponent n:

$$\rho = tanh^{-1}\left(\left(\frac{r}{R}\right)^n \beta_S\right) \tag{7.3}$$

In addition, the distribution introduced in Eq. 7.2 has to be multiplied for the parameter *norm* which takes into account the normalization of the distribution and corresponds to the integral of the Blast-Wave over the full p_T range. However, since the number of parameters of the Blast-Wave function is larger than the measured yield values, it has been chosen to fix them to those of the ^{3}He distribution [124], leaving only the normalization as free parameters. The two individual fits well describe the measured p_T spectra of $^3_{\Lambda}H$ and $^3_{\Lambda}\overline{H}$ and this suggests that also their emission from the medium created in the collision is driven by the radial flow, which indicates the presence of a medium. Indeed, the Blast-Wave distribution is derived in a phenomenological model that describes the hadron spectra from heavy ion collisions in terms of a few collective variables, in particular temperature, longitudinal, and transverse (or radial) flow. The latter one is a collective motion that, in heavy ion collision, is interpreted as related to the pressure gradients of a deconfined medium.

In order to give a quantitative estimate of the radial flow effect from the $(^{3}_{\Lambda}\overline{\mathrm{H}})^{3}_{\Lambda}\mathrm{H}$ production it is necessary to perform a fit to the production spectra using the Blast-Wave with all the parameters free and not constrained as in this case. This will be possible by analysing the data sample of Pb–Pb collisions that will be collected at the end of 2018, where an increase by a factor 2 of the statistics, especially for the central collisions, is expected and this will lead to a production spectra with measured yields in narrower p_{T} interval.

The total yields per rapidity unit in the 10–40% centrality class are obtained from the integral of the aforementioned individual fit function over the full p_{T} range and the results are reported in Table 7.1.

	Yields 10–40%	
	$\mathrm{d}N/\mathrm{d}y \times$ B.R. $\times 10^{-5}$	$\langle\, \mathrm{d}N_{ch}/\mathrm{d}\eta \rangle$
$^{3}_{\Lambda}\mathrm{H}$	$1.32 \pm 0.22(\mathrm{stat.}) \pm 0.13(\mathrm{syst.})$	826 ± 22
$^{3}_{\Lambda}\overline{\mathrm{H}}$	$1.23 \pm 0.20(\mathrm{stat.}) \pm 0.16(\mathrm{syst.})$	826 ± 22

Table 7.1.: Integrated yields per rapidity unit $\mathrm{d}N/\mathrm{d}y$ times the Branching Ratio (B.R.) of the 2 body decay channel, for the $^{3}_{\Lambda}\mathrm{H}$ and $^{3}_{\Lambda}\overline{\mathrm{H}}$ in the centrality class 10–40% of the Pb–Pb collisions at $\sqrt{s_{\mathrm{NN}}}$= 5.02 TeV. For the analysed centrality class the average $\langle\, \mathrm{d}N_{ch}/\mathrm{d}\eta \rangle$ is reported.

7.1.2. dN/dy as a function of centrality

Similarly, combining the information described in Sec. 5.1, the corrected total yields in the three centrality classes 0–10%, 10–30%, 30–50% are evaluated as:

$$\frac{\mathrm{d}N}{\mathrm{d}y} = \frac{1}{N_{\mathrm{ev}}} \frac{f_{\mathrm{missing}}}{\epsilon \cdot f_{\mathrm{absorption}}} \frac{\mathrm{d}N_{\mathrm{raw}}}{\mathrm{d}y} \tag{7.4}$$

where N_{ev} is the total number of analysed events, ϵ is the acceptance $\times$ efficiency correction, $f_{\mathrm{absorption}}$ is the absorption correction and f_{missing} is the estimated fraction of the total yields in the unmeasured p_{T} regions, since the raw yields are measured in the 2-9 GeV/c interval (see Sec. 5.1). The estimate of the yield in the unmeasured regions is done using the ^{3}He Blast-Wave function previously introduced in Chapter 5 and the missing fraction is evaluated as the ratio of the integral in the unmeasured regions to the total integral. The total corrected yields per rapidity unit for the three centrality classes are reported in Table 7.2.

Yields *vs* centrality			
	$\mathrm{d}N/\mathrm{d}y \times$ B.R. $\times 10^{-5}$		
	${}^{3}_{\Lambda}\mathrm{H}$	${}^{3}_{\Lambda}\overline{\mathrm{H}}$	$\langle \mathrm{d}N_{ch}/\mathrm{d}\eta \rangle$
0–10%	3.50 $\pm$ 0.77(stat.) $\pm$ 0.42(syst.)	3.32 $\pm$ 0.70(stat.) $\pm$ 0.48(syst.)	1756 $\pm$ 52
10–30%	1.31 $\pm$ 0.33(stat.) $\pm$ 0.17(syst.)	1.49 $\pm$ 0.36(stat.) $\pm$ 0.23(syst.)	983 $\pm$ 25
30–50%	0.83 $\pm$ 0.23(stat.) $\pm$ 0.10(syst.)	0.91 $\pm$ 0.25(stat.) $\pm$ 0.13(syst.)	415 $\pm$ 14

Table 7.2.: Integrated yields per rapidity unit $\mathrm{d}N/\mathrm{d}y$ times the B.R. of the 2 body decay channel, for the ${}^{3}_{\Lambda}\mathrm{H}$ and ${}^{3}_{\Lambda}\overline{\mathrm{H}}$ in the centrality classes analysed of the Pb–Pb collisions at $\sqrt{s_{\mathrm{NN}}}$= 5.02 TeV. For each analysed centrality class the average $\langle \mathrm{d}N_{ch}/\mathrm{d}\eta \rangle$ is reported.

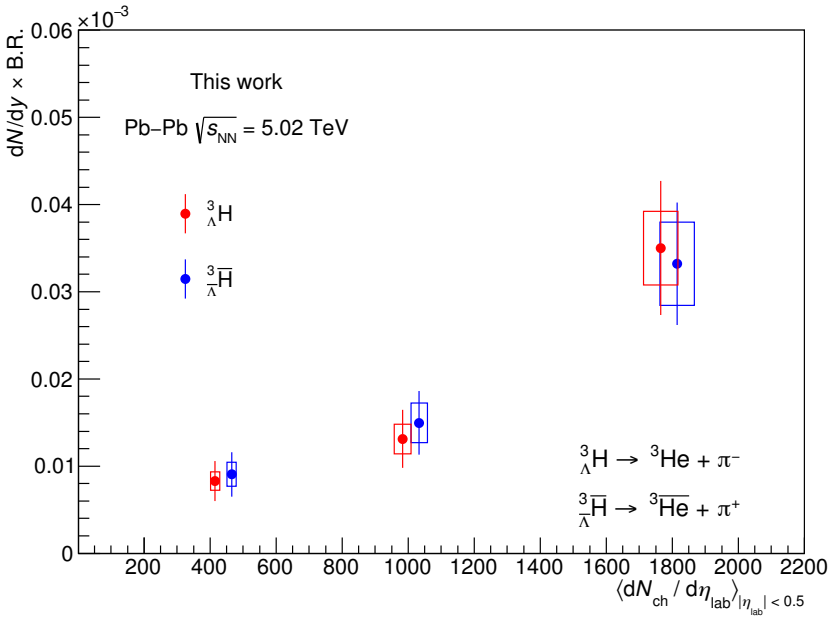

Figure 7.3.: $\mathrm{d}N/\mathrm{d}y$ times the B.R. of the 2 body decay channel for the ${}^{3}_{\Lambda}\mathrm{H}$ (red) and the ${}^{3}_{\Lambda}\overline{\mathrm{H}}$ (blue). The vertical bar and the box are statistical and systematic uncertainty, respectively. Points relative to hypermatter and anti-hypermatter are horizontally shifted for visibility.

The measured $\mathrm{d}N/\mathrm{d}y$ are shown as a function of the $\langle \mathrm{d}N_{ch}/\mathrm{d}\eta \rangle$ in Figure 7.3, in red for the ${}^{3}_{\Lambda}\mathrm{H}$ and in blue for the ${}^{3}_{\Lambda}\overline{\mathrm{H}}$ where an increasing trend with the charged particle multiplicity is observed.

A more quantitative approach to investigate the scaling of the ${}^{3}_{\Lambda}\mathrm{H}$ production with the charged particle multiplicity is through the double ratio defined as:

$$\left(\frac{({}^{3}_{\Lambda}\mathrm{H}+{}^{3}_{\Lambda}\overline{\mathrm{H}})_i}{({}^{3}_{\Lambda}\mathrm{H}+{}^{3}_{\Lambda}\overline{\mathrm{H}})_j}\right) / \left(\frac{\langle \mathrm{d}N_{ch}/\mathrm{d}\eta\rangle_i}{\langle \mathrm{d}N_{ch}/\mathrm{d}\eta\rangle_j}\right) \tag{7.5}$$

where i and j are two different centrality classes in which the $({}^{3}_{\Lambda}\overline{\mathrm{H}})^{3}_{\Lambda}\mathrm{H}$ $\mathrm{d}N/\mathrm{d}y$ and the charged particle multiplicity $\langle\ \mathrm{d}N_{ch}/\mathrm{d}\eta\rangle$ are measured. This double ratio is evaluated for the 10–30%, 30–50% and 10–40% with respect to the results obtained in the most central class (0–10%). In the calculation the yields are also corrected for the Branching Ratio (B.R.) of the 2 body decay channel, which is assumed to be 25% [57], and this corresponds to an increase by a factor 4 of all $\mathrm{d}N/\mathrm{d}y$.

Double ratios	
0–10%/10–30%	$1.35 \pm 0.31(\mathrm{stat.}) \pm 0.19(\mathrm{syst.})$
0–10%/30–50%	$0.93 \pm 0.23(\mathrm{stat.}) \pm 0.13(\mathrm{syst.})$
0–10%/10–40%	$1.25 \pm 0.24(\mathrm{stat.}) \pm 0.15(\mathrm{syst.})$

Table 7.3.: Results of the double ratio as defined in Eq.7.5 between the ${}^{3}_{\Lambda}\mathrm{H}+{}^{3}_{\Lambda}\overline{\mathrm{H}}$ $\mathrm{d}N/\mathrm{d}y$ and the $\langle\ \mathrm{d}N_{ch}/\mathrm{d}\eta\rangle$ in the 0–10% centrality and the same values measured in the other three centrality classes. The $\mathrm{d}N/\mathrm{d}y$ are divided for the B.R. of the 2 body decay channel which is assumed to be 25% [57].

The results of the double ratios are reported in Table 7.3, where the statistical and systematic uncertainties are propageted is performed separately, and they are in agreement with the unity within 1σ, defined as the sum in quadrature of the statistical and systematic uncertainties. Thus, the $({}^{3}_{\Lambda}\overline{\mathrm{H}})^{3}_{\Lambda}\mathrm{H}$ production scales with the charged particle production, which means also with the number of participants and thus with the collision centrality.

The scaling with the charged particle multiplicity can be interpreted in the statistical hadronisation model as related to the volume of the medium created in the heavy ion collision. Indeed, as introduced in Sec. 2.2.1, the yield of each particle species depends on the volume V of the system and, since the size of V is assumed to increase while going from semi-central (30–50%) to central (0–10%) collisions, the average number of produced particles as well as the relative abundance of each of them are expected to increase.

Also in a coalescence approach [142] the $\mathrm{d}N/\mathrm{d}y$ is expected to scale with the charged particle multiplicity, since an increased particle production lead to a higher number of baryons which could coalesce. However, other model implementations [143] describe the

coalescence as an interplay between the $\langle \mathrm{d}N_{ch}/\mathrm{d}\eta \rangle$ and the increase of the volume of the system, measured through the Hanbury-Brown-Twiss radii of the pion sources as described in [143], which lead to a reduction of the baryon density and thus to a less probability to coalesce while the centrality increases.

7.2. Antimatter-to-matter ratio

An important assumption for all the models describing the particles production at the LHC energies is that the baryon chemical potential μ_B is 0, the so called *transparency regime*, which has been also experimentally verified [144].

Both coalescence and thermal models predict that the antimatter-to-matter ratio is 1 for a system with vanishing baryon chemical potential. If the μ_B of the system is null or close to zero, the number of baryons and antibaryons in the system is the same and in the coalescence model there is no difference between the probability of producing a ${}^{3}_{\Lambda}\mathrm{H}$ or an ${}^{3}_{\overline{\Lambda}}\overline{\mathrm{H}}$. In the thermal model approach the fugacity of a particle species $\lambda_i \propto e^{B_i \mu_B / T}$, where B_i is the baryon number of a particle species, is the only different term in the expected $\mathrm{d}N/\mathrm{d}y$ of ${}^{3}_{\Lambda}\mathrm{H}$ and ${}^{3}_{\overline{\Lambda}}\overline{\mathrm{H}}$. Thus, if a vanishing baryon chemical potential is assumed, the fugacities of ${}^{3}_{\Lambda}\mathrm{H}$ and ${}^{3}_{\overline{\Lambda}}\overline{\mathrm{H}}$ coincide and their yields are the same according to the Statistical Hadronisation Model [81].

The ${}^{3}_{\overline{\Lambda}}\overline{\mathrm{H}}/{}^{3}_{\Lambda}\mathrm{H}$ ratio has been estimated both as a function of the transverse momentum and as a function of the charged particle multiplicity. Figure 7.4 shows the ratio between the ${}^{3}_{\overline{\Lambda}}\overline{\mathrm{H}}$ and the ${}^{3}_{\Lambda}\mathrm{H}$ p_{T} spectra measured in the 10–40% centrality class. The vertical bar corresponds to the statistical uncertainty and the box to the systematic one. The ratios are in agreement with the unity in the whole measured p_{T} region.

Figure 7.5 shows the same ratio as a function of the charged particle multiplicity, obtained in the three centrality classe 0–10%, 10–30% and 30–50%, which is also in agreement with unity. The uncertainty on the x-axis is that one associated to the measured charged particle multiplicity [122].

Moreover, the numerical value of the ratios are reported in Table 7.5 for both cases. The agreement of these ratios with the unity confirm the assumption of μ_B close to zero for the model describing the particle and (hyper-)nuclei production at the LHC energies.

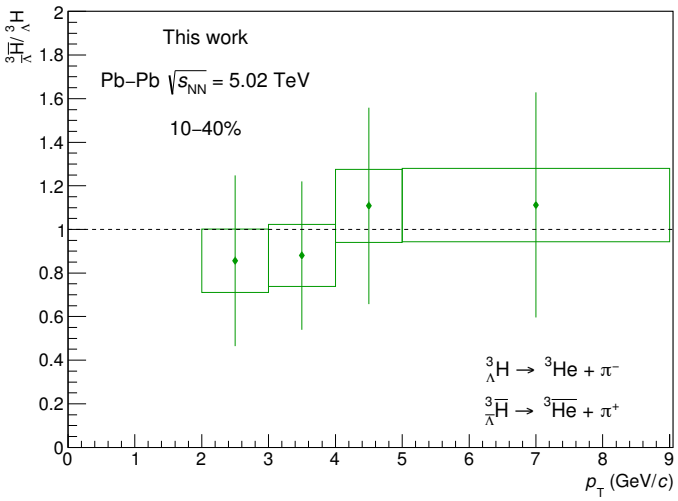

Figure 7.4.: $^3_\Lambda\overline{\mathrm{H}}/^3_\Lambda\mathrm{H}$ ratio as a function of p_T in the centrality class 10–40%. The dotted line represent the expected value of 1 under the assumption of μ_B=0.

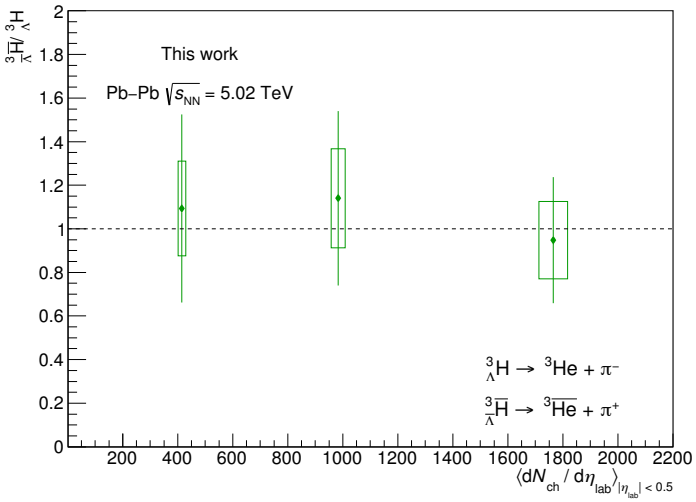

Figure 7.5.: $^3_\Lambda\overline{\mathrm{H}}/^3_\Lambda\mathrm{H}$ ratio as a function of the $\langle\, \mathrm{d}N_{ch}/\mathrm{d}\eta\rangle$ of the corresponding centrality class. The dotted line represent the expected value of 1 under the assumption of μ_B=0.

7.3. $^3_\Lambda$H over ^{3}He ratio

In the heavy ion collisions, the evolution of the ratio between hypernuclei and nuclei $\mathrm{d}N/\mathrm{d}y$ with the charged particle multiplicity is an important observables to investigate the hypernuclei production mechanism. In particular, the $(^3_\Lambda\overline{\mathrm{H}})^3_\Lambda\mathrm{H}$ over $(^3\overline{\mathrm{He}})^3\mathrm{He}$ ratio is

$^{3}_{\Lambda}\overline{\mathrm{H}}/^{3}_{\Lambda}\mathrm{H}$	
vs $\langle\, \mathrm{d}N_{ch}/\mathrm{d}\eta \rangle$	
0–10%	0.94 $\pm$ 0.28(stat.) $\pm$ 0.18(syst.)
10–30%	1.15 $\pm$ 0.39(stat.) $\pm$ 0.23(syst.)
30–50%	1.10 $\pm$ 0.43(stat.) $\pm$ 0.22(syst.)
vs p_{T} (GeV/c)	
2-3	0.86 $\pm$ 0.39(stat.) $\pm$ 0.15(syst.)
3-4	0.88 $\pm$ 0.34(stat.) $\pm$ 0.14(syst.)
4-5	1.10 $\pm$ 0.45(stat.) $\pm$ 0.17(syst.)
5-9	1.11 $\pm$ 0.51(stat.) $\pm$ 0.17(syst.)

Table 7.4.: Results of the $^{3}_{\Lambda}\overline{\mathrm{H}}/^{3}_{\Lambda}\mathrm{H}$ ratio as a function of the $\langle\, \mathrm{d}N_{ch}/\mathrm{d}\eta \rangle$ and of the p_{T} in the top and bottom part of the table. The ratio as a function of p_{T} is in the 10–40% centrality class.

evaluated as a function of the charged particle multiplicity $\langle\, \mathrm{d}N_{ch}/\mathrm{d}\eta \rangle$, using the relation:

$$Ratio = \frac{(\mathrm{d}N/\mathrm{d}y)_{^{3}_{\Lambda}\mathrm{H}}}{(\mathrm{d}N/\mathrm{d}y)_{^{3}\mathrm{He}}} \tag{7.6}$$

According to the thermal model interpretation, at the LHC energies, the ratio is fixed by the temperature of the source, thus it is constant with the charged particle multiplicity evolution. For instance, the Statistical Hadronisation Model [81] predicts a ratio of 0.35 for $^{3}_{\Lambda}\mathrm{H}/^{3}\mathrm{He}$ and 0.37 for $^{3}_{\Lambda}\overline{\mathrm{H}}/^{3}\overline{\mathrm{He}}$.

The aforementioned ratio is evaluated for the 0–10% and 10–40% centrality classes, since the $^{3}\mathrm{He}$ and $^{3}\overline{\mathrm{He}}$ $\mathrm{d}N/\mathrm{d}y$ have been measured in the same classes for the data sample of Pb–Pb collisions at $\sqrt{s_{\mathrm{NN}}}$= 5.02 TeV [124]. The $^{3}_{\Lambda}\mathrm{H}$ and $^{3}_{\Lambda}\overline{\mathrm{H}}$ $\mathrm{d}N/\mathrm{d}y$ used in the calculation are corrected for the B.R. of the 2 body decay channel (B.R. = 25%).

Ratio			
	$^{3}_{\Lambda}\mathrm{H}/^{3}\mathrm{He}$	$^{3}_{\Lambda}\overline{\mathrm{H}}/^{3}\overline{\mathrm{He}}$	$\langle\, \mathrm{d}N_{ch}/\mathrm{d}\eta \rangle$
0–10%	0.52 $\pm$ 0.11(stat.) $\pm$ 0.13(syst.)	0.55 $\pm$ 0.12(stat.) $\pm$ 0.15(syst.)	1756 $\pm$ 52
10–40%	0.36 $\pm$ 0.06(stat.) $\pm$ 0.08(syst.)	0.35 $\pm$ 0.06(stat.) $\pm$ 0.09(syst.)	826 $\pm$ 22

Table 7.5.: Results of the $(^{3}_{\Lambda}\overline{\mathrm{H}})^{3}_{\Lambda}\mathrm{H}$ over $(^{3}\overline{\mathrm{He}})^{3}\mathrm{He}$ ratio in two different centrality classes in Pb–Pb collisions at $\sqrt{s_{\mathrm{NN}}}$= 5.02 TeV.

The results in the 0–10% centrality class are higher compared to the prediction, but still in agreement within 1σ, while the ratio in the 10–40% is closer to the expected one.

These results are also shown as a function of $\langle \mathrm{d}N_{ch}/\mathrm{d}\eta \rangle$ in Figures 7.6 and 7.7 as green circles for the ${}^{3}_{\Lambda}\mathrm{H}$ and ${}^{3}_{\Lambda}\overline{\mathrm{H}}$, respectively. The ratios are compared with those measured by STAR [56] (open square) in Au-Au collisions at $\sqrt{s_{\mathrm{NN}}}$= 200 GeV and ALICE [70] (red circle) in Pb–Pb collisions at $\sqrt{s_{\mathrm{NN}}}$= 2.76 TeV. In particular the values of the ratios measured in Pb–Pb collisions at two different energies, show a hint of increasing trend with the $\langle \mathrm{d}N_{ch}/\mathrm{d}\eta \rangle$, which is more pronounced for the ${}^{3}_{\Lambda}\overline{\mathrm{H}}$. However, since the ${}^{3}_{\Lambda}\overline{\mathrm{H}}$ yield is similar to that of the ${}^{3}_{\Lambda}\mathrm{H}$ this slightly higher values of the ${}^{3}_{\Lambda}\overline{\mathrm{H}}/{}^{3}\overline{\mathrm{He}}$ might be related to a lower ${}^{3}\overline{\mathrm{He}}$ yield. Nevertheless, considering both the statistical and systematic uncertainties the ratios in the same class are in agreement.

In particular, the two ratios at the highest $\langle \mathrm{d}N_{ch}/\mathrm{d}\eta \rangle$ are in agreement with the GSI-Heidelberg [81] and THERMUS [145] statistical hadronisation model, which assume a thermal equilibrium for the medium created in the collision and a T_{chem} = 156 MeV, and with the Hagedorn resonance gas model [146]. On the other hand, the ratio measured in Pb–Pb collisions at $\sqrt{s_{\mathrm{NN}}}$=5.02 TeV is slightly higher than the prediction of the non-equilibrium thermal model SHARE [147].

Finally, the ${}^{3}_{\Lambda}\mathrm{H}/{}^{3}\mathrm{He}$ ratio is compared with the prediction of the THERMUS model as a function of the chemical freeze-out temperature T_{chem}. Figure 7.8 shows the measured ratio in the 0–10% centrality class as a red line, the orange band is the sum of the statistical and systematic uncertainty and the gray line is the THERMUS prediction. The measured ${}^{3}_{\Lambda}\mathrm{H}/{}^{3}\mathrm{He}$ ratio, considering 1σ, is in agreement with the THERMUS prediction starting from T_{chem} = 155 MeV up to the maximum available from the calculation that is T_{chem} = 250 MeV.

The latter value of T_{chem} is higher with respect to the one usually describing the particle production from thermal model of 156 MeV. This might be due to the fact that the ratio is performed with two particles with a small mass difference, showing a mild temperature dependence. Thus, it will be important to perform the same ratio using particles lighter than the ${}^{3}\mathrm{He}$ (e.g. proton) and compare it with the thermal predictions, which at the moment are not available. The expectation is that the larger mass difference will enhance the dependence on the chemical freeze-out temperature and will allow to better define the T_{chem} range. Moreover the ratio between the ${}^{3}_{\Lambda}\mathrm{H}$ and light hadrons will allow to better understand the production mechanism. Indeed, the coalescence model predicts an increasing trend with $\langle \mathrm{d}N_{ch}/\mathrm{d}\eta \rangle$, while the thermal model predicts a saturation of the aforementioned ratio since it is fixed by the chemical freeze-out temperature.

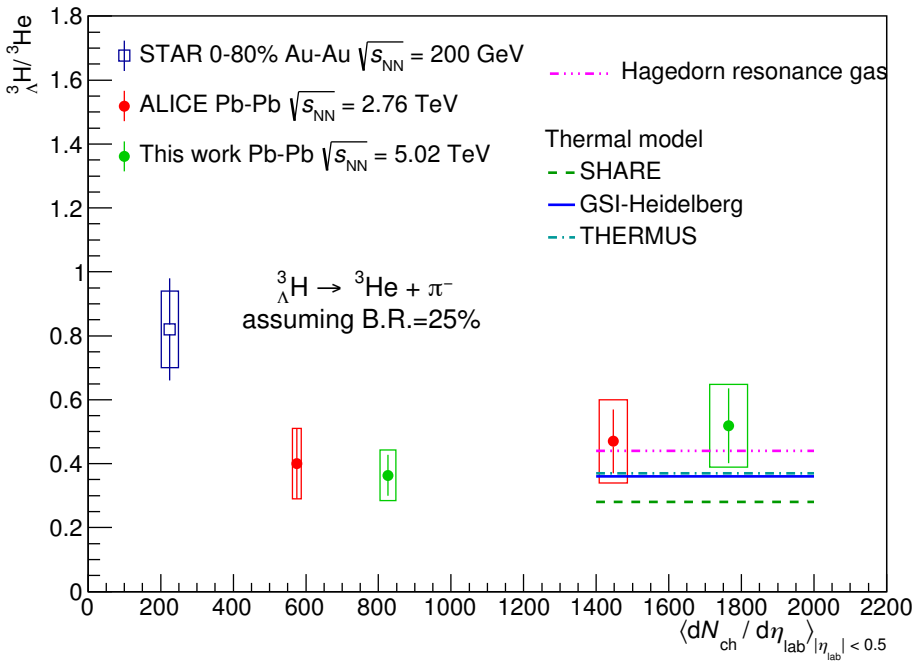

Figure 7.6.: $^3_\Lambda$H/^{3}He as a function of the average charged particle multiplicity $\langle \mathrm{d}N_{ch}/\mathrm{d}\eta \rangle$ measured in Pb–Pb collisions at $\sqrt{s_{\mathrm{NN}}}$= 5.02 TeV (green circle). The results are compared with the published ratios of STAR (open square) [56] and ALICE (red circle) [70] and theoretical lines as described in the legend.

Thanks to the data sample of central Pb–Pb collisions that will be collected by the ALICE experiment at the end of 2018 it will also possible to reduce the uncertainties and obtained a more precise result.

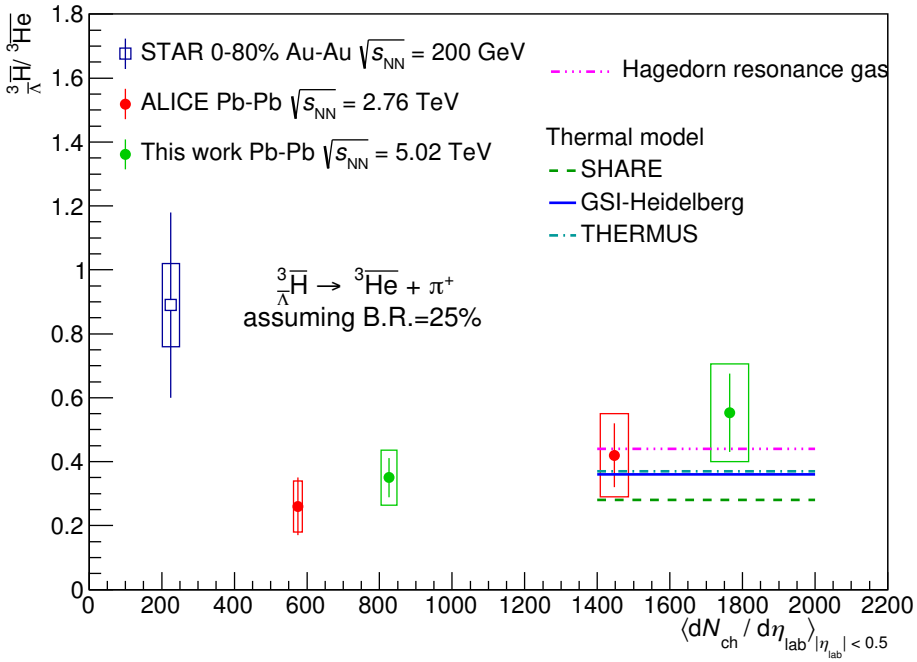

Figure 7.7.: $^3_\Lambda\overline{\mathrm{H}}/{}^3\overline{\mathrm{He}}$ as a function of the average charged particle multiplicity $\langle \mathrm{d}N_{ch}/\mathrm{d}\eta \rangle$ measured in Pb–Pb collisions at $\sqrt{s_{\mathrm{NN}}}$= 5.02 TeV (green circle). The results are compared with the published ratios of STAR (open square) [56] and ALICE (red circle) [70] and theoretical lines as described in the legend.

7.4. S_3 ratio

According to the authors of [148], the $^3_\Lambda\mathrm{H}/{}^3\mathrm{He}$ ratio can be dependent from the differences in the kinematics of different particle species due to collective motions. Thus they introduced the S_3 ratio defined as:

$$S_3 = \frac{^3_\Lambda\mathrm{H}}{^3\mathrm{He}} \times \frac{p}{\Lambda} \tag{7.7}$$

as a valuable tool to probe the nature of the medium created in the heavy ion collisions. In Eq. 7.7 Λ and p represent the measured $\mathrm{d}N/\mathrm{d}y$. This double ratio is extremely interesting since in thermal production it does not depend on the chemical potential of the particles and any additional canonical correction factor for strangeness is cancelled.

The $^3_\Lambda\mathrm{H}/{}^3\mathrm{He}$ ratio evaluated in the 0–10% and 10–40% centrality classes (see Sec. 7.3) is used to calculate the quantity reported in Eq. 7.7. Then also the Λ over p ratio is computed, using the preliminary yields [130, 149] obtained from the related production analysis in

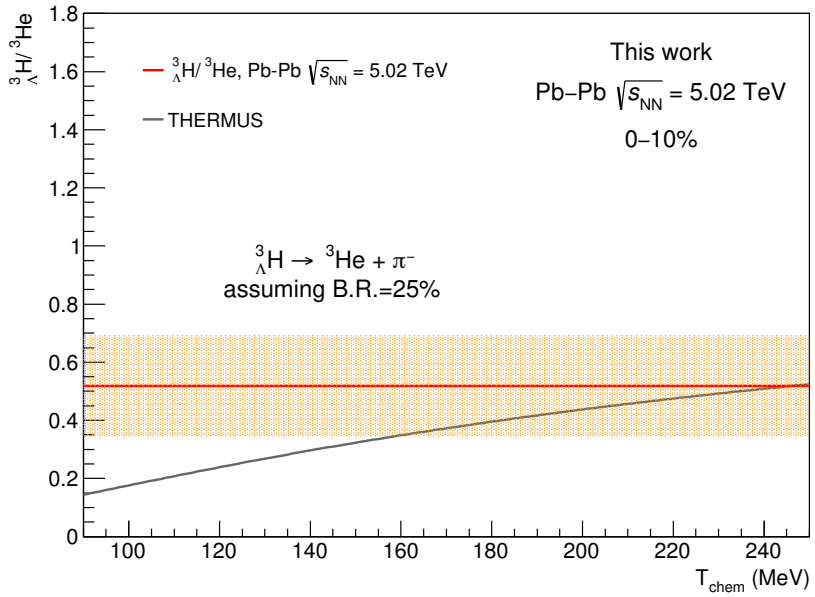

Figure 7.8.: $^3_\Lambda$H/^{3}He ratio (red line) evaluated for the 0–10% centrality class of Pb–Pb collisions at $\sqrt{s_{\rm NN}}$= 5.02 TeV as a function of the chemical freeze-out temperature T_{chem}. The orange band is the sum in quadrature of the statistical and systematic uncertainties. The results is compared with the THERMUS prediction (gray line) [145].

Pb–Pb collisions at $\sqrt{s_{\rm NN}}$= 5.02 TeV collected by the ALICE experiment. The results are reported in Table 7.6.

	S$_3$	
	$\frac{^3_\Lambda\mathrm{H}}{^3\mathrm{He}} \times \frac{p}{\Lambda}$	$\frac{^3_\Lambda\overline{\mathrm{H}}}{^3\overline{\mathrm{He}}} \times \frac{\overline{p}}{\Lambda}$
0–10%	0.61 $\pm$ 0.14(stat.) $\pm$ 0.16(syst.)	0.65 $\pm$ 0.14(stat.) $\pm$ 0.19(syst.)
10–40%	0.42 $\pm$ 0.07(stat.) $\pm$ 0.09(syst.)	0.40 $\pm$ 0.07(stat.) $\pm$ 0.1(syst.)

Table 7.6.: Results of the S$_3$ ratio in two different centrality classes in Pb–Pb collisions at $\sqrt{s_{\rm NN}}$= 5.02 TeV for the $^3_\Lambda$H and $\frac{3}{\Lambda}\overline{\mathrm{H}}$. The $(\frac{3}{\Lambda}\overline{\mathrm{H}})^3_\Lambda$H d$N$/d$y$ are corrected assuming a B.R. = 25% [57] for the 2 body decay channel.

Moreover, the S$_3$ for the 0–10% class can be compared with other experimental results as well as with the theoretical predictions for the most central collisions in Figure 7.9. Only the GSI-Heidelberg and the Hybrid UrQMD models predict the S$_3$ for the most central collisions at the LHC energies and they are in agreement with the measurements presented in this work at 5.02 TeV. The GSI-Heidelberg is a thermal model, as introduced in Chapter 2, which predicts the particle yields assuming a complete thermalization of the medium, with

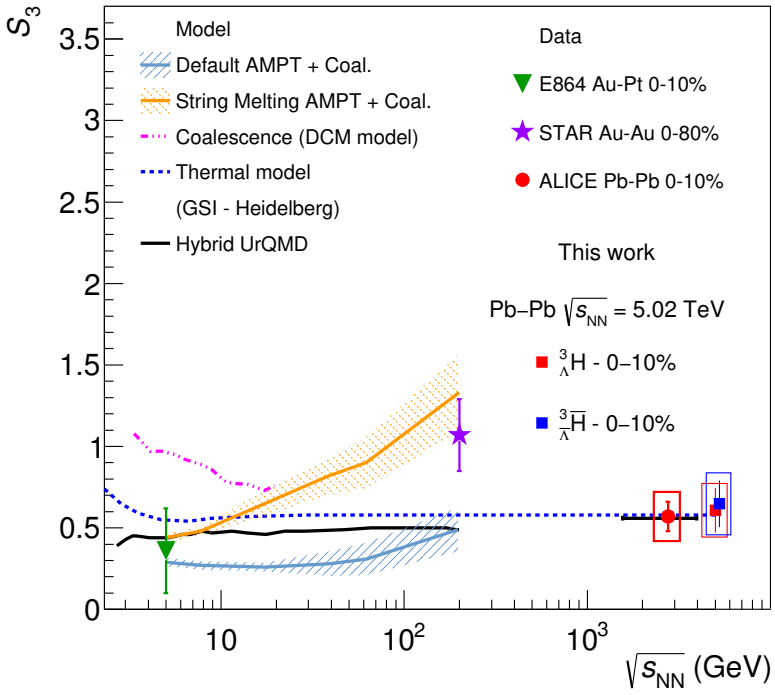

Figure 7.9.: Evolution of the S_3 with collision energy $\sqrt{s_{NN}}$. The red and blue full square are the results for the $^{3}_{\Lambda}$H and $^{3}_{\bar{\Lambda}}\bar{H}$ at 5.02 TeV, while the full markers are those obtained by other experiments and at different energies as explained in the legend. The blue square is horizontally shifted for visibility. The solid lines are the S_3 predictions by different thermal and coalescence models as described in the legend.

μ_B = 0 and T_{chem} = 156 MeV. The Hybrid UrQMD model, instead, combines the hadronic transport approach with an hydrodynamical stage for the hot and dense medium created in the heavy ion collision. The evolution of S_3 is also predicted by the DCM (Dubna Cascade Model) [85] coalescence model and the AMPT (A Multi-Phase Transport Model for Relativistic Heavy Ion Collision) [150] coalescence model. They predict a rising trend with the collision energy which is not comparable with the results obtained by the ALICE experiment at 2.76 TeV [70] and in this thesis. The results are also in agreement with that measured by the E864 experiment at lower energy [148], while they do not confirm the rising trend shown by STAR [56].

7.5. Comparison with thermal model

The statistical hadronisation model predicts, as already described, the particles production using a thermodynamic approach, where the key parameter for the abundance of each particle species is the chemical freeze-out temperature T_{chem}.

However, in the case of the $(^3_\Lambda\overline{\mathrm{H}})^3_\Lambda\mathrm{H}$ production yield an important role is played also by the B.R. for the analysed decay channel. In this thesis the B.R. for the $^3_\Lambda$H 2 body decay channel is assumed to be 25% [57], since it is also the same assumption done for the published results by STAR [56] and ALICE [70]. As a consequence, the theoretical predictions are also done as a function of the B.R. for the decay channel of the $^3_\Lambda$H.

Figure 7.10a and 7.10b show the measured $\mathrm{d}N/\mathrm{d}y \times$ B.R. as a horizontal line, where the bands represent statistical and systematic uncertainties added in quadrature, and the different theoretical models as lines. The theoretical predictions were performed assuming a possible variation of the B.R. in the range 15-35%, based on [151].

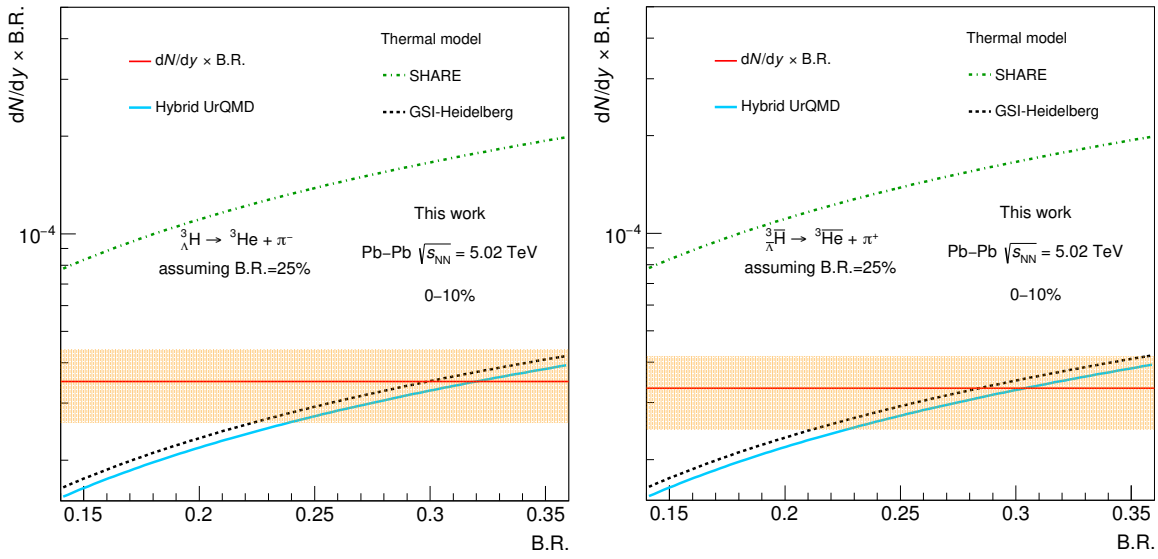

(a) $^3_\Lambda$H **(b)** $^3_\Lambda\overline{\mathrm{H}}$

Figure 7.10.: $\mathrm{d}N/\mathrm{d}y \times$ B.R. as a function of the B.R. for the $^3_\Lambda$H (a) and the $^3_\Lambda\overline{\mathrm{H}}$ (b). The red line is the measured yield where the B.R. is assumed to be 25% and the orange band is the sum in quadrature of the statistical and systematic uncertainties. The result is compared with three different theoretical model predictions as described in the legend.

The measured $\mathrm{d}N/\mathrm{d}y$ for the $^3_\Lambda$H and $^3_\Lambda\overline{\mathrm{H}}$ are in agreement with the statistical hadronisation model [81], which assumes a completely thermalized medium with a chemical

freeze-out temperature of T_{chem} = 156 MeV, in the B.R. range 22–35%. Similarly, they agree with the Hybrid UrQMD model starting from B.R. $\sim$ 23%. The latter one is an hydrodinamical model, which combines the hadronic transport approach with an initial hydrodynamical stage for the hot and dense phase of a heavy ion collision. For the assumed B.R. of 25% both curves tend to underestimate the $\mathrm{d}N/\mathrm{d}y$. On the other hand, the non-equilbrium thermal model SHARE [147], which assumes a T_{chem} = 138 MeV and a non-thermalization of strangeness quark, overestimates the p_{T}-integrated yield by a factor which goes from 2 to 5 in the considered B.R. range.

7.6. Coalescence parameter

The class of the coalescence models for the production of $(^{3}_{\Lambda}\overline{\mathrm{H}})^{3}_{\Lambda}\mathrm{H}$ in heavy ion collisions can be investigated by computing the coalescence parameters B_3 for the $^{3}_{\Lambda}\mathrm{H}$ and $^{3}_{\Lambda}\overline{\mathrm{H}}$, defined as:

$$B_3 = E_{^{3}_{\Lambda}\mathrm{H}} \frac{\mathrm{d}^3 N_{^{3}_{\Lambda}\mathrm{H}}}{\mathrm{d}p^3_{^{3}_{\Lambda}\mathrm{H}}} \left(E_p \frac{\mathrm{d}^3 N_p}{\mathrm{d}p^3_p} \right)^{-2} \left(E_\Lambda \frac{\mathrm{d}^3 N_\Lambda}{\mathrm{d}p^3_\Lambda} \right)^{-1} \tag{7.8}$$

where the first term is the $(^{3}_{\Lambda}\overline{\mathrm{H}})^{3}_{\Lambda}\mathrm{H}$ invariant momentum spectrum[1], while the other two terms are the proton [130] and Λ [149] primary spectra, respectively. In this definition the neutron spectrum is assumed to be the same as the one of the proton, since the ALICE experiment can not measure it directly. This assumption is based on the results of the production of $\pi^{\pm}$ which are compatible both at RHIC [17, 18] and LHC [19] energies. Figure 7.11a and 7.11b show the measured coalescence parameters B_3 as a function of the transverse momentum scaled by the mass number A=3 for the $^{3}_{\Lambda}\mathrm{H}$ (red marker) and the $^{3}_{\Lambda}\overline{\mathrm{H}}$ (blue marker) in Pb–Pb collisions at $\sqrt{s_{\mathrm{NN}}}$= 5.02 TeV and they show a similar trend. Moreover, the $^{3}_{\Lambda}\mathrm{H}$ is compared with the B_3 measured by the ALICE experiment in Pb–Pb collisions at $\sqrt{s_{\mathrm{NN}}}$= 2.76 TeV in the most central collision class (0–10%). Even if the comparison is done for the B_3 measured at two different energies, the plot shows an ordering with the collision centrality. This can be explained in the coalescence model framework as a decreasing volume V_{eff} of the source going from central to semi-central collisions. If the V_{eff} is bigger, the probability of having a proton, a neutron and a Λ close enough in the phase space to form a bound state is lower, thus the B_3 is smaller. On the other hand, the B_3 measured in this thesis for the $^{3}_{\Lambda}\mathrm{H}$ and $^{3}_{\Lambda}\overline{\mathrm{H}}$ are obtained in narrow p_{T} intervals with respect to those

[1] where $E\frac{\mathrm{d}^3 N}{\mathrm{d}p^3} = \frac{1}{2\pi p_{\mathrm{T}}} \frac{\mathrm{d}^2 N}{\mathrm{d}p_{\mathrm{T}}\mathrm{d}y}$

measured in Pb–Pb collisions at $\sqrt{s_{\rm NN}}$= 2.76 TeV and show almost flat trend as a function of $p_{\rm T}$/A, as assumed in the coalescence models.

The coalescence approach is not only employed in heavy ion collisions but has been also used in astrophysical researches [152]. Indeed, one of the major problem in dark matter searches is a satisfactory estimate of secondary anti-nuclei flux. The authors in [152] try to do this estimate using a scale law of the nuclear coalescence with the volume of the hadronic emission region. In particular they are interested in the coalescence of anti-nuclei in pp collision, since astrophysical anti-nuclei are dominantly produced in pp collisions. However they published a curve for the evolution of the B_3 as a function of the radius of the emitting source R. This curve is produced assuming the size of a ^{3}He, thus the comparison of the measured $(^3_{\Lambda}\overline{\rm H})^3_{\Lambda}$H B_3 is qualitatively. In particular, the B_3 parameters for the lowest and highest $p_{\rm T}$ are compared, as shown in Figure 7.12 for the $^3_{\Lambda}$H and in Figure 7.13 for the $^3_{\Lambda}\overline{\rm H}$. These plots also show the ^{3}He B_3 measured in heavy ion collisions by the ALICE [123], STAR [153] and NA44/NA49 [154] experiments. They are in agreement with the B_3 at, respectively, low and high $p_{\rm T}$ measured by the ALICE experiment in Pb–Pb collisions at $\sqrt{s_{\rm NN}}$= 2.76 TeV [123]. However the comparison with the curve gives a range of the radius R of the emitting source from 3.5 to 4.5 fm, considering both the low and high $p_{\rm T}$, which is slightly higher than those measured by the ALICE experiment at 2.76 TeV even if in agreement within the uncertainties. This curve, as already anticipated, is obtained for the coalescence of a bound state with the size of ^{3}He. A more quantitative comparison will be possible only with curves predicting the B_3 as a function of R for a bound state like the $^3_{\Lambda}$H, which at the moment are not available in literature.

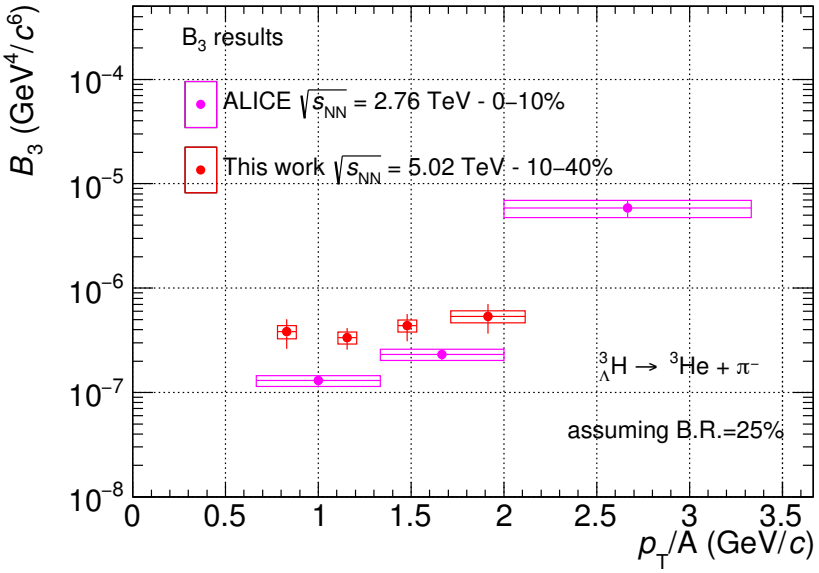

(a) $^{3}_{\Lambda}\mathrm{H}$

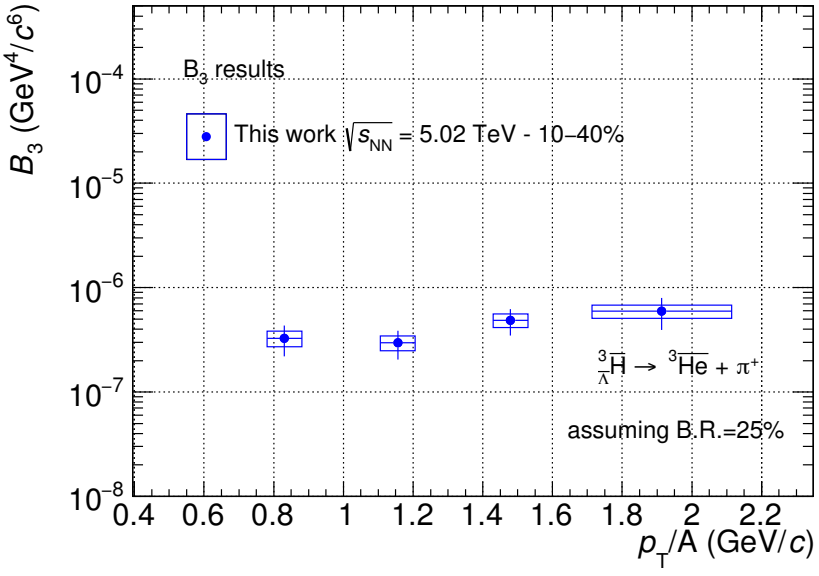

(b) $^{3}_{\overline{\Lambda}}\overline{\mathrm{H}}$

Figure 7.11.: (a): $^{3}_{\Lambda}\mathrm{H}$ B_3 as a function of $p_{\mathrm{T}}/\mathrm{A}$ measured in the 10–40% centrality class of Pb–Pb collisions at $\sqrt{s_{\mathrm{NN}}}$= 5.02 TeV (red marker). The magenta points is the B_3 of the $^{3}_{\Lambda}\mathrm{H}$ measured by the ALICE experiment in the 0–10% centrality class of Pb–Pb collisions at $\sqrt{s_{\mathrm{NN}}}$= 2.76 TeV [70]. (b): $^{3}_{\overline{\Lambda}}\overline{\mathrm{H}}$ B_3 as a function of $p_{\mathrm{T}}/\mathrm{A}$ measured in the 10–40% centrality class of Pb–Pb collisions at $\sqrt{s_{\mathrm{NN}}}$= 5.02 TeV (blue marker).

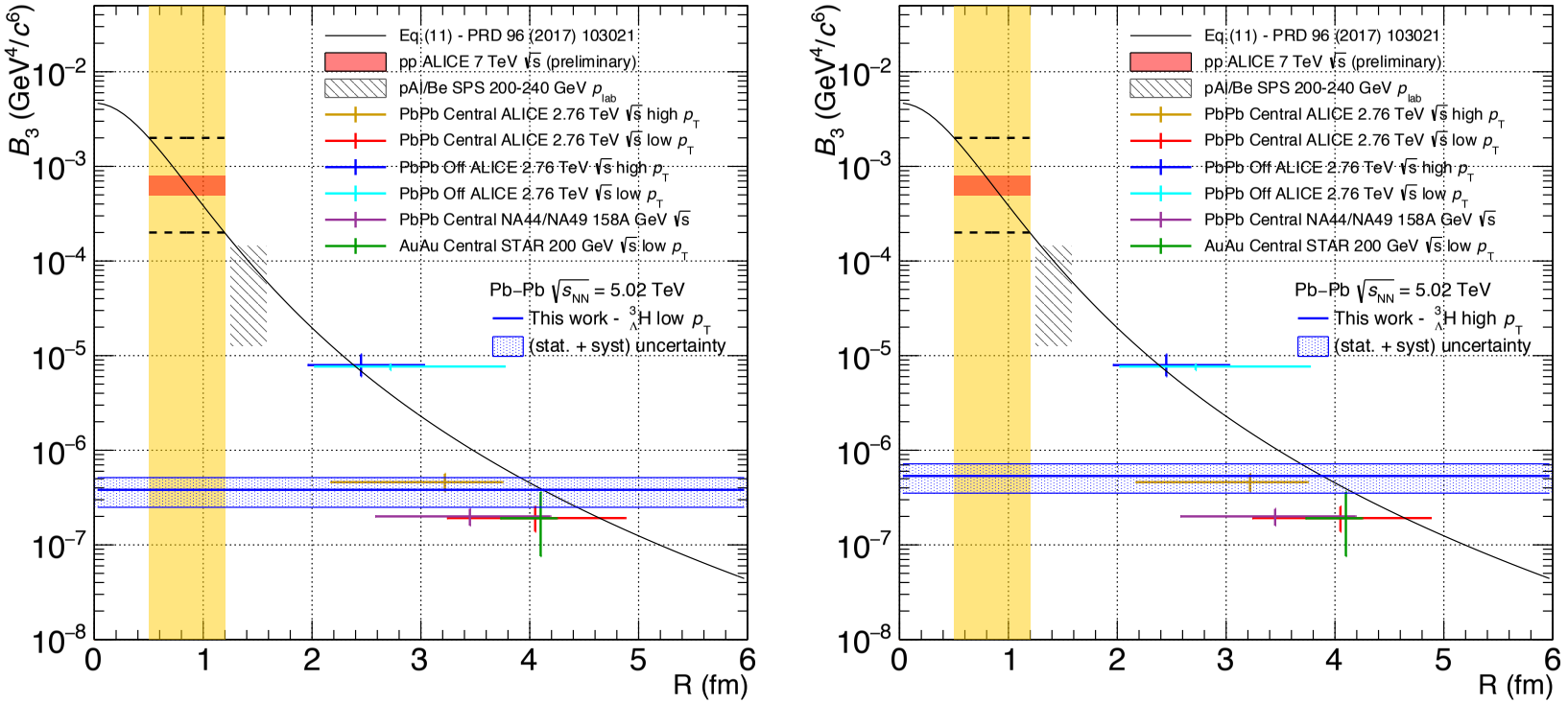

(a) low p_T **(b)** high p_T

Figure 7.12.: (a): $^3_\Lambda$H B_3 (blue solid line) for the lowest p_T interval measured in 10–40% centrality in Pb–Pb collisions at $\sqrt{s_{NN}}$= 5.02 TeV. (b): $^3_\Lambda$H B_3 (blue solid line) for the highest p_T interval measured in 10–40% centrality in Pb–Pb collisions at $\sqrt{s_{NN}}$= 5.02 TeV. The black curve is the prediction of the B_3 as a function of R, assuming the size of the ^{3}He. The colored markers are ^{3}He B_3 measured in the other experiments as described in the legend.

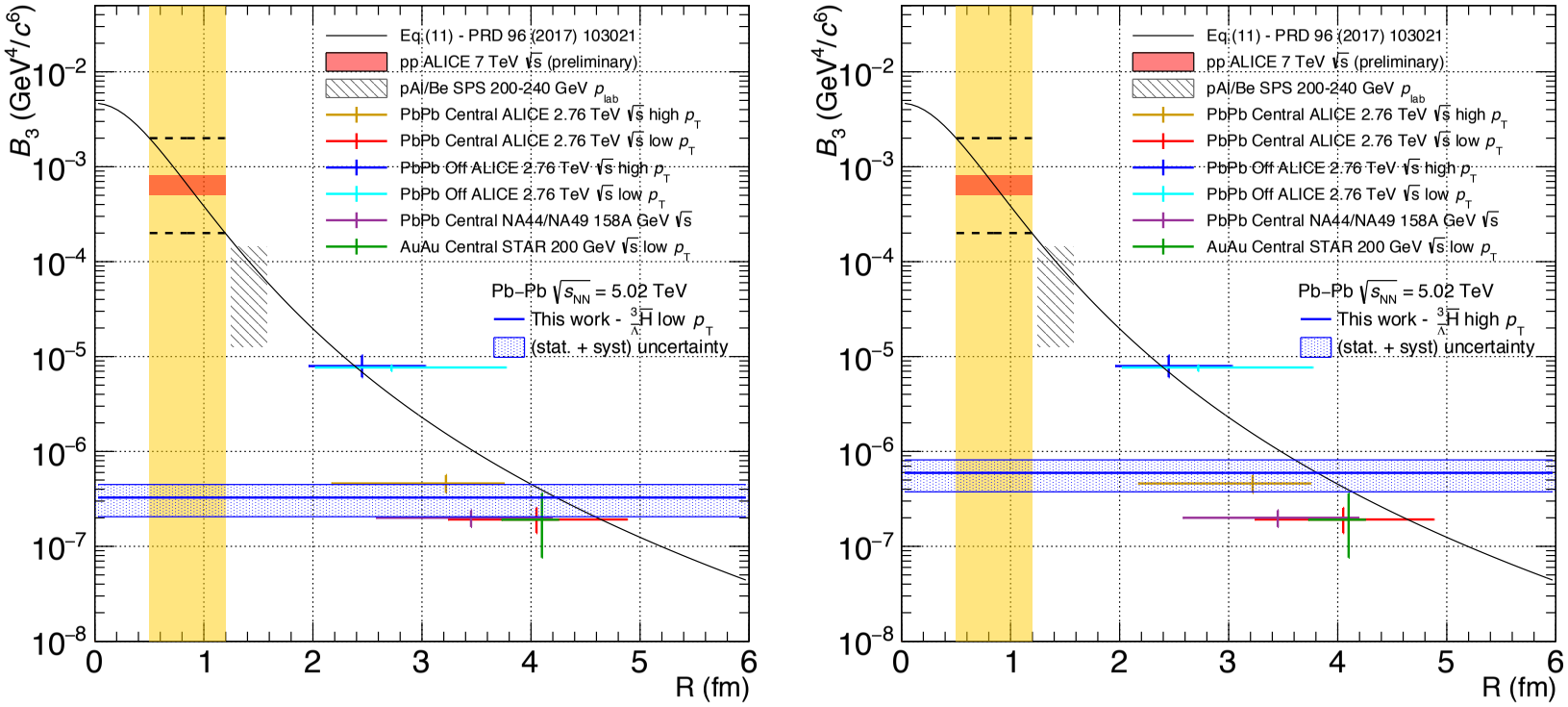

(a) low p_T **(b)** high p_T

Figure 7.13.: (a): $^3_{\Lambda}\overline{H}$ B_3 (blue solid line) for the lowest p_T interval measured in 10–40% centrality in Pb–Pb collisions at $\sqrt{s_{NN}}$= 5.02 TeV. (b): $^3_{\Lambda}\overline{H}$ B_3 (blue solid line) for the highest p_T interval measured in 10–40% centrality in Pb–Pb collisions at $\sqrt{s_{NN}}$= 5.02 TeV. The black curve is the prediction of the B_3 as a function of R, assuming the size of the ^{3}He. The colored markers are ^{3}He B_3 measured in the other experiments described in the legend.

7.7. Thermal fit

Finally, the ${}^{3}_{\Lambda}\mathrm{H}$ and ${}^{3}_{\Lambda}\overline{\mathrm{H}}$ $\mathrm{d}N/\mathrm{d}y$ are included in the so-called “thermal fit", which is a fit with a thermal model to the whole measured $\mathrm{d}N/\mathrm{d}y$ at the same energy and in the same centrality class. In this case the fit is done using the hadrons, nuclei and hypernuclei yields measured in Pb–Pb collisions at $\sqrt{s_{\mathrm{NN}}}$= 5.02 TeV in the 0–10% centrality class. The fit is done with three different statistical thermal model: the GSI-Heidelberg [81], the THERMUS model [155] and the SHARE model [147]. They depends on the chemical freeze-out temperature T_{chem}, the baryon chemical potential μ_B and the source volume V. There are two additional parameters, called γ_q and γ_s, which allow the possibility to assume an incomplete thermal equilibration for the non-strange particles (i.e. $\pi^{\pm}$, p, d, ^{3}He) and the strange particles (i.e. K^{0}_{s}, Λ, Ξ, Ω, ${}^{3}_{\Lambda}\mathrm{H}$), respectively. In all the models it is possible to fix or leave this γ factors free. However, the GSI-Heidelberg and the THERMUS model are always used fixing the γ_q to 1, assuming a complete thermalization of all non-strange particles.

In every thermal fit the ${}^{3}_{\Lambda}\mathrm{H}$ and the ${}^{3}_{\Lambda}\overline{\mathrm{H}}$ $\mathrm{d}N/\mathrm{d}y$ are corrected for the B.R. = 25% for the 2 body decay channel and then included in the list of the particle yields.

Figure 7.14a shows the results of thermal fit done with the GSI-Heidelberg model [156], while in Figure 7.14b the data are compared with the fit result through a ratio. The outcome of the fit is a chemical freeze-out temperature T_{chem} = 153 MeV and a baryon chemical potential μ_B = 0.1 MeV, which is close to the expected null value. Particle yields of light flavor hadrons and (hyper-)nuclei are described over 7 order of magnitude with deviation within 3σ for most of them. Only the preliminary yields of protons and $\Xi^{\pm}$ show a larger deviation. In particular, the deviation of the protons might be related to a baryon annihilation in the hadronic phase or to an incomplete hadron spectrum.

The fit with the THERMUS model [157] is shown Figure 7.15. In this case the K^{*} yield is not included in the fit and all the other $\mathrm{d}N/\mathrm{d}y$ are fitted with two model configurations both with μ_B fixed to 0. In the first one the γ_s is not constraint, and this gave as result γ_s = 1.17 pm 0.04 and T_{chem} = 153 $\pm$ 2 MeV, which is in agreement with the T_{chem} of GSI-Heidelberg. The second configuration assumes γ_s = 1 and the result is still in agreement with the previous one but the temperature decreases to 152 $\pm$ 2 MeV since a complete strangeness equilibration is requested. Also the comparison of the volumes between the two configurations go in the same direction, since waiting for a complete thermalization of strange particle implies a larger time for the medium to thermalize and to expand.

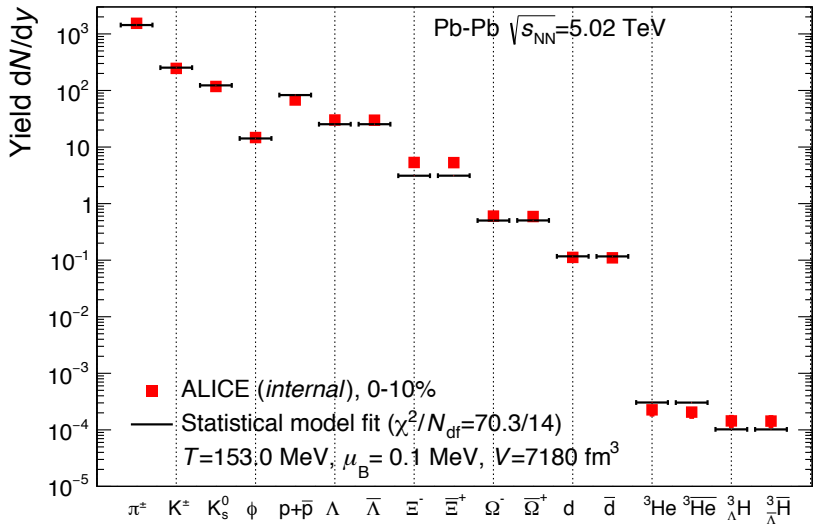

(a) Thermal fit to the dN/dy measured in Pb–Pb collisions at $\sqrt{s_{NN}}$= 5.02 TeV with the GSI-Heidelberg model [156].

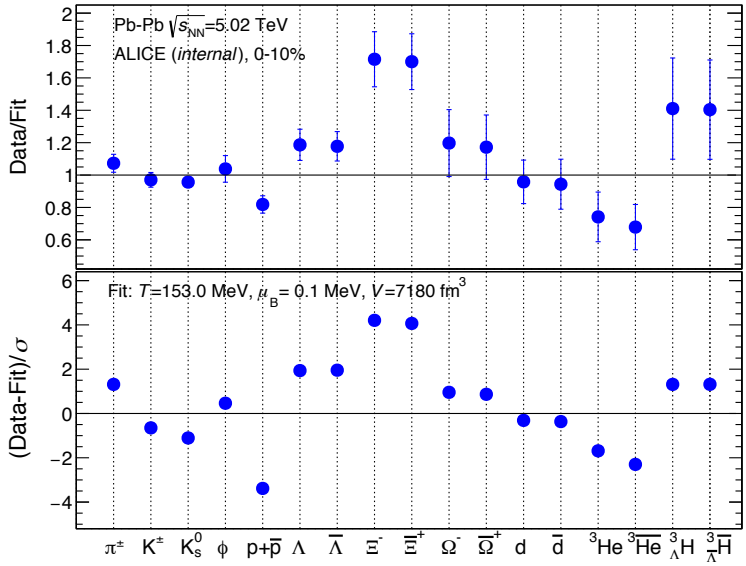

(b) Ratio of the measured dN/dy in Pb–Pb collisions at $\sqrt{s_{NN}}$= 5.02 TeV with the result of the fit (top) and deviation from the fit result in number of σ (bottom).

The last thermal fit is done with the SHARE model [158] and is shown in Figure 7.16. The fit is performed with three different configurations of the model. The first one uses γ_s and γ_q as free parameters, which means assuming an incomplete equilibration of both non-strange and strange particles. Firstly, the fit is performed without including nuclei and $(^3_{\bar{\Lambda}}\bar{\text{H}})^3_\Lambda$H leading to T_{chem} = 160 $\pm$ 10 MeV, γ_s = 0.95 $\pm$ 0.22 and γ_s = 0.89 $\pm$ 0.14. Then it is done including the (hyper-)nuclear yield sector with strong reduction of the T_{chem} = 139

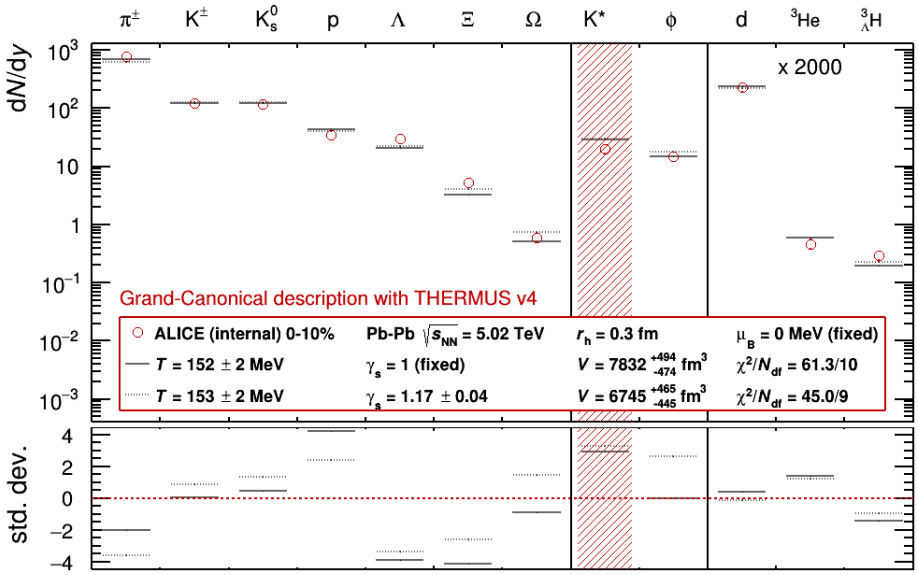

Figure 7.15.: Thermal fit to the dN/dy measured in Pb–Pb collisions at $\sqrt{s_{\rm NN}}$= 5.02 TeV with the THERMUS model [157]. The bottom part show the deviation from the fit (Fit-data) in number of σ.

$\pm$ 1 MeV and an increase of both γ_s = 2.08 $\pm$ 0.10 and γ_s = 1.63 $\pm$ 0.05. Also looking the results of the fit done with this configuration, shows a larger deviation of the nuclei and $(^3_\Lambda\overline{\rm H})^3_\Lambda$H from the model. The second configuration of the SHARE model assumes a complete thermalization of the non-strange particle (γ_q=1) and the result is T_{chem} = 154 $\pm$ 3 MeV, γ_s = 1.14 $\pm$ 0.05, which are in agreement with the THERMUS model used in the same configuration. Finally, the fit is performed fixing both γ_s and γ_q, that is the other configuration used for THERMUS and the unique one for the GSI-Heidelberg and the result of T_{chem} = 154 $\pm$ 3 MeV is in agreement with both two models.

The $^3_\Lambda$H and the $^3_\Lambda\overline{\rm H}$ dN/dy have been included in the thermal fits performed with three different thermal model, used in different configurations. The thermal models with a T_{chem} = 153 and γ_s unconstrained, better describe the dN/dy measured in this thesis and their deviation from the resulting fit is below 1σ. When the γ_s is fixed to 1 the yields are reproduced as well, but with a slightly higher significance. The closing remark from the thermal fits is that the $^3_\Lambda$H and $^3_\Lambda\overline{\rm H}$ can be produced thermally from the medium created in the heavy ion collision. This extremely surprisingly, since most of the theorists of the QGP tend to be in favor of a coalescence production mechanism for these loosely bound objects.

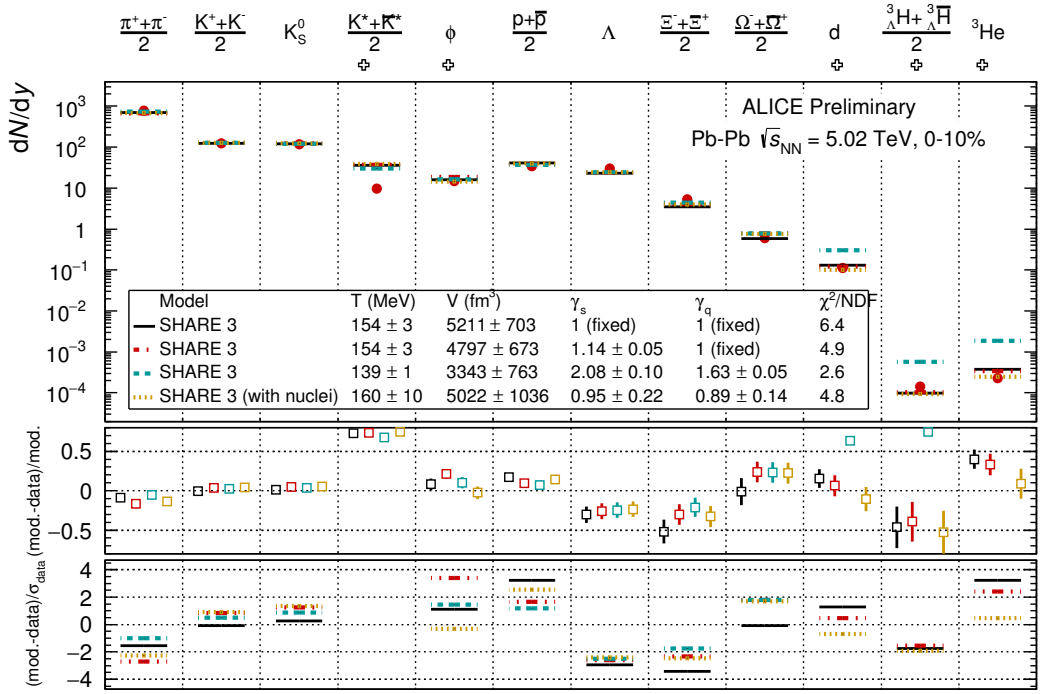

Figure 7.16.: Thermal fit to the $\mathrm{d}N/\mathrm{d}y$ measured in Pb–Pb collisions at $\sqrt{s_{\mathrm{NN}}}$= 5.02 TeV with the SHARE model [158]. The bottom part show the difference (Fit-data) normalized to the fit result and to the $\mathrm{d}N/\mathrm{d}y$ uncertainty.

Chapter 8.

Conclusion

"You certainly usually find something, if you look, but it is not always quite the something you were after."

— *The Hobbit*, J.R.R. Tolkien, 1892–1975

This thesis project was focused on lightest known Λ-hypernucleus, the ${}^{3}_{\Lambda}\mathrm{H}$ and there were two goals: the lifetime estimate with the highest possible precision and the measurement of the production in order to better understand the mechanism for the formation of light (anti-)hypernuclei in heavy ion collisions. The highlights of the work described in the previous chapters can be summarised in two plots.

The first one, Figure 8.1, shows the collection of the lifetime values available in literature compared to the results obtained in this thesis studying the two body and three body decay channels. The estimate from the two body decay analysis has been performed using two different techniques and improving the precision with respect to the previous results [70]. Still more important is the first measurement of the lifetime value from the three body decay channel which shows a good agreement with the other two values found in this analysis, even if the analysis has been performed using only half of the events of the Pb–Pb collisions at $\sqrt{s_{\mathrm{NN}}}$= 5.02 TeV collected during 2015 data taking period. The future months will be fundamental to analyse the full data sample and, thus, to improve the prevision for the final result.

However the obtained results, both from two and three body decay channels, seem to go in the direction predicted from the theory of a lifetime slightly below the free Λ lifetime. The most important aspect for any future analysis in this field, in order to solve the "lifetime puzzle", is the precision of the final measurement. In this sense the Pb–Pb data taking period of the ALICE experiment at the end of 2018 will be crucial to improve the available

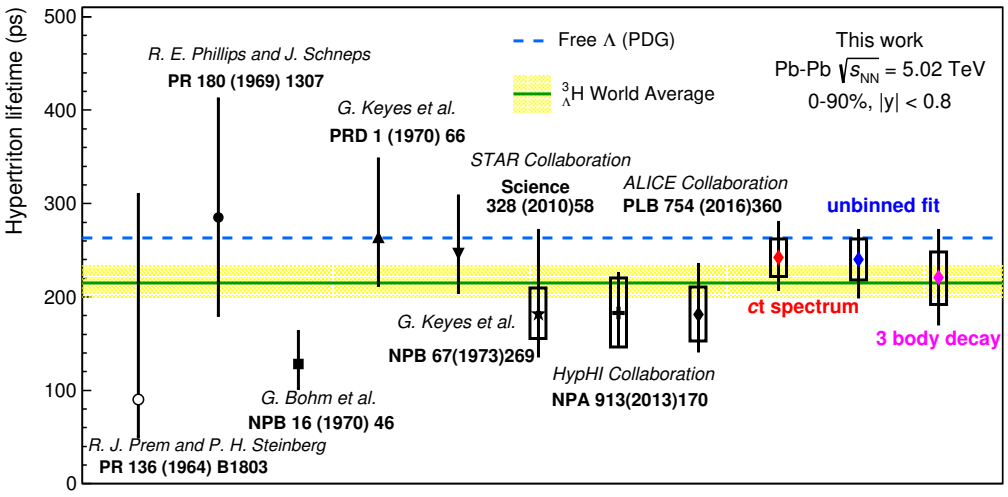

Figure 8.1.: $^3_\Lambda$H lifetime values (red, blue and magenta diamonds) obtained in this analysis compared to published results. The band represents the average of the published $^3_\Lambda$H lifetime measurements ($\tau = 216^{+19}_{-16}$ ps), while the dashed line is the lifetime of Λ from the Particle Data Group.

data sample. In addition, experimental inputs on this open question of the hypernuclear physics, are expected from fixed target experiments where it might be possible to perform a direct time measurement.

The second aim of this thesis was the study of the production of the $^3_\Lambda$H in order to improve the knowledge about the formation mechanism of the light (anti-)hypernuclei in heavy ion collisions. As already described in Chapter 2, there are two classes of models: the Statistical Hadronisation Models and the Coalescence Models. These two approaches predict the formation of the $^3_\Lambda$H in two different stages of the heavy ion collision evolution: the SHM at the *chemical freeze-out* and the coalescence at the *kinetic freeze-out*. The results presented for the $\mathrm{d}N/\mathrm{d}y$ as a function of the $\langle\, \mathrm{d}N_{ch}/\mathrm{d}\eta \rangle$ and for the B_3 showed a good agreement with the interpretation of the production via baryons coalescence. On the other hand the production p_T spectra in semi-central collisions and the S_3 in the most central collisions are in agreement with the description provided by the SHM of a thermal production from an expanding source described with relativistic hydrodynamics.

In particular, among the several presented results for the $^3_\Lambda$H production, it is surprising the agreement of the measured $\mathrm{d}N/\mathrm{d}y$ in the thermal fits, Figure 8.2, performed to all the hadron species measured by the ALICE experiment. This is an important open point of the

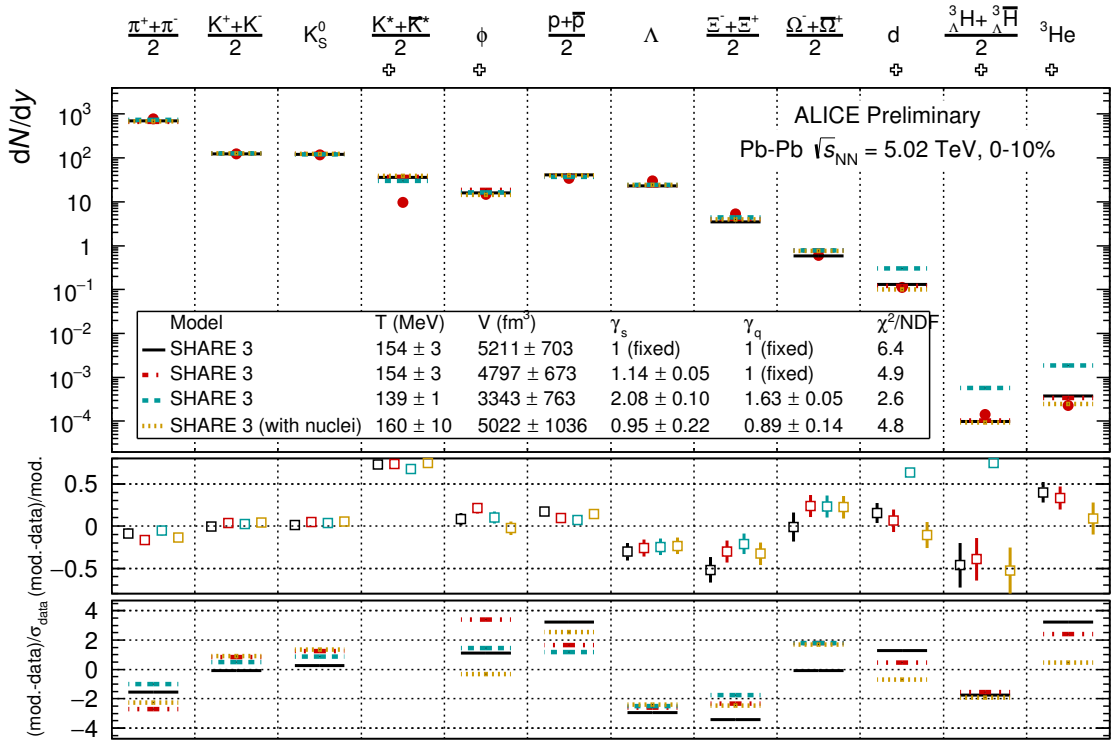

Figure 8.2.: Thermal fit to the dN/dy measured in Pb–Pb collisions at $\sqrt{s_{\mathrm{NN}}}$= 5.02 TeV with the SHARE model [80]. The bottom part shows the difference (Fit-data) normalized to the fit results and to the dN/dy uncertainty.

high energy nuclear physics, since the $^{3}_{\Lambda}$H is a loosely bound object and it is not expected to survive in such a hot medium.

The analysis results presented in this work challenge theoretical models for (anti-)hypernuclei production and suggest additional experimental effort to reduce the uncertainties affecting the measurements with the aim of constraining the models.

Appendix A.

Monte Carlo cut study

This appendix is devoted to the different set of cuts tested on the MC production that have been only introduced and discussed in Sec.4.3.2. The set of cuts are reported in Table A.1. The figures related to Set 2 are presented in Sec.4.3.2. Here the invariant mass spectra of ${}^{3}_{\Lambda}\mathrm{H}$ and ${}^{\overline{3}}_{\overline{\Lambda}}\overline{\mathrm{H}}$ as well as the S/B ratio and significance[1] are reported for the other selection criteria configurations.

MC preliminary study						
	Set 1	Set 2	Set 3	Set 4	Set 5	Set 6
DCA^{π}_{PV} (cm)	≥ 0.4	≥ 0.2	≥ 0.1	≥ 0.1	≥ 0.2	≥ 0.4
$c\tau$ (cm)		> 1			> 0.5	
$\mathrm{DCA}_{^3\mathrm{He},\pi}$ (cm)			$< 0.7, 0.3, 0.1$			
$\cos(\theta_{pointing})$			$> 0.94, 0.99, 0.995$			

Table A.1.: Sets of different selection criteria tested on the MC production. More details in the Sec.4.3.2.

The fitting function is the sum of a gaussian and pol3 for the signal and background contribution respectively. S and B, the signal and background counts respectively, are obtained integrating the corresponding function in the mass window $\pm 3\sigma$ with respect to the mean value from the gaussian distribution.

[1] Significance defined as $\mathrm{S}/\sqrt{\mathrm{S}+\mathrm{B}}$

Set 1

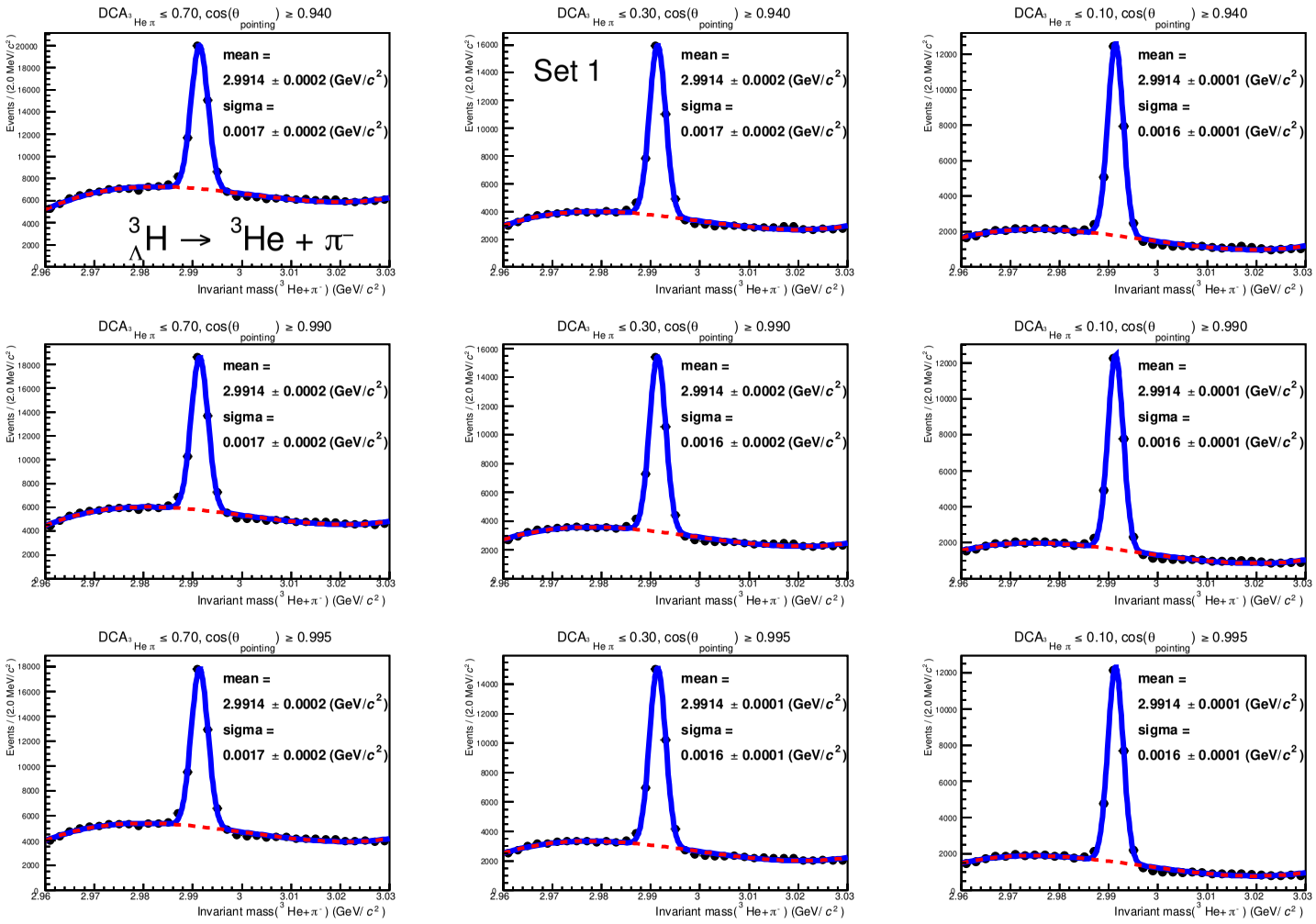

Figure A.1.: $^3_\Lambda$H invariant mass spectra from Set 1. Fixed cuts: $DCA^{\pi}_{PV} > 0.4$ cm, $ct > 1$ cm and $|y| < 0.5$. Cut variation: $DCA_{^3He,\pi} < 0.7, 0.3, 0.1$ cm and $\cos(\theta_{pointing}) > 0.94, 0.99, 0.995$, reported on top of each plot. Fit are performed with sum of a gaussian (signal) and a pol3 (background).

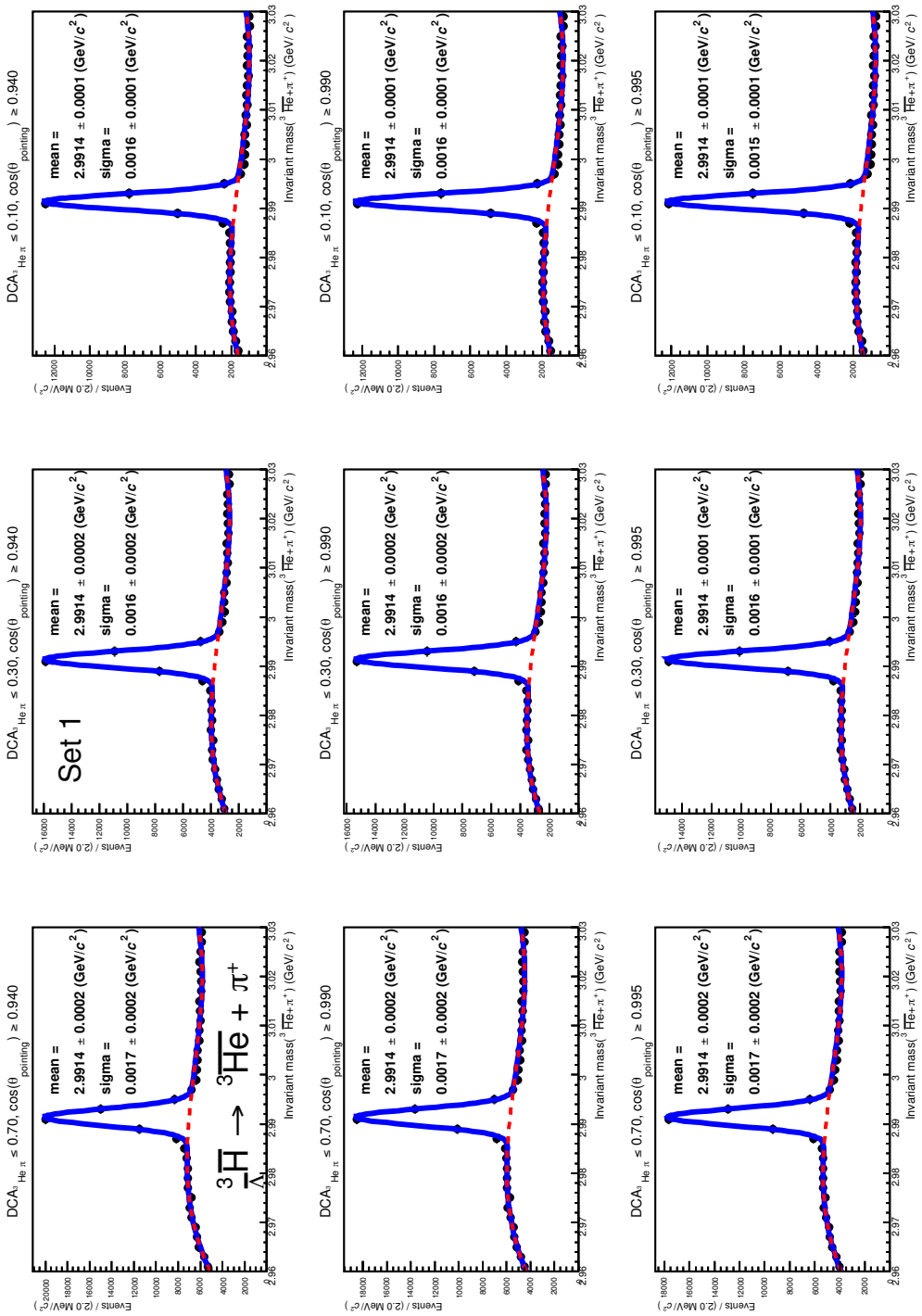

Figure A.2.: $^{3}_{\Lambda}\overline{\mathrm{H}}$ invariant mass spectra from Set 1. Fixed cuts: $\mathrm{DCA}^{\pi}_{PV} > 0.4$ cm, $c\tau > 1$ cm and $|y| < 0.5$. Cut variation: $\mathrm{DCA}_{^3\mathrm{He},\pi} < 0.7, 0.3, 0.1$ cm and $\cos(\theta_{pointing}) > 0.94, 0.99, 0.995$, reported on top of each plot. Fit are performed with sum of a gaussian (signal) and a pol3 (background).

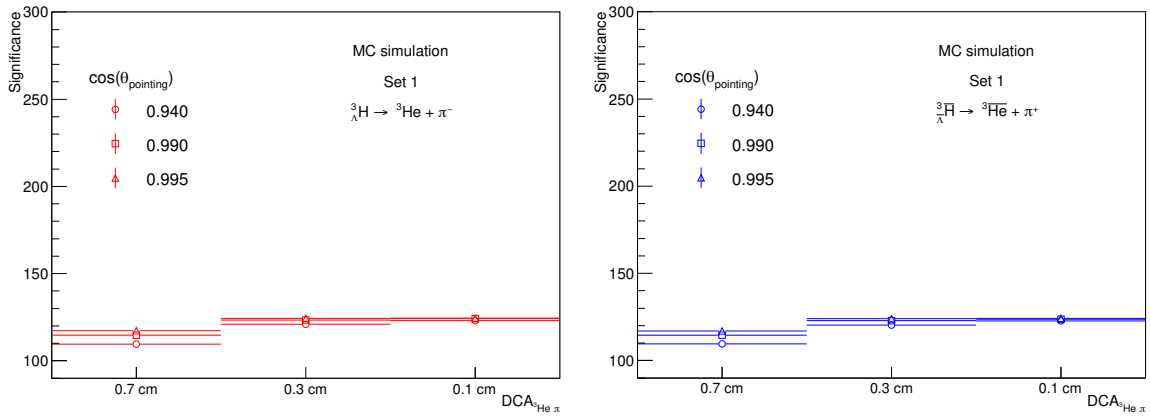

(a) Significance – ${}^{3}_{\Lambda}\mathrm{H}$

(b) Significance – ${}^{3}_{\Lambda}\overline{\mathrm{H}}$

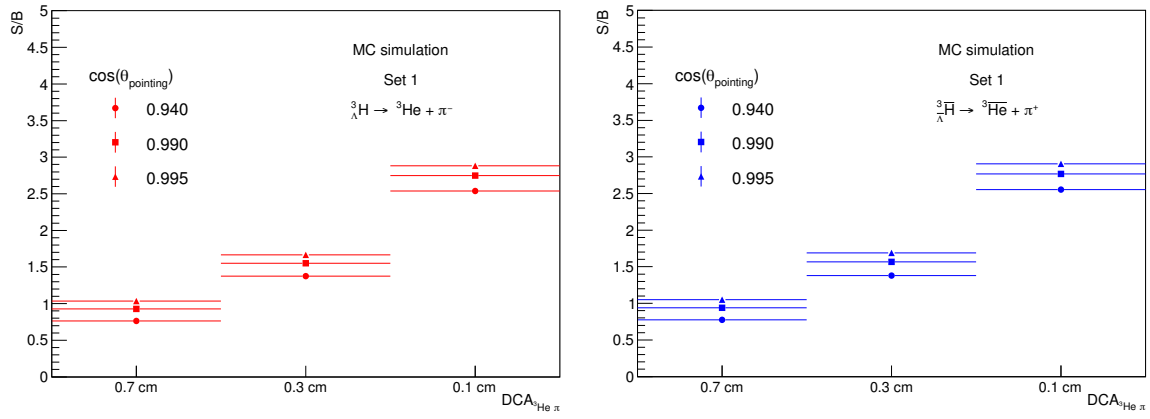

(c) S/B – ${}^{3}_{\Lambda}\mathrm{H}$

(d) S/B – ${}^{3}_{\Lambda}\overline{\mathrm{H}}$

Figure A.3.: Trend of the Significance (top) and S/B ratio (bottom) for ${}^{3}_{\Lambda}\mathrm{H}$ (left) and ${}^{3}_{\Lambda}\overline{\mathrm{H}}$ (right) reconstructed and selected with cuts of Set 1.

Set 3

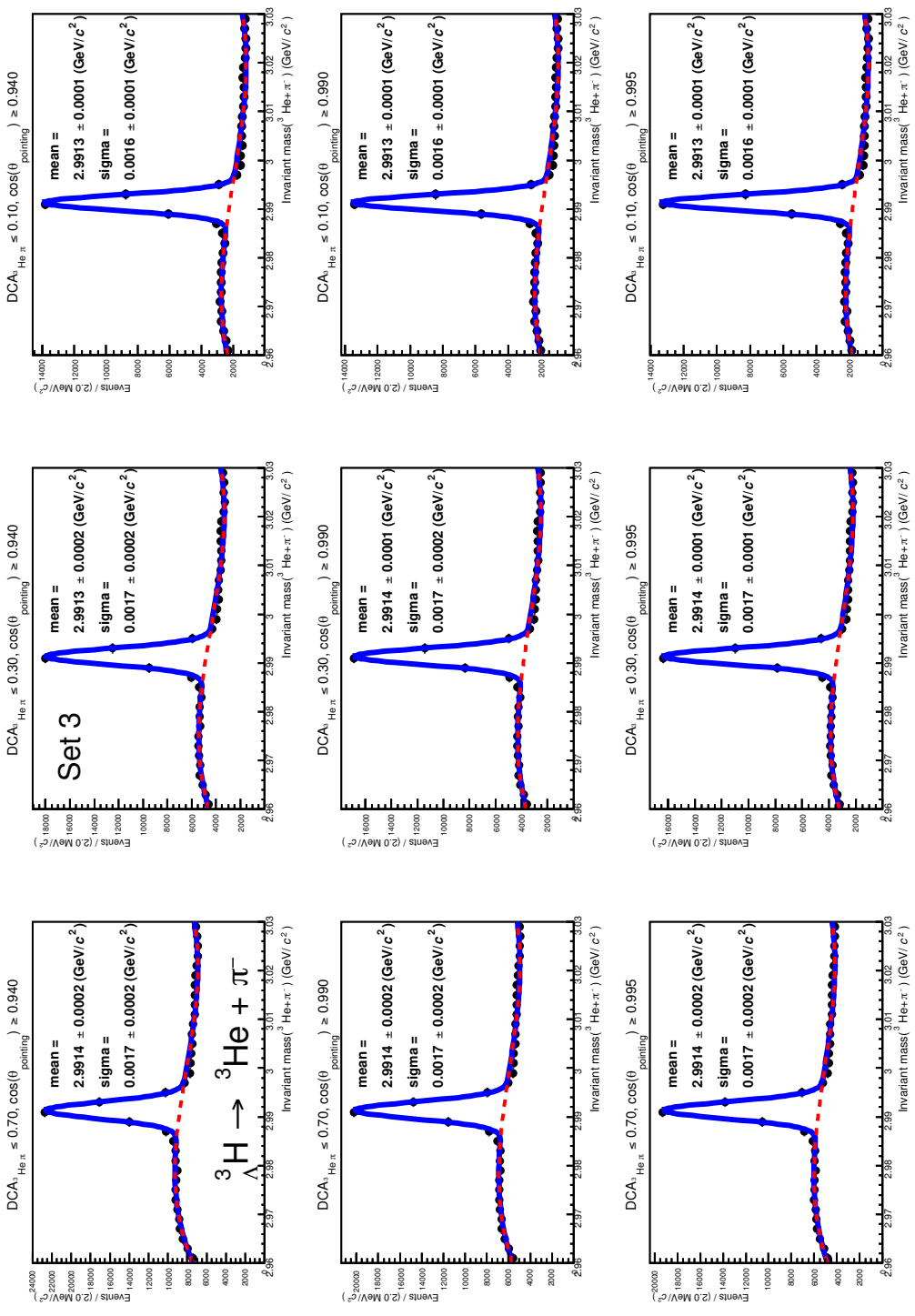

Figure A.4: $^{3}_{\Lambda}$H invariant mass spectra from Set 3. Fixed cuts: $DCA^{\pi}_{PV} > 0.1$ cm, $ct > 1$ cm and $|y| < 0.5$. Cut variation: $DCA_{^{3}He,\pi} < 0.7, 0.3, 0.1$ cm and $\cos(\theta_{pointing}) > 0.94, 0.99, 0.995$, reported on top of each plot. Fit are performed with sum of a gaussian (signal) and a pol3 (background).

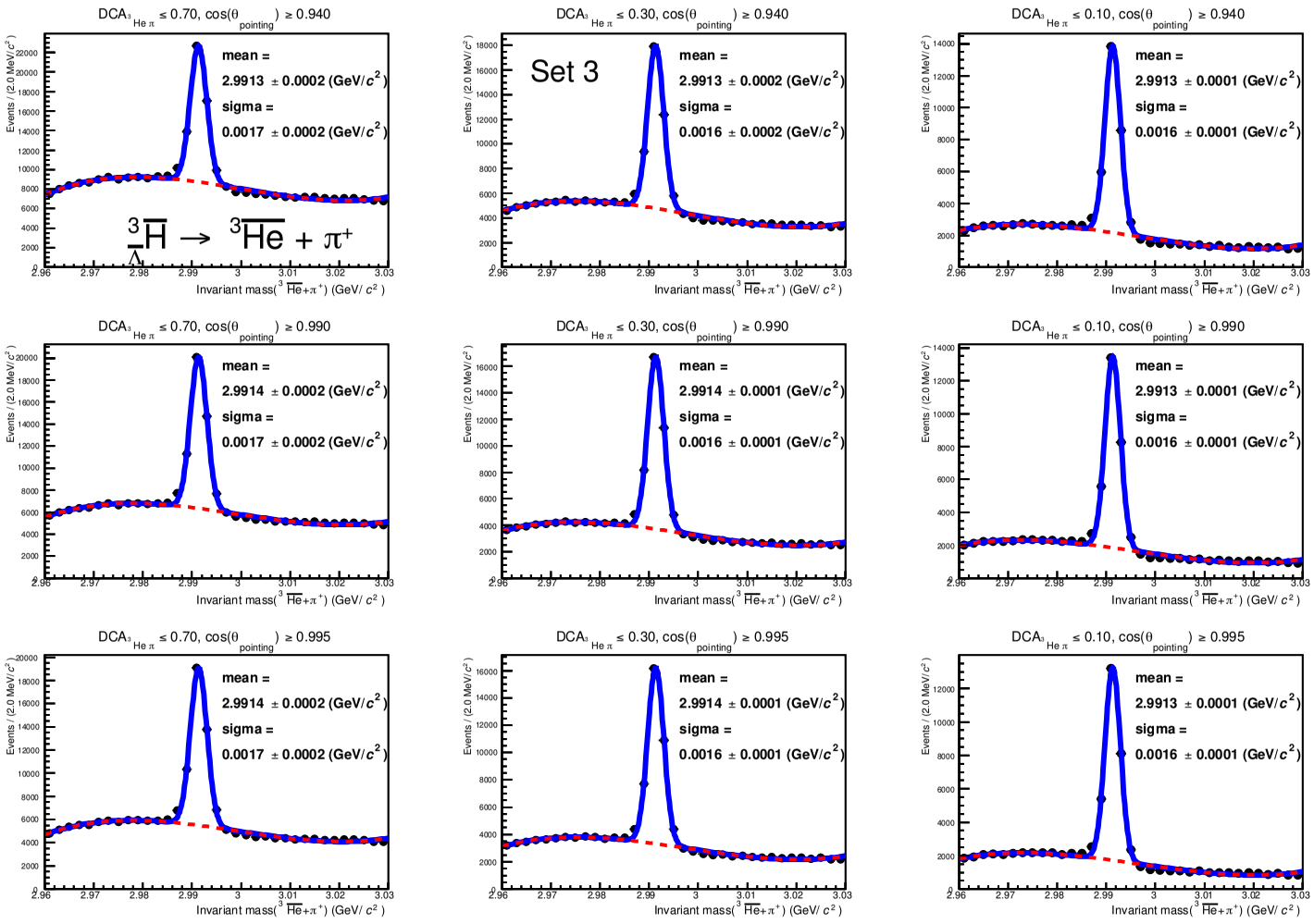

Figure A.5.: $^3_{\bar{\Lambda}}\overline{\mathrm{H}}$ invariant mass spectra from Set 3. Fixed cuts: $\mathrm{DCA}^{\pi}_{PV} > 0.1$ cm, $ct > 1$ cm and $|y| < 0.5$. Cut variation: $\mathrm{DCA}_{^3\mathrm{He},\pi} < 0.7, 0.3, 0.1$ cm and $\cos(\theta_{pointing}) > 0.94, 0.99, 0.995$, reported on top of each plot. Fit are performed with sum of a gaussian (signal) and a pol3 (background).

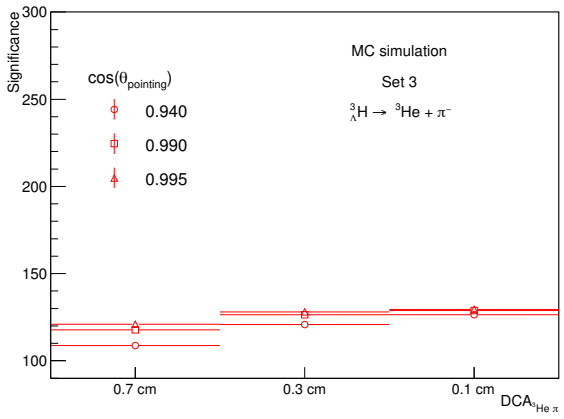

(a) Significance – ${}^3_\Lambda\mathrm{H}$

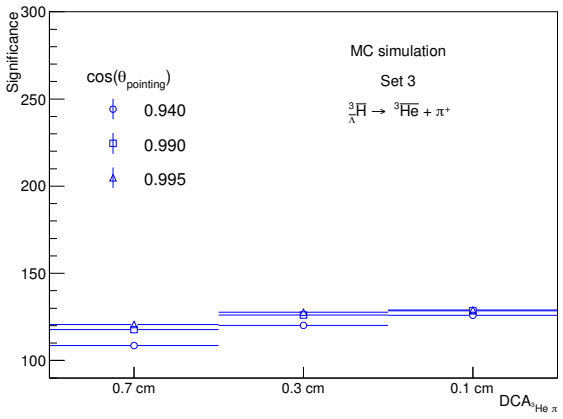

(b) Significance – ${}^3_\Lambda\overline{\mathrm{H}}$

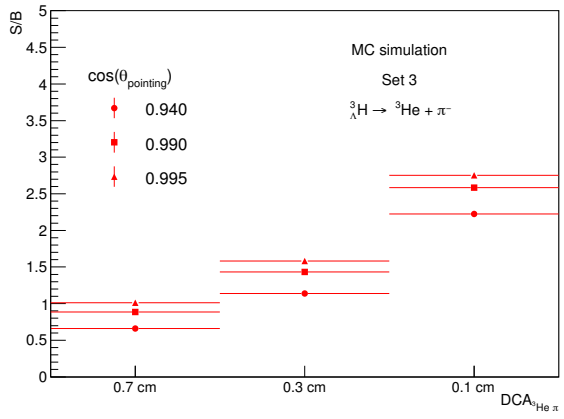

(c) S/B – ${}^3_\Lambda\mathrm{H}$

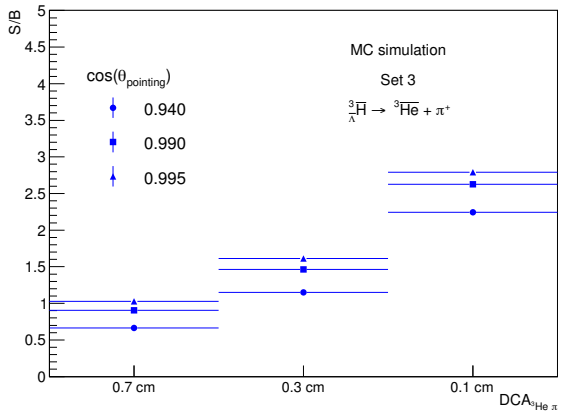

(d) S/B – ${}^3_\Lambda\overline{\mathrm{H}}$

Figure A.6.: Trend of the Significance (top) and S/B ratio (bottom) for ${}^3_\Lambda\mathrm{H}$ (left) and ${}^3_\Lambda\overline{\mathrm{H}}$ (right) reconstructed and selected with cuts of Set 3.

Set 4

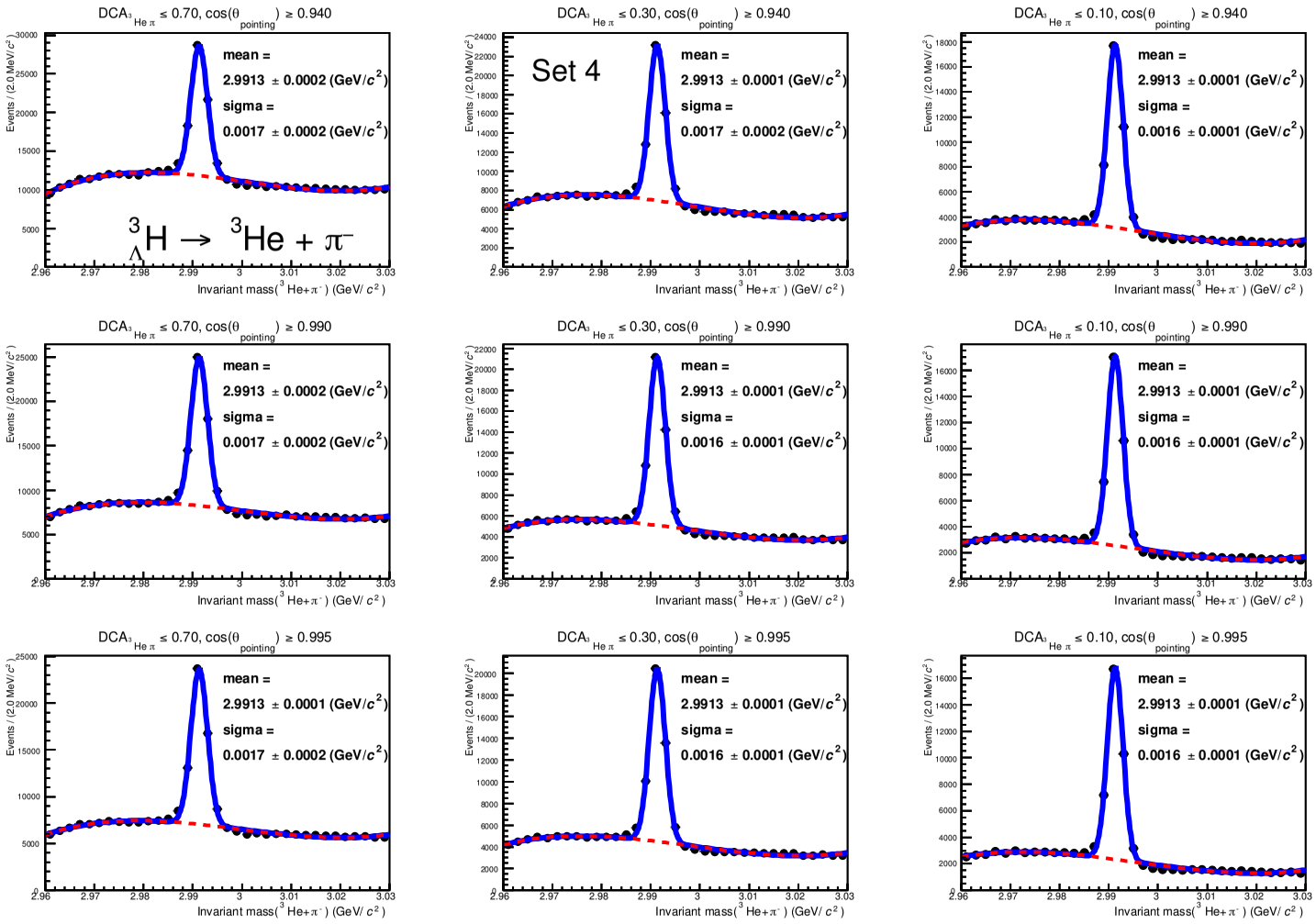

Figure A.7.: ${}^{3}_{\Lambda}\mathrm{H}$ invariant mass spectra from Set 4. Fixed cuts: $\mathrm{DCA}^{\pi}_{PV} > 0.1$ cm, $ct > 0.5$ cm and $|y| < 0.5$. Cut variation: $\mathrm{DCA}_{^3\mathrm{He},\pi} < 0.7, 0.3, 0.1$ cm and $\cos(\theta_{pointing}) > 0.94, 0.99, 0.995$, reported on top of each plot. Fit are performed with sum of a gaussian (signal) and a pol3 (background).

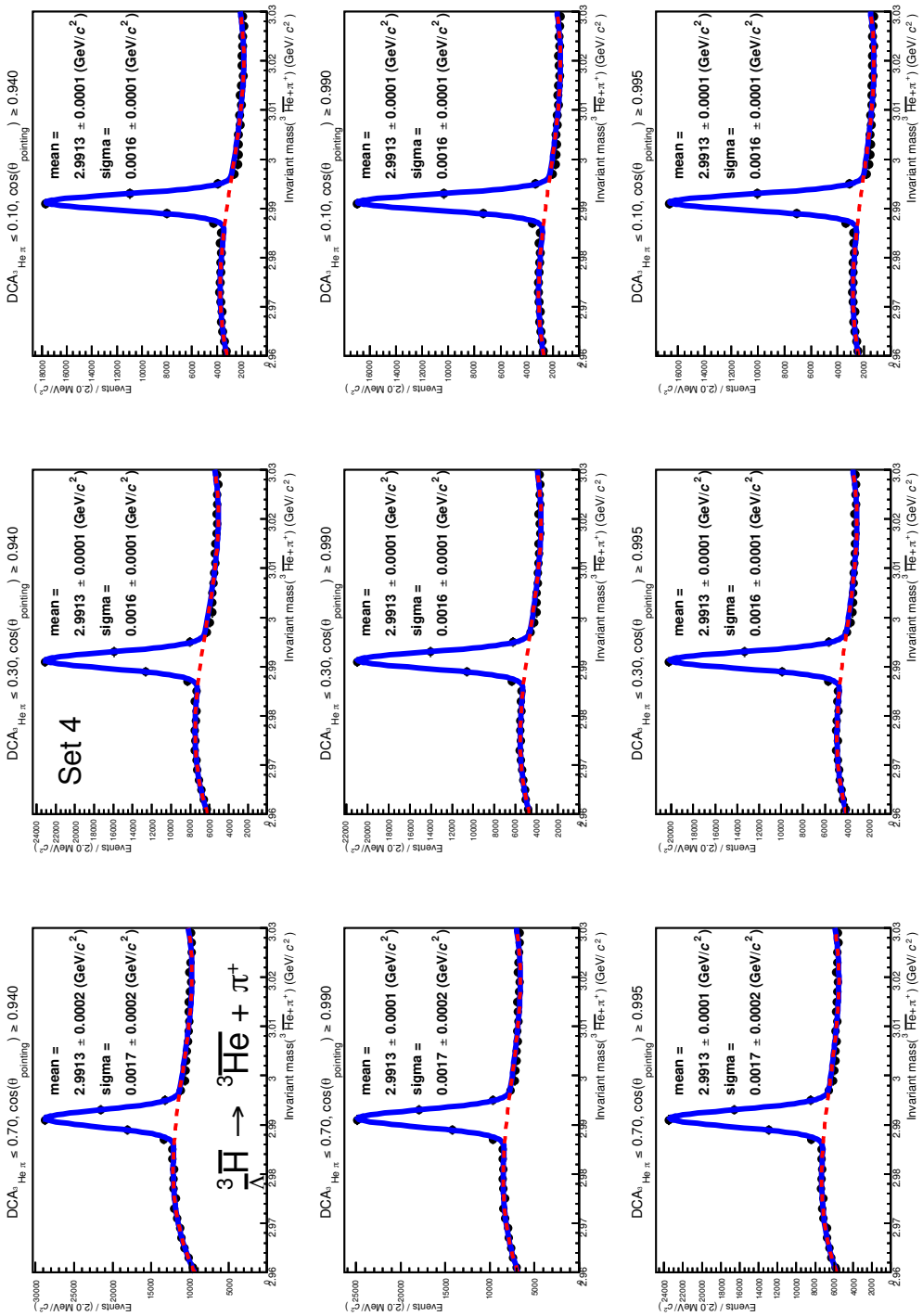

Figure A.8.: $^{3}_{\Lambda}\overline{\mathrm{H}}$ invariant mass spectra from Set 4. Fixed cuts: $\mathrm{DCA}^{\pi}_{pV} > 0.1$ cm, $ct > 0.5$ cm and $|y| < 0.5$. Cut variation: $\mathrm{DCA}_{^3\mathrm{He},\pi} < 0.7$, 0.3, 0.1 cm and $\cos(\theta_{pointing}) > 0.94$, 0.99, 0.995, reported on top of each plot. Fit are performed with sum of a gaussian (signal) and a pol3 (background).

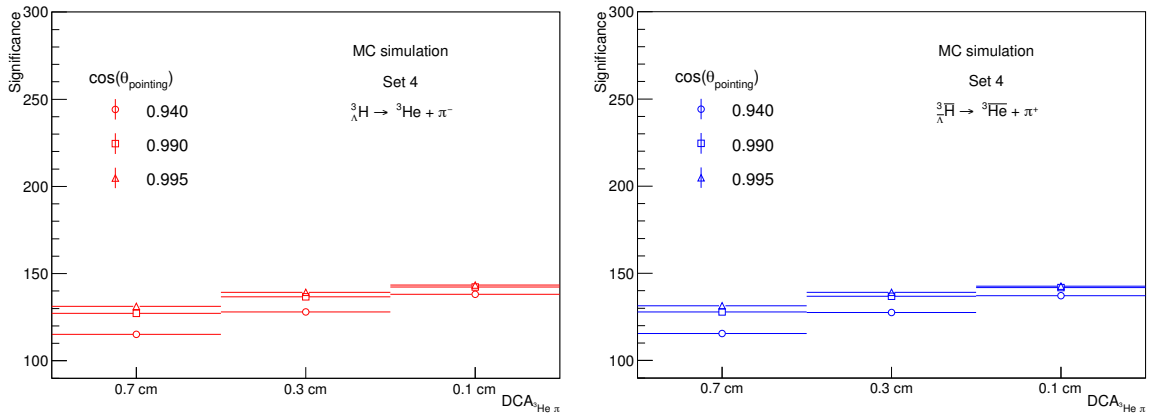

(a) Significance – ${}^{3}_{\Lambda}\mathrm{H}$ **(b)** Significance – ${}^{3}_{\Lambda}\overline{\mathrm{H}}$

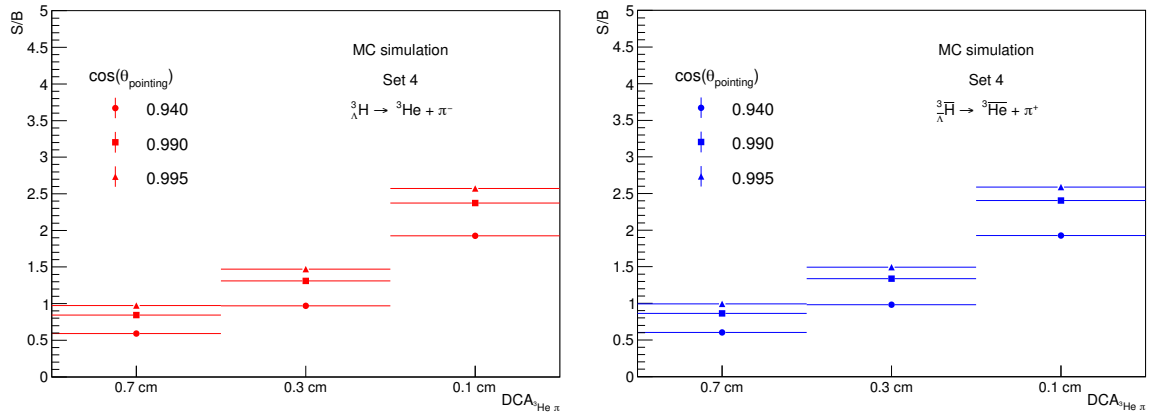

(c) S/B – ${}^{3}_{\Lambda}\mathrm{H}$ **(d)** S/B – ${}^{3}_{\Lambda}\overline{\mathrm{H}}$

Figure A.9.: Trend of the Significance (top) and S/B ratio (bottom) for ${}^{3}_{\Lambda}\mathrm{H}$ (left) and ${}^{3}_{\Lambda}\overline{\mathrm{H}}$ (right) reconstructed and selected with cuts of Set 4.

Set 5

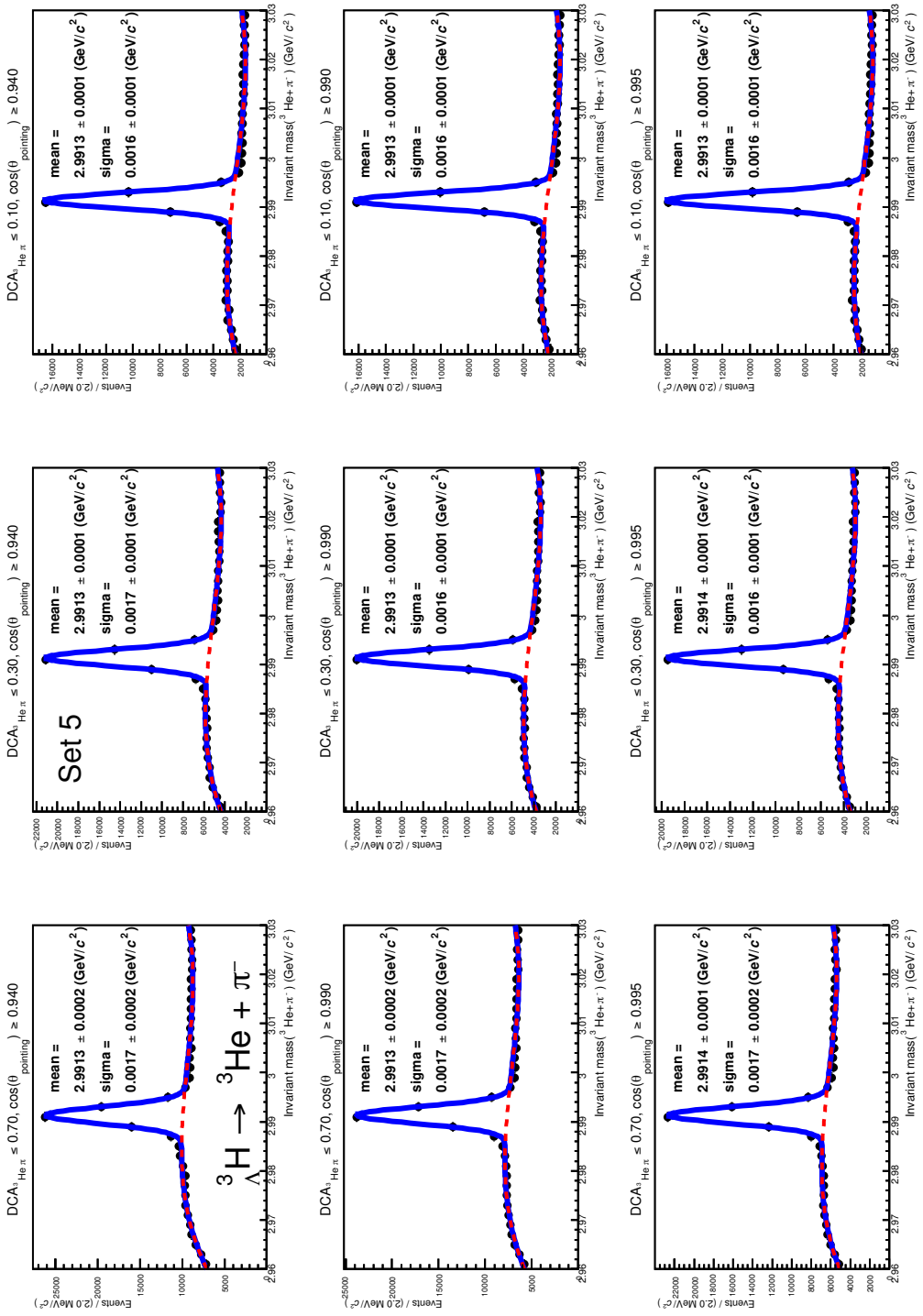

Figure A.10: $^3_\Lambda$H invariant mass spectra from Set 5. Fixed cuts: $\mathrm{DCA}^{\pi}_{PV} > 0.2$ cm, $ct > 0.5$ cm and $|y| < 0.5$. Cut variation: $\mathrm{DCA}_{^3\mathrm{He},\pi} < 0.7, 0.3, 0.1$ cm and $\cos(\theta_{pointing}) > 0.94, 0.99, 0.995$, reported on top of each plot. Fit are performed with sum of a gaussian (signal) and a pol3 (background).

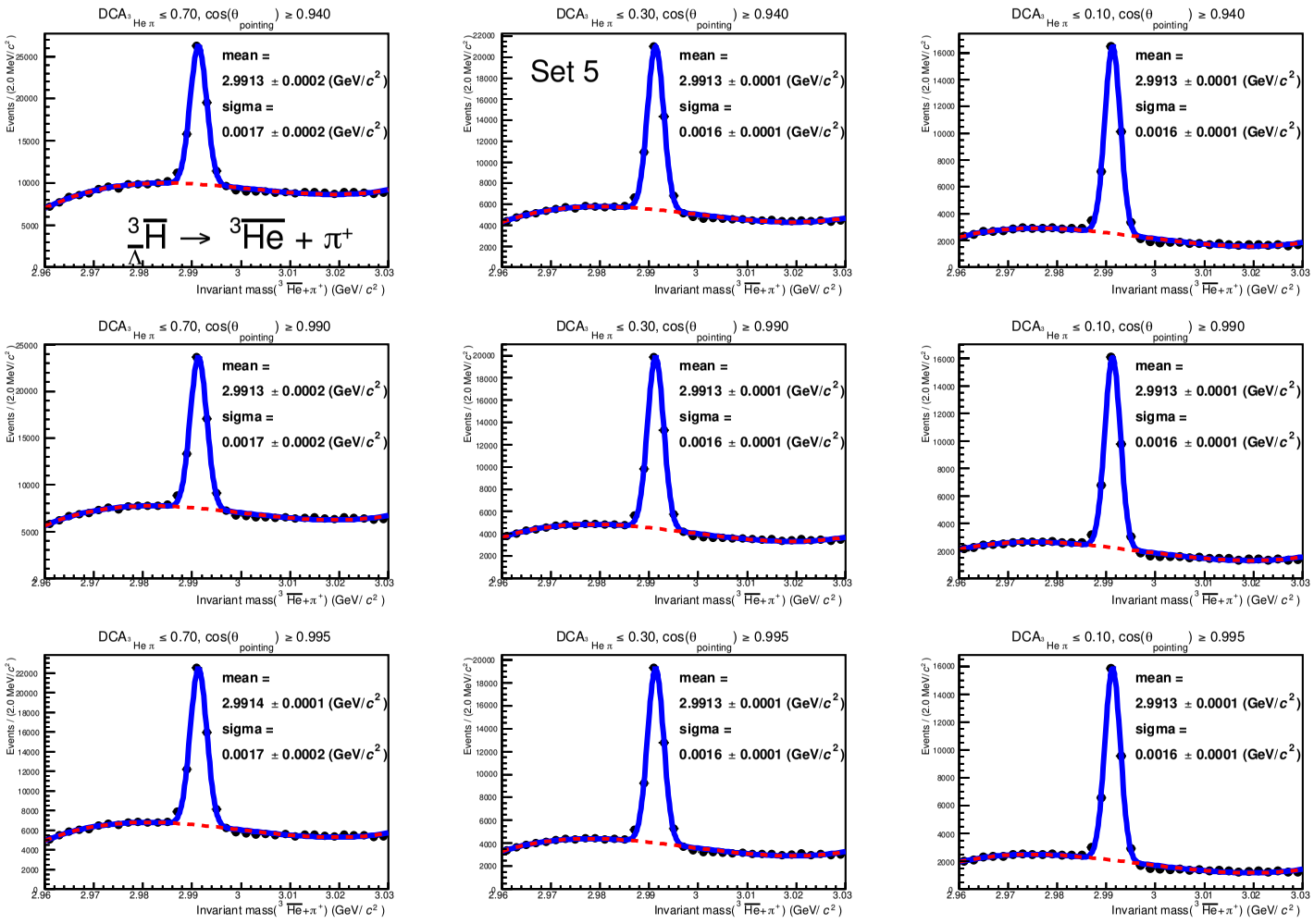

Figure A.11.: $^{3}_{\overline{\Lambda}}\overline{\mathrm{H}}$ invariant mass spectra from Set 5. Fixed cuts: $\mathrm{DCA}^{\pi}_{PV} > 0.2$ cm, $ct > 0.5$ cm and $|y| < 0.5$. Cut variation: $\mathrm{DCA}_{^3\mathrm{He},\pi} < 0.7$, 0.3, 0.1 cm and $\cos(\theta_{pointing}) > 0.94$, 0.99, 0.995, reported on top of each plot. Fit are performed with sum of a gaussian (signal) and a pol3 (background).

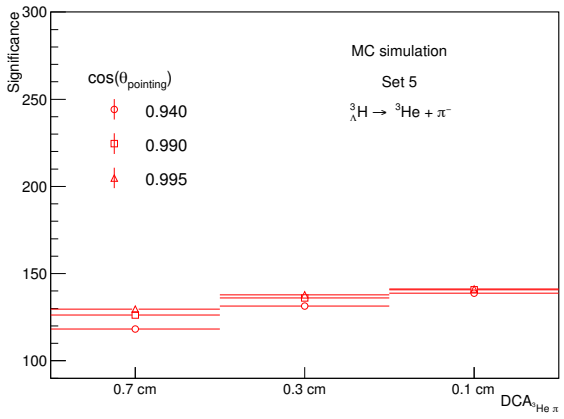

(a) Significance – $^3_\Lambda\mathrm{H}$

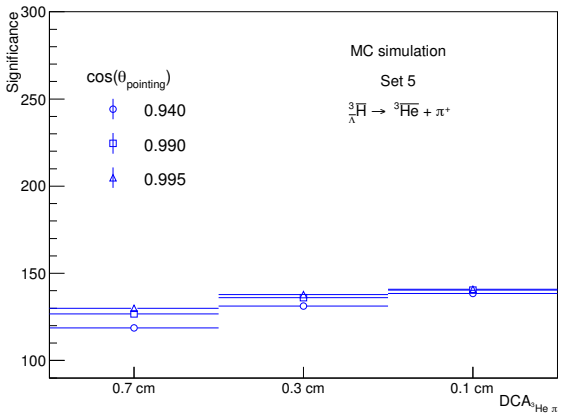

(b) Significance – $^3_\Lambda\overline{\mathrm{H}}$

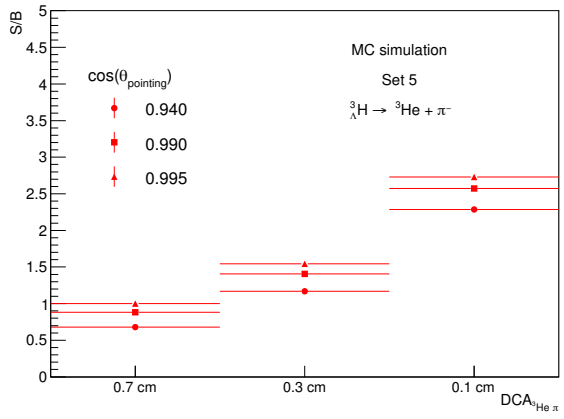

(c) S/B – $^3_\Lambda\mathrm{H}$

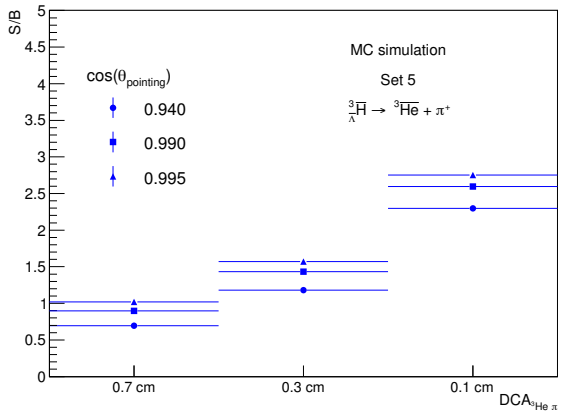

(d) S/B – $^3_\Lambda\overline{\mathrm{H}}$

Figure A.12.: Trend of the Significance (top) and S/B ratio (bottom) for $^3_\Lambda\mathrm{H}$ (left) and $^3_\Lambda\overline{\mathrm{H}}$ (right) reconstructed and selected with cuts of Set 5.

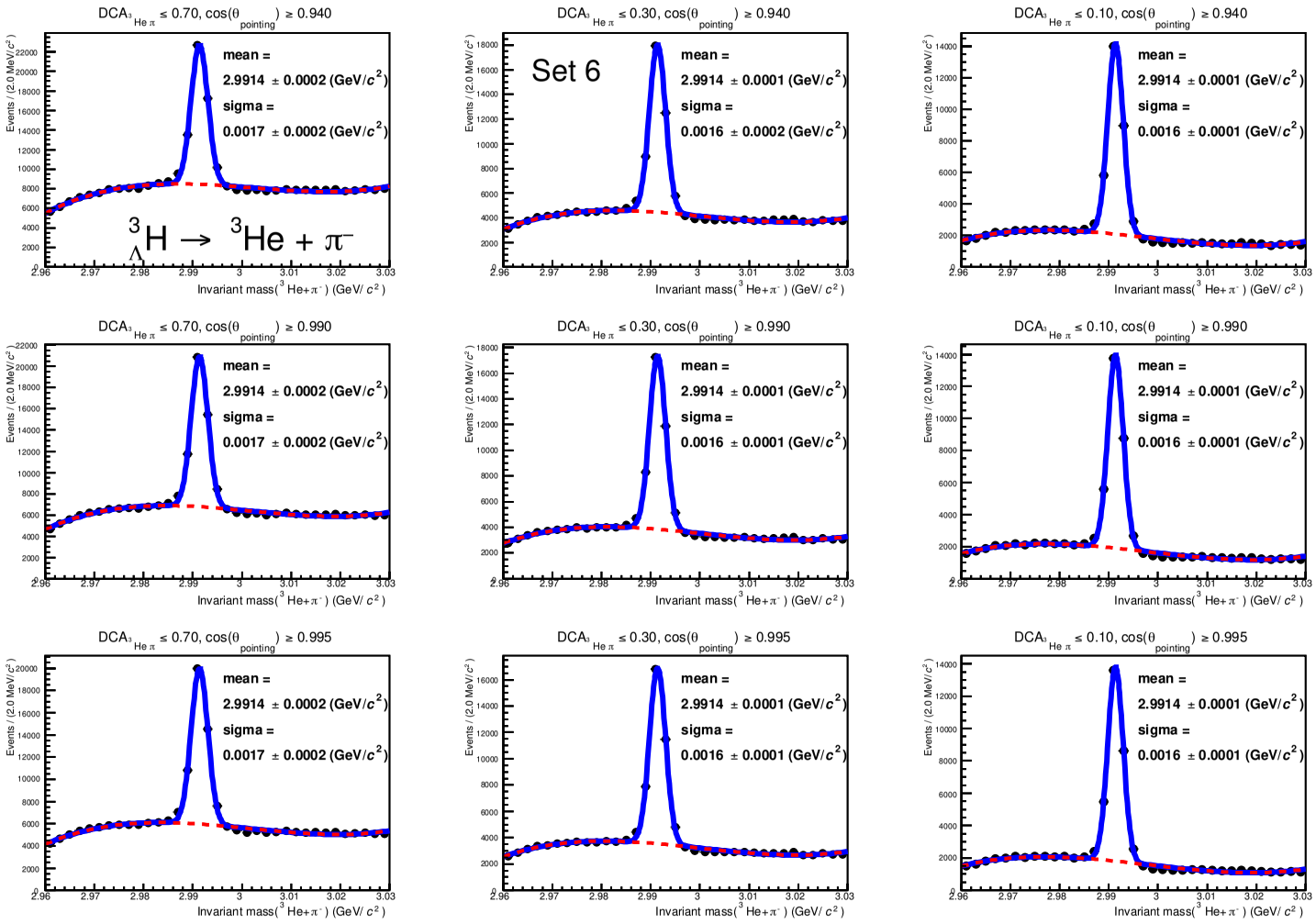

Figure A.13.: ${}^{3}_{\Lambda}\mathrm{H}$ invariant mass spectra from Set 6. Fixed cuts: $\mathrm{DCA}^{\pi}_{PV} > 0.4$ cm, $c\tau > 0.5$ cm and $|y| < 0.5$. Cut variation: $\mathrm{DCA}_{^3\mathrm{He},\pi} < 0.7, 0.3, 0.1$ cm and $\cos(\theta_{pointing}) > 0.94, 0.99, 0.995$, reported on top of each plot. Fit are performed with sum of a gaussian (signal) and a pol3 (background).

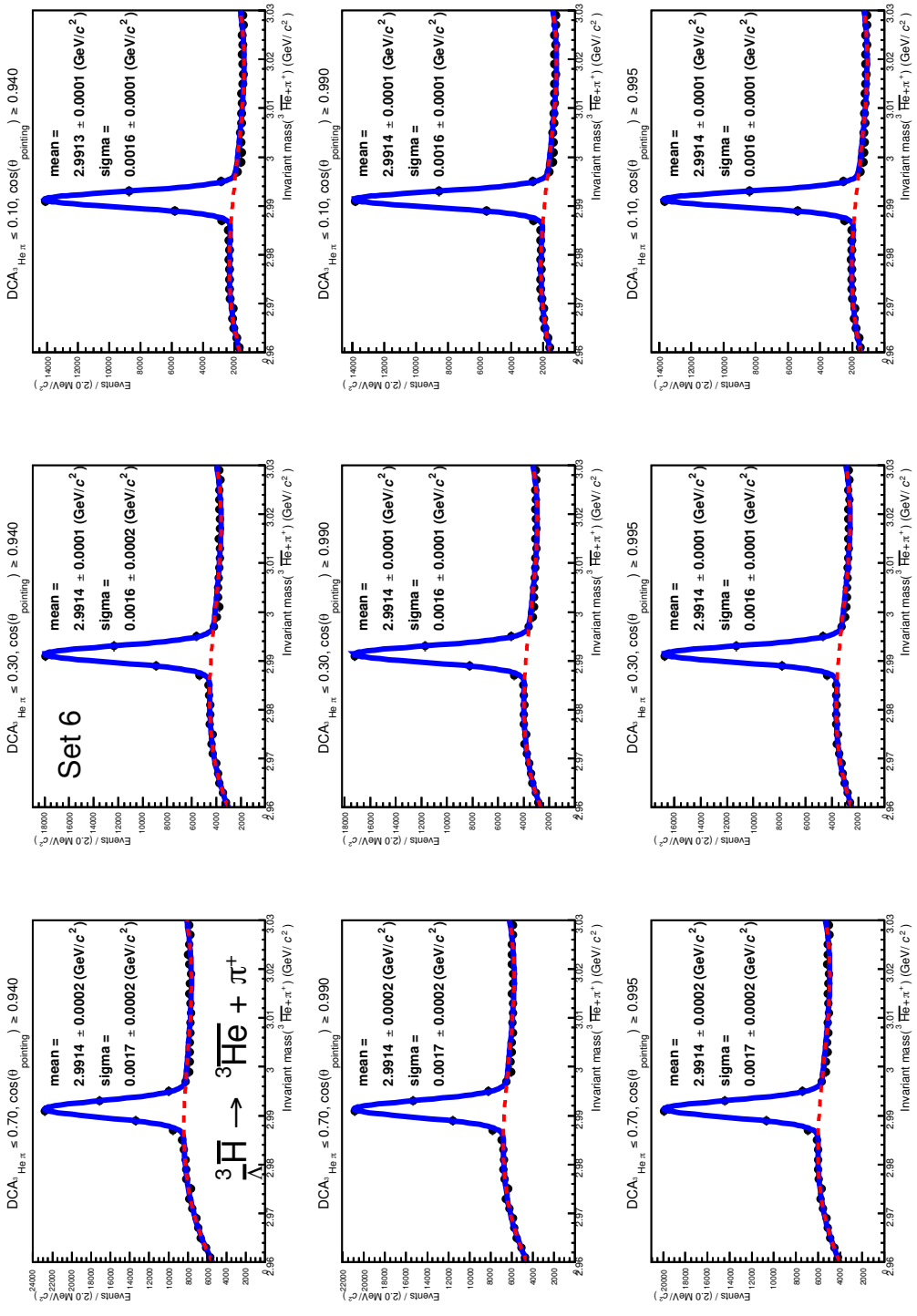

Figure A.14: $^3_{\Lambda}\overline{H}$ invariant mass spectra from Set 6. Fixed cuts: $DCA^{\pi}_{PV} > 0.4$ cm, $ct > 0.5$ cm and $|y| < 0.5$. Cut variation: $DCA_{^3He,\pi} < 0.7, 0.3, 0.1$ cm and $\cos(\theta_{pointing}) > 0.94, 0.99, 0.995$, reported on top of each plot. Fit are performed with sum of a gaussian (signal) and a pol3 (background).

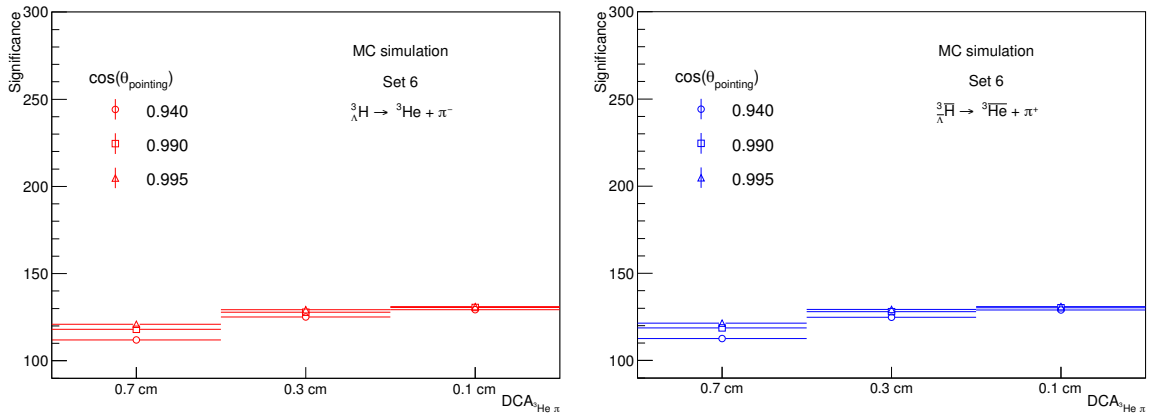

(a) Significance – ${}^{3}_{\Lambda}\mathrm{H}$

(b) Significance – ${}^{3}_{\overline{\Lambda}}\overline{\mathrm{H}}$

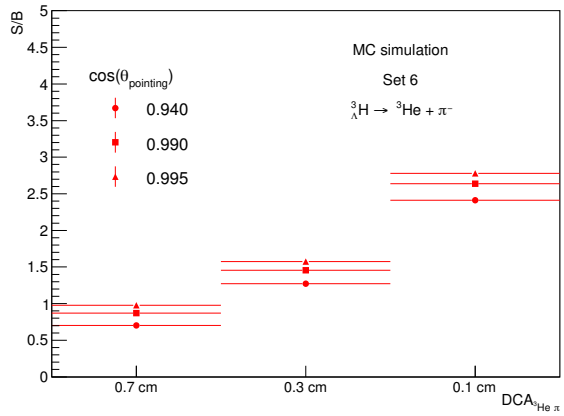

(c) S/B – ${}^{3}_{\Lambda}\mathrm{H}$

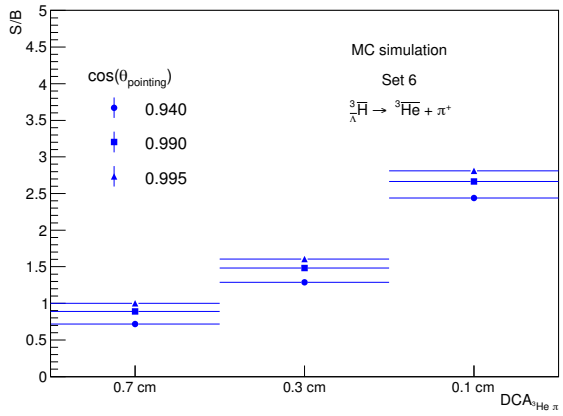

(d) S/B – ${}^{3}_{\overline{\Lambda}}\overline{\mathrm{H}}$

Figure A.15.: Trend of the Significance (top) and S/B ratio (bottom) for ${}^{3}_{\Lambda}\mathrm{H}$ (left) and ${}^{3}_{\overline{\Lambda}}\overline{\mathrm{H}}$ (right) reconstructed and selected with cuts of Set 6.

Appendix B.

Spectrum distributions

Several distributions are used in this thesis and for different purposes: to fit the $(^{3}_{\Lambda}\overline{\mathrm{H}})^{3}_{\Lambda}\mathrm{H}$ p_{T} spectra, to evaluate the weighted average for the efficiency, to extrapolate the yields in the unmeasured p_{T} region and to perform the study of systematic uncertainties. In this appendix these functions are shortly described.

B.1. Blastwave

The Blastwave distribution is based on the phenomenological model for hadronic matter production in heavy ion collisions, published in [20]. The distribution is written as:

$$\frac{1}{p_{\mathrm{T}}}\frac{\mathrm{d}N}{\mathrm{d}p_{\mathrm{T}}} \propto \int_{0}^{R} r\mathrm{d}r m_{\mathrm{T}} I_{0}\left(\frac{p_{\mathrm{T}} sinh\rho}{T_{kin}}\right) K_{1}\left(\frac{m_{\mathrm{T}} cosh\rho}{T_{kin}}\right) \tag{B.1}$$

where the parameter ρ contains the dependence on the velocity profile, since it is expressed as:

$$\rho = tanh^{-1}\left(\left(\frac{r}{R}\right)^{n}\beta_{\mathrm{T}}\right) \tag{B.2}$$

In the previous equations, $m_{\mathrm{T}} = \sqrt{p_{\mathrm{T}}^{2} + m^{2}}$ is the transverse mass, I_0 and K_1 the modified Bessel functions, r is the radial distance on the transverse plane, T_{kin} is the kinetic freeze-out temperature, β_{T} is the average transverse velocity and n is the exponent of the velocity profile.

B.2. Boltzmann

$$\frac{1}{p_{\mathrm{T}}}\frac{\mathrm{d}N}{\mathrm{d}p_{\mathrm{T}}} \propto N \cdot p_{\mathrm{T}} \cdot \sqrt{p_{\mathrm{T}}^2 + m_{\mathrm{T}}^2} \cdot exp\left(-\frac{\sqrt{p_{\mathrm{T}}^2 + m^2}}{T}\right) \tag{B.3}$$

where N is the normalization factor, p_{T} is the transverse momentum, m and m_{T} are the mass and the transverse mass of the particle and T is a parameter identified with the temperature.

B.3. m_{T} exponential

$$\frac{1}{p_{\mathrm{T}}}\frac{\mathrm{d}N}{\mathrm{d}p_{\mathrm{T}}} \propto N \cdot p_{\mathrm{T}} \cdot exp\left(-\frac{\sqrt{p_{\mathrm{T}}^2 + m_{\mathrm{T}}^2}}{T}\right) \tag{B.4}$$

where N is the normalization factor, p_{T} is the transverse momentum, m_{T} is the transverse mass of the particle and T is a parameter identified with the temperature.

B.4. exponential

The simple exponential as a function of p_{T} is written as:

$$\frac{1}{p_{\mathrm{T}}}\frac{\mathrm{d}N}{\mathrm{d}p_{\mathrm{T}}} \propto N \cdot p_{\mathrm{T}} \cdot exp\left(-\frac{p_{\mathrm{T}}}{T}\right) \tag{B.5}$$

where N is the normalization factor, p_{T} is the transverse momentum and T is a parameter identified with the temperature of the system created in the collision.

B.5. Fermi-Dirac and Bose-Einstein

These two distributions are taken from the corresponding statistics of Bose-Einstein and Fermi-Dirac, which are written as:

$$\frac{1}{p_{\mathrm{T}}}\frac{\mathrm{d}N}{\mathrm{d}p_{\mathrm{T}}} \propto N \cdot p_{\mathrm{T}} \cdot \frac{1}{\left(exp\left(\frac{\sqrt{p_{\mathrm{T}}^2+m^2}}{T}\right) \pm 1\right)} \tag{B.6}$$

where the plus in the exponent is for a Fermi-Dirac distribution, while the minus is used in the Bose-Einstein distribution. N is the normalization factor, p_{T} is the transverse momentum, m is the mass of the particle and T is a parameter identified with the temperature.

Bibliography

[1] M. Gell-Mann, Phys. Lett. **8**, 214 (1964).

[2] G. Zweig, An SU(3) model for strong interaction symmetry and its breaking. Vers. 2, in *Developments in the quark theory of hadrons. VOL. 1. 1964 - 1978*, edited by D. Lichtenberg and S. P. Rosen, pp. 22–101, 1964.

[3] H. Fritzsch and M. Gell-Mann, eConf C **720906V2**, 135 (1972).

[4] H. Fritzsch, M. Gell-Mann, and H. Leutwyler, Phys. Lett. **B47**, 365 (1973).

[5] Particle Data Group, C. Patrignani *et al.*, Chin. Phys. C **40**, 100001 (2016 and 2017 update).

[6] K. G. Wilson, Phys. Rev. D 10, 2445 (1974).

[7] T. Boeckel and J. Schaffner-Bielich, Phys. Rev. D 85, 103506 (2012).

[8] M. Fromerth and J. Rafelski, astro-ph/0211346, (2003).

[9] M. G. Alford, A. Schmitt, K. Rajagopal, and T. Schafer, Rev. Mod. Phys. **80**, 1455 (2008).

[10] A. Chodos, R. L. Jaffe, K. Johnson, C. B. Thorn, and V. F. Weisskopf, Phys. Rev. D 9, 3471 (1974).

[11] F. Becattini, *An introduction to the Statistical Hadronization Model* - international school on *Quark-Gluon Plasma and Heavy Ion Collisions: past, present, future*, torino, december 8-14, 2008, (2009).

[12] M. Bluhm, P. Alba, W. Alberico, A. Beraudo, and C. Ratti, Nuc. Phys. **A929**, 157 (2014).

[13] H. Satz, Phys. Rep. **403**, 33 (2004).

[14] M. L. Miller, K. Reygers, S. J. Sanders, and P. Steinberg, Ann. Rev. Nucl. Part. Sci. **57**, 205 (2007).

[15] U. Heinz, *Concepts of heavy ion physics* - european school of of *High-energy physics*, pylos, 2002 - proceedings, (2004).

[16] C. Gale, S. Jeon, and B. Schenke, Int. J. Mod. Phys **A28**, 1340011 (2013).

[17] STAR, B. I. Abelev *et al.*, Phys. Rev. C **79**, 034909 (2009).

[18] PHENIX, S. S. Adler *et al.*, Phys. Rev. C **69**, 034909 (2004).

[19] ALICE, B. Abelev *et al.*, Phys. Rev. Lett. **109**, 252301 (2012).

[20] E. Schnedermann, J. Sollfrank, and U. Heinz, Phys. Rev. C **48**, 2462 (1993).

[21] Y. A. Karpenko and Y. M. Sinyukov, J. Phys **G38**, 124059 (2011).

[22] P. Bozek, Phys. Rev. C 85, 034901 (2012).

[23] A. M. Poskanzer and S. A. Voloshin, Phys. Rev. C 58, 1671 (1998).

[24] ALICE, J. Adam *et al.*, Phys. Rev. Lett. **116**, 132302 (2016).

[25] B. Andersson, G. Gustafson, and B. Söderberg, Zeitschrift für Physik C Particles and Fields **20**, 317 (1983).

[26] P. Koch, B. Muller, and J. Rafelski, Phys. Rept. **142**, 167 (1986).

[27] STAR, J. Adams *et al.*, Phys. Rev. Lett. **92**, 182301 (2004).

[28] STAR, J. Adams *et al.*, Phys. Rev. Lett. **98**, 62301 (2007).

[29] STAR, J. Adams *et al.*, Phys. Rev. C **77**, 044908 (2008).

[30] ALICE, B. Abelev *et al.*, Phys. Rev. Lett. **111**, 222301 (2013).

[31] ALICE, B. Abelev *et al.*, Phys. Lett. B **728**, 216 (2014), erratum **734**, 409 (2014).

[32] F. Becattini and G. Pettini, Phys. Rev. C 67, 015205 (2003), hep-ph/0204340.

[33] T. Sjöstrand, S. Mrenna, and P. Skands, Comp. Phys. Comm. **178**, 852 (2008), 0710.3820.

[34] T. Pierog, I. Karpenko, J. M. Katzy, E. Yatsenko, and K. Werner, Phys. Rev. C 92, 034906 (2015), 1306.0121.

[35] C. Bierlich and J. R. Christiansen, Phys. Rev. D 92, 094010 (2015), 1507.02091.

[36] ALICE, J. Adam *et al.*, Nature Physics **13**, 535 (2017).

[37] CMS, V. Khachatryan *et al.*, JHEP **04**, 39 (2017).

[38] ALICE, J. Adam *et al.*, JHEP **03**, 81 (2016).

[39] H. Chung, J. Lee, and D. Kang, J. Korean Phys. Soc. **52**, 1151 (2008).

[40] HotQCD, A. Bazavov *et al.*, Phys. Rev. D 90, 094503 (2014), 1407.6387.

[41] CMS, A. M. Sirunyan *et al.*, (2017), 1706.05984.

[42] ALICE, B. Abelev *et al.*, Phys. Rev. Lett. **109**, 072301 (2012), 1202.1383.

[43] P. Braun-Munzinger and J. Stachel, Phys. Lett. B **490**, 196 (2000), nucl-th/0007059.

[44] E07, J. Yoshida *et al.*, J. Phys. Ser. Conf. Proc. **18**, 011030 (2017).

[45] E05, T. Gogami *et al.*, J. Phys. Ser. Conf. Proc. **18**, 011031 (2017).

[46] M. Danysz and J. Pniewsky, Phil. Mag. **44**, 348 (1953).

[47] O. Hashimoto and H. Tamura, Prog. Part. Nuc. Phys. **57**, 564 (2006).

[48] W. Alberico and G. Garbarino, Phys. Rep. **369**, 1 (2002).

[49] J. M. Lattimer and M. Prakash, Science **304**, 536 (2004).

[50] E. Botta, T. Bressani, and G. Garbarino, EPJ A **48**, 41 (2012).

[51] A. Feliciello and T. Nagae, Rep. Prog. Phys. **78**, 096301 (2015).

[52] R. Dalitz, Phys. Rev. **112**, 605 (1958).

[53] H. Park *et al.*, Phys. Rev. C **61**, 054004 (2000).

[54] M. Agnello *et al.*, Nucl. Phys. A **954**, 176 (2016).

[55] D. Davis, Nuc. Phys. A **7**54, 3 (2005).

[56] STAR, B. I. Abelev *et al.*, Science **328**, 58 (2010).

[57] H. Kamada, J. Golak, K. Miyagawa, H. Witała, and W. Glockle, Phys. Rev. C **57**, 1595 (1998).

[58] G. Bohm *et al.*, Nucl. Phys. B **16**, 46 (1970).

[59] M. Block *et al.*, Proc. of the International Conference on hyperfragments, St. Cergue 28-30 March, 1963.

[60] R. Prem and P. Steinberg, Phys. Rev. **136**, B1803 (1964).

[61] Y. Kang *et al.*, Phys. Rev. **139**, B401 (1965).

[62] G. Keyes *et al.*, Phys. Rev. Lett. **20**, 819 (1968).

[63] R. Phillips and J. Schneps, Phys. Rev. Lett. **20**, 1383 (1968).

[64] R. Phillips and J. Schneps, Phys. Rev. **180**, 1307 (1969).

[65] G. Keyes *et al.*, Phys. Rev. D **1**, 66 (1970).

[66] G. Keyes *et al.*, Nucl. Phys. B **67**, 269 (1973).

[67] S. Avramenko *et al.*, Nucl. Phys. A **547**, 95c (1992).

[68] J. Zhu *et al.*, Nucl. Phys. A **904**, 551c (2013).

[69] HypHI, C. Rappold *et al.*, Nuc. Phys. **A 913**, 170 (2013).

[70] ALICE, J. Adam *et al.*, Phys. Lett. B **754**, 360 (2016).

[71] R. Dalitz and M. Rayet, Il Nuovo Cim. A **46**, 786 (1966).

[72] J. Congleton, J. Phys. G, Nucl Part. Phys. **18**, 339 (1992).

[73] J. Kapusta, Phys. Rev. C **21**, 1301 (1980).

[74] E. Fermi, Prog. Theor. Phys. .

[75] R. Hagedorn, Nuovo Cim. Suppl. **3**, 147 (1965).

[76] R. Hagedorn, Nuovo Cim. **A56**, 1027 (1968).

[77] P. Braun-Munzinger, V. Koch, T. Schafer, and J. Stachel, Phys. Rep. **621**, 76 (2016), 1510.00442.

[78] P. Braun-Munzinger, K. Redlich, and J. Stachel, (2003), nucl-th/0304013.

[79] V. Vovchenko and H. Stoecker, J. Phys. Conf. Ser. **779**, 012078 (2017), 1610.02346.

[80] G. Torrieri *et al.*, Comput. Phys. Commun. **167**, 229 (2005), nucl-th/0404083.

[81] A. Andronic, P. Braun-Munzinger, J. Stachel, and H. Stocker, Phys. Lett. B **697**, 203 (2011), 1010.2995.

[82] S. Butler and C. Pearson, Phys. Rev. Lett. **7**, 69 (1961).

[83] A. Schwarzchild and C. Zupancic, Phys. Rev. **129**, 854 (1963).

[84] A. Mekjian, Phys. Rev. Lett. **38**, 640 (1977).

[85] J. Steinheimer *et al.*, Phys. Lett. B **7 14**, 85 (2012), 1203.2547.

[86] ATLAS, G. Aad *et al.*, Phys. Lett. B 716, 1 (2012).

[87] CMS, S. Chatrchyan *et al.*, Phys. Lett. B 716, 30 (2012).

[88] LHCb, R. Aaij *et al.*, Phys. Rev. Lett. **119**, 112001 (2017).

[89] X. Altuna *et al.*, **C**ERN-SL-96-023-OP, 4 (1996), http://cds.cern.ch/record/306911.

[90] CERN Machine Group, A. M. Asner *et al.*, CERN-DIR-TECH-84-01 , 75 (1984), https://cds.cern.ch/record/152775.

[91] CERN, The accelerator complex, https://cds.cern.ch/record/1997193, (2012).

[92] L. Evans and P. Bryant, Journal of Instrumentation **3**, S08001 (2008).

[93] L. Evans, Lecture Notes of the *Les Houches Summer School 'Theoretical Physics to Face the Challenge of LHC': Volume 97, August 2011* , 1 (2015).

[94] M. Giovanozzi, Lecture Notes of the *Les Houches Summer School 'Theoretical Physics to Face the Challenge of LHC': Volume 97, August 2011* , 35 (2015).

[95] O. S. Bruning *et al.*, LHC Design Report, http://cds.cern.ch/record/782076, (2004).

[96] ALICE, K. Aamodt *et al.*, JINST **308**, S08002 (2008).

[97] ALICE, P. Cortese *et al.*, J. Phys. **G30**, 1517 (2004).

[98] ALICE, C. W. Fabjan *et al.*, J. Phys. **G32**, 1295 (2006).

[99] ALICE, B. Abelev *et al.*, Int. J. Mod. Phys. **A29**, 1430044 (2014).

[100] F. Wittgenstein *et al.*, Construction of the L3 Magnet.

[101] ALICE, J. Adam *et al.*, JCAP **1601**, 032 (2016).

[102] ALICE, K. Aamodt *et al.*, JINST **503**, P03003 (2010).

[103] J. Alme *et al.*, Nucl. Instum. Meth., A **622**, 316 (2010).

[104] ALICE, J. Adam *et al.*, Eur. Phys. J. **132**, 99 (2017).

[105] ALICE, E. Abbas *et al.*, JINST **8**, P10016 (2013).

[106] C. W. Fabjan *et al.*, *ALICE trigger data-acquistion high-level trigger and control system* Technical Design Report ALICE (CERN, 2004).

[107] F. Carena *et al.*, Nucl. Instum. Meth., A **741**, 130 (2014).

[108] K. Mikolaj *et al.*, J. Phys. Conf. Ser. **664**, 082023 (2015).

[109] R. Brun *et al.*, *GEANT: Detector Description and Simulation Tool; Oct 1994*CERN Program Library (CERN, Geneva, 1993), Long Writeup W5013.

[110] S. Agostinelli *et al.*, Nucl. Instum. Meth., A **506**, 250 (2003).

[111] FLUKA, Manual online, https://www.fluka.org, (2010).

[112] R. Frühwirth, Nucl. Instum. Meth., A **262**, 444 (1987).

[113] WLCG, http://wlcg.web.cern.ch, (2017).

[114] AliEn, http://alien.web.cern.ch/.

[115] ROOT, http://www.root.cern.ch, (1995).

[116] M. Ivanov, I. Belikov, P. Hristov, and K. afaík, Nucl. Instum. Meth., A **566**, 70 (2006).

[117] W. Blum, W. Riegler, and L. Rolandi, *Particle Detection with Drift Chambers* 2nd ed. (Springer-Verlag, 2008).

[118] ALICE, S. Acharya *et al.*, (2017), 1710.07531.

[119] ALICE, B. Abelev *et al.*, Phys. Rev. C 88, 044909 (2013).

[120] X.-N. Wang and M. Gyulassy, Phys. Rev. D **44**, 3501 (1991).

[121] ALICE, J. Adam *et al.*, Phys. Rev. Lett. **116**, 222302 (2016).

[122] ALICE, J. Adam *et al.*, ALICE-PUBLIC-2015-008, https://cds.cern.ch/record/2118084, (2015).

[123] ALICE, J. Adam *et al.*, Phys. Rev. C **93**, 024917 (2016).

[124] M. Puccio, Private communication.

[125] ALICE, E. Abbas *et al.*, Eur. Phys. J C **73**, 2496 (2013).

[126] ALICE, K. Aamodt *et al.*, Phys. Rev. Lett. **105**, 072002 (2010).

[127] ALICE, J. Adam *et al.*, Phys. Lett. B **754**, 235 (2016), 1509.07324.

[128] M. Evlanov, A. Sokolov, V. Tartakovsky, S. Khorozov, and Y. Lukstinsh, Nucl. Phys. A **632**, 624 (1998).

[129] S. Kox *et al.*, Phys. Lett. B **159**, 15 (1985).

[130] N. Jacazio, Private communication.

[131] R. Barlow, Systematic errors: Facts and fictions, in *Advanced Statistical Techniques in Particle Physics. Proceedings, Conference, Durham, UK, March 18-22, 2002*, pp. 134–144, 2002, hep-ex/0207026.

[132] ALICE, S. Acharya *et al.*, (2018), 1802.09145.

[133] V. Verkerke and D. Kirkby, *RooFit users manual, v2.91*, 2008.

[134] L. Kreis, Master thesis.

[135] J. Neyman, Phil. Trans. R. Soc. Lond. A **236**, 333 (1937).

[136] S. S. Wilks, Ann. Math. Statist. **9**, 60 (1938).

[137] ALICE, S. Acharya *et al.*, Eur. Phys. J C **77**, 658 (2017), 1707.07304.

[138] STAR, L. Adamczyk, (2017), arXiv:1710.00436.

[139] C. Rappold *et al.*, Phys. Lett. B 728, 543 (2014).

[140] ALICE, B. Abelev *et al.*, J. Phys. G **41**, 087002 (2014).

[141] ALICE, C. Lippmann *et al.*, *Upgrade of the ALICE Time Projection Chamber*, http://cds.cern.ch/record/1622286, (2014).

[142] G. Chen, H. Chen, J. Wu, D.-S. Li, and M.-J. Wang, Phys. Rev. C **88**, 034908 (2013).

[143] R. Scheibl and U. Heinz, Phys. Rev. C **59**, 1585 (1999), nucl-th/9809092.

[144] M. Floris, Nuc. Phys. A **931**, 103 (2014), QUARK MATTER 2014.

[145] J. Cleymans *et al.*, Phys. Rev. C **84**, 054916 (2011), 1105.3719.

[146] S. Pal and W. Greiner, Phys. Rev. C **87**, 054905 (2013).

[147] M. Petran, J. Letessier, V. Petracek, and J. Rafelski, Phys. Rev. C **8**8, 034907 (2013), 1303.2098.

[148] E864 Collaboration, T. A. Armstrong *et al.*, Phys. Rev. C **70**, 024902 (2004).

[149] M. Sefcik, Private communication.

[150] Z.-W. Lin, C. M. Ko, B.-A. Li, B. Zhang, and S. Pal, Phys. Rev. C **72**, 064901 (2005).

[151] G. Keyes, J. Sacton, J. Wickens, and M. Block, Nuc. Phys. B **6 7**, 269 (1973).

[152] K. Blum, K. C. Y. Ng, R. Sato, and M. Takimoto, Phys. Rev. D **96**, 103021 (2017).

[153] H. Liu *et al.*, Int. J. Mod. Phys. E **16**, 3280 (2007).

[154] NA49 Collaboration, T. Anticic *et al.*, Phys. Rev. C **94**, 044906 (2016).

[155] S. Wheaton, J. Cleymans, and M. Hauer, Comp. Phys. Comm. **180**, 84 (2009).

[156] A. Andronic, Private communication.

[157] B. Hyppolite, Private communication.

[158] B. Doenigus, Private communication.

Acknowledgements

These three years have been a long journey with many good times and also some hard moments, which I lived together with many people that I wish to thank.
First of all I would like to thank Elena Botta and Stefania Bufalino, not only for their supervision but also for the extraordinary support and useful suggestions provided during all my activities.
I want to thank Massimo Masera and Francesco Prino, who have always spent some time to discuss with me about the reconstruction, the analysis techniques and the comparison with the theoretical models.
I would like to deeply thank Stefania Beolè, Elena Bruna, Alessandro Bruno, Luciano Ramello and Mario Sitta for the help and the support I received during these three years in many different aspects: from the statistics to the building of the new ITS, from the data analysis to the on-call period at CERN.

All my colleagues in Torino deserve a special acknowledgements: Yasser Corrales, Livio Bianchi, Anastasia Barbano, Maximiliano Puccio, Fabrizio Grosa, Luca Barioglio, Ivan Ravasenga, Nicolò Jacazio... I'm really grateful for the discussions, all the time spent together and the long coffee breaks!

A special thank to Benjamin Doenigus who supported me during these three years and helped me a lot to learn more about the hypernuclei and light flavour physics.
A second special thank to the people of the ARC, in particular to Andrea Alici and Manuel Colocci, who really made the time I spent at CERN unique and enjoyable.

I would like to say a special "thank you" to Silvia for being close to me in these years, even when it was very hard and difficult. I also want to thank her family, Anna, Renato and Andrea for being an important presence in these three years.
An important and unique thank to my best friend Federico, who always remembered me that " life is a matter of black and white".

Finally I would like to thank my parents, Marco and Daniela, my brother, Enrico, for supporting me in every single moment and for being so patient the last three years.

Last but not least, I would like to thank Gianni, Luciana, Sergio and Stefanina, who have been present and have been my first supporter every single day.

S.T.

Torino, April 2018